AN NMR STUDY OF ADSORBED HELIUM· FILMS

by

ANTHONY J. KENT

Bedford College
Regent's Park
London

Submitted for the Degree of Doctor of Philosophy

to

The University of London 1985

To Dennis and Eileen Kent

My Parents

ABSTRACT

The properties of submonolayer Helium-3 films adsorbed on two totally different but planar substrates, Mylar† film and exfoliated graphite have been studied using NMR.

The nuclear magnetic relxation times T_1 and T_2 have been measured as functions of fractional monolayer completion, temperature, substrate plane orientation and Larmor frequency using a specially designed and constructed NMR spectrometer system.

The results obtained with a Mylar film substrate are consistent with the formation of patches of solid ^{3}He at regions of preferential adsorption on the substrate.

Measurements of T_2 in very low coverage ^{3}He films on exfoliated graphite also indicate that the adsorbate forms areas of relatively high density solid, in agreement with the thermodynamic analysis of Elgin and Goodstein.

Finally, detailed measurements of T_2 as a function of all of the above parameters at low areal densities will help us to characterise the relaxation processes for the fluid phase of ^{3}He on exfoliated graphite.

†Mylar is the tradename of poly(ethelene-terephthalate) film, marketed by Du Pont.

ACKNOWLEDGEMENTS

I wish to express my thanks to my supervisor, Dr. B.P. Cowan, for his assistance and direction. Thanks also to the Bedford College Physics Department and Professor E.R. Dobbs for providing support and facilities for the project.

Special thanks to the technical staff who assisted with this project, Mr. F.A. Grimes and Mr. A. King in the mechanical workshop, Mr. A. Betts in the electronics workshop and Mr. F.W. Greenough in our laboratory.

Thanks also to Mr. M.R. Evans in the Microprocessor Support Unit and the Computer Unit staff. Finally, thanks to my parents for their support and encouragement.

Financial support for myself and the projectfrom the S.E.R.C. is gratefully acknowledged.

CONTENTS

Page No.

INDEX TO DIAGRAMS AND GRAPHS

Tables

CHAPTER 1

INTRODUCTION

1.1 Why Study Adsorbed (Helium) Films ?

When we speak of an ADSORBED FILM we refer to a system consisting of a layer of particles of one substance, the adsorbate, held by attractive forces of a Van-der-Waals nature to the surface of a, normally solid, adsorber. The layer may be one or more particles thick on the surface. For a small group of substances, the noble gasses, the forces of attraction to most surfaces far outweigh the interactions between the gas atoms, these gasses therefore make ideal adsorbates.

In an adsorbed film motion of the adsorbate in a direction normal to the surface is restricted but lateral motion is allowed. If the adsorber is ideal, that is if its surface is perfectly smooth and uniform, there is no lateral variation of the adatom potential. The adsorber then serves only as a substrate to confine the adsorbate to a plane. We then have what is known as a quasi-two dimensional system.

The properties of two dimensional (2-D) systems have been of interest to theoreticians for many years [1]. It has been hypothesised that the reduced dimensionality gives rise to many new physical phenomena, and many effects found in bulk matter such as superfluidity and superconductivity are considered unlikely in two dimensions. The adsorbed films provide an opportunity to test these predictions. Furthermore, in the case of adsorbed Helium one has the opportunity to observe quantum effects in two dimensions. It is also possible to increase our understanding of the behaviour of conventional bulk matter by extending the experimental and theoretical findings in corresponding 2-D systems.

1.2 The Phases of Helium Adsorbed on Graphite

The properties of a wide range of different adsorbed systems have been investigated experimentally [2]. However it is found that there are very few substrates that even approximate to the ideal requirements of an exposed flat homogeneous crystalline surface, while still offering a sufficiently large surface to permit studies of adsorption. The most successful substrates tried to date include various forms of graphite such as graphitized carbon black [3] and exfoliated graphite. Both of these substrates offer exposed basal planes of graphite for adsorption. Vapor pressure isotherms [4] taken for a variety of adsorbates on these substrates show a stepwise behaviour, consistent with the formation of distinct layers of the adsorbate on the surface as predicted theoretically [5]. It was discovered in the case of exfoliated graphite that these steps were sharper and there were also observed sub-step details thought to be due to the formation of various surface phases in the film. These differences are due to the rather larger areas of exposed basal plane in exfoliated graphite, about 100Å across on average.

From detailed thermodynamic measurements made by many groups it has been possible to construct an impressive phase diagram for submonolayer Helium adsorbed on Grafoil†, see figure (1.1). The main elements of this phase diagram are :

Coverage, X < 0.1 Monolayer ; Inhomogeneity

Careful vapor pressure measurements in this region [6] have indicated that a small proportion of the Grafoil surface (∿ 2%)

† Grafoil is the tradename for commercially available exfoliated graphite, manufactured and marketed by the Union Carbide Corporation, Carbon Products Division, New York, U.S.A.

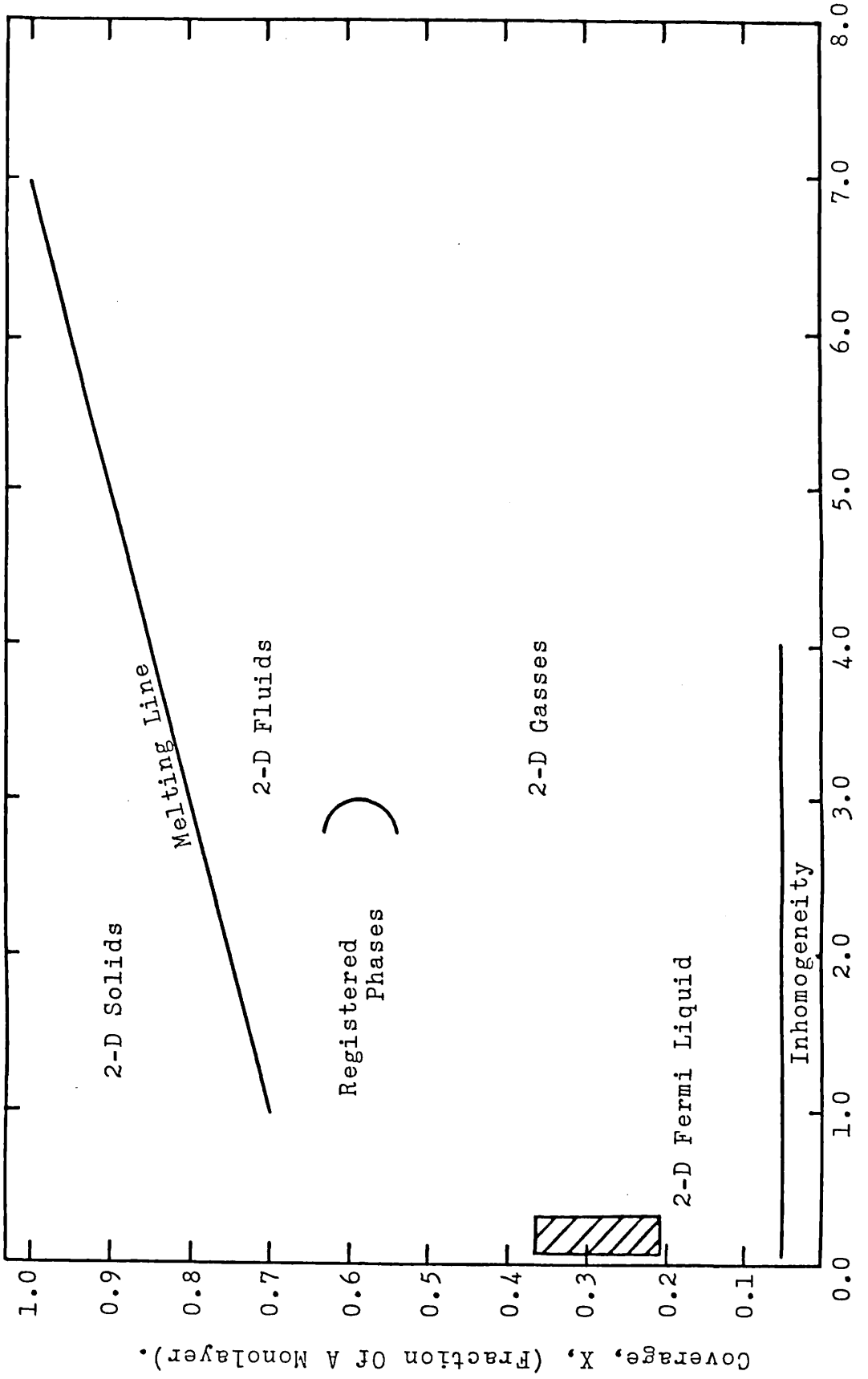

Figure 1.1, The Phase Diagram For Helium-3 Adsorbed On Grafoil.

provides for preferential adsorbtion. Relatively immobile patches of Helium atoms form at these regions which dominate the properties of such low coverage films.

$0.1 < X < 0.4$; The 2-D gas phase

Specific heat measurements at coverages in this range [7] [8] show the specific heat to be equal to k_B per atom, as expected for a 2-D gas. Adsorption isotherm measurements [9] in this range of coverage show the isoteric heat of adsorption to be nearly independent of coverage and in the region of 160K. The substrate serves only to confine the adatoms to the plane, in which they are effectively free and highly mobile.

$0.4 < X < 0.7$;

Apart from special properties near $X = 0.6$, this region is essentially an extension of the 2-D gas phase. However, due to the increased density adatom-adatom interactions play a larger part in determining the properties of the film.

$X \simeq 0.6$; Registered Phase

A series of specific heat peaks observed at temperatures near 3K at this coverage [8] [10] [11] are associated with a second order phase transition from an irregular 2-D gas to an ordered lattice in registry with the substrate. There are just enough Helium atoms present to occupy one out of three of the carbon hexagon sites in the basal planes, forming a triangular lattice with spacing 4.2Å. These conclusions are supported by the results of neutron diffraction experiments [12], in which Bragg peaks have been observed indicating an ordered structure of the type described.

0.7 < X < 1 ; The Solid Phase

Specific heat measurements [8] [13] in this range of coverages indicated a T^2 law as predicted for a 2-D Debye type solid. Neutron scattering results [12] supported this and showed the solid to have a triangular lattice structure. At higher temperatures specific heat anomalies were observed which were associated with the solid melting. Adsorption isotherm measurements near monolayer completion (X = 1) [14] gave the monolayer coverage for ^{3}He on bare Grafoil as 0.395 cm^3 (STP)/m^2 which represents an areal density of 0.106 atoms $\mathring{A}^{-2}$ equivalent to an interatomic separation 3.27$\mathring{A}$ at X = 1. To achieve this separation in bulk ^{3}He would require a pressure of 400 bar.

X > 1 ; Multilayer Films

The stepwise behaviour of the adsorption isotherms indicated the formation of distinct layers of adatoms. At low densities the second layer behaves as an imperfect 2-D gas [15], however, it appears that when some third layer atoms are present the second layer solidifies at temperatures below 0.98K and 2K for ^{3}He and ^{4}He respectively [16] [17]. At about X = 4 it appears [18] that bulk condensation begins to take place.

1.3 NMR Studies of Adsorbed ^{3}He

Nuclear Magnetic Resonance (NMR) is a technique that is able to yield fairly directly information regarding the dynamics of the surface film, through the effect of the spectrum of local field fluctuations experienced by the adatoms as they move on the surface. In order to obtain sufficient signal to perform an NMR experiment, of the order tens of m^2 of adsorption surface are required, hence

the necessity for porous substrates of high specific surface area.

The first reported observation of NMR in adsorbed ^{3}He films was made in 1963 [19] since then the technique has been applied in a wide range of experimental situations [20]. Early work was carried out on 13x zeolite molecular sieve substrates [21] [22], these consist of many small interconnected pores about 13Å in diameter. Later a porous glass, Vycor consisting of pores 70Å in diameter was used [23]. Both these substrates suffered from surface heterogeneity, in that for coverages less than a complete monolayer the adsorbed films displayed localised solid behaviour. Another problem with these substrates is that the orientation of the adsorption surface with respect to the applied field, a parameter important in the interpretation of the results, is isotropic. A C.W. NMR study of ^{3}He adsorbed on carbon black has been carried out at a Larmor frequency of 20.5 MHz [24]. Broad lines were observed, the breadth being dependent on both temperature and coverage. The results were interpreted in terms of the high density submonolayer films being solid with some internal motion due to thermally activated vacancies and or quantum tunnelling. At $X \simeq 0.6$ (Registry) linewidths of 1 gauss were obtained indicating a 2-D solid with lattice spacing 4.2Å.

Many groups have performed NMR experiments on ^{3}He adsorbed on Grafoil, the results have complemented the thermodynamic measurements discussed briefly in §1.2. Recalling the phase diagram (figure 1.1), what follows is a brief summary of previous contributions of NMR to our understanding of the various phases of adsorbed ^{3}He :

$X < .1$;

Little NMR data has been taken at such low coverages due to small signal size. That which has been obtained [25] suggests that the properties of the film may be dominated by a small fraction of the adsorbate which remains relatively immobile at regions of preferential

adsorption in the substrate, in possible agreement with thermodynamic data.

$.1 < X < .6$;

NMR measurements of magnetic susceptibility χ and nuclear magnetic relaxation times T_1 and T_2 (see Chapter 3) over this range of coverage have supported 2-D gas like behaviour.

The susceptibility measurements [25] [26] [27] [28] show Curie's Law to be obeyed down to temperatures of the order (1-2)K where the onset of quantum degeneracy is observed. It is claimed that the second virial coefficient theory best explains the departures from Curie's Law for $X \lesssim 0.3$.

The relaxation times are found to be proportional to the square root of absolute temperature at Larmor frequencies around 1 MHz [25]. As a rule of thumb, T_2 is proportional to τ_c^{-1}, τ_c being the characteristic time for a spin to sample dipolar or other local fields, and for a classical 2-D gas τ_c^{-1} is proportional to $\sqrt{T}$. This $\sqrt{T}$ dependence was not, however, observed at 10 MHz [29].

There is a problem with NMR measurements on the 2-D fluid phase on Grafoil, in that the relaxation times are found to be much shorter than they would be if the adatoms were experiencing only the dipolar fields of their neighbours in the film. This has been attributed [30] to the magnetic properties of the substrate; Grafoil consists of many small crystallites of Graphite between 1000 and 10,000 Å across, about 100 Å thick and separated by voids about 100 Å wide. These crystallites or platelets are mis-orientated in the plane, the RMS mis-orientation being about 24°. Graphite has a highly anisotropic diamagnetic susceptibility [31], it being some 60 times stronger along the c-axis than in other directions. So as the adatoms diffuse rapidly through the Grafoil they relax by sampling the inhomogeneous local fields set up around the crystallites.

Furthermore, Grafoil contains some paramagnetic impurities which can provide a strong spin-lattice relaxation mechanism at low areal densities.

Relaxation by diffusion in Grafoil local fields is expected to lead to T_2^{-1} being proportional to the square of the Larmor frequency or applied field. As a general rule of thumb $T_2^{-1} \simeq \gamma^2 \langle b_{loc}^2 \rangle \tau_c$ where in this case the mean square local fields $\langle b_{loc}^2 \rangle \propto B_o^2$ where B_o is the applied field. However, measurements at 0.3, 1 and 2 MHz, [25] showed T_2^{-1} to vary approximately linearly with frequency with the T_2 values obtained at 10 MHz [29] lying on the same line. It appears then that the relaxation processes in the 2-D fluid phase are not yet fully understood and this could be a problem if NMR is to be used to study the degenerate 2-D Fermi liquid phase which may be present at lower temperatures.

$X \simeq 0.6$, Registry

Near to this coverage sharp dips in the values of T_2 at 10 MHz [29] and T_1 at 1 MHz [25] were observed, the values being a minimum somewhere near X = 0.58 (perfect registry). No dips were observed in T_1 at 10 MHz or T_2 at 1 MHz. This difference is attributed to the effect of the substrate local fields. The dips result from a slowing of the motion of the adatoms as the registered solid phase is formed. The minimum values of T_1 indicated that rapid quantum tunnelling was occurring in the solid, tunnelling frequency $J/2\pi \simeq 1.5$ MHz. At coverages slightly above and below perfect registry an activation energy law has been used to explain the thermal activation of interstatials or vacancies which then tunnel through the lattice increasing the relaxation time.

$0.7 < X < 1$; Incommensurate Solid

NMR measurements of the magnetic susceptibility χ [25] [26] show Curie's Law behaviour as expected for a 2-D solid with departures at the lowest temperatures being attributed to RF heating of the sample, more of a problem in the solid due to the low specific heat capacity. Nuclear magnetic relaxation time measurements [25] [29] [32] show the solid to be more interesting than thermodynamic or other methods could indicate. There is, as expected, a reduction in the relaxation times but not to the rigid lattice value. This is due to the effects of quantum exchange in the solid, the estimated exchange values decreasing from 10^7 sec^{-1} at $X = 0.7$ to 10^5 sec^{-1} at $X = 1$. No marked changes in the relaxation times are observed at melting though there is some evidence from NMR data [20] that the Kosterlitz Thouless model of melting [33] in 2-D, in which the solid first melts to a hexatic liquid crystal phase and then to a homogeneous fluid with no sudden changes, is applicable to the ^3He films on Grafoil.

$X > 1$;

Following the completion of the first layer the relaxation times start to rise rapidly. It has been found [34], that for small amounts of second layer present rapid interlayer exchange is taking place but this seems to slow up as more second layer atoms are added and the relaxation becomes non-exponential. It is also concluded from NMR measurements that the second layer does not solidify as at first thought, when third layer atoms are present.

In conclusion, therefore, we can see that NMR techniques provide a unique means of furthering our understanding of adsorbed Helium films and a large amount of useful work has been done. However,

there are still some questions to be answered using NMR, such as what is the behaviour of the very low coverage films, and what are the relaxation processes in the 2-D gas phase. The present work will be partly concerned with these problems.

1.4 Mylar Film. A Possible Substrate for NMR Work

It has already been mentioned in §1.3 that the magnetic properties of Grafoil are apt to cause difficulties in NMR experiments. There is therefore a need for a substrate that is non-magnetic, but which unlike other non-magnetic substrates used in the past (Vycor, Zeolite), has a planar adsorption surface. It was decided that Mylar film might be a suitable candidate.

Mylar (Du-Pont) or Melinex (ICI) are tradenames for Poly(ethylene terephtalate) film, the chemical structure is shown below :

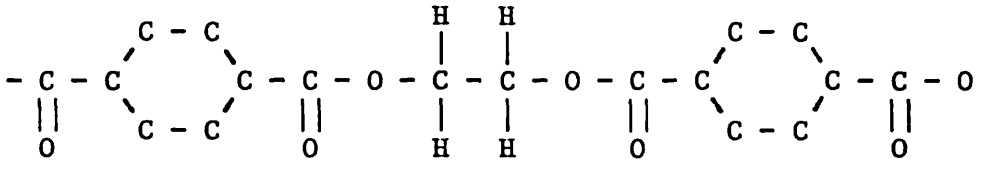

On a macroscopic scale the surface is fairly flat as shown in the electron micrographs of optical grade mylar, figure 1.2, though about 5-6% of the surface is interrupted by mounds or crater-like defects (there is also a certain amount of dust and dirt visible in the lower magnification picture). On an atomic scale, however, the surface can be expected to be somewhat amorphous unlike the perfect crystalline surfaces of the exposed basal planes in Grafoil. This will not be a problem so long as the lateral fluctuations in the Van-der-Waals potential between the surface and the adatoms are separated by distances small compared to the thermal De-Broglie wavelength of the adatoms (about 10Å for ^{3}He @ 1K).

.1mm

1μm

Figure 1.2, Electron Micrographs Of Surface Of Optical Grade Mylar Film. (The large crater in the higher magnification picture is beam damage)

Adsorption isotherm studies of ^{4}He on Mylar film [18] have indicated that the surface is relatively heterogeneous with an isoteric heat of adsorption of approximately 75K. It was also reported [18] that the tight packing of Mylar sheets reduced gas transport. The monolayer coverage is approximately 0.354 $cm^3(STP)/m^2$ about 16% less than for Helium on Grafoil.

CHAPTER 2

THE THEORY OF NMR IN 2-D SYSTEMS

2.1 Introduction

In this chapter the theory of NMR in 2-Dimensional (2-D) systems is presented. There are some striking differences between the proposed NMR behaviour of 2-D systems and the corresponding bulk systems. Such as the anisotropy in the relaxation times with respect to the orientation of the substrate plane in the applied field B_o. Also, the partial degeneracy of the dipolar Hamiltonian with respect to rotational motion means that in the case of rapid diffusion only the translational component of the motion can effectively average the dipolar fields. This gives rise to a long t^{-1} tail on the dipolar autocorrelation function instead of a $t^{-3/2}$ tail in the case of bulk systems. This long time tail results in a logarithmic divergence of the dipolar spectral density function as $\omega \to 0$. However, when the normal to the substrate plane makes an angle of $\cos^{-1} \sqrt{1/3}$ with B_o the long tail disappears and these functions are well behaved. Various theories have differed in their treatment of this anomalous behaviour and the different approaches will be compared in this chapter.

The reader should note that the equations in this chapter have been written with the SI system of units in mind, rather than c.g.s. as is found in most of the literature. Hence, B is in Tesla, γ in $sec^{-1}Tesla^{-1}$, d in metres etc.,

2.2 Pulse NMR, an introduction

Consider an assembly of like spins within a static magnetic field B_o, orientated along the z-axis. The Hamiltonian operator $\mathcal{H}$ for the system can be decomposed in the following manner,

$$\mathcal{H} = \mathcal{H}_z + \mathcal{H}_d + \mathcal{H}_m \qquad (2.2.1)$$

where $\mathcal{H}_z$ is the pure spin or Zeeman Hamiltonian,

$$\mathcal{H}_z = \hbar\gamma I_z B_o = \hbar\omega_o I_z \qquad (2.2.2)$$

γ is the magnetogyric ratio, I_z the z component of the spin angular momentum operator, and ω_o the Larmor frequency of precession of the transverse spin components I_+ and I_-.

The Hamiltonian $\mathcal{H}_m$ represents the energy of all the non spin degrees of freedom, principally, the particle motion. Since $\mathcal{H}_z$ and $\mathcal{H}_m$ operate in disjoint spaces it is evident that they must commute.

$$[\mathcal{H}_z, \mathcal{H}_m] = 0 \qquad (2.2.3)$$

The remaining term $\mathcal{H}_d$ represents the interaction between $\mathcal{H}_z$ and $\mathcal{H}_m$ and is commonly the internuclear magnetic dipolar interaction.

In thermal equilibrium the system can be represented by a density operator [35] taking the Boltzmann form,

$$\rho_{eq} = \frac{\exp - \beta\mathcal{H}}{\mathrm{Tr}\ \{\exp - \beta\mathcal{H}\}} \qquad (2.2.4)$$

where $\beta = {}^{1}/_{kT}$, T is the absolute temperature. Now $\mathcal{H}_d$ is sufficiently small to be ignored in ρ for the present, and since the remaining two components $\mathcal{H}_z$ and $\mathcal{H}_m$ commute ρ may be factorised.

$$\rho_{eq} = \frac{\exp - \beta \mathcal{H}_m}{Tr\ \{\exp - \beta \mathcal{H}_m\}} \cdot \frac{\exp - \beta \mathcal{H}_z}{Tr\ \{\exp - \beta \mathcal{H}_z\}} \qquad (2.2.5)$$

At high spin temperatures, i.e. low spin polarization we are in the Curie Law region and are permitted to approximate ρ_{eq} by [36] ,

$$\rho_{eq} = \rho_m\ (1 - \beta\omega_o I_x)/Tr\{1\} \qquad (2.2.6)$$

The equilibrium magnetization M_z is given in terms of $\langle I_z \rangle$,

$$M_z = \frac{1}{\mu_o} N\gamma\hbar\langle I_z \rangle \qquad (2.2.7)$$

where N is the number of spins per unit volume and the expectation value of the z component of the angular momentum is given by

$$\langle I_z \rangle = Tr\ \{\rho_{eq} I_z\}. \qquad (2.2.8)$$

If a solenoid coil is placed around the assembly of spins with its axis perpendicular to B_o, along the y-axis say, figure 2.1, and a strong pulse of R.F. current at frequency ω_o is passed through the windings, then a transverse field is produced about which the spins will precess. If the strength B_1 and duration τ of the pulse is such that the magnetization is tipped just 90^o away from the direction of B_o into the transverse plane, then we have applied what is known as a 90^o pulse, i.e.,

$$\gamma B_1 \tau = \pi/2 \qquad (2.2.9)$$

(a)

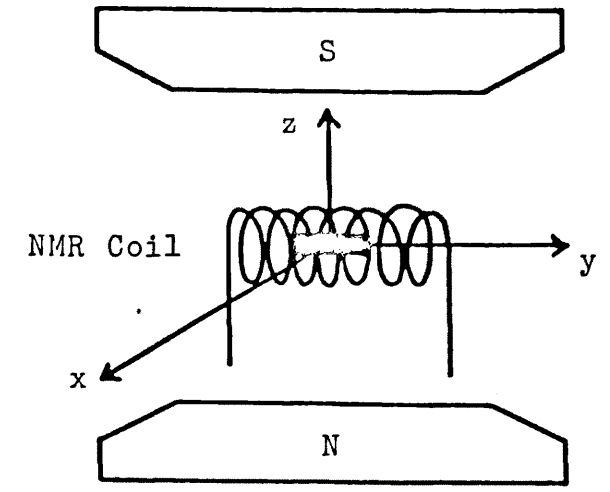

(b)

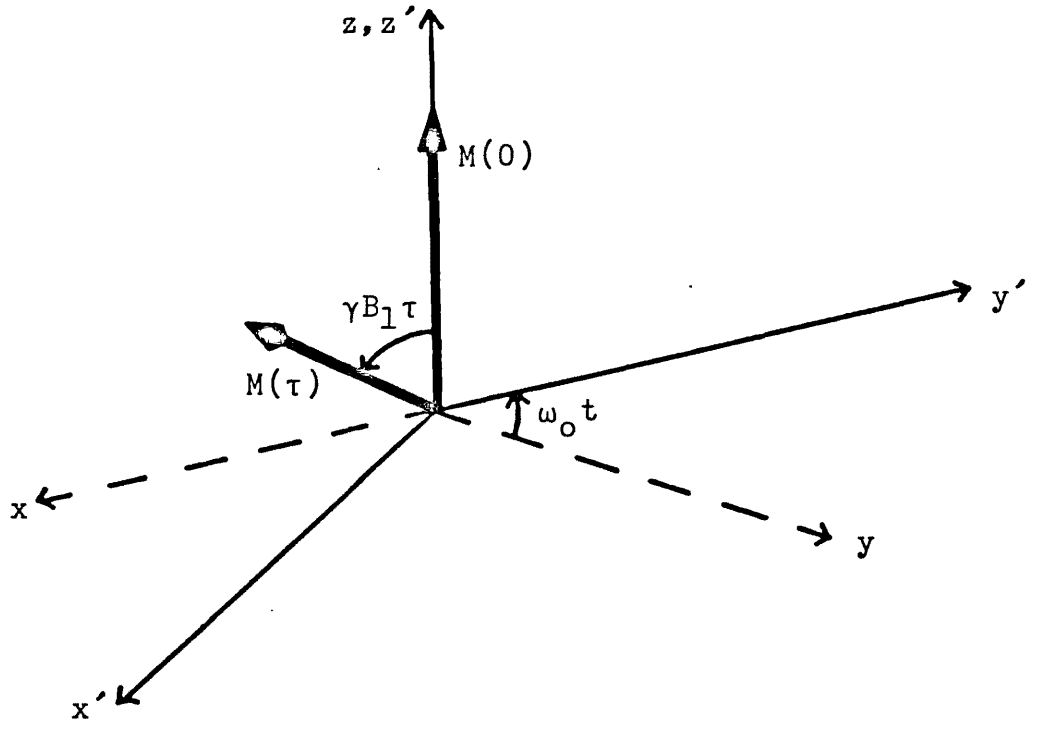

Figure 2.1, (a) Arrangement in the laboratory frame for the observation of pulse NMR.

(b) x′, y′ and z′ are a set of axes rotating at frequency ω_o w.r.t. the laboratory axes, in this frame of reference the RF pulse rotates the magnetization about the y′ axis by an angle $\gamma B_1 \tau$.

The magnetization, now in the transverse plane will precess about B_o inducing a voltage in the coil the amplitude of which is observed to decay in time as the spins dephase.

$$M_+(t) = M_x(t) + iM_y(t) = M_+(0)F(t)e^{i\omega_o t} \qquad (2.2.10)$$

This is known as the Free Induction Decay (F.I.D) and F(t) is the transverse relaxation function.

Now consider the effect of the 90^o pulse from the quantum mechanical point of view. The 90^o pulse transforms I_z into I_x and the equilibrium density operator ρ_{eq} becomes,

$$\tilde{\rho} = 1 - \beta\omega_o I_x/Tr\ \{1\} \qquad (2.2.11)$$

The ρ_m part of ρ_{eq} has been temporarily ignored since it is unaffected by operations in spin space. Now

$$M_+(t) = \frac{1}{\mu_o} N\gamma\hbar\langle I_+(t)\rangle \qquad (2.2.12)$$

therefore

$$M_+(t) = \frac{1}{\mu_o} N\gamma\hbar\ Tr\{\tilde{\rho}(t)\ I_+\} \qquad (2.2.13)$$

which leads to

$$F(t) = \exp - i\omega_o t\ Tr\ \{I_+(t)\ I_-\} / Tr\ \{I_+\ I_-\} \qquad (2.2.14)$$

If on the other hand a longer pulse is applied such that,

$$\gamma B_1 \tau = \pi \qquad (2.2.15)$$

this is called a 180^o pulse, which transforms M_z into $-M_z$. Following the pulse the longitudinal magnetization will, over a period of time, recover to its equilibrium value. The longitudinal magnetization does not, however, induce a voltage in the coil, so to observe the recovery of M_z it is necessary to apply a 90^o pulse some time after the 180^o pulse and observe the amplitude of the free induction decay following it. The 180^o pulse transforms I_z into $-I_z$ hence ρ_{eq} becomes,

$$\rho' = (1 + \beta\omega_o I_z) \;/\; \mathrm{Tr}\,\{1\} \qquad (2.2.16)$$

The system is allowed to relax for time t then a 90^o pulse is applied which is represented by the operator R such that $RI_zR^{-1} = I_x$,

$$\tilde{\rho}'(t) = R\rho'(t)\,R^{-1} \qquad (2.2.17)$$

the transverse magnetization following the pulse is given by

$$M_x = \frac{1}{\mu_o} N\gamma\hbar\ \mathrm{Tr}\,\{I_x R\rho'(t)\,R^{-1}\} \qquad (2.2.18)$$

Since the trace is invariant under cyclic permutations

$$M_x = \frac{1}{\mu_o} N\gamma\hbar\ \mathrm{Tr}\,\{R^{-1}I_x R\,\rho'(t)\} \qquad (2.2.19)$$

Now $R^{-1} I_x R = I_z$, and so the normalized longitudinal relaxation function L(t) is given by,

$$L(t) = \frac{Tr\ \{I_z\ I_z(t)\}}{Tr\ \{I_z^2\}} \qquad (2.2.20)$$

The time development of the spin angular momentum operators I_+ and I_z is generated by $\mathcal{H}$ according to the Heisenburg equation ,

$$\frac{\hbar}{i}\frac{dI(t)}{dt} = [\mathcal{H},\ I(t)] \qquad (2.2.21)$$

Transforming into the interaction representation, i.e., a frame of reference moving under the influence of $\mathcal{H}_z$ and $\mathcal{H}_m$, F(t) becomes,

$$F(t) = Tr\ \{I_+(t)I_-\}\ /\ Tr\ \{I_+I_-\} \qquad (2.2.22)$$

L(t) remains in the same form as eq. (2.2.20), but the time development of the spin operators is now generated according to,

$$\frac{\hbar}{i}\frac{dI(t)}{dt} = [\mathcal{H}_d^*(t),\ I(t)] \qquad (2.2.23)$$

where $\mathcal{H}_d^*$ is the dipolar Hamiltonian in the interaction representation,

$$\mathcal{H}_d^*(t) = e^{\frac{i}{\hbar}(\mathcal{H}_z + \mathcal{H}_m)t}\ \mathcal{H}_d\ e^{-\frac{i}{\hbar}(\mathcal{H}_z + \mathcal{H}_m)t} \qquad (2.2.24)$$

It is now possible to see how observing the time development of the magnetization of a sample following 90^o or 180^o pulses can lead to an understanding of the microscopic motions of the spins inside the sample. This is the great advantage of NMR over measurements of

thermodynamic quantities like specific heat.

2.3 General Properties of the Relaxation Functions. The Kubo Approach

In order to study the properties of the relaxation functions F(t) and L(t) it is appropriate to perform a perturbation expansion to some order in $\mathcal{H}_d^*(t)$. Unfortunately, even though $\mathcal{H}_d$ is small any expansion to a finite order in $\mathcal{H}_d^*$ diverges for long times. The Kubo [37] approach overcomes this difficulty by expanding the function $\psi(t)$ where

$$F(t) = \exp \psi(t) \tag{2.3.1}$$

to some order in $\mathcal{H}_d^*$. This ensures convergence as $t \to \infty$; it respresents an infinite series in which the high order terms are approximated in terms of the lower order ones. The expansion is carried as far as the first non vanishing term which is of the order $\mathcal{H}_d^{*2}$. This has the significance that the phase accumulated by the spins in the rotating frame is a Gaussian random function;the justification a consequence of the central limit theorem.

Performing the expansion and assuming that $\mathcal{H}_d^*$ is a stationary random process, leads to the results [38].

$$F(t) = \exp\left[-\int_o^t (t-\tau) \frac{\mathrm{Tr}\{[I_+, \mathcal{H}_d][\mathcal{H}_d^*(-\tau), I_-]\}}{\hbar^2 \, \mathrm{Tr}\{I_+ I_-\}} d\tau\right] \tag{2.3.2}$$

and similarly for L(t),

$$L(t) = \exp\left[-\int_o^t (t-\tau) \frac{\mathrm{Tr}\{[I_z, \mathcal{H}_d][\mathcal{H}_d^*(-\tau), I_z]\}}{\hbar^2 \, \mathrm{Tr}\{I_z^2\}} d\tau\right] \tag{2.3.3}$$

2.4 Evaluation of the Relaxation Functions

The internuclear magnetic dipolar Hamiltonian, $\mathcal{H}_d$, is given by

$$\mathcal{H}_d = \frac{\mu_o}{4\pi} \hbar^2\gamma^2 \sum_{i<j} [\underline{I}^i.\underline{I}^j - 3 \frac{(\underline{I}^i.\underline{r}_{ij})(\underline{I}^j.\underline{r}_{ij})}{r_{ij}^2}] /r_{ij}^3 \qquad (2.4.1)$$

It is helpful to separate $\mathcal{H}_d$ into its spin flip components [39],

$$\mathcal{H} = \sum_{m=-2}^{m=2} D_m \qquad (2.4.2)$$

where

$$D_m = \frac{\mu_o}{4\pi} \hbar^2\gamma^2 \sqrt{\frac{4\pi}{5}} \sum_{i<j} Y_2^{-m}(\theta_{ij}, \phi_{ij}) T_{ij}^m (-1)^m / r_{ij}^3 \qquad (2.4.3)$$

the $Y_2^{-m}(\theta_{ij}, \phi_{ij})$ are spherical harmonics and T_{ij}^m the corresponding irreducible tensor spin operators. The significance of the T_{ij}^m is that they couple together eigenstates of $\mathcal{H}_z$ separated in energy by $m\hbar\omega_o$.

The time dependence in $\mathcal{H}_d^*$, eq. (2.2.24), is in terms of the D_m,

$$\mathcal{H}_d^*(-\tau) = \sum_{m=-2}^{m=2} D_{-m}(\tau)\, e^{-im\omega_o\tau} \qquad (2.4.4)$$

where

$$D_{-m}(\tau) = e^{-\frac{i}{\hbar}(\mathcal{H}_z + \mathcal{H}_m)\tau} D_m\, e^{\frac{i}{\hbar}(\mathcal{H}_z + \mathcal{H}_m)\tau} \qquad (2.4.5)$$

and the relaxation functions eqs. (2.3.2 & 3) become

$$F(t) = \exp(-\int_o^t (t-\tau) \sum_{m=-2}^{m=2} \frac{1}{2} (6-m(m+1)) G_m(\tau)\, e^{-im\omega_o \tau} d\tau) \qquad (2.4.6)$$

$$L(t) = \exp(-\int_o^t (t-\tau) \sum_{m=-2}^{m=2} m^2 G_m(\tau)\, e^{-im\omega_o \tau} d\tau) \qquad (2.4.7)$$

The autocorrelation functions, $G_m(\tau)$, of the dipolar Hamiltonian components are

$$G_m(\tau) = Tr\ \{D_m(0) D_{-m}(\tau)\} \ /\ Tr\ \{I_z^2\} \qquad (2.4.8)$$

and, using eq. (2.4.3)

$$G_m(\tau) = \frac{1}{N} \frac{\mu_o^2}{20\pi} \hbar^2 \gamma^4 \sum_{i<j} \sum_{k<\ell} \frac{Y_2^{-m}(\theta_{ij}, \phi_{ij}) Y_2^m(\theta_{k\ell}(\tau), \phi_{k\ell}(\tau))}{r_{ij}^3 \quad r_{k\ell}^2(\tau)} \Gamma_{ijk\ell}^m(\tau) \qquad (2.4.9)$$

The four-spins correlation function

$$\Gamma_{ijk\ell}^m(\tau) = N \frac{Tr\ \{T_{ij}^m(0) T_{k\ell}^{-m}(\tau)\}}{Tr\ \{I_z^2\}} \qquad (2.4.10)$$

is introduced to account for motion in spin space.

If the $G_m(\tau)$ decay to zero in a time short compared to the times of interest, the integrals in (2.4.6 & 7) can be extended to infinity [40]. The relaxation is then exponential,

$$L(t) \propto \exp\left(-\frac{t}{T_1}\right)$$

$$F(t) \propto \exp\left(-\frac{t}{T_2}\right) \qquad (2.4.11)$$

T_1 is called the longitudinal or spin-lattice relaxation time and T_2 the transverse or spin-spin relaxation time,

$$\frac{1}{T_1} = J_1(\omega_o) + 4\,J_2(2\omega_o)$$

$$\frac{1}{T_2} = \left(\frac{3}{2}\right) J_o(0) + \left(\frac{5}{2}\right) J_1(\omega_o) + J_2(2\omega_o) \qquad (2.4.12)$$

where the spectral density functions $J_m(\omega)$ are the Fourier transforms of the $G_m(\tau)$

$$J_m(\omega) = \int_{-\infty}^{\infty} G_m(\tau) \exp im\omega\tau \, d\tau \qquad (2.4.13)$$

Approximate treatment of these functions is quite straightforward in the case of bulk systems with rapid diffusive motion which ensures a rapid decay of the $G_m(\tau)$, and leads to the same results as obtained by Bloembergen, Purcell and Pound (BPP) [41].

2.5 The Spin Echo

In an inhomogeneous magnetic field there will be another coupling Hamiltonian $\mathcal{H}_g$, in addition to the dipolar coupling $\mathcal{H}_d$,

$$\mathcal{H}_g = \sum_i I_z^i \omega_i \qquad (2.5.1)$$

where ω_i/γ is the field "seen" by the i^{th} spin. Following a 90^o pulse the spins within the sample will dephase faster than given by F(t) eq. (2.2.22) due to their different Larmor precession frequencies. It is possible to separate the contributions from $\mathcal{H}_d$ and $\mathcal{H}_g$ in an experiment with the help of spin echoes [42].

To form a spin echo a 180^o pulse is applied some time t after the initial 90^o pulse. The 180^o pulse has no effect on $\mathcal{H}_d$ but it transforms $\mathcal{H}_g$ into $-\mathcal{H}_g$. The echo is observed a time t after the 180^o pulse, figure 2.2, and its height is given by [43],

$$E(2t) = E(0) \exp\left[-\frac{2t}{T_2}\right] \exp\left(-\frac{2}{3}\gamma^2 G^2 D t^3\right) \qquad (2.5.2)$$

Where G is the field gradient and D the self diffusion coefficient of the spins in the sample. If the magnet is good (small G) or the diffusion is slow (small D) the echo height is just

$$E(2t) = E(0) \exp\left[-\frac{2t}{T_2}\right]$$

Alternatively, one may measure D by purposefully applying a sufficiently large field gradient.

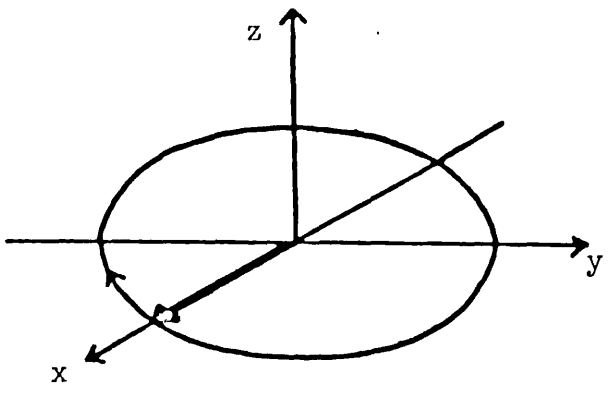

(i) Magnetization along the x-axis immediately after a 90° pulse.

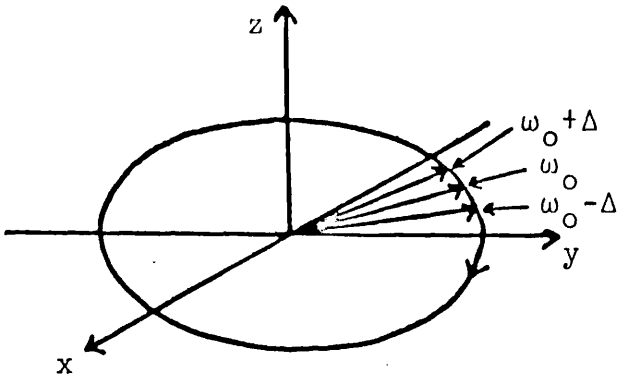

(ii) At time τ later the precessing spins have dephased.

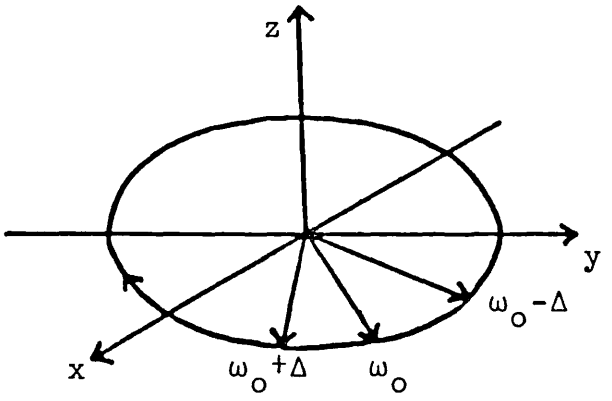

(iii) The 180° pulse rotates the spins 180° about the y-axis.

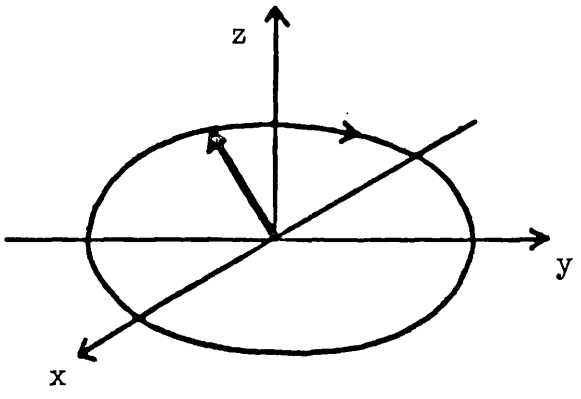

(iv) A further time τ later the spins have re-phased giving rise to an echo signal, shown below.

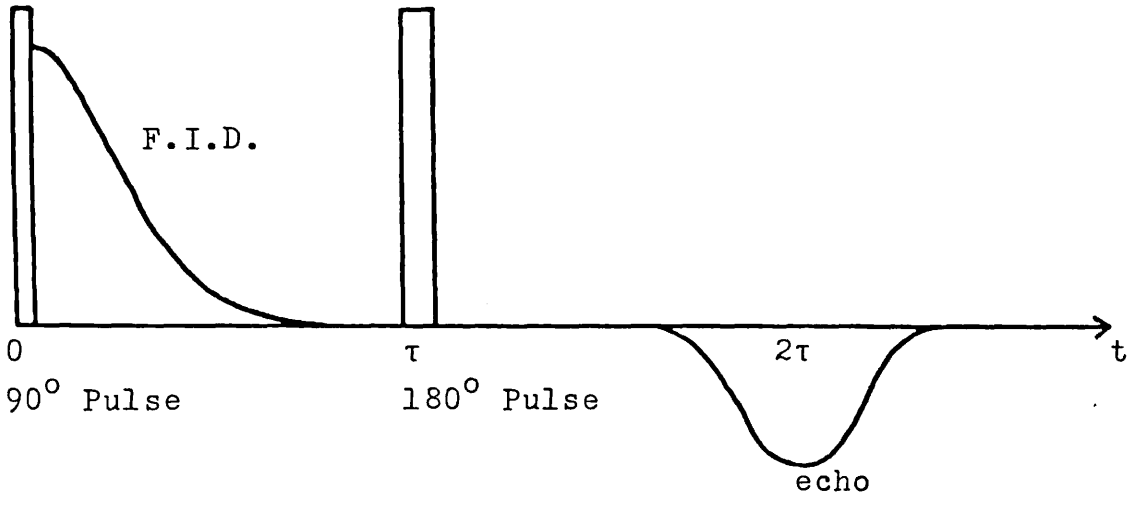

Figure 2.2, Formation Of A Spin Echo.

2.6 The Correlation Functions for 2-D Systems

In the case of a planar system it is convenient to transform the positional functions into the substrate plane. Allowing the normal to this plane to be at an angle β to the direction of B_o and defining the y-axis to be always in the substrate plane, then the spherical harmonics transform in the following manner [44],

$$Y_2^q(\theta, \phi) = \sum_{p=-2}^{p=2} D^2_{pq}\ (0,\beta,0)\ Y_2^p(\tfrac{\pi}{2}, \phi) \qquad (2.6.1)$$

where $D^2_{pq}\ (0,\beta,0)$ is the Wigner rotation operator, and ϕ now refers to the azimuthal angles the spins make in the plane. Operating with this on the expression for $G_m(\tau)$ eq. (2.4.9) gives,

$$G_o(\tau) = \frac{27\mu_o^2}{1024\pi^2}\,\hbar^2\gamma^2\,[(\tfrac{1}{3} - \cos^2\beta)^2 g_o(\tau) + \frac{\sin^4\beta}{2}\, g_2(\tau)] \qquad (2.6.2)$$

$$G_1(\tau) = \frac{9\mu_o^2}{512\pi^2}\,\hbar^2\gamma^4\,[\cos^2\beta\sin^2\beta\ g_o(\tau) + \frac{(1+\cos^2\beta)\sin^2\beta}{2}\, g_2(\tau)] \qquad (2.6.3)$$

and

$$G_2(\tau) = \frac{9\mu_o^2}{2048\pi^2}\,\hbar^2\gamma^4\,[\sin^4\beta\ g_o(\tau) + \frac{(\cos^4\beta + 6\cos^2\beta+1)}{2}\, g_2(\tau)] \qquad (2.6.4)$$

where the correlation functions $g_n(\tau)$ are given by

$$g_n(\tau) = \frac{4}{3N} \sum_{i<j} \sum_{k<\ell} \frac{\exp(-in\phi_{ij}(0))\exp(in\phi_{k\ell}(\tau))}{r_{ij}^3(0)\ r_{k\ell}^3(\tau)}\, \Gamma^n_{ijk\ell}(\tau) \qquad (2.6.5)$$

It is clear that the $g_o(\tau)$ term is independent of the orientations ϕ_{ij}, $\phi_{k\ell}$ of the spins, therefore even in the case of rapid motion $g_o(\tau)$ would be expected to decay to zero much more slowly than $g_2(\tau)$. This is not a problem with the G_1 and G_2 correlation functions as the oscillating $\exp(im\omega_o\tau)$ terms in the expressions for F(t) and L(t) eqs. (2.4.6 & 7) will ensure convergence of the integrals. However, the presence of the adiabatic G_o term in the expression for F(t) may be expected to cause problems.

2.7 Relaxation in a 2-D Classical Fluid

For purely classical motion, by which we mean that only the positional r_{ij} parts of $\mathscr{H}_d$ are time dependent, the zero time value of the four spins correlation function $\Gamma^m_{ijk\ell}(0)$ is used. For a spin - $\frac{1}{2}$ system the positional correlation functions become,

$$g_n(\tau) = \frac{1}{N} \sum_{i\neq j} \frac{\exp\{-in(\phi_{ij}(0) - \phi_{ij}(\tau))\}}{r_{ij}^3(0)\ r_{ij}^3(\tau)} \qquad (2.7.1)$$

The time dependence of the ϕ_{ij} is so complicated that probablistic arguments must be applied in order to evaluate $g_n(\tau)$. The summation is then approximated by an integral over the probability distribution function [45],

$$\sum_{i\neq j} \rightarrow N\alpha \int_{r_o>a} d\underline{r}_o \int_{r>a} d\underline{r}\ P(\underline{r} - \underline{r}_o, \tau) \qquad (2.7.2)$$

where $P(r-r_o, \tau)$ is the probability density for finding two spins which were orginally a distance r_o apart a distance r apart after a time τ, a is the radius of closest approach of two spins and α is the spin density for all r>a. For 2-D diffusive motion $P(\underline{r},\tau)$ may be

approximated by the Gaussian Expression,

$$P(\underline{r}, \tau) = (1/8\pi D\tau) \exp(-r^2/8D\tau) \qquad (2.7.3)$$

Combining eqs. (2.7.3), (2.7.2) and (2.7.1) leads to the following expression for the $g_n(\tau)$,

$$g_n(\tau) = \frac{2\pi\alpha}{a^4} \int_o^\infty dx\, x^3 \exp(-\tau x^2/\tau_d) \left[\int_x^\infty \frac{J_n(y)}{y}\, dy\right]^2 \qquad (2.7.4)$$

where τ_d is the time taken by a spin to diffuse through a distance a, $\tau_d = (a^2/2D)$, and the $J_n(y)$ are n^{th} order Bessel functions. It is not possible to evaluate (2.7.4) in analytic form, figure 2.3 shows a computer calculation of $g_o(\tau)$ and $g_n(\tau)$ which agrees with the results obtained by others [46] and [47]. The $g_o(\tau)$ term has a long tail while $g_2(\tau)$ decays to zero relatively quickly. At $\tau = 0$, $g_o = g_2 = \pi\alpha/2a^4$.

(2.7a) Spin Lattice Relaxation and T_1 ;

The convergence of the integral in the expression for L(t) is ensured by the presence of the oscillating $\exp(im\omega_o\tau)$ terms. So the relaxation is exponential and T_1 is given by

$$\frac{1}{T_1} = \frac{9\mu_o^2}{512\pi^2} \hbar^2\gamma^4 \left[\cos^2\beta\sin^2\beta\, j_o(\omega_o) + \frac{(1+\cos^2\beta)\sin^2\beta}{2}\, j_2(\omega_o) + \sin^4\beta\, j_o(2\omega_o) + \frac{(\cos^4\beta + 6\cos^2\beta + 1)}{2}\, j_2(2\omega_o)\right] \qquad (2.7.5)$$

the reduced spectral density functions $j_n(\omega)$ are obtained by Fourier transforming the $g_n(\tau)$,

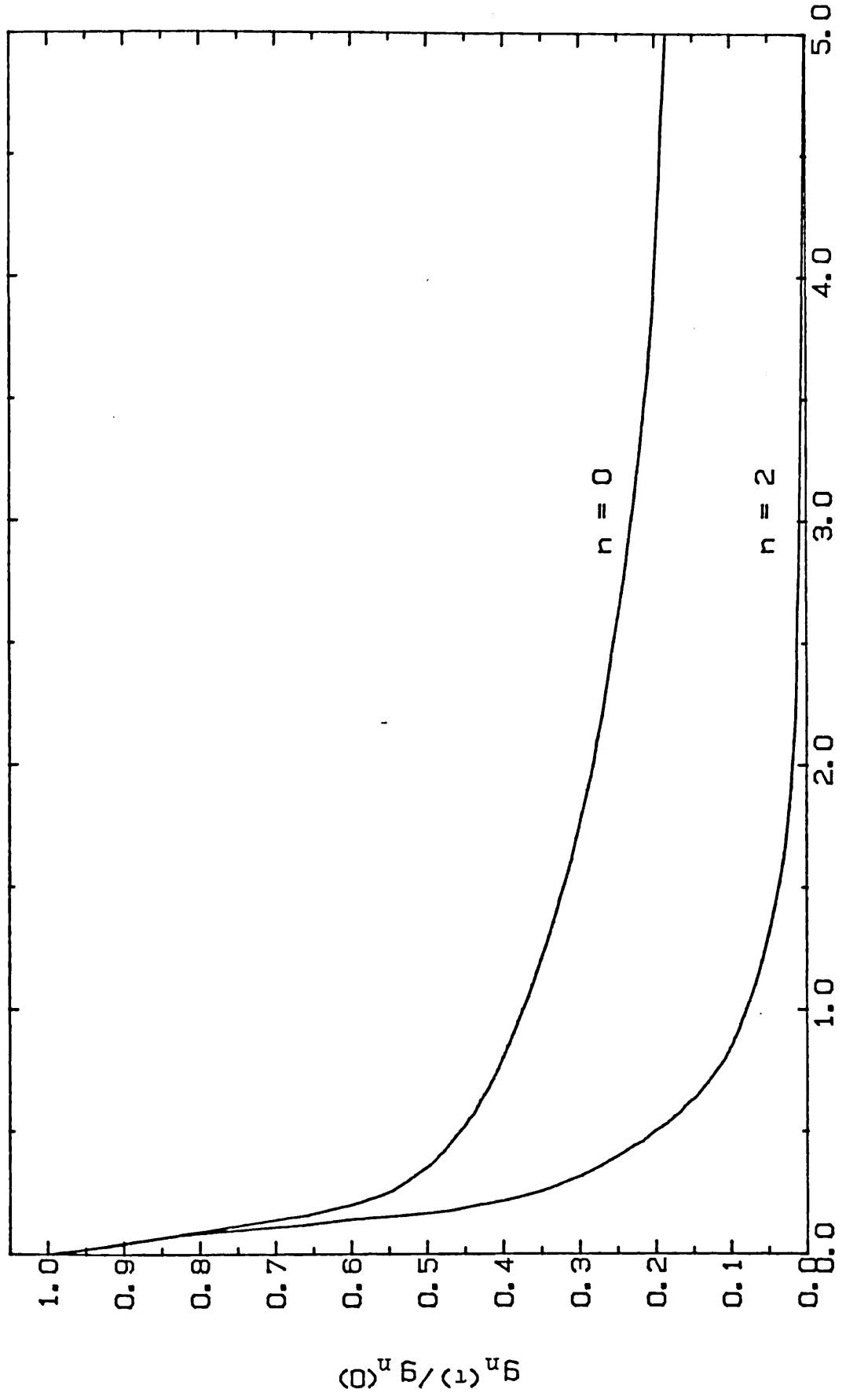

Figure 2.3. The Components Of The Dipolar Autocorrelation Function For A 2-D Diffusive Fluid.

$$j_n(\omega) = \frac{2\pi\alpha}{a^4}\tau_d \int_o^\infty \frac{2x^5}{x^4 + \omega^2\tau_d^2}\left[\int_x^\infty \frac{J_n(y)}{y^2}\,dy\right]^2 d_x \qquad (2.7.6)$$

Figure 2.4, shows the result of a computer calculation of $j_o(\omega)$ and $j_2(\omega)$. For $\omega_o\tau_d < 1$ the j_2 component levels off to a constant value, $0.72\, g(0)\tau_d$, while j_o continues to diverge. The anisotropy in T_1 is plotted in figure 2.5 for various values of $\omega_o\tau_d$, since purely diffusive motion is assumed it is not practical to extend the range of $\omega_o\tau_d$ beyond unity. Note that for $\omega_o\tau_d \simeq 1$, that is near where the T_1 minimum is expected, there is little anisotropy in T_1.

(2.7.b) Spin-Spin Relaxation and T_2 ;

The presence of the adiabatic, m=0, term in the expression for F(t), means that the integral cannot be simply extended to infinity to give exponential relaxation. This is due to the long time tail on the $g_o(\tau)$ function. The contribution from the non-adiabatic terms is however exponential due to the presence of the oscillating $\exp(im\omega_o\tau)$ terms, and so also is the contribution to G_o from the relatively fast decaying $g_2(\tau)$ term. F(t) may be factorised and written in the following form,

$$F(t) = \exp\left[-\frac{t}{T_2^{na} + T_2'}\right] \exp -\frac{81\mu_o^2}{1024\pi^2}\hbar^2\gamma^4\left[\frac{1}{3} - \cos^2\beta\right]\int_o^t (t-\tau)g_o(\tau)d\tau$$

(2.7.7)

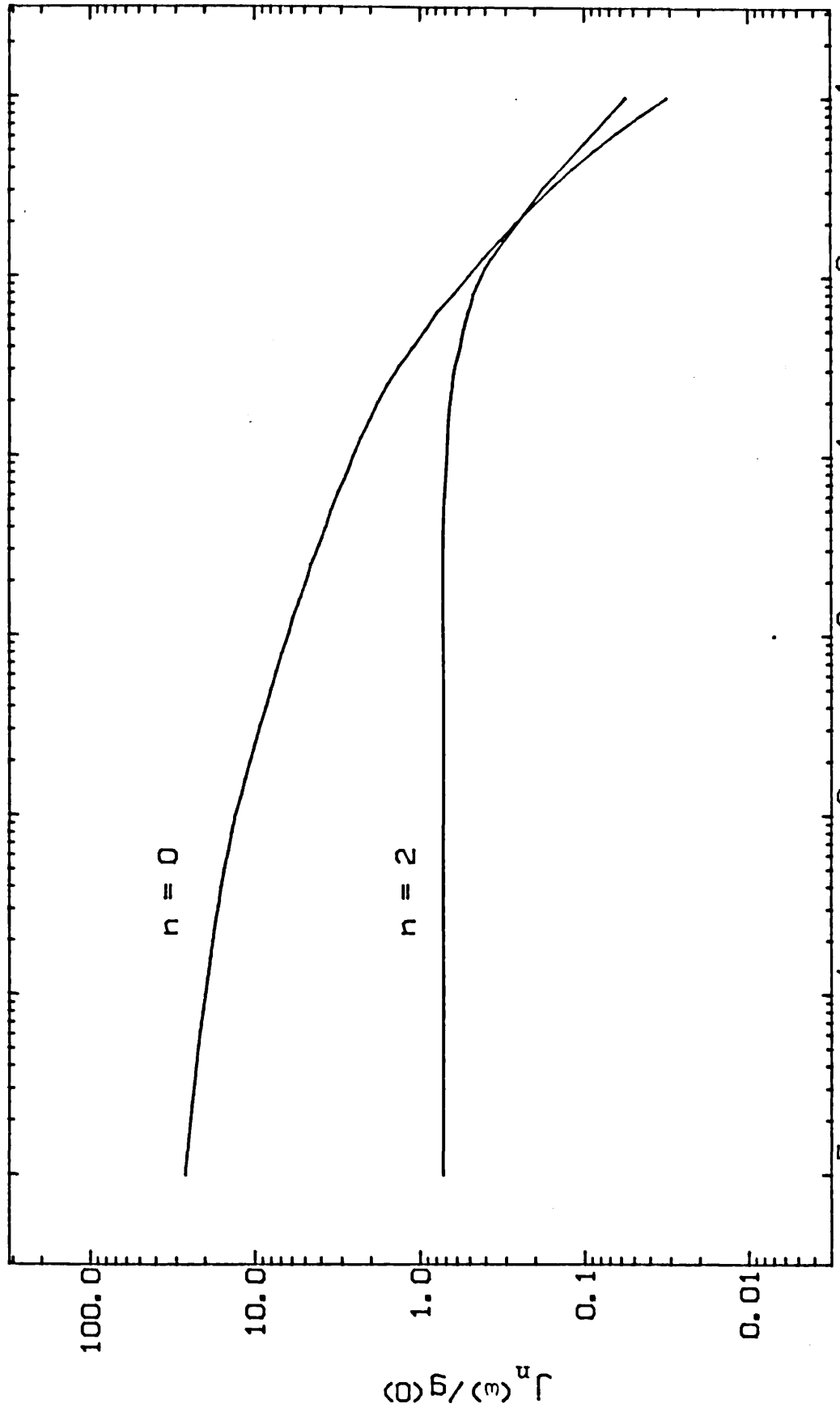

Figure 2.4, The Spectral Density Functions For A 2-D Diffusive Fluid.

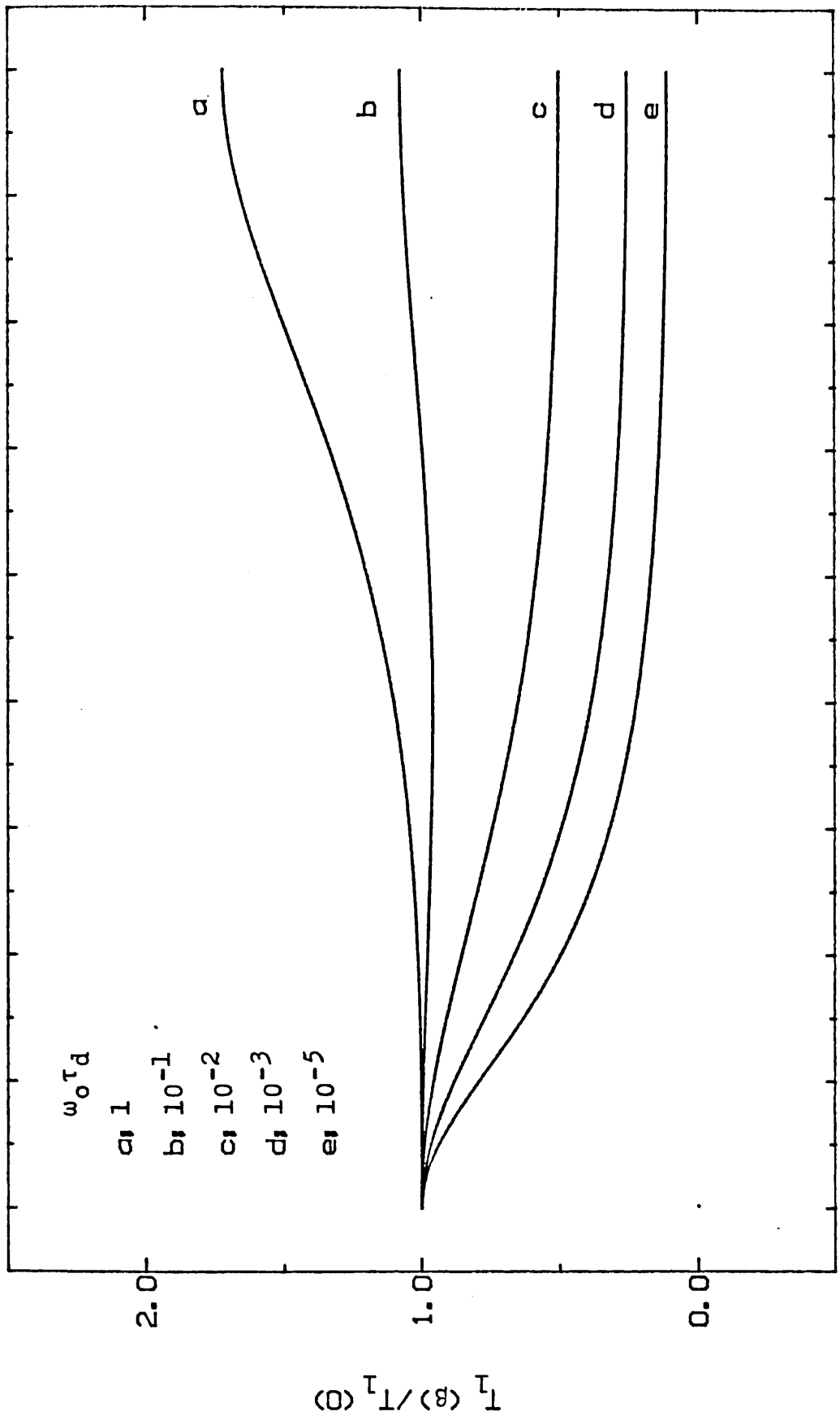

Figure 2.5. Anisotropy Of The Spin-Lattice Relaxation Time T_1. In a 2-D Diffusive Fluid.

the non-adiabatic contribution T_2^{na} is given by

$$\frac{1}{T_2^{na}} = \frac{9\mu_o^2}{1024\pi^2}\hbar^2\gamma^4\left[5\cos^2\beta\sin^2\beta\ j_o(\omega_o) + \frac{5(1+\cos^2\beta)\sin^2\beta}{2}\ j_2(\omega_o) + \right.$$

$$\left. + \frac{\sin^4\beta}{2}\ j_o(2\omega_o) + \frac{\cos^4\beta + 6\cos^2\beta + 1}{4}\ j_2(2\omega_o)\right] \qquad (2.7.8)$$

and T_2' by

$$\frac{1}{T_2'} = \frac{81\mu_o^2}{2048\pi^2}\hbar^2\gamma^4\ \ \frac{\sin^4\beta}{2}\ j_2(0) \qquad (2.7.9)$$

It only remains to decide how to treat the non-exponential contribution,

$$\exp - \frac{81\mu_o^2}{1024\pi^2}\hbar^2\gamma^4\left(\frac{1}{3} - \cos^2\beta\right)^2 \int_o^t (t-\tau)g_o(\tau)\ d\tau$$

One approach [29] is to assume that after a time τ_c a spin reaches the edge of the finite substrate plane and the correlation of the local dipolar fields disappears. This leads to a levelling off of the $j_o(\omega)$ function to a constant value for $\omega<\omega_c\simeq\pi/2\tau_c$. The contribution is then exponential with decay constant T_2'' given by

$$\frac{1}{T_2'} = \frac{81\mu_o^2}{1024\pi^2}\hbar^2\gamma^4\left(\frac{1}{3} - \cos^2\beta\right)^2 j_o(\omega_c) \qquad (2.7.10)$$

The problem with this approach is that the g_o correlation function is only sensitive to variations in the separation between spins, it is unlikely therefore that reaching the edge of the plane would have such a drastic effect.

In an alternative approach [48] $g_o(\tau)$ is approximated by

$$\frac{g_o(\tau)}{g_o(0)} = \frac{1}{1 + \tau/2\tau_d} \qquad (2.7.11)$$

which has the correct long time behaviour, performing the integral in the expression for F(t) gives,

$$F(t) = \exp\left(-\frac{t}{T_2^{na}+T_2'}\right)\exp -\frac{81\mu_o^2}{512\pi^2}\hbar^2\gamma^4\left(\frac{1}{3} - \cos^2\beta\right)^2 g_o\,\tau_d t\,\left(\ln\frac{t}{2\tau_d} - 1\right)$$

(2.7.12)

Now for $t \gg \tau_d$ the logarithm is a slowly varying function of t.
So the relaxation will be nearly exponential with a relaxation rate given by the implicit expression,

$$\frac{1}{T_2} = \left(\frac{1}{T_2^{na} + T_2'}\right) + \frac{81\mu_o^2}{512\pi^2}\hbar^2\gamma^4\left(\frac{1}{3} - \cos^2\beta\right)^2 \frac{2\pi\alpha}{a^4}\tau_d\left(\ln\frac{T_2}{2\tau_d e}\right)$$

(2.7.13)

The assumption that the times of interest, t, are long compared to τ_o is certainly justified in the case of a diffusive fluid. The presence of the "anomalous" contribution to $G_o(\tau)$ from the $g_o(\tau)$ function means that when $\omega_o\tau_d \ll 1$, $T_2 \neq T_1$, whilst in a corresponding bulk system $T_2 = T_1$. Figure 2.6 shows the anisotropy in T_2, τ_d is maintained constant at 10^{-11} seconds, which is typical for the fluid phase of adsorbed ^{3}He. The peak near $\beta = \cos^{-1}\sqrt{\frac{1}{3}} = 54.7^o$ is due to the disappearance of the anomalous contribution at this angle.

2.8 Relaxation in a 2-D solid

If the spins are fixed on a rigid lattice the only important contribution to F(t) is from the adiabatic $G_o(0)$ term. If we still use the Kubo type expression,

$$F(t) = \exp\left\{ -3 \int_o^t (t-\tau) G_o(0)\, d\tau \right\}, \qquad (2.8.1)$$

the relaxation then takes on a Gaussian form

$$F(t) = \exp - \frac{1}{2} M_2\, t^2 \qquad (2.8.2)$$

where M_2 is the second moment of the resonance line [49] and is given by,

$$M_2 = 3G_o(0) = \frac{\mathrm{Tr}\,\{[I_+, D_o][D_o, I_-]\}}{\hbar^2\, \mathrm{Tr}\{I_+ I_-\}} \qquad (2.8.3)$$

For a two-dimensional triangular lattice M_2 has been calculated [50], and is written

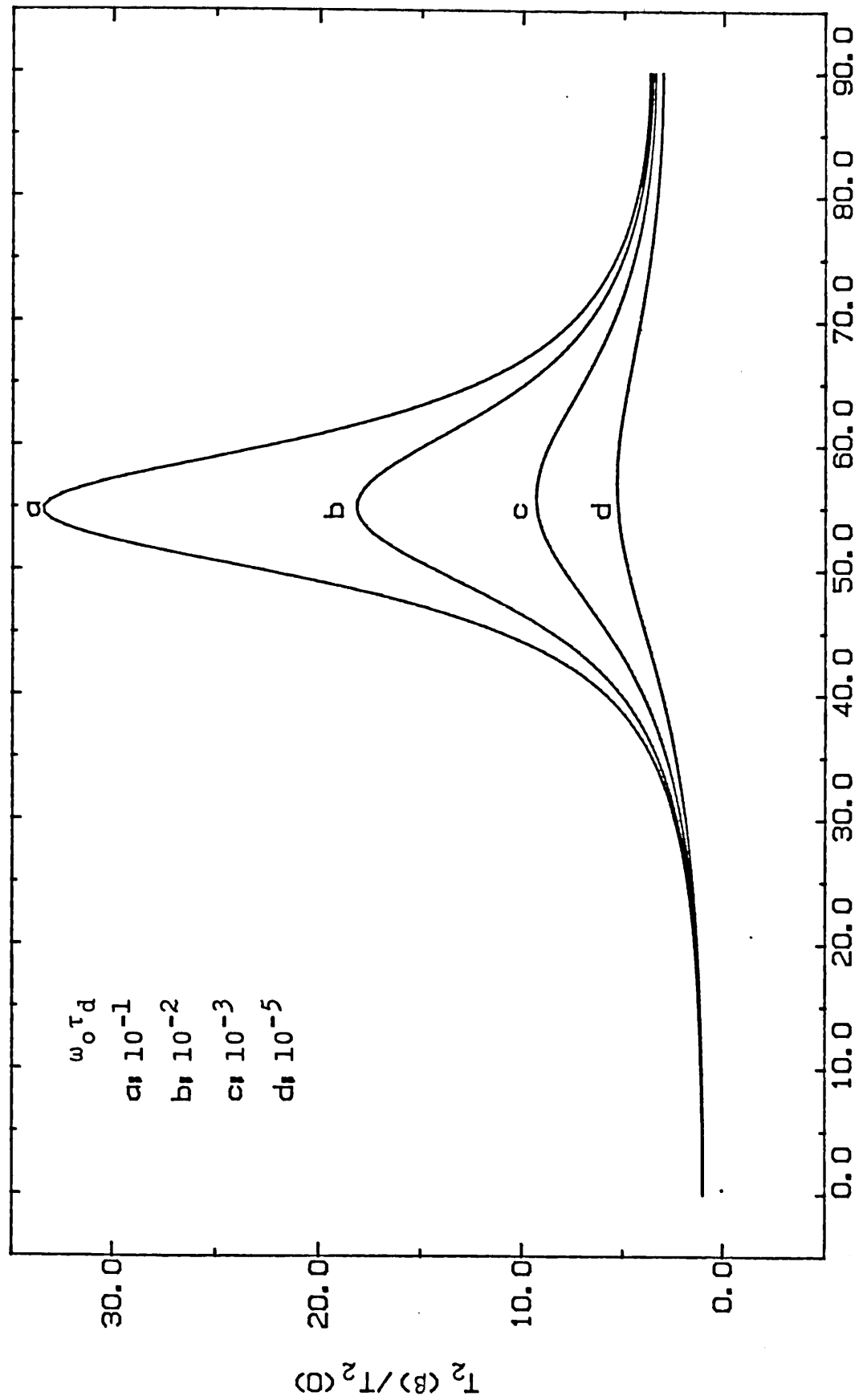

Figure 2.6. Anisotropy Of The Spin-Spin Relaxation Time, T_2. In a 2-D Diffusive Fluid.

$$M_2 = \frac{\mu_o^2 \hbar^2 \gamma^4}{44.11} \; I(I+1) \; \frac{\{1-3\sin^2\beta + (\frac{27}{8})\sin^4\beta\}}{d^6} \qquad (2.8.4)$$

T_2 is then defined for the Gaussian relaxation by,

$$\frac{1}{T_2} = (2\ell n2)^{1/2} M_2^{1/2}. \qquad (2.8.5)$$

The validity of this approach has been supported by calculation of the fourth moment, M_4 [50].

As far as L(t) is concerned, the absence of an adiabatic contribution means that there is no dipole-dipole relaxation process. Other processes must be responsible for spin-lattice relaxation in a rigid lattice [35].

In the solid phase of adsorbed helium there is normally some motion of the atoms due to the diffusion of vacancies in the lattice and/or quantum exchange [51]. When such motion is very slow, one approach to the calculation of the relaxation times is the so-called "long jump limit" [29]. In this approach it is assumed that the dipolar interaction between two spins at time t=0 becomes negligably small after a single "jump". The probability distribution function $P(r-r_o,\tau)$ in (2.7.2) is then given by [52],

$$P(r-r_o,\tau) = \delta(r-r_o)\, e^{-\tau/\tau_d} + \frac{1}{A}\,(1-e^{-\tau/\tau_d}) \qquad (2.8.6)$$

In the limit of large substrate plane area A, the second term can be ignored. The following expressions for T_1 and T_2 are then obtained,

$$\frac{1}{T_1} = \frac{9\mu_o^2}{256\pi^2}\hbar^2\gamma^4\frac{\pi\alpha}{a^4}\left\{\left[\cos^2\beta\sin^2\beta + \frac{(1+\cos^2\beta)\sin^2\beta}{2}\right]\left(\frac{\tau_d}{\omega_o^2\tau_d^2+1}\right) + \right.$$

$$\left. + \left[\sin^4\beta + \frac{(\cos^4\beta + 6\cos^2\beta + 1)}{2}\right]\left(\frac{2\tau_d}{4\omega_o^2\tau_d^2+1}\right)\right\} \qquad (2.8.7)$$

and,

$$\frac{1}{T_2} = \frac{9\mu_o^2}{512\pi^2}\hbar^2\gamma^4\frac{\pi\alpha}{a^4}\left\{9\left[\left(\frac{1}{3} - \cos^2\beta\right)^2 + \frac{\sin^4\beta}{2}\right]\tau_d + \right.$$

$$+ \left[5\cos^2\beta\sin^2\beta + \frac{5(1+\cos^2\beta)\sin^2\beta}{2}\right]\left(\frac{\tau_d}{\omega_o^2\tau_d^2+1}\right) +$$

$$\left. + \left[\frac{\sin^4\beta}{2} + \frac{(\cos^4\beta + 6\cos^2\beta + 1)}{4}\right]\left(\frac{2\tau_d}{4\omega_o^2\tau_d^2+1}\right)\right\} \qquad (2.8.8)$$

Figure 2.7 shows the anisotropy in T_1 for various values of $\omega_o\tau_d$ and Figure 2.8 shows the anisotropy in T_2. For quantum exchange $\tau_d \simeq 1/2J$, where J is the exchange frequency.

In the hydrodynamic limit the Heisenburg exchange Hamiltonian,

$$\mathcal{H}_x = 2J \sum_{i<j} \underline{I}^i.\underline{I}^j \qquad (2.8.9)$$

or a multiple spin exchange Hamiltonian [53] must lead to spin diffusion [54]. An approach to the evaluation of the relaxation times under these conditions follows closely the method used in the case of

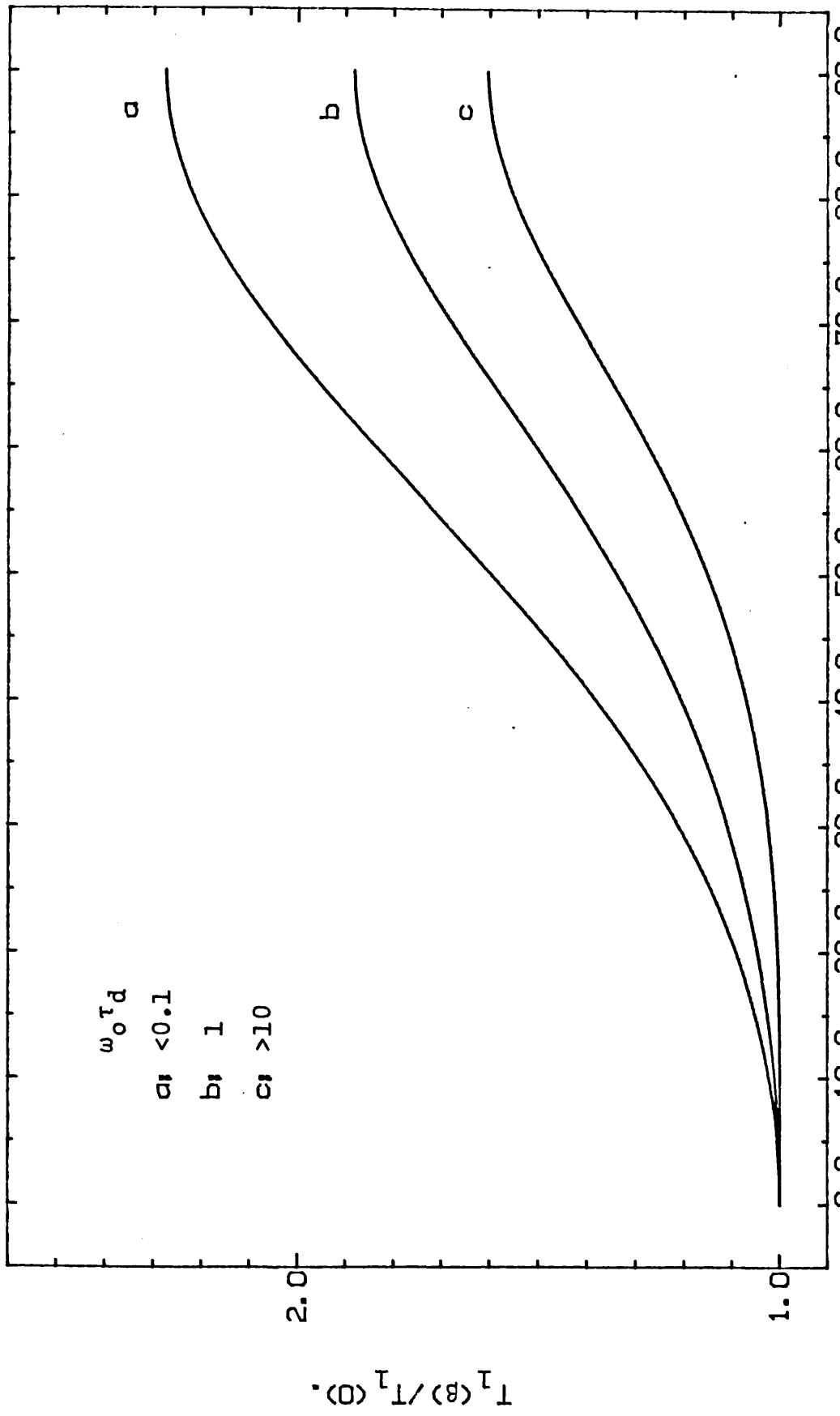

Figure 2.7. Anisotropy Of The Spin-Lattice Relaxation Time, T_1. In a 2-D Solid With Slow Motion.

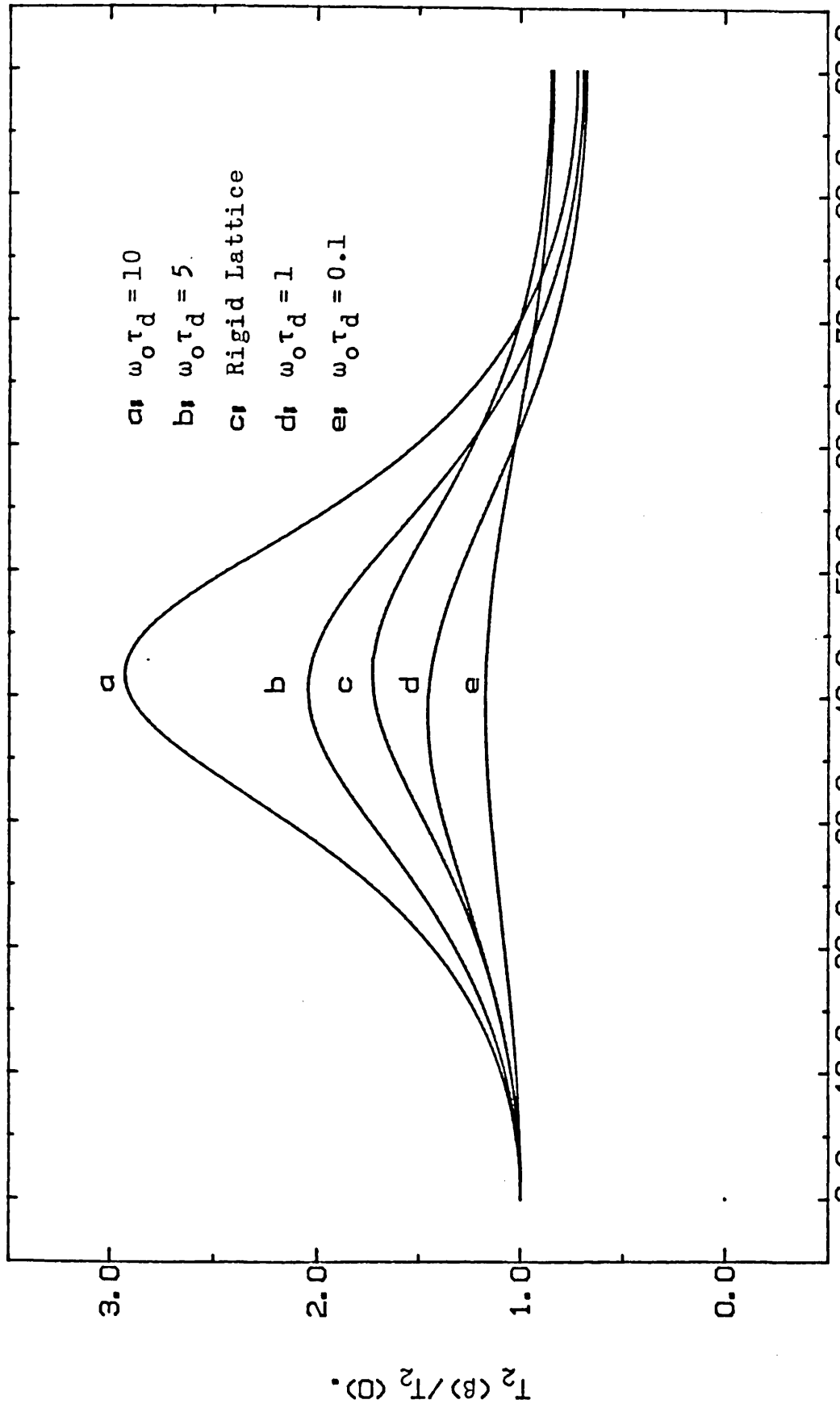

Figure 2.8. Anisotropy Of The Spin-Spin Relaxation Time, T_2. In a 2-D Solid With Slow Motion.

a diffusive fluid §2.7. However, in this case it is the spin components of $g_n(\tau)$ eq. (2.6.5) that are dependent on time,

$$g_n(\tau) = \frac{4}{3N} \sum_{\substack{i<j \\ k<\ell}} \frac{\exp[-in(\phi_{ij}-\phi_{k\ell})]}{r_{ij}^3 \, r_{k\ell}^3} \Gamma^n_{ijk\ell}(\tau) \qquad (2.8.10)$$

The short time behaviour of $g_n(\tau)$ can be found with a moment expansion and the long time behaviour by analogy with the fluid case. These asymptotic forms are then joined to give a complete expression. The expressions obtained for T_1 and T_2 are the same as eq. (2.7.5) and eq. (2.7.13) respectively, except that τ_d is replaced by $.375J^{-1}$ and the spectral density functions are given by,

$$\frac{j_o(\omega)}{g(0)} = \frac{0.6676}{1.2485J} \left[2g\left(\frac{\omega_o}{1.2485J}\right) - 1 + \frac{\omega_o}{1.2485J} F\left(\frac{\omega_o}{1.2485J}\right) \right] +$$

$$+ \frac{0.4117}{J} \exp - \left(\frac{\omega_o^2}{32.902J^2}\right) \qquad (2.8.11)$$

$$\frac{j_2(\omega)}{g(0)} = \frac{0.2287}{J} \exp - \left(0.2181 \frac{\omega_o}{J}\right) + \frac{0.4117}{J} \exp - \left(\frac{\omega_o^2}{32.902J^2}\right)$$

(2.8.12)

where $g(\omega_o/1.2485J) = \int_o^\infty (\sin y)/[y + (\omega_o/1.2485J)]\, dy$

and $F(\omega_o/1.2485J) = \int_o^\infty (\cos y)/[y + (\omega_o/1.2485J)]\, dy$

As in the diffusive fluid the $j_o(\tau)$ term diverges logarithmically as $\frac{\omega}{J} \to 0$ while the $j_2(\tau)$ term levels off to a constant value for $\frac{\omega}{J} \lesssim 1$. The anisotropies in T_1 and T_2 have the same general features as those for the diffusive fluid, figures 2.5 & 6.

2.9 Relaxation in Grafoil Local Fields, (The Conventional View)

When studying the fluid phase of Helium-3 adsorbed on Grafoil it is necessary to take into account the effects of the substrate local fields. These fields are due to the anisotropic diamagnetism of the angularly mis-oriented graphite crystallites of which Grafoil is composed, see §1.3. A spin diffusing across the surface will relax as a result of the variations in the local fields that it sees. If it is assumed that these variations have a well defined correlation length, a, approximately equal to the size of the graphite crystals, then the temporal variation of the field seen by a spin as it diffuses on the Grafoil surface is very similar to that experienced by a spin diffusing in a bounded gradient [55], [56].

If a is sufficiently small that $(<\Delta\omega_z^2>^{1/2}a^2/D)<<1$, where $<\Delta\omega_z^2>/\gamma^2$ is the mean square local field variation and D the diffusion coefficient. For times short compared to the time taken by a spin to diffuse the distance a, $t<<a^2/2D$, the spin echo decay is given by the familiar cubic expression for diffusion in a field gradient,

$$F(t) = \exp\left(-<\Delta\omega_z^2>Dt^3/6a^2\right) \qquad (2.9.1)$$

For long times, $t>>a^2/2D$ the echo relaxation becomes exponential and the decay constant T_2 is given by

$$T_2^{-1} = <\Delta\omega_z^2>a^2/60D \qquad (2.9.2)$$

Now consider a Grafoil sheet oriented with its normal at an angle β to the magnetic field B_o. The graphite platelets are mis-oriented in the plane by angle α. Initially a spin is at some arbitrary point on the surface whose orientation is α_1 after diffusing some distance it is at a point on the surface whose orientation is α_2. Providing the distance travelled is greater than a there is no correlation between α_1 and α_2. The difference in the z-component of the field between the two points is then the difference in the demagnetizing fields of the two platelets

$$\Delta B_z = B_o \chi_c S\{\cos^2(\beta+\alpha_2) - \cos^2(\beta+\alpha_1)\} \qquad (2.9.3)$$

where χ_c is the c-axis susceptibility of graphite, $\chi_c = 0.00085$. The "shape factor" S is a dimensionless number and is related to the geometry of the platelet, e.g. for spherical geometry $S = \frac{2}{3}$, a cylinder $S = \frac{1}{2}$, and for an infinite flat slab $S = 0$. The mean square variation in B is

$$\langle \Delta B_z^2 \rangle = B_o^2 \chi_c^2 S^2 \langle \{\cos^2(\beta+\alpha_2) - \cos^2(\beta+\alpha_1)\}^2 \rangle \qquad (2.9.4)$$

where the average is taken with respect to the distributions of α_1 and α_2 which are assumed to be Gaussian with rms value δ. Performing the average gives

$$\langle \Delta B_z^2 \rangle = \chi_c^2 B_o^2 S^2 \{(1-e^{-4\delta^2}) + (e^{-8\delta^2} - e^{-4\delta^2})\cos 4\beta\} \qquad (2.9.5)$$

For a finite flat disk of diameter d and thickness t with the normal to its surface parallel to the direction of magnetization, an order of magnitude estimate of the shape factor is, $s \simeq t/d$. This

situation corresponds approximately to the average graphite crystal in Grafoil, where $d \simeq 1\mu m$ and $t \simeq 100\text{Å}$ giving $S \simeq 0.01$. So, given the value of δ, one can in principle obtain an estimate of T_2 by substituting $\gamma^2\langle\Delta B_z^2\rangle$ for $\langle\Delta\omega_z^2\rangle$ in eq. (2.9.2). If this process is responsible for spin-spin relaxation then T_2 is expected to be proportional to B_o^2 (or ω_o^2) and to show a $\cos^4\beta$ angular dependence.

CHAPTER 3

THE APPARATUS

3.1 The Cryostat

Built in the college's physics workshop, the cryostat was designed to support an Oxford Instruments 7mK dilution refrigerator. However, for the purposes of the present work it is used only as a ^{4}He cryostat over the range 1 - 20K. The dilution refrigerator being replaced by the sample rotating mechanism to be described later.

The cryostat, figure 3.1, has a 0.5 litre copper ^{4}He pot, by pumping on this temperatures between 4.2 and 1.1K can be achieved and maintained for approximately 72 hours before the pot needs re-filling from the ^{4}He bath through a needle valve. To reach the higher temperatures 4.2 to 20K a heater consisting of a 1K wirewound resistor firmly attached to the pot is used.

Bolted directly to the ^{4}He pot and sealed with an indium "O" ring is a large copper vacuum can (inner vacuum can) which contained the experimental sample chamber and low pressure ($\sim$1 torr) ^{4}He exchange gas to maintain thermal contact between the sample and the pot. Surrounding the ^{4}He pot and the inner vacuum can is another large can (outer vacuum can) pumped to a high vacuum to thermally isolate the pot from the ^{4}He bath.

The ^{4}He bath is contained within a specially built Oxford Instruments dewar which has superinsulation, a nitrogen jacket and a ^{4}He vapor shield at $\sim$40K. The cryostat service lines are of thin walled stainless steel tubing to minimise thermal conduction. Liquid ^{4}He consumption averaged at 7 litres over a 24 hour period including transfer losses.

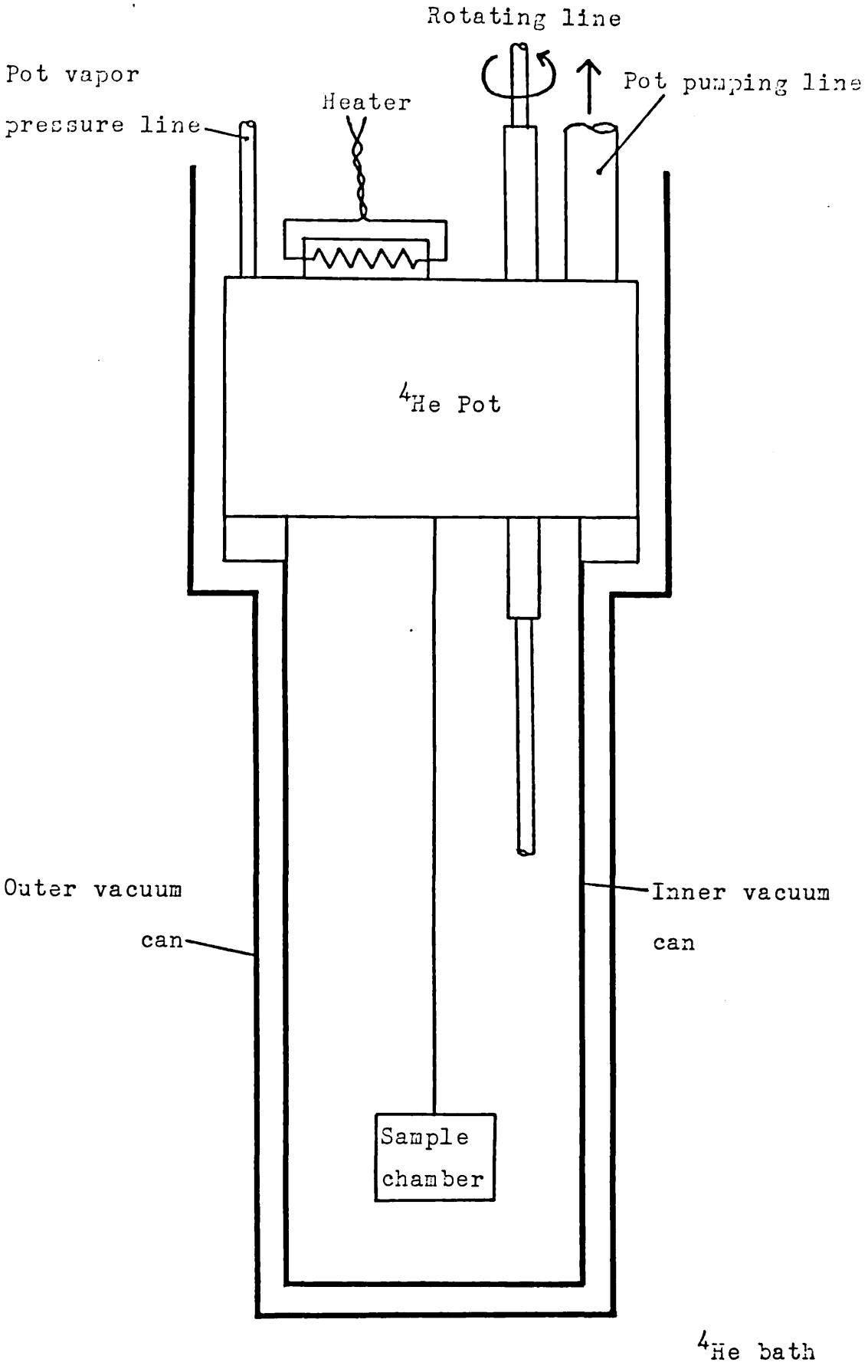

Figure 3.1, The Cryostat.

3.2 Temperature Measurement and Regulation System

For primary thermometry there is a Wallace and Tiernan precision pressure gauge and an oil manometer both measuring the ^4He vapor pressure in the pot. The pot temperature is then obtained from the T_{54} temperature scale. At the start of each run the primary thermometer is used to calibrate the secondary thermometers, Speer† and Allen-Bradley†† resistors located on the pot and at other points in the cryostat, figure 3.2, and connected to an SHE potentiometric conductance Bridge with digital read out.

Secondary pot thermometry consists of two pairs of resistors each located at the top and bottom of the pot. Each pair consists of a 47Ω¼W Allen-Bradley and a 470Ω½W Speer pressed firmly into holes in a copper block in tight thermal contact with the pot. The resistor leads are thermally anchored to the pot. The 47Ω Allen-Bradley resistor is used to measure the pot temperature over the range 2 to 20K where its change of resistance with temperature is most rapid, and for the same reason the 470Ω Speer resistor is used at temperatures below 2K. The nominal values 47Ω and 470Ω were chosen partly because at 2K the resistances are of the same order of magnitude so not requiring a change of range on the bridge when the resistors are swapped.

The resistor leads from the pot and other points within the cryostat are taken to a selector unit which uses reed relays to enable resistors to be selected manually or under external computer control. The B.C.D. output from the conductance bridge is taken via an interface unit to a microcomputer (RML380Z) where the temperature T is calculated using the following empirical formulae [57][58]:

† Product of the Speer Resistor Company, U.S.A.

†† Product of the Allen Bradley Resistor Company, U.S.A.

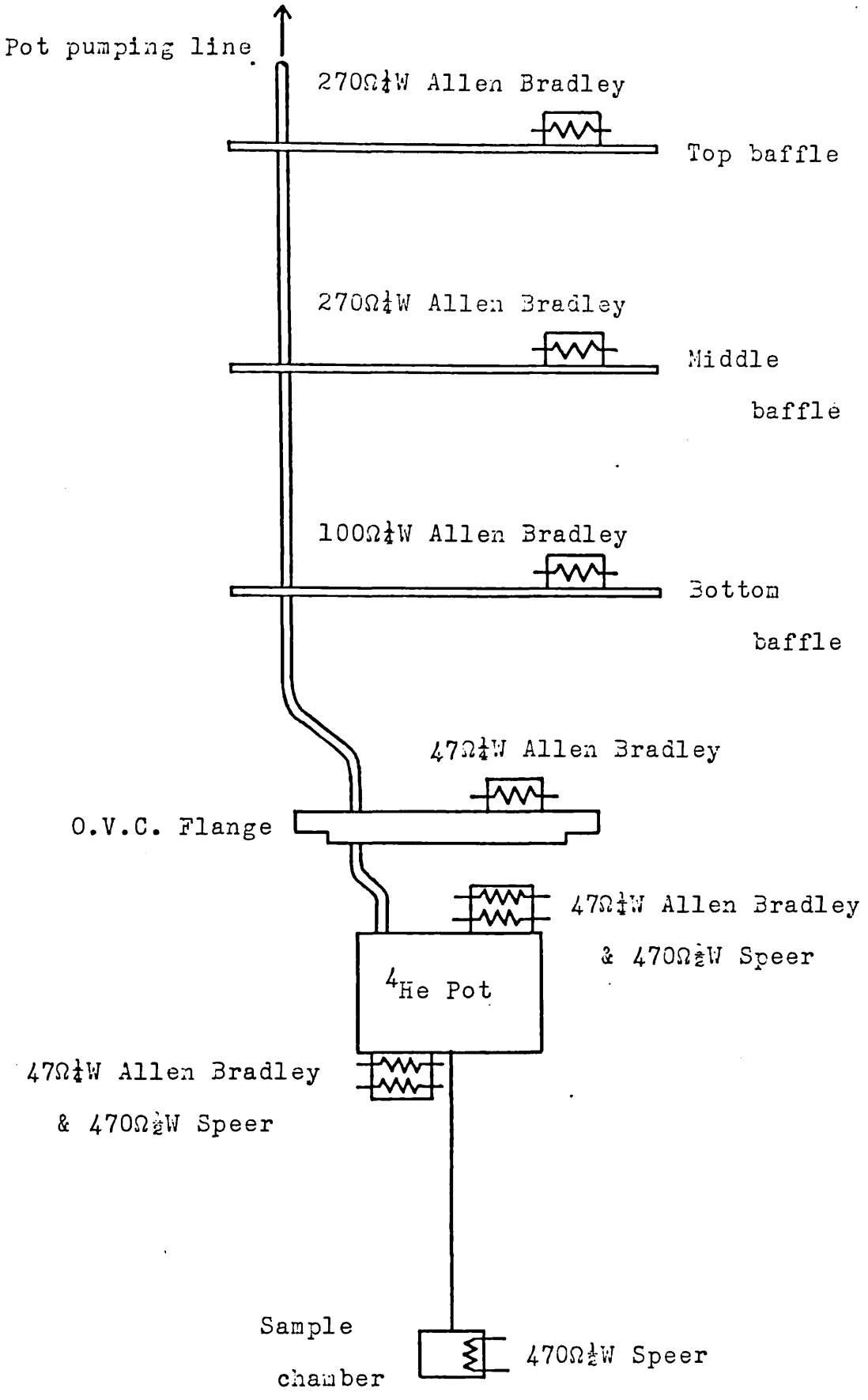

Figure 3.2, Positioning Of Temperature Sensors In Cryostat.

Allen-Bradley Resistors

$$\frac{1}{T} = \frac{k}{\mathrm{Log}_{10}R} + a + b\mathrm{Log}_{10}R \qquad (3.2.1)$$

Speer Resistors

$$\mathrm{Log}_{10}T = \frac{C}{\mathrm{Log}_{10}R} + A + B\mathrm{Log}_{10}R \qquad (3.2.2)$$

where R is the resistance. The constants k, a and b and A, B and C are determined by fitting eqs (3.2.1) and (3.2.2) to the temperature calibration graphs at three points chosen to minimise the maximum error over the range of the fit. Accuracies to within <5mK are easily achieved using the above formulae and this method of fitting. The Allen-Bradley resistors are found to be reproducible from run to run even after heating the pot well above room temperature to repair a solder joint. For the 47Ω Allen-Bradley resistor at the top of the pot the constants are:

$k = 1.189$ $a = -1.5685$ $b = 0.5156$

The Speer resistors are not so reproducible between runs with a shift on the temperature scale of anything up to ±30 mK being observed, Typical values of the constants for the 470Ω Speer resistor at the bottom of the pot are:

$A = 109.04$ $B = -62.005$ $C = 8.793$

The computed temperature is written via the interface unit to a digital display mounted in the resistor selector unit.

The microcomputer is also responsible for ^{4}He pot temperature regulation. By comparing the measured temperature with the requested temperature (between 1.2 and 20K) and then controlling a solenoid valve in the pot pumping line or the pot heater both via the interface unit, the computer is able to maintain temperatures stable to within a

few mK. Figure 3.3 shows schematically the temperature regulation system.

3.3 The Microcomputer System

The RML380Z† microcomputer system introduced in §3.2 uses a Z80A CPU (central processing unit) with 56K of RAM, about 52K of which is free for user programs and data, 8K of ROM contains the monitor program. It has two double sided 5¼ inch floppy disc drives giving a total of 300K byte storage capability and it runs the standard CP/M [59] operating system. Connection with the outside world is made via a PIO (parallel input/output) board. There are six available 8 bit ports plus handshake lines, each port can be configured as an input, an output or bidirectional. Four ports are actually used, one each for data in, data out, control out and status in.

A general purpose interface and control unit was developed in our electronics workshop. It has provision for fifteen interfaces. Decoding is arranged so that one 8 bit control word from the computer both selects the interface and specifies the operation required. If this operation should be to send or receive data then the data byte is next passed via the data ports. If an event that requires immediate response from the microcomputer should occur, such as a conductance bridge overflow during temperature measurement, then a status condition is set up which can be used to interrupt the CPU. The byte on the status line is then used by the CPU in deciding what action to take.

Software for the system is a combination of machine code and high level language. Machine code routines written in assembly language are used for the exchange of data and control information between the microcomputer and the interfaces. These have the advantage of much

† RML is the trade name for Research Machines Limited, Oxford, England.

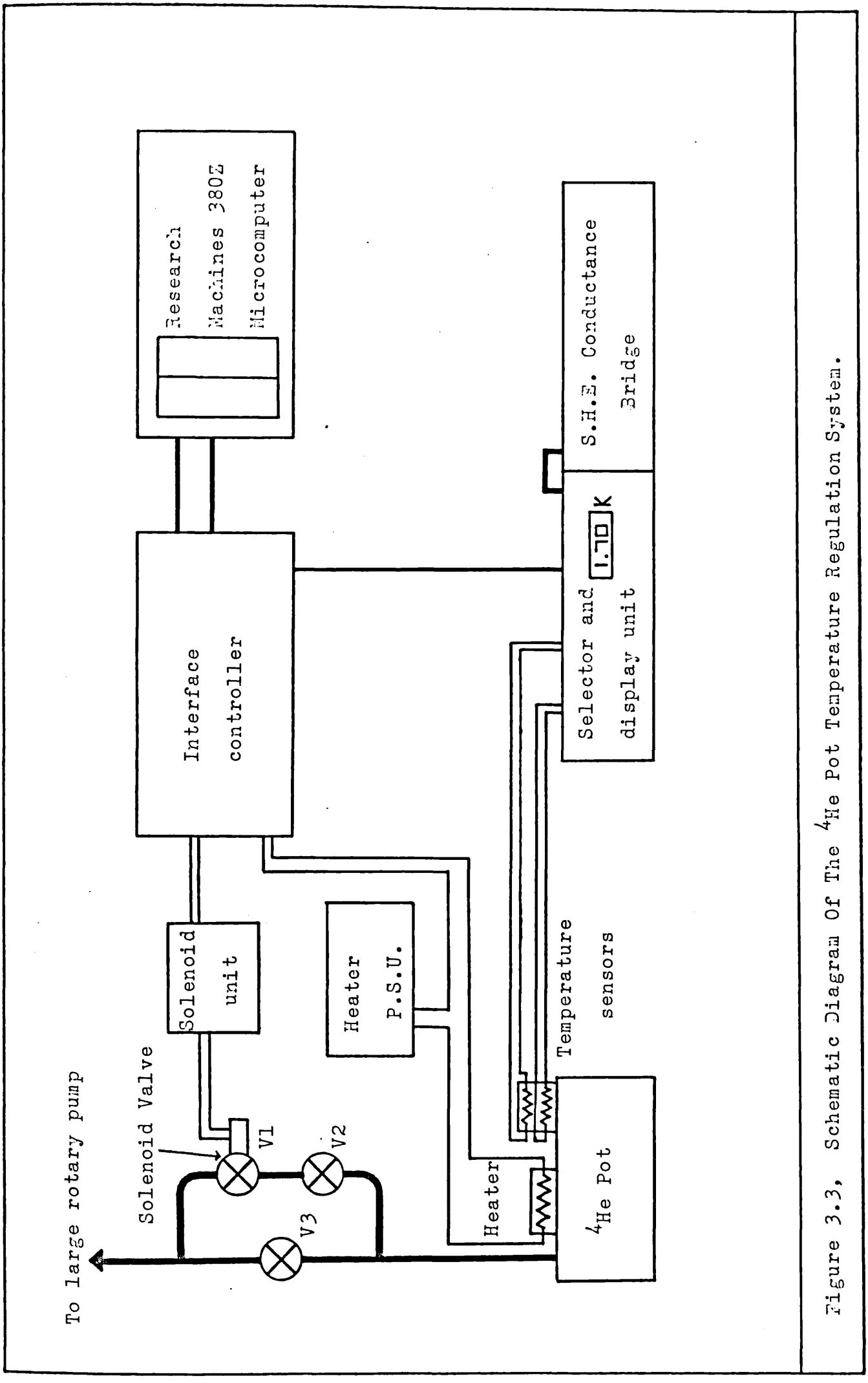

Figure 3.3, Schematic Diagram Of The ^{4}He Pot Temperature Regulation System.

greater speed. However, to perform tasks which require floating point arithmetic it is much simpler to use a high level language (in this case Basic). To simplify implementation of this approach the system is configured to have a 32K memory limit as far as CP/M and any software operating under it, e.g. Basic, are concerned. The machine code routines are written to operate at addresses higher than 32K, this avoids complications such as corruption and overwriting of memory locations. Data communication between software procedures is performed via a memory scratchpad in the region above 32K. The software used to regulate the pot temperature is described in Appendix 1 to illustrate the operation of the system.

An Epson MX80FT dot matrix printer is attached to the micro-computers RS232 serial output for the provision of hard copy of programs and data.

3.4 The Sample Chambers

The sample chambers shown in figure 3.4 were each machined from a single block of stycast 1266, the outside dimensions of both the Mylar and Grafoil chambers being identical to make them interchangeable within the rotating mechanism. The lid contains a 470Ω½W Speer resistor thermometer, this is arranged so that its long axis is normal to the substrate planes, hence it is in direct contact with the maximum number of planes. To further increase thermal contact some of the ceramic coating of the resistor has been filed away. The lid is glued to the rest of the sample chamber using stycast 1266. A four turn spiral of 1/16th inch diameter thin walled stainless steel tube filling line is sealed into the sample chamber, this is sufficient to take up a 90^{o} rotation of the sample chamber without damage to the seal.

(a) Mylar

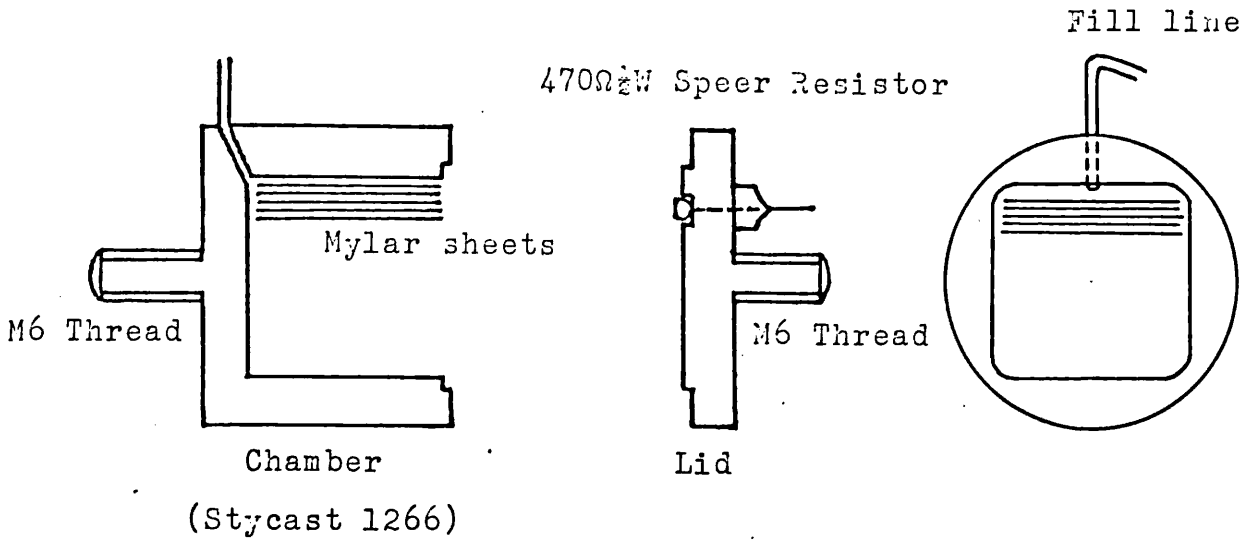

(b) Grafoil

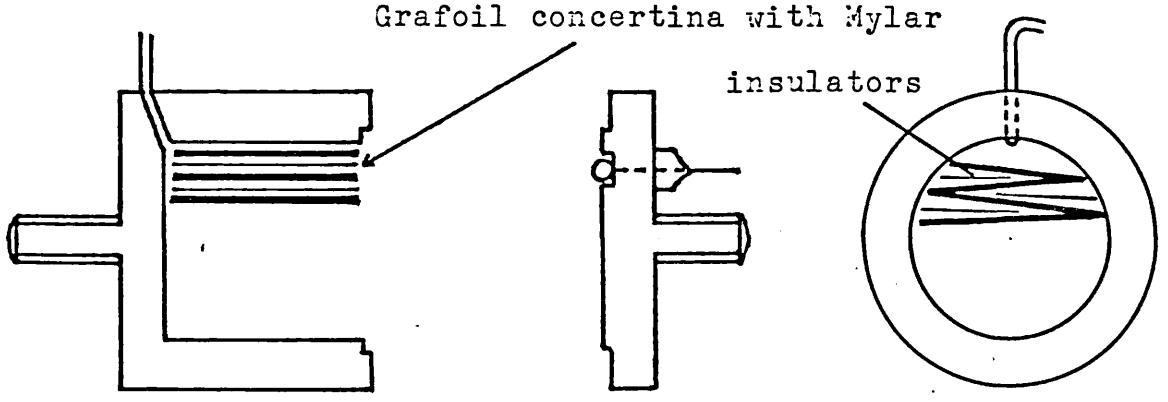

Figure 3.4, The Sample Chambers, (actual size).

The interior of the Mylar sample chamber is a one inch cube packed with 2200 sheets of optical grade Mylar film 0.01 mm thick. The total area for adsorption is approximately 2.6 m^2. No special substrate preparation techniques were used though care was taken when handling the film to avoid contamination with dust and grease. Any dust on the sheets was blown off with a high pressure helium jet before they were installed in the sample chamber. Following assembly and leak testing the sample chamber was connected to a high vacuum system for several days to outgas.

The inside of the Grafoil sample chamber is cylindrical in shape, one inch long and one inch in diameter. A strip of 0.4 mm thick Grafoil 8.53 grammes in weight was folded into a concertina to fit in the chamber. To reduce eddy current heating the layers of Grafoil are insulated from one another by inserting sheets of Mylar between them. To expel water vapor and other contaminents adsorbed from the atmosphere the Grafoil was baked in vacuo at 1000^{o}C for 8 hours before assembly of the sample chamber. To avoid re-contamination of the Grafoil the chamber assembly was carried out in a glove bag with a helium atmosphere. Following leak testing the Grafoil sample chamber was connected to a high vacuum system for a few days.

3.5 The Rotating Mechanism

An important aspect of the present work is to investigate how the nuclear magnetic relaxation times are affected by changes in the orientation of the substrate planes with respect to the magnetic field. It is therefore necessary to be able to rotate the sample chamber without stopping the run and opening the cryostat. The cryostat already had a spare tube running from the top down to the inner vacuum chamber for this purpose. Our mechanical workshop built a mechanism to support and rotate the sample chamber, figure 3.5. Bevel gears are used to change the drive axis from vertical to horizontal.

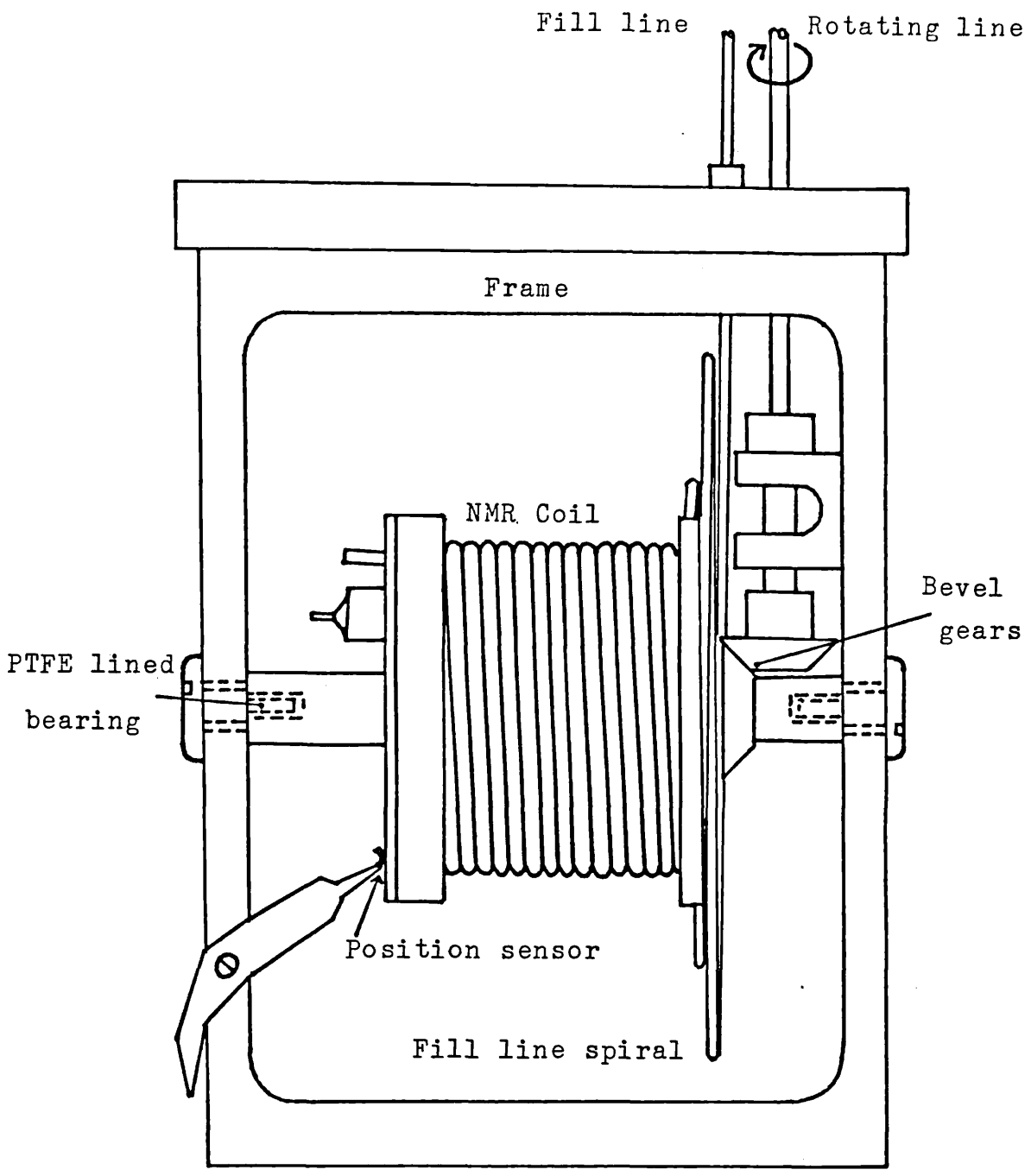

Figure 3.5, The Sample Chamber Rotating Mechanism.

It is not possible to see the sample chamber during a run so a method of sensing its orientation is required. Fitted to the end of the sample chamber is a disc of paxolin printed circuit board etched to leave a set of radially distributed gold plated copper pads 9^{o} wide and separated by 9^{o}, these pads are all electrically connected. Pressing against the sensor disc is a phosphor bronze spring strip. This arrangement comprises the position sensor. Using a continuity tester to indicate when the phosphor bronze strip makes or breaks contact with a copper pad, it is possible to count round from the starting point in 9^{o} steps. The rotating mechanism and the position sensor is shown in figures 3.6 and 3.7.

3.6 The Gas Handling System

The requirement to accurately measure out small quantities of ^{3}He for admission to the Mylar sample chamber necessitated the construction of a small gas handling system at the cryostat head. This cut the length of pipework required and in particular the sample line to a minimum.

The gas handling system is shown in figure 3.8, the gas store and associated pipework has a volume of 18.8 cm^{3}. Precision pressure measurements are made using a Druck digital pressure indicator enabling tiny fractions of a cc (STP) of ^{3}He to be measured out via the needle valve. A second Druck gauge head is attached to the sample line; it is used to ensure that all the sample is admitted to the chamber and to make Isotherm measurements. There is also a 77K charcoal trap to clean the sample before admitting to the sample chamber.

3.7 NMR Magnet and Power Supply

The Oxford Instruments superconducting magnet consists of four separate windings. The main solenoid will produce fields of up to 2 Tesla at a current of 50 Amps and will operate in persistent mode.

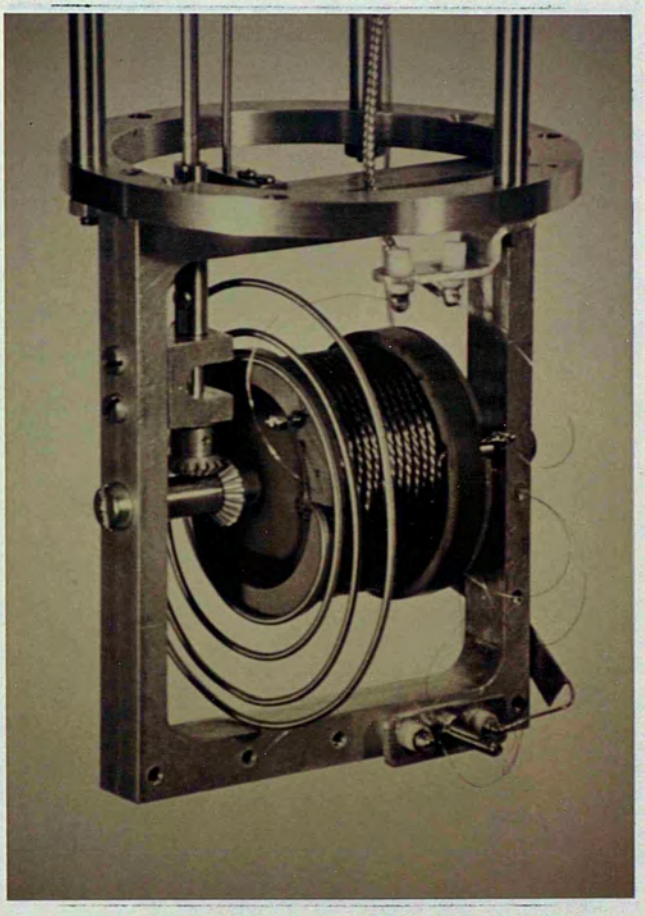

Figure 3.6, The Rotating Mechanism Showing The Bevel Drive Gears And The Spiral Filling Line.

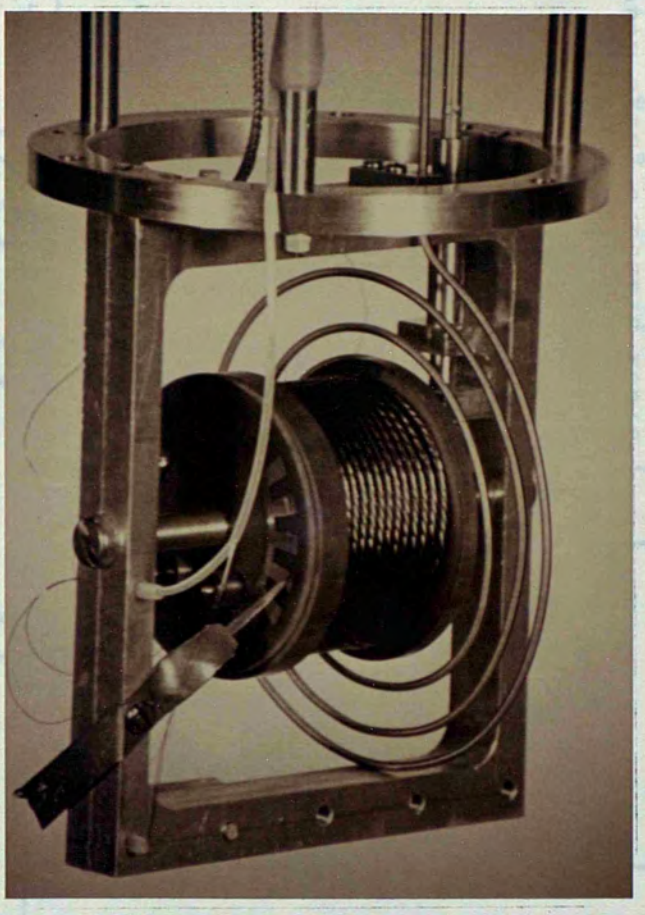

Figure 3.7, The Rotating Mechanism Showing The Position Sensor.

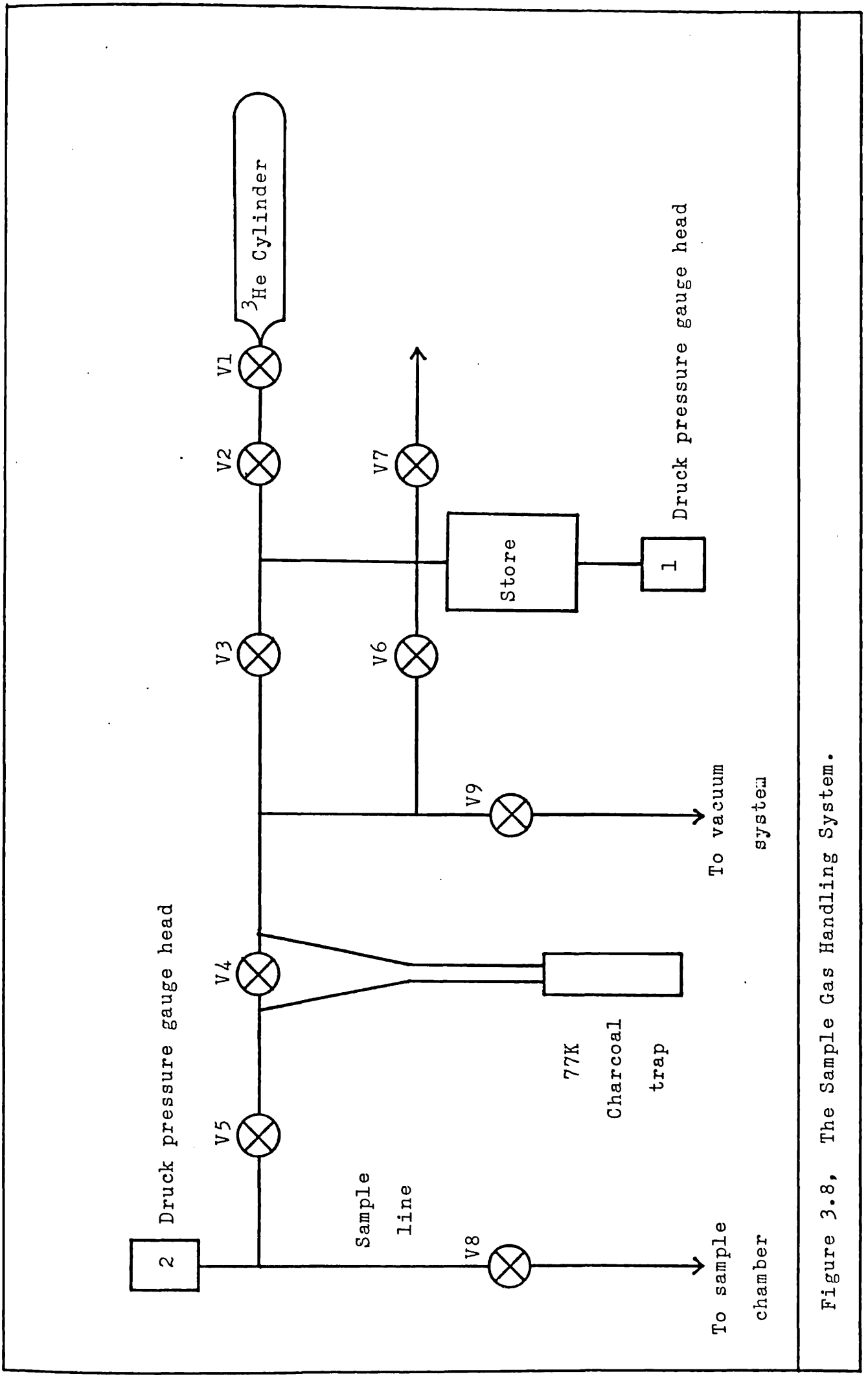

Figure 3.8, The Sample Gas Handling System.

To improve homogeneity a persistent mode Z_1 shim coil is provided, the manufacturers claim a homogeneity of 1 part in 10^5 over a one inch cube at the centre of the solenoid. There are also a pair of Helmholtz coils to provide a field gradient or shift, these do not operate in the persistent mode.

A current regulated power supply is used to power the magnet. It has dual current capability which enables the mean current supplied to the Helmholtz coils to be varied whilst maintaining a constant current difference and vice versa. It has heater supplies for the main coil and the shim. It is capable of supplying 6½ amps to the main coil representing a Larmor frequency of about 8.3 MHz for ^{3}He.

The current is regulated by maintaining constant the voltage across a standard sense resistor in series with the magnet coil; this voltage is also fed to a 4½ digit digital voltmeter to display the current.

3.8 The NMR Probe

The probe, comprising the NMR coil and associated tuning and matching components is the central part of the NMR apparatus. No amount of work perfecting the receiver can compensate for a badly designed or constructed probe. To maximise the signal to noise ratio of the received signal the coil must be well designed, of high Q and the losses in the probe circuits kept to a minimum [60][61].

A single parallel tuned NMR coil was chosen which subject to the restraints of the cryogenic environment is most convenient when it comes to tuning and frequency changing. The coil consists of 14 turns of wire made up from seven strands of enamelled copper wire. The use of multi-stranded "(Litz)" wire results in a coil of higher Q-factor at frequencies where skin depth effects become important; it is also easier to wind them than a single strand of the same overall thickness. The coil is wound onto a tufnol bobbin which is a close fit over the sample chamber; it is 25 mm long, 42 mm in diameter and has an inductance of 7.8 microhenries.

To obtain resonance at the nominal NMR frequency of 5MHz a parallel tuning capacitance of 130pF is required. Part of this, ∿ 50pF is provided by the home-made co-axial line running down the cryostat, the rest is due to a 33pF silvered mica capacitor at the bottom of the line (which also serves as thermal anchoring), and the tuning capacitor at the top of the line. The Q of the probe circuit at 5MHz is 125 with the Mylar sample chamber and 28 with the Grafoil one, the reduction being due to eddy current losses in the Grafoil.

When a single coil probe is used a duplexer is required to protect the input of the pre-amplifier from the high voltage transmitter pulse, and to isolate the transmitter during receive periods. A form of Q-switching is also required so that during and just after transmit periods the Q of the NMR coil is low to reduce ring-down time, but during receive periods the Q must be high for maximum sensitivity. There are a number of circuits in the literature [62], [63] & [64], but many have the disadvantage that frequency changing is then difficult. The circuit shown in figure 3.9 fulfils the above requirements and is broadband. It includes elements for matching the probe impedance to the transmitter and pre-amplifer. The operation is as follows. The 50ohm transmitter output impedance is matched to the probe in the quadrifilar wound torodial transformer T_1, the resulting high voltage transmitter pulse (∿ 1000V) first passes through the high pass filter stage comprising C_1, R_1 and R_2. The pulse switches on crossed diode pair XD2 and appears across the NMR coil. Another pair of crossed diodes connected across the input of the pre-amplifer clamp the voltage at that point to ∿ 0.6V hence protecting the input transistor. Immediately after the transmitter pulse the ringing voltage across the coil is sufficient to keep diodes XD2 in the on (or low impedance) state, so R_1 and R_2 continue to damp the coils Q until the voltage has rung down to < 0.6V. After that the transmitter is isolated from the coil and pre-amplifier. The

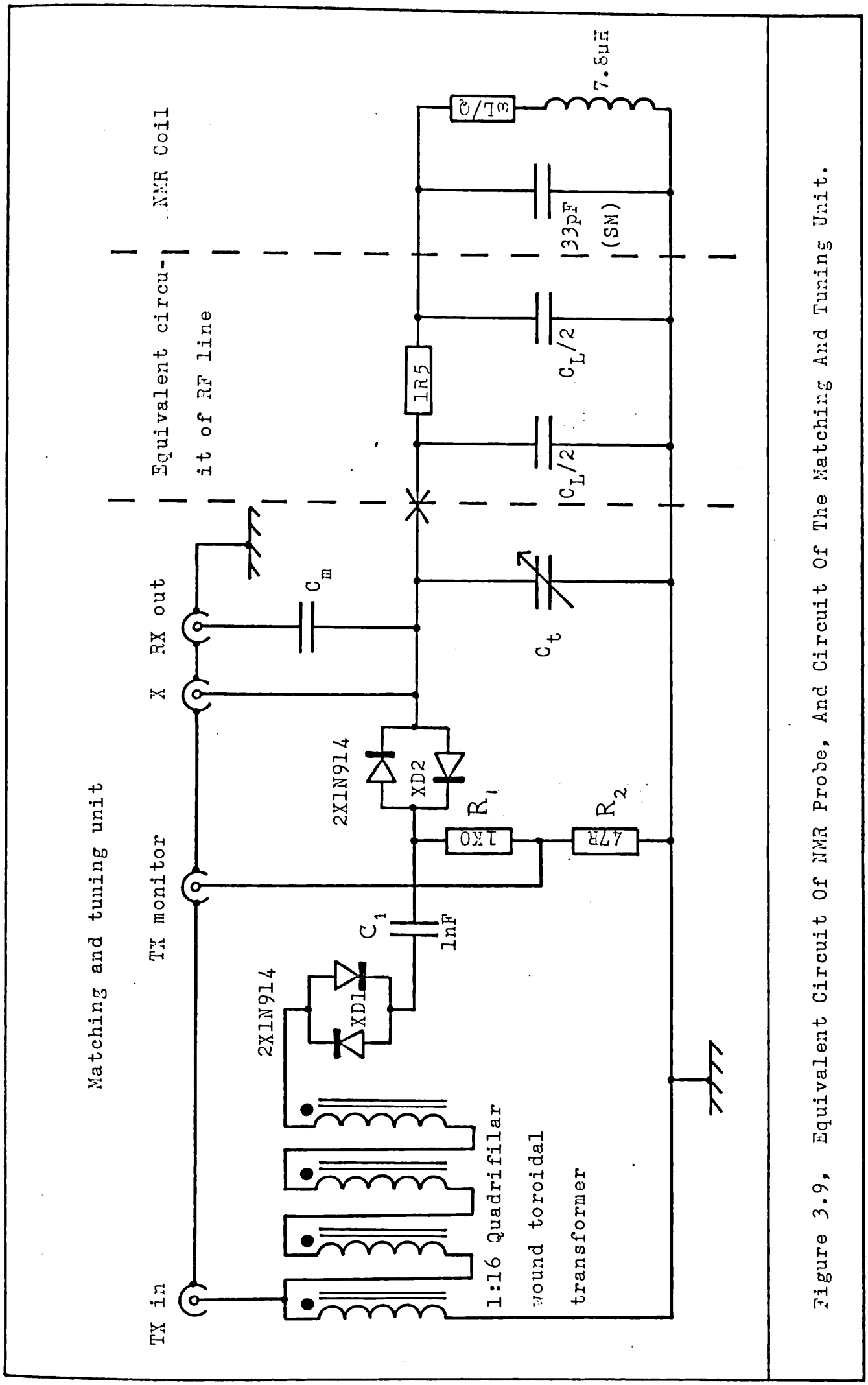

Figure 3.9, Equivalent Circuit Of NMR Probe, And Circuit Of The Matching And Tuning Unit.

capacitor C_m matches the impedance of the probe resonant circuit to the optimum input resistance of the pre-amplifier. If C is the total capacitance in parallel with the coil, the resistance "seen" by the input transistor is

$$\frac{1}{R} = \left(\frac{1}{Q\omega L}\right) + \frac{Q\omega C_m^2}{C+C_m} \qquad (3.8.1)$$

where ω is the resonant frequency

$$\omega^2 = 1/L(C + C_m) \qquad (3.8.2)$$

therefore

$$C_m^2 = \left(\frac{1}{Q\omega^3 L}\right) \left(\frac{1}{R} - \frac{1}{Q\omega L}\right) \qquad (3.8.3)$$

provided that $Q^2 >> 1$.

Small frequency changes (±5%) are brought about by adjusting C_T, however, to obtain larger changes extra inductance or capacitance must be connected at point X. Some degrading of performance is to be expected if the frequency is pulled a long way by this method. In practice it was found that NMR frequencies between 1 and 10MHz could be achieved with only a single tuning operation required, and without too severe a reduction in performance.

3.9 The NMR Spectrometer

A block diagram of the conventional coherent pulse spectrometer system is shown in figure 3.10. Conventional, that is, only as far as the functions of the various blocks are concerned. In order to produce a high sensitivity broadband spectrometer the latest advances in electronic component technology have been exploited in

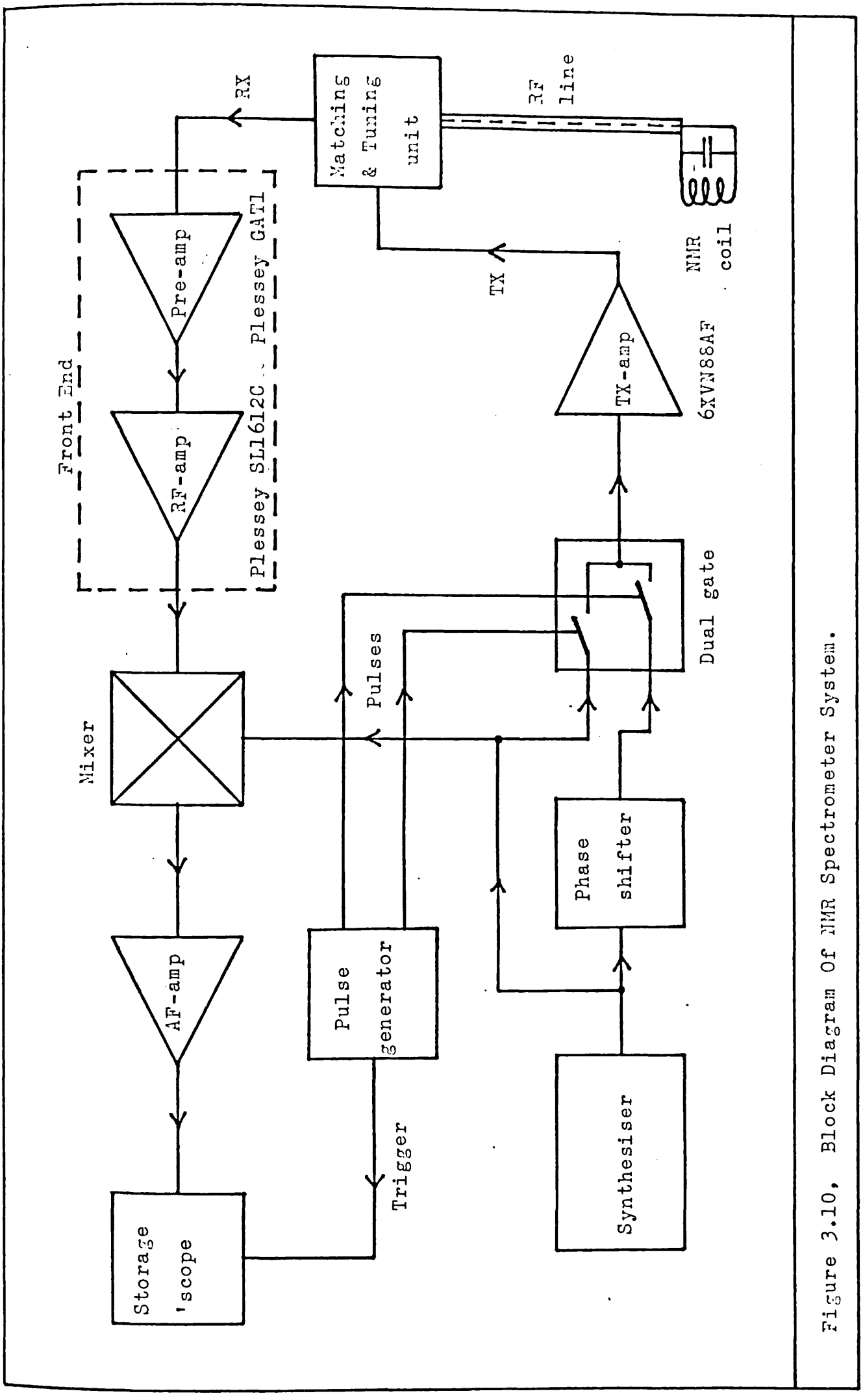

Figure 3.10, Block Diagram Of NMR Spectrometer System.

the design of many of the circuits. The spectrometer system can be divided into two parts, the pulse transmitter to prepare the magnetization and the receiver which amplifies and detects the tiny voltage induced in the coil by the precessing magnetization.

(a) The Receiver

The requirements for a pulse NMR receiver are that it should have a high sensitivity and signal to noise ratio. The dead time, that is the time taken to recover full signal sensitivity following a transmitter pulse, should be no longer than the time taken for the probe voltage to ring down to the noise level. The receiver should also be broadband, thus cutting down the number of tuning operations required when the frequency is changed.

Figure 3.11 shows the circuit of the receiver front end. A gallium arsenside JFET is used in the first (pre-amplifier) stage, this device was chosen because of its relatively high transconductance g_m and low junction capacitance C_j. The optimum noise performance of a JFET is achieved when the signal source impedance (real) is given by, [65];

$$R_s \simeq 1.6M/fg_m \qquad (3.9.1)$$

where f is the frequency and M is the "figure of merit" of the device,

$$M = g_m/2\pi C_j \qquad (3.9.2)$$

The transistor used (Plessey GAT 1) has g_m = 14mS and C_j = 2pF, hence at 5MHz, R_s = 25.5kΩ. This value will, in practice, be somewhat lower due to additional shunt capacities at the input e.g., the input protection diodes. Excellent performance is obtained at 5MHz by assuming the actual value of R_s to be about 5KΩ and choosing the

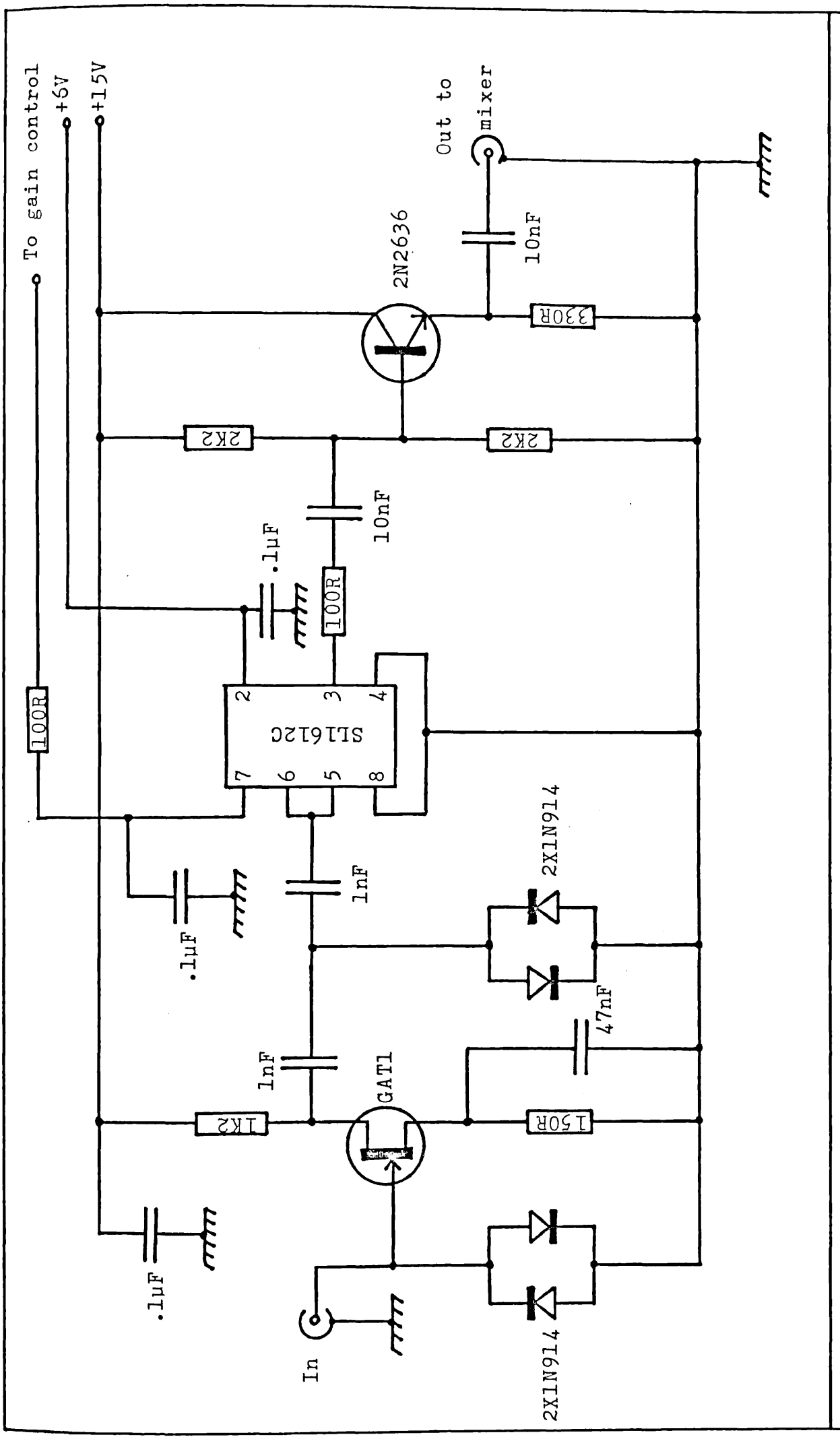

Figure 3.11, Cicuit Of The Combined Receive Pre-Amplifier And RF Amplifier.

probe matching capacitor, C_m, accordingly, see §3.8.

In the interests of broadband response a resistive drain load is used, the stage gain being approximately 10X with the 1.2kΩ load resistor as shown. The first stage output is fed via a crossed diode limiter to the main RF amplifier stage which provides most of the signal frequency gain required to overcome the detector noise. An integrated circuit SL1612C (Plessey) is used in this stage, it is a broadband (0.1 to 15MHz) RF amplifier IC with a voltage controlled gain of up to 30dB. It has the advantages of low noise, simplicity of circuit construction, small size, and being directly coupled internally it recovers quickly from saturation. The output is buffered to 50Ω by an emitter follower stage and fed via a co-axial line to the detector stage. The receiver front end is built in a die cast box and mounted at the cryostat head thus avoiding the use of long co-axial lines for carrying small signals. Figure 3.14(b) shows the associated remote gain control voltage switch and power line filter unit.

The detector stage is a Minicircuits SRA12 double balanced mixer demodulator, this device has a broadband frequency response and wide dynamic range. The modulated RF signal is applied to one of its inputs, to the other is applied a steady RF reference voltage at the Larmor frequency. The mixer multiplies the two inputs to produce sum and difference frequencies at the output. The difference frequency which is the signal envelope is filtered and amplified in the AF amplifier stage.

Finally, the signal is displayed for measurement on a Gould Advance OS 4100 Digital Storage Oscilloscope that has been modified to provide signal averaging facilities.

(b) Transmitter

The required pulse sequence is generated as a series of rectangular TTL pulses with the necessary widths and delays. The transmitter circuits use these to gate pulses of RF at the Larmor frequency which are then amplified up to instantaneous powers of the order 1kW before application to the NMR coil. Such high powers are required to satisfy the need for the B_1 field produced to be much larger than the inhomogeneity in B_o across the sample volume. The rise and fall times of the pulses must be as short as possible, and there must be no RF or noise feed through during "off" periods.

Figure 3.12 shows one channel of the dual channel RF gate. No attempt has been made to preserve a sinewave output as this complicates the design and is unnecessary anyway since most transmitters work in class C or switching mode (class D). The broadband amplifier stage TR_1 amplifies the RF input of about 1V to TTL level ($\sim$3V) suitable for one input of the Shottky NAND gate. The input is biased near its switching point using VR1 so that when a positive TTL pulse is applied to the second input, the output is a packet of RF square-waves with a 1:1 mark/space ratio. The output is fed to one input of a second NAND gate which sums both channels. Schmidt trigger gates are used to ensure good pulse shapes and high isolation when in the OFF state.

The power amplifier circuit is shown in figure 3.13; it respresents a departure from conventional design in that the output transformer is untuned. Resulting in a broadband transmitter, and due to the absence of signal frequency ringing from the output transformer, fast pulse rise and fall times. The fundamental is selected from the near square wave output of the transmitter by the NMR probe tuned circuit.

The power amplifier will deliver peak pulse amplitudes of up to 250V into 50Ω loads from six Siliconix VN88AF VMOS power FET's

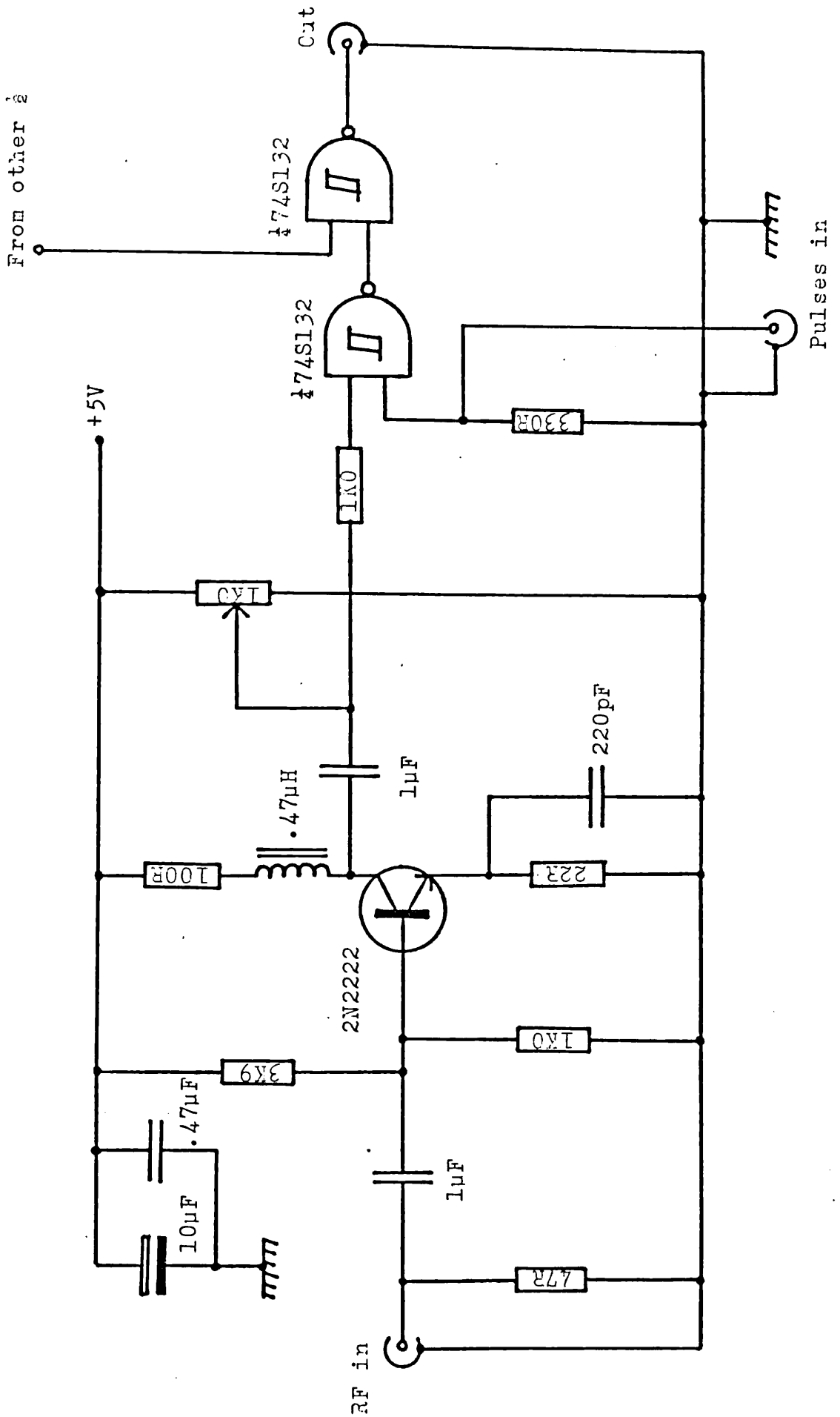

Figure 3.12, Circuit Diagram Of One Channel Of Dual Channel RF Gate.

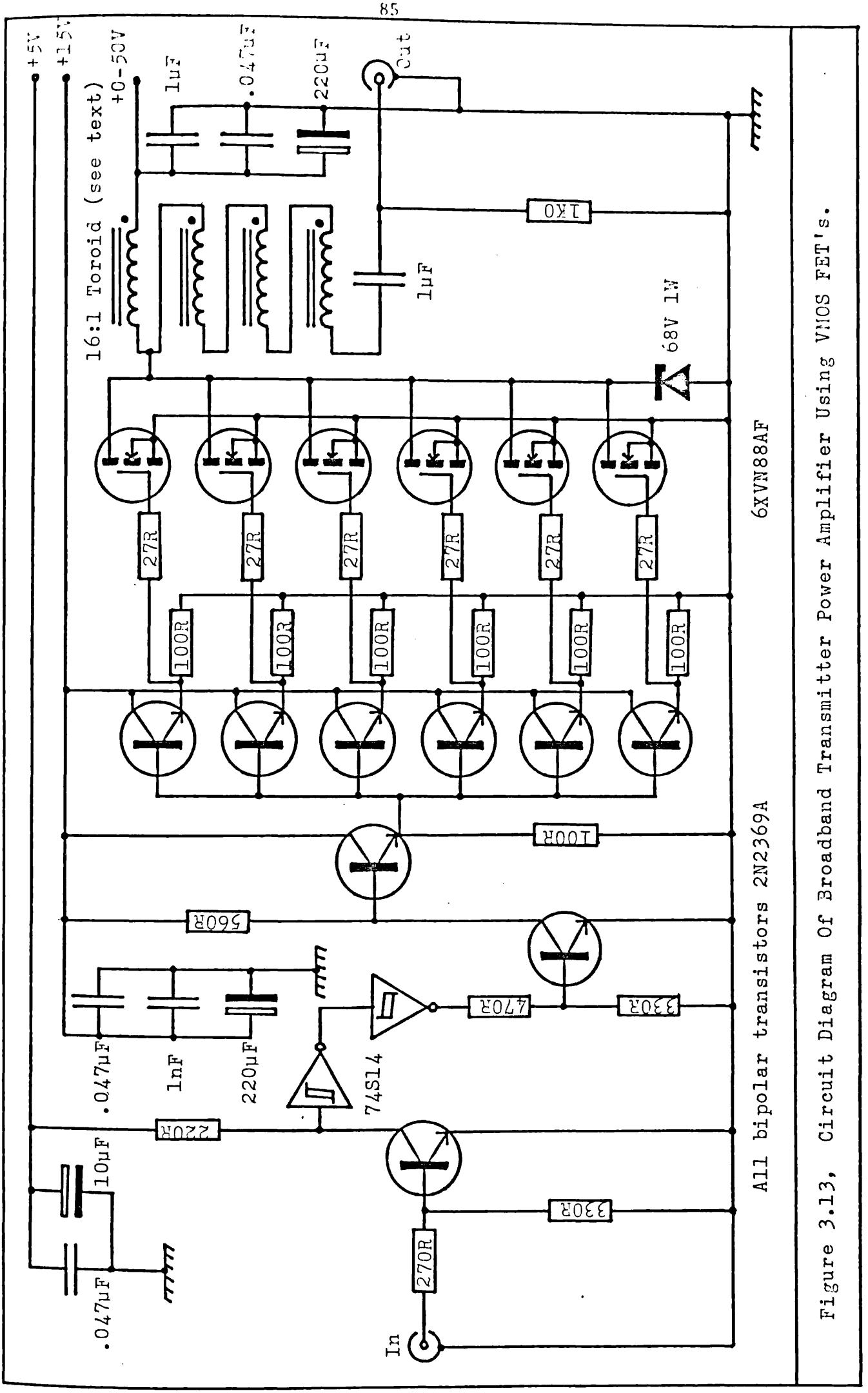

Figure 3.13, Circuit Diagram Of Broadband Transmitter Power Amplifier Using VMOS FET's.

operating in class D, switching mode. The advantages of VMOS FET's [66] are high gain, no minority carrier storage time, no thermal runaway, greatly inhibited secondary breakdown characteristic and the drain current is limited by electron velocity saturation. These features result in a device that can be readily paralleled without "current hogging" and which is tolerant of mismatched and reactive loads. The devices are very cost effective when compared with bipolar transistors in this application.

The effective gate circuit of the VMOS FET consists of a resistance of about $10^{12}\Omega$ in parallel with about 30pF capacitance. To achieve the fast switching times necessary in RF applications, the driver stage must be a low impedance high current source, hence minimising the time taken to charge the gate capacitance. In the amplifier each VMOS FET is driven by an emitter follower satisfying these requirements.

The combined drain impedance of 3Ω is matched to the 50Ω output load impedance using a 16:1 quadrifilar wound toroidal transformer T1. Toroidal transformers [67] have the advantages of being self-shielding and compact. The following points regarding the design of T1 are important; the core chosen must be large enough to cope with the transmitter power without saturating. The low frequency half power point occurs when the reactance of the windings is approximately equal to the impedance the winding is "looking into", while the high frequency limit is set by the stray capacitance in the windings. When constructing a broadband transformer it is therefore better to use a low frequency core material and few turns, thus reducing the stray capacitance. As the frequency increases the core material becomes inefficient and disappears electrically. A typical transformer covers about a decade in frequency. Two amplifiers were constucted, one covers the range 1 to 10MHz and uses a Micrometals T157-2 dust iron toroidal core with 10 turns quadrifilar wound, the other covers 0.1 to 1MHz

using a Mullard FX 3854 Ferrite toroid also with 10 turns quadrifilar wound. Identical transformers are used in the NMR probe matching unit described in §3.8.

The VMOS FET drains are protected from potentially destructive transients generated by the output transformer by a 68V zener diode, this diode also protects against the application of excessive supply voltage. The amplifier is also very tolerant of mismatched, open and short circuit loads.

Other elements of the transmitter amplifier circuit are an input stage consisting of TR1 and IC1 which shapes the input pulses, and ensures a high isolation when there is no input. TR2 is an amplifier stage which increases the TTL levels to the 15 volts required to drive the VMOS FET's into saturation and TR3 is a pre-driver.

The circuit in figure 3.14(a) provides a variable drain supply voltage from 0-50V for the VMOS FET's. An integrated high voltage regulator is used to set the charging voltage of the two 1000μf capacitors at the output, these capacitors provide the short duration high current pulses, up to 18A, required by the VMOS FET's.

Common to both the Receive and Transmit sections of the spectrometer is the RF frequency source, a Rockland Model 5600 Synthesizer, providing stable frequencies from 50kHz to 160MHz in 0.1Hz steps, locked to a 10MHz crystal standard. In order to prevent overloading of the synthesizer output and to ensure that the transmit and receive sections are fully isolated, a Buffer/Isolator providing four independent 50Ω outputs from one 50Ω input has been constructed, figure 3.15. It also includes a detector and voltage comparator stage, which enables the output to be set to the optimum level (1Vpk-pk) for the other circuits. The phase shifter, figure 3.16, can be inserted between the RF source and the mixer or the RF source and the gate, and enables the RF reference and signal inputs to the

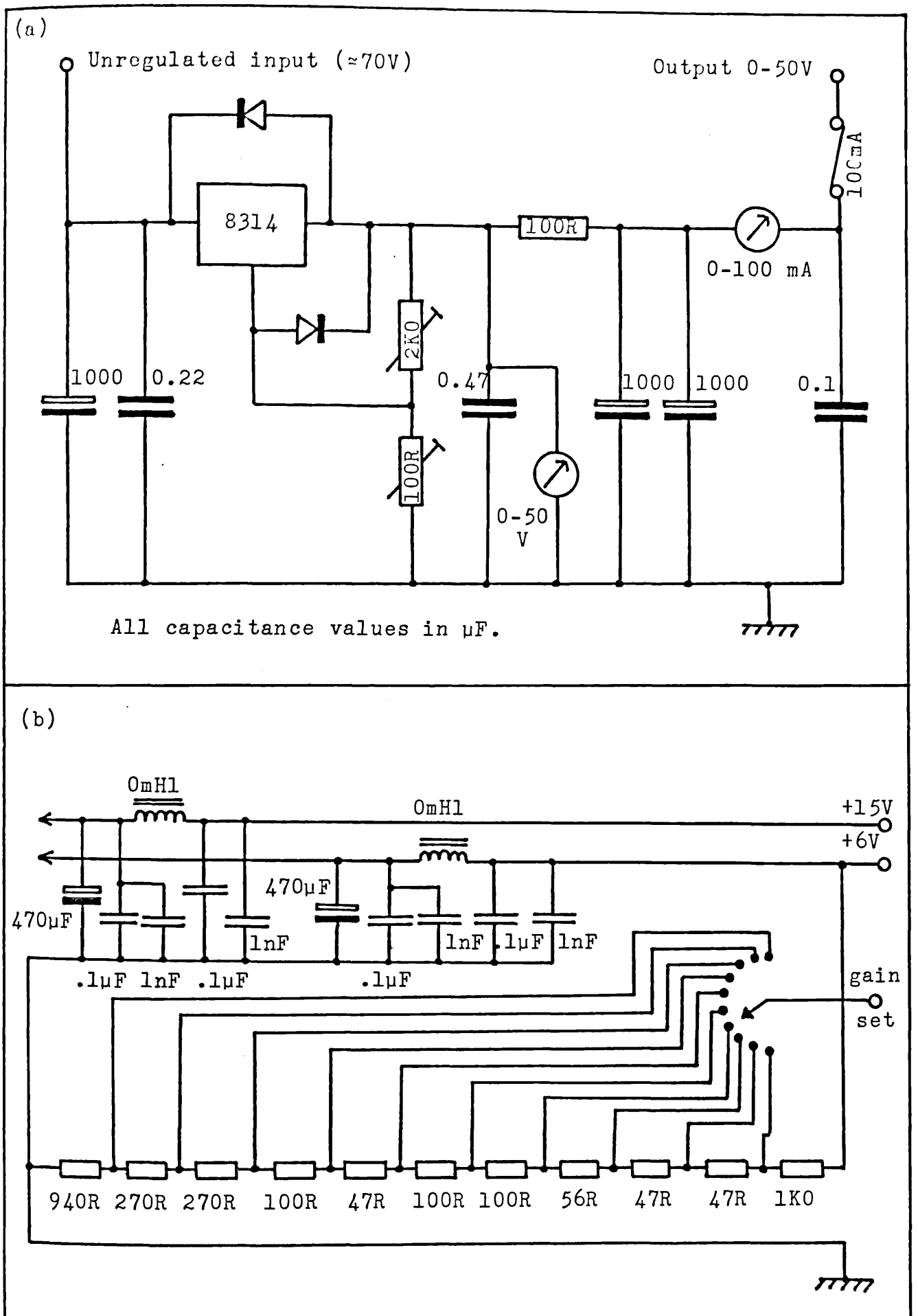

Figure 3.14, Power Supplies, (a) 0-50V For Transmitter.
(b) For Receiver Front End.

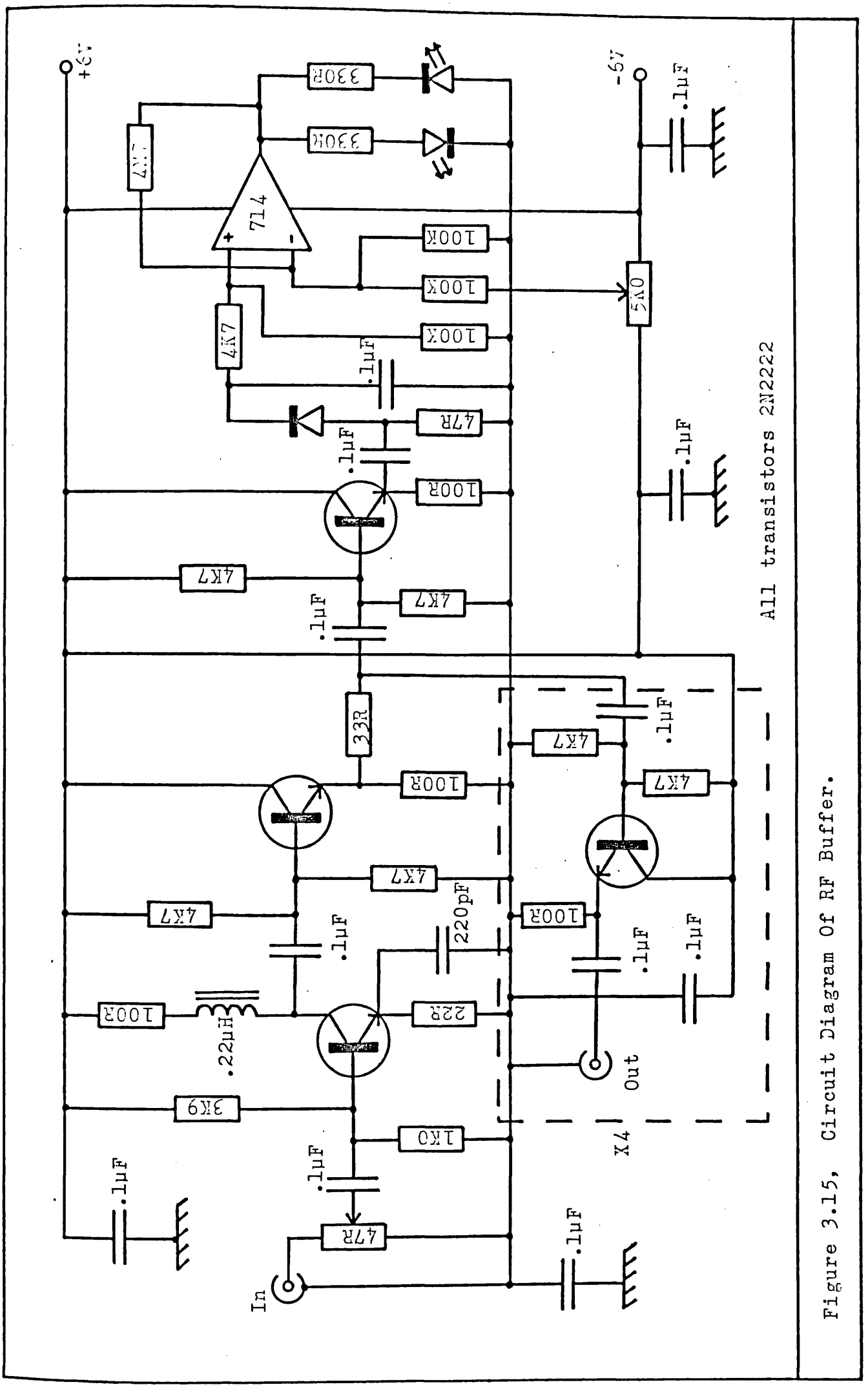

Figure 3.15, Circuit Diagram Of RF Buffer.

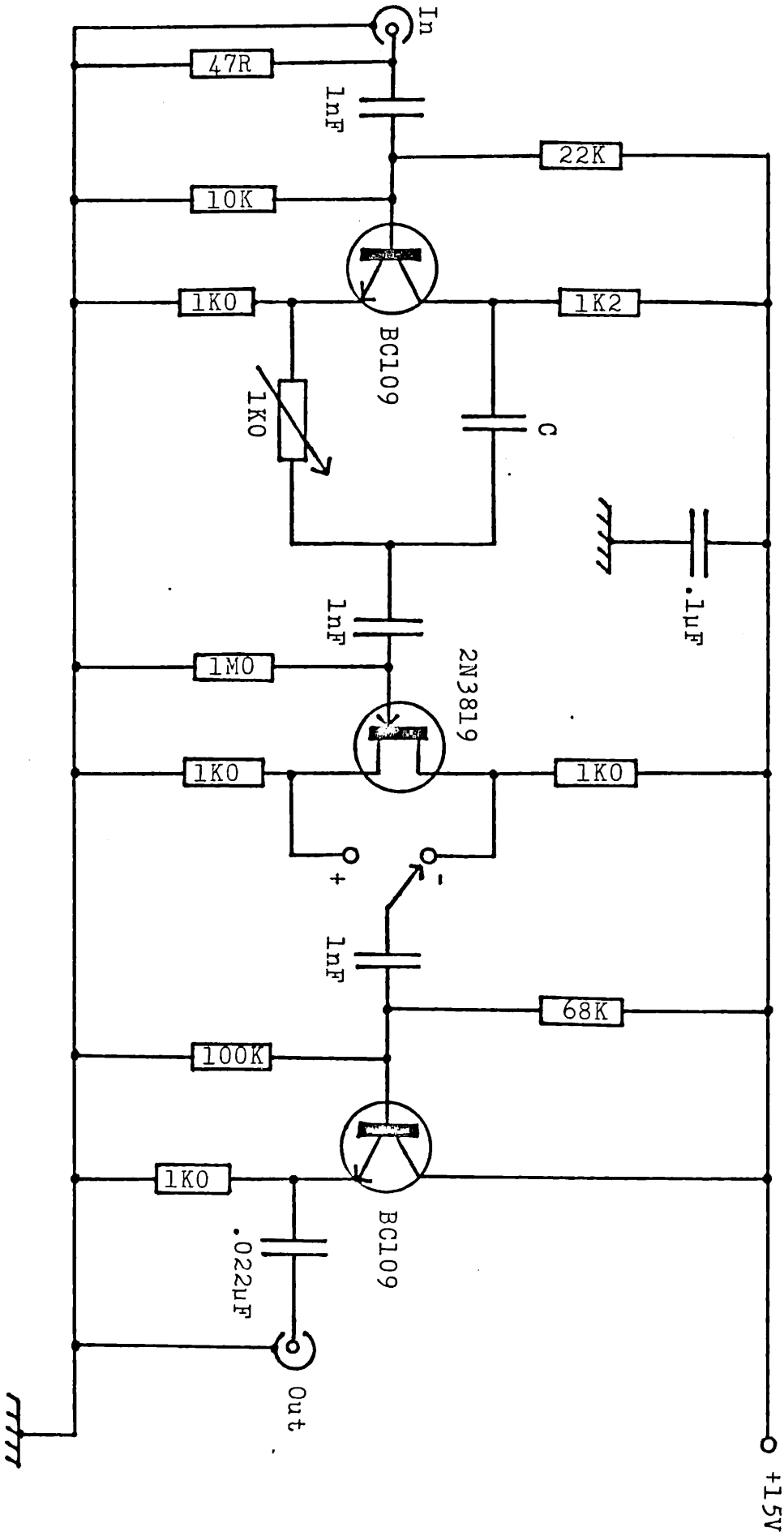

Figure 3.16, The Phase Shifter, For 5MHz; C=100 pF.

mixer to be put in phase.

The spectrometer system as a whole performs very well, the minimum signal level for a 1:1 signal to noise is about 1.5μV at 5MHz. This figure compares with the Johnson noise generated by the resistive losses in the NMR probe circuit. With the aid of the signal averaging facilities it was possible to observe at 5MHz and 1.2k the signal from 0.005 monolayers of ^{3}He in the Grafoil sample chamber, about 1.6×10^{19} spins. The dead time amounts to about 90μs which is comparable to the time taken for the probe to ring down from 0.6V to 1μV. No extra Q-damping is considered necessary for our experiments.

3.10 The Pulse Generator

The requirements are for a pulse generator capable of generating the variety of pulse sequences needed for pulse NMR accurately and in an easily controlled manner. The simplest sequences required in T_1 and T_2 measurements can contain up to three pulses while in multipluse NMR studies of solids sequences of much greater complexity are needed. The usual approach to pulse generator design has been to produce a number of mark/space generator cards using monostables or digital counters. A number of these cards can then be cascaded to produce the required complexity of sequence. A master controller including sequence repeat timer and interfaces for external control is also included in the final unit. The disadvantage with this approach is that an instrument capable of generating some of the more sophisticated sequences is likely to become complicated to build and use. An alternative and successful approach is to use a minicomputer to control the generation of sequences [68]. However, this is rather an expensive solution in terms of both cash and computer time.

For the purposes of the present work only the simple sequences are required, however, with an eye to possible future experiments an

economical microprocessor based pulse sequencer has been developed. The principal feature of the design is that only two programmable mark/space generators are used to generate sequences containing any multiplicity of pulses, under control of an interrupt driven central processing unit. While one mark/space generator is counting the other is being re-programmed for the next pulse. A pre-trigger facility is also included, this generates a trigger pulse for the display oscilloscope a given time before an expected event, e.g., a spin echo, so that it is always centered on the screen.

Figure 3.17 shows a block diagram of the pulse generator system. The CPU is a Z80A running at 4MHz, it is provided with 4K bytes of ROM (read only memory) for program storage and 2K bytes of RAM (random access memory) for pulse sequence data and stack storage. An Intel 8279C takes care of scanning the keyboard and strobing the display, the CPU reads and writes to this via the data bus. The mark/space generators are based around Z80A CTC's (counter timer circuits), these programmable counters are easily interfaced to the Z80 system bus and can be programmed to generate a vectored interrupt [69]. The main clock for the mark/space generators is 1MHz, derived from the 4MHz main system clock which is in turn derived from the 10MHz reference in the Rockland synthesizer. The pulses are fed from the mark/space generators to a demultiplexer unit which routes them to separate outputs and allows some of them to be re-combined to a common output if desired.

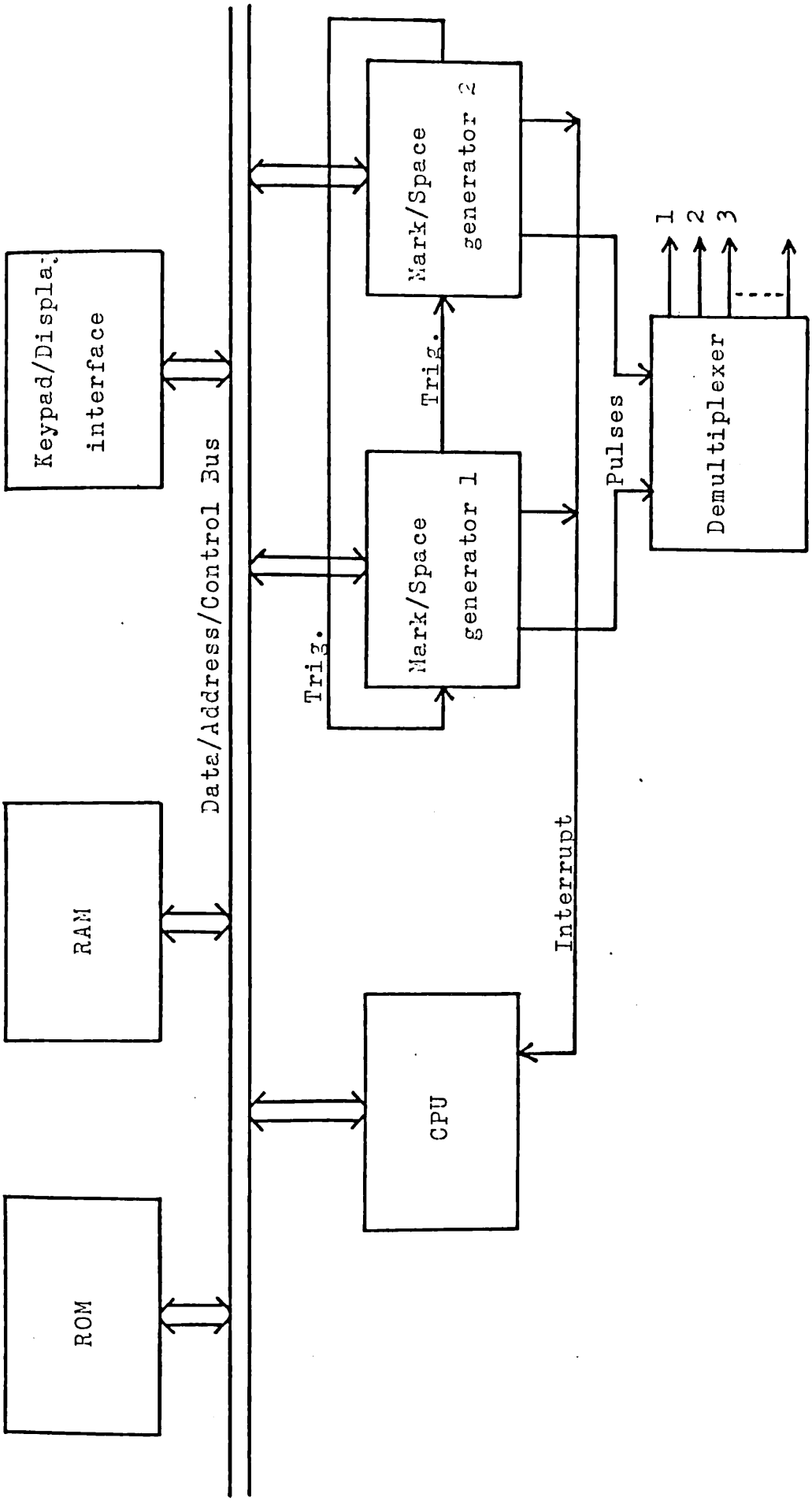

Figure 3.17, Block Diagram Of Microprocessor Based Pulse Generator.

CHAPTER 4

EXPERIMENTAL TECHNIQUES

4.1 Preparing for, and starting an experimental run

Once the cryostat had been closed up and before starting the run the dewar and vacuum cans were evacuated, also while at room temperature the sample chamber was pumped. A V.G. Anavac, residual gas analyser, connected to the vacuum system was used to check that the sample chamber was clear of all of the ^{3}He from the previous run. Approximately 1 torr of ^{4}He exchange gas was admitted to the two vacuum cans before pre-cooling. The ^{4}He pot needle valve was closed and the ^{4}He pot evacuated using its own pump.

The cryostat was pre-cooled to 77K by filling the inside with liquid nitrogen to a level just above the OVC mounting flange. The Dewar's nitrogen jacket was also filled at the same time. After having been left at least 12 hours, the nitrogen remaining inside was removed and the first liquid ^{4}He transfer started. The first transfer was stopped when the Oxford Instruments superconducting wire helium depth indicator read 50%, 0% representing the top of the magnet. The cryostat was left a few hours to reach thermal equilibrium, then the ^{4}He exchange gas was removed from the OVC. Subsequent transfers were made as required, usually every other day, to a level no higher than "75%". Nitrogen transfers are under the automatic control of an Oxford Instruments capacitive nitrogen depth indicator.

Table 4.1 shows typical conductance values of the temperature sensing resistors when the cryostat is at room temperature, during pre-cooling and when at thermal equilibrium after helium transfer.

4.2 Sample Preparation

The same procedure for measuring, admitting to the chamber, and annealing the ^{3}He sample gas was used regardless of whether the Mylar or Grafoil chamber was in place. Referring back to the diagram

Table 4.1. Typical values of the temperature sensors at room temperature, during pre-cooling and after helium transfer.

Resistor Position see also Figure 3.2	Type & Nominal Value	Room Temp. Conductance mmHo	77K pre-cool	Helium Cold
Top Baffle	¼W AB 270Ω	3.563	3.150	2.866
Middle Baffle	¼W AB 270Ω	3.677	2.970	1.767
Bottom Baffle	¼W AB 100Ω	9.163	7.880	1.111
O.V.C. Flange	¼W AB 47Ω	17.375	16.250	2.369
4He Pot (Top)	¼W AB 47Ω	16.898	15.766	2.030
	½W SP 470Ω	1.990	1.716	0.936
^{4}He Pot (Bottom)	¼W AB 47Ω	13.655	12.375	1.935
	½W SP 470Ω	2.043	1.756	0.970
Sample Chamber	½W SP 470Ω	1.958	1.705	0.950
Magnet Top Splash Over	½W SP 220Ω	4.248	3.785	2.289
Magnet Bottom S/O	½W SP 220Ω	4.166	3.773	2.319

AB = Allen Bradley Resistor

SP = Speer Resistor

of the sample gas handling system, figure 3.8. If necessary the store was first filled to a pressure of about an atmosphere with fresh ^{3}He from the cylinder of 99.98% pure ^{3}He. The required amount of sample was then measured out via the needle valve by observing the pressure change ΔP in the store on the Druck gauge, (ΔP in millibars, [70];

$$V_{sample}\ (\text{C.C. @ STP}) = 18.83\Delta P/[1013.25(1 + 0.00367T)] \qquad (4.2.1)$$

The sample was passed into the charcoal trap at 77K to be cleaned and then by opening V5 and V8 it was admitted to the sample chamber at 1K. The sample line pressure being monitored by Druck gauge head 2 to ensure that all of the sample had been admitted to the chamber before V8 was closed.

The sample was annealed by heating the sample chamber to 20K and leaving to cool slowly overnight to 4.2K. The high annealing temperature was used to ensure reproducible results at all coverages, particularly the very lowest.

In the following chapters all coverages are expressed in what we call fractions of a monolayer. The volume of ^{3}He at STP required to complete the monolayer was determined from the 4.2K isotherms, Figures 4.1 and 4.2, using the point B criterion [8]. The monolayer capacities are 0.67cc STP for the Mylar sample chamber and 59.5cc STP for the Grafoil chamber.

4.3 Setting a Stable Working Temperature

The temperature is regulated by the microcomputer system as described in §3.2. To arrive at a stable working temperature other than 4.2K, it was first necessary to enter the required temperature and desired tolerance to the 380Z microcomputer. If a reduction in temperature was requested the solenoid valve, see figure 3.3, was

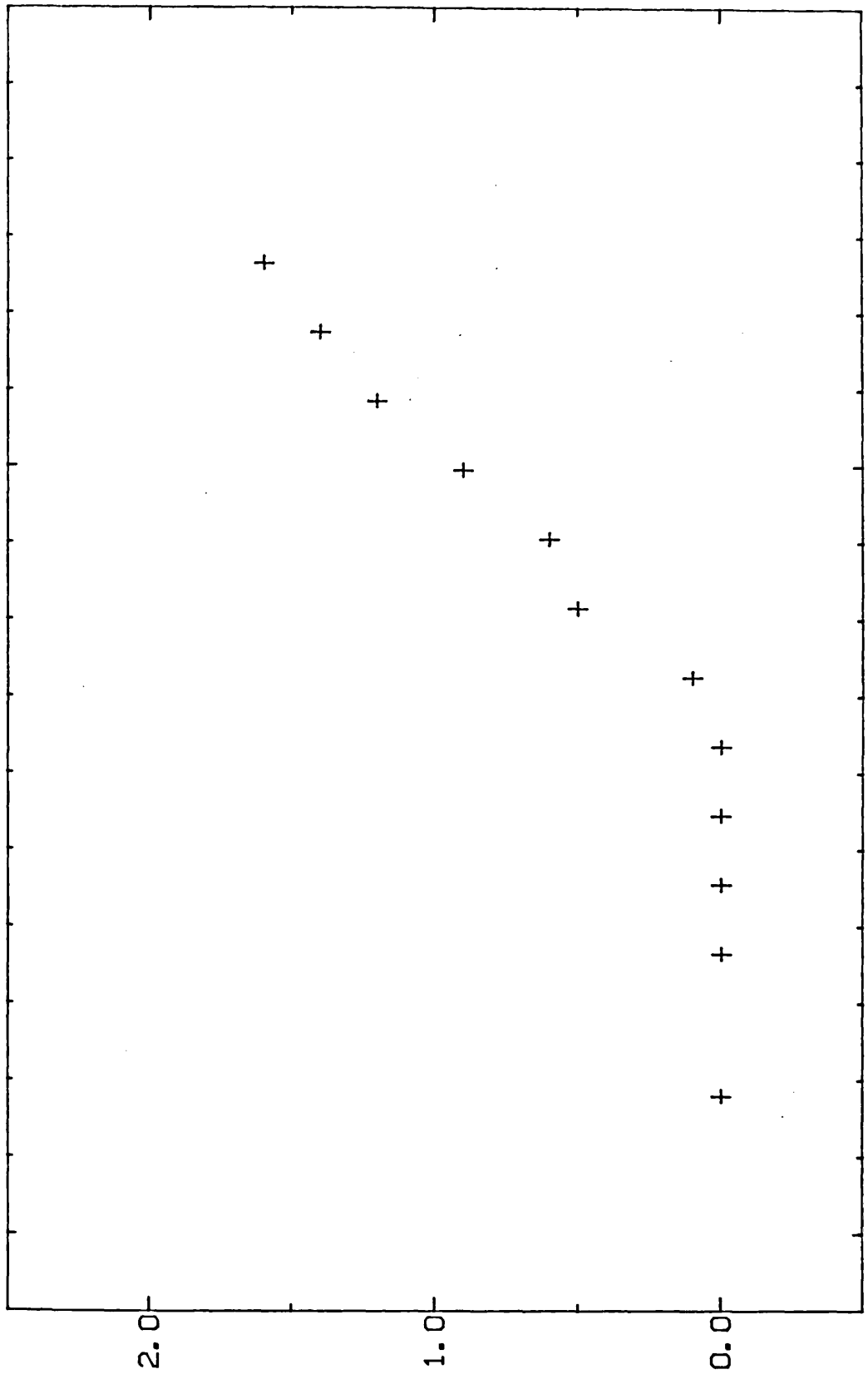

Figure 4.1, 4.2 K Isotherm For Helium-3 Adsorbed On Mylar Film.

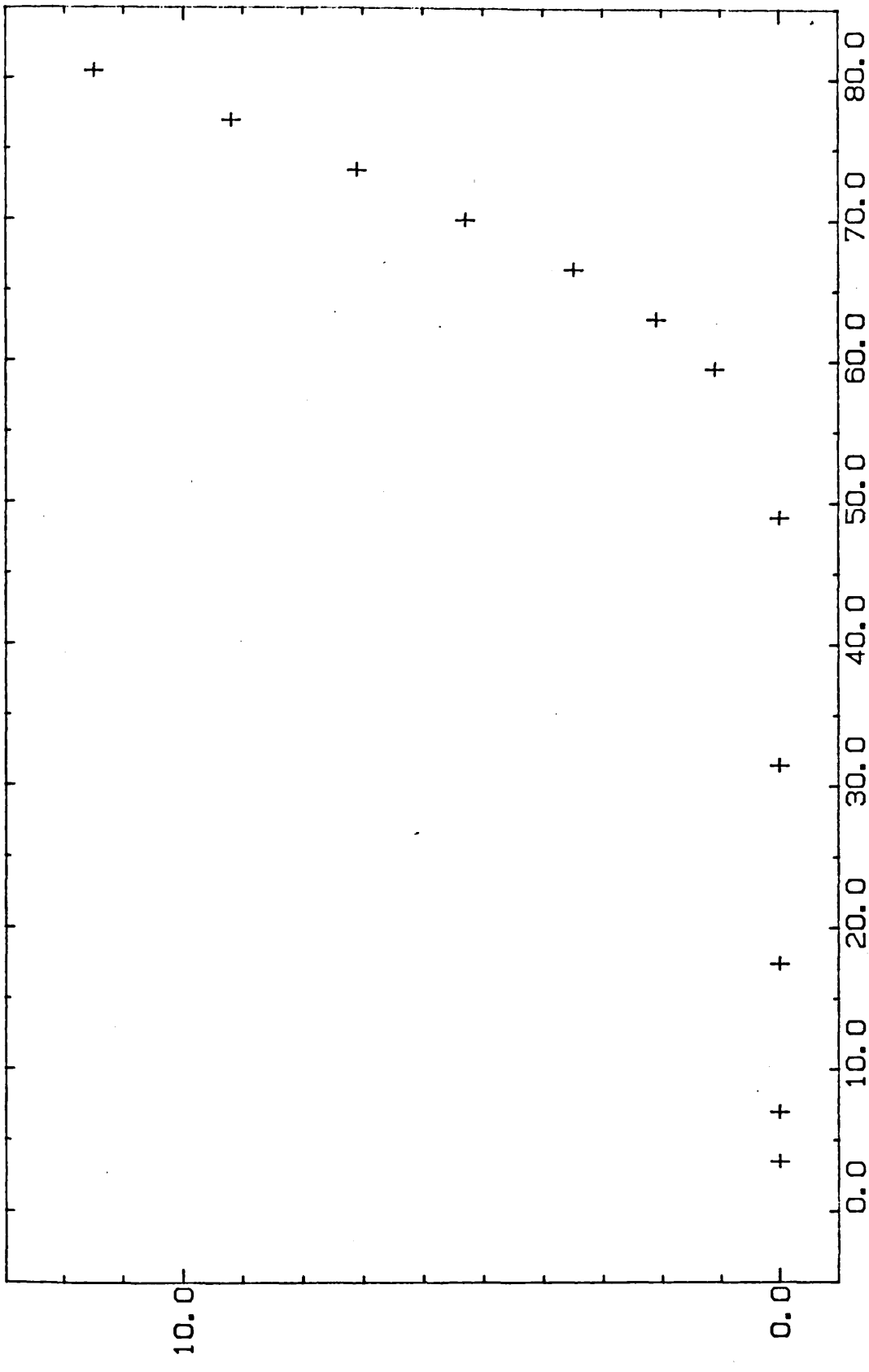

Figure 4.2, 4.2 K Isotherm For Helium-3 Adsorbed On Grafoil.

automatically opened. A solenoid valve can only be fully open or fully closed so the operator has to set the optimum pumping speed required by regulating the series valve V2. When the required temperature was reached it was maintained between the tolerance limits by the on/off action of the solenoid valve under computer control. If a temperature less than 1.5K was required the pumping speed through the solenoid was insufficient due to its restricted orifice. The supplementary parallel valve V3 was then opened only far enough to maintain a temperature just above that required, the solenoid did the rest.

To obtain temperatures above 4.2K the ^{4}He in the pot had to be boiled away first. The pot heater supply voltage then had to be set to a level which enabled the required temperature to be reached in a resonable time without the risk of overshoot. The on/off action of a relay under computer control and in series with the heater and its power supply maintained the temperature between the desired tolerance limits. Table 4.2 shows the optimum heater supply voltages required to arrive at and maintain certain temperatures.

The exchange gas in the IVC ensured that the sample chamber temperature followed that of the ^{4}He pot. However, when the temperature was changed the sample chamber was checked to ensure that it was in equilibrium with the pot before NMR data was taken.

4.4 NMR and Data Taking Techniques

Firstly the NMR signal was found and tuned up using the following procedure; the frequency synthesizer was set to the proposed NMR frequency somewhere in the range 1.5 to 8.4MHz. Exact frequencies like 2,3,4,5 MHz were to be avoided because of the possibility of beats between the synthesizer output and the clocks in other instruments. It was found sufficient to shift the frequency by about 50KHz, i.e., 5.05MHz instead of 5.00MHz. A small

Table 4.2. Heater voltages required to achieve ^{4}He pot temperatures above 4.2K.

Required Temperature	Voltage	Power Supplied mW
5	2	4
6	3	9
7	4	16
8	5	25
10	7	49
12	10	100
14	13	169
16	17	289
18	21	441
20	30	900

Table 4.3. Recommended 90° pulse lengths TX voltage = 40V.

Frequency MHz	Pulse length μsec
1	10
2	17
3	25
4	33
5	40
6	50
7	57
8	65
9	73

amount of RF was bled into the probe circuit via the monitor point on the probe matching and tuning unit, figure 3.9, and with the necessary extra capacitance or inductance at point X, the tuning capacitor, T_c was adjusted for maximum RF output from the receive amplifier.

To find the signal a train of approximate 90^o pulses each separated by one second was applied to the NMR coil. Table 4.3 shows the approximate 90^o pulse lengths required, with the transmitter supply voltage set to 40V. The magnet was then wound up to the required field for resonance, which for ^3He is given when the magnet current is equal to 0.772 F_o amps, where F_o is the NMR frequency. Alternatively, the current was adjusted until the free induction decay was observed. Once obtained the FID was fine tuned by adjusting the synthesizer frequency to produce a smooth and flat envelope, which was then maximised by adjusting the phase shifter.

The pulse lengths were fine tuned by applying a train of approximate 180^o pulses, and then, by adjusting the transmitter supply voltage the FID was zeroed. At which point the applied pulses were exactly 180^o. The spectrometer was then ready for taking the T_1 and T_2 data by application the relevant pulse sequences.

Two methods were used for the measurement of T_2 depending on its length. For T_2 values longer than about 500μs the 90^o-τ-180^o-echo method was used, see §2.5, the echo heights being read directly from the oscilloscope screen. While for T_2 less than about 500μs it was obtained by analysing chart recorder plots of the free induction decay following a single 90^o pulse. The doubly balanced mixer output is very sensitive to the phase difference between the signal and reference inputs when their frequency is the same, so, when recording the FID, the reference was detuned by a few KHz. This resulted in a decaying beat pattern the envelope of which had the same shape as a perfectly "in phase" FID. To extract T_2 from the FID data it was necessary to

correct for the contribution from the inhomogeneous field. This procedure was easy with the Grafoil sample chamber in place, the FID was exponential with a decay constant T_2^* given by,

$$\frac{1}{T_2^*} = \frac{1}{T_2} + \frac{1}{T_2'} \qquad (4.4.1)$$

When it was possible to measure T_2 by spin echoes a FID was used to find T_2^*, using these the contribution, T_2', from inhomogeneous field and Grafoil effects could be determined. At 5MHz the value of T_2' was measured as 1.2ms. With the Mylar sample chamber in place the FID was non-exponential, due to a Gaussian-like contribution from the magnet.

$$F(t) = F(0)e^{-t/T_2} e^{-t^2/\delta} \qquad (4.4.2)$$

Again, by taking data at a point where both a FID and spin echoes could be obtained, it was possible to evaluate δ and use this when correcting the FID data. However, when making the calculations the value of time t relative to the origin must be used, rather than just the differences between them as in the exponential case. The value of δ when at 5MHz was $(1.15 \pm .1)10^5$ S^2.

It was sometimes found necessary, particularly when studying very low coverage films on Grafoil, to signal average a considerable number of times. This can require quite some considerable length of time since it is normal to allow a period of about 5 x T_1 between repeat sequences for the magnetization to recover nearly all of its equilibrium value. Not allowing this recovery time, τ_R, results in a loss of signal, since (signal) $\propto (1-e^{-\tau_R/T_1})$. However, the final signal to noise ratio is proportional to the square root of the number, N, of averages. If we allow a fixed period of time, t, in which we

must obtain the best result then,

$$N = t/\tau_R \tag{4.4.3}$$

combining both contributions, the final signal to noise after time t is,

$$\left(\frac{S}{N}\right)_t = (\text{constant}) \times \left(t/\tau_R\right)^{1/2} \left(1 - e^{-\tau_R/T_1}\right) \tag{4.4.4}$$

Maximising this expression with respect to τ_R, gives for the optimum value of τ_R,

$$(\tau_R)_{opt} = 1.26\ T_1 \tag{4.4.5}$$

To measure T_1 the size, $h(\tau)$ of the free induction decay following the second pulse in a 90°-τ-90° sequence was observed. If the relaxation was exponential,

$$h(\tau) = h(\infty)\ (1 - e^{-\tau/T_1}) \tag{4.4.6}$$

The reason for choosing this sequence rather than the more usual 180°-τ-90° sequence, is that because the longitudinal magnetization is always zero following a 90° pulse whatever its value beforehand, it was unnecessary to wait several T_1's between sequences. This speeded up data taking when a large number of averages were required. About 100ms separation between the second 90° pulse of one sequence and the first 90° pulse of the next was allowed. Like when making T_2 measurements on the FID, it was found helpful to de-tune the FID by a few kHz and measure the peak to peak height of the beat pattern produced.

4.5 Data Analysis

As the NMR data points were recorded they were plotted on semilogarithmic paper (in the case of T_1 $h(\infty) - h(\tau)$ was plotted, where $h(\infty) \equiv h(t)$ for $\tau >> T_1$) to check that the relaxation was exponential. If so the points were entered to exponential least squares fitting programs running interactively on a VAX11/780 computer or more slowly on an HP41C personal calculator. The programs work by first obtaining an approximate "guess" value of the relaxation time by taking logs and using linear least squares fitting. The "guess" is then supplied to an iterative routine which fits the data to

$$h(\tau) = h(0)\, e^{-2\tau/T_2} \qquad (4.5.1)$$

for the T_2 data, and

$$h(\tau) = h(\infty) - h'\, e^{-\tau/T_1} \qquad (4.5.2)$$

for the T_1 data. The three parameter equation for longitudinal relaxation is used instead of (4.4.6) to allow for slight inaccuracies in the 90° pulse lengths which result in $h(\tau)$ not being exactly zero at $\tau = 0$. A particular advantage of directly fitting (4.5.2) to the data is that any error in measurement of $h(\infty)$ is not carried through to all of the points as in methods of T_1 calculation which rely on transformation of the data to a straight line.

The errors in T_2 values obtained by the above methods were between ±1% and ±5%, while for T_1 errors were between ±5% and ±10%. Correlation coefficients were generally good, being somewhere between 0.990 and 0.999. Figure 4.3 shows a typical set of T_1 data, the solid line is the fit of (4.5.2) produced by the program.

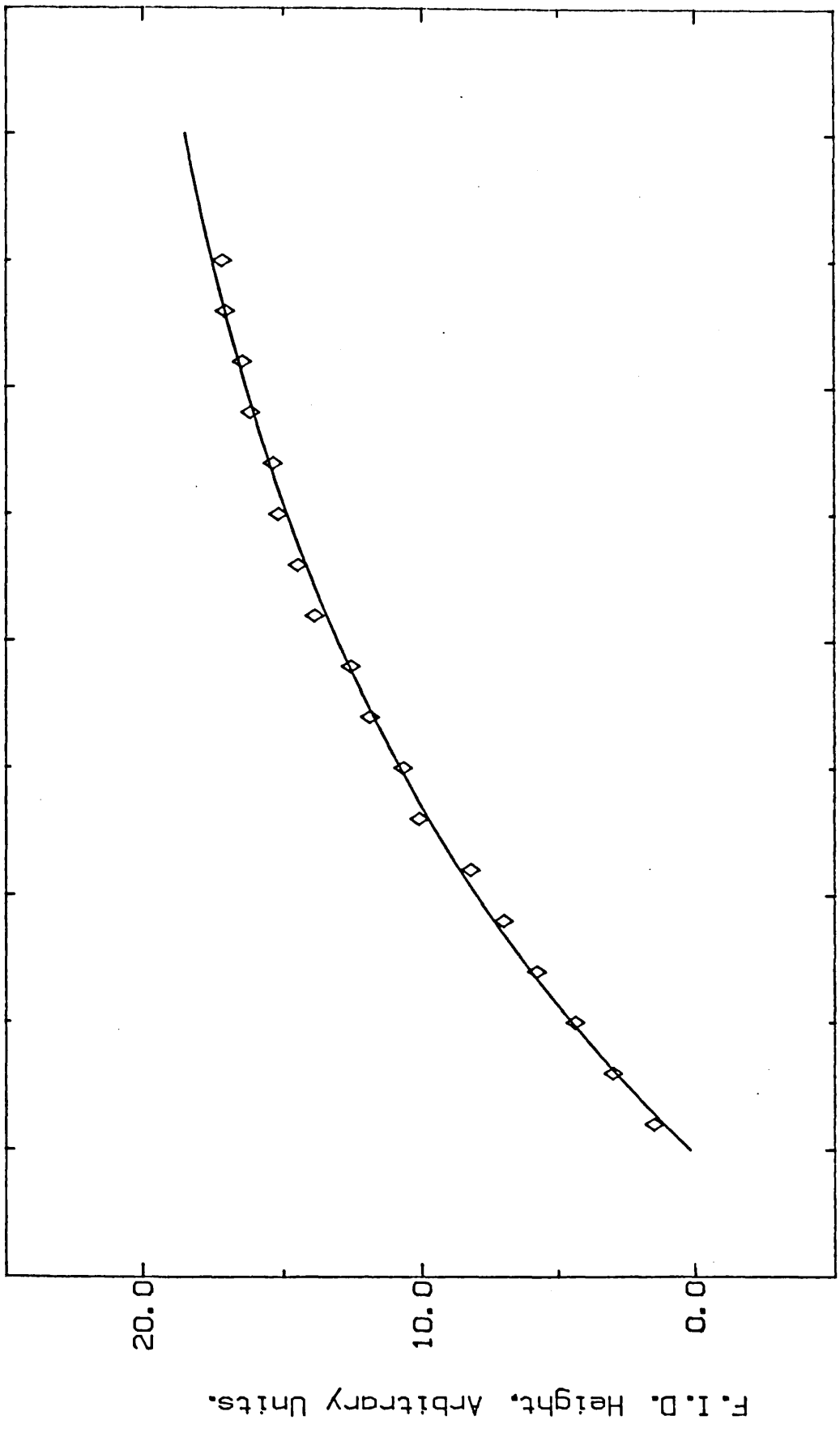

Figure 4.3, Growth Of Longitudinal Magnetization For Helium-3 On Grafoil, Coverage=0.3 Monolayers, T=1.06 K, β=90°.

CHAPTER 5

THE NMR PROPERTIES OF ^{3}HE ADSORBED ON MYLAR FILM - RESULTS AND DISCUSSION

5.1 Introduction

A preliminary investigation into the NMR properties of ^{3}He on Mylar Film has been carried out and selected results are presented in this chapter. The reason for not presenting all of the results is that, regardless of coverage, the same general trends were observed. This is a consequence of the physical properties of the adsorbed film which will be discussed later. Table 5.1 summarises all of the data taken during the course of this investigation. All data was taken at $\omega_o/2\pi$ = 5MHz and at $\beta = 0^o$ unless otherwise stated.

5.2 Dependence of Relaxation Times on Coverage

Figure 5.1 shows T_2 as a function of coverage at 1.2K at orientation β = 0 and 90^o. T_2 increases approximately linearly with X, this implies that, for a homogeneous film, the motion is a rapidly increasing function of X, an impossible state of affairs. A plausible explanation is that the adsorbate is inhomogeneous, a small fraction of it remaining solid at 1.2K regardless of coverage [71]. The relaxation time in the resulting two phase system is given by [72],

$$\frac{1}{T_2} = \left(\frac{x}{X}\right) \frac{1}{T_2'} + \left(\frac{X-x}{X}\right) \frac{1}{T_2''} \qquad (5.2.1)$$

where x is the fraction of the monolayer that is solid and T_2' the relaxation time in the solid phase. The relaxation time in the relatively mobile phase is T_2''. Equation (5.2.1) is valid providing that the rate of exchange of spins between the two phases is much faster than the relaxation time, otherwise the relaxation will be observed as the sum of two exponentials. The observed relaxation

Table 5.1

Summary of data taken

Variable / Coverage	Temperature 4.2 → 1.2K	Orientation β @ 4.2K	Orientation β @ 1.2K	Frequency ω_o @ 4.2K
0.3	T_2	-	T_2	-
0.5	T_1 , T_2	-	-	-
0.66	χ, T_1, T_2 @ β = 0 & 90	T_1 , T_2	-	-
0.88	χ, T_1, T_2 @ β = 0 & 90	T_1 , T_2	T_1 , T_2	-
0.99	χ, T_1, T_2	T_1 , T_2	T_1 , T_2	-
1.12	T_1 , T_2	-	T_2	-
6	-	T_1 , T_2	-	T_1 , T_2

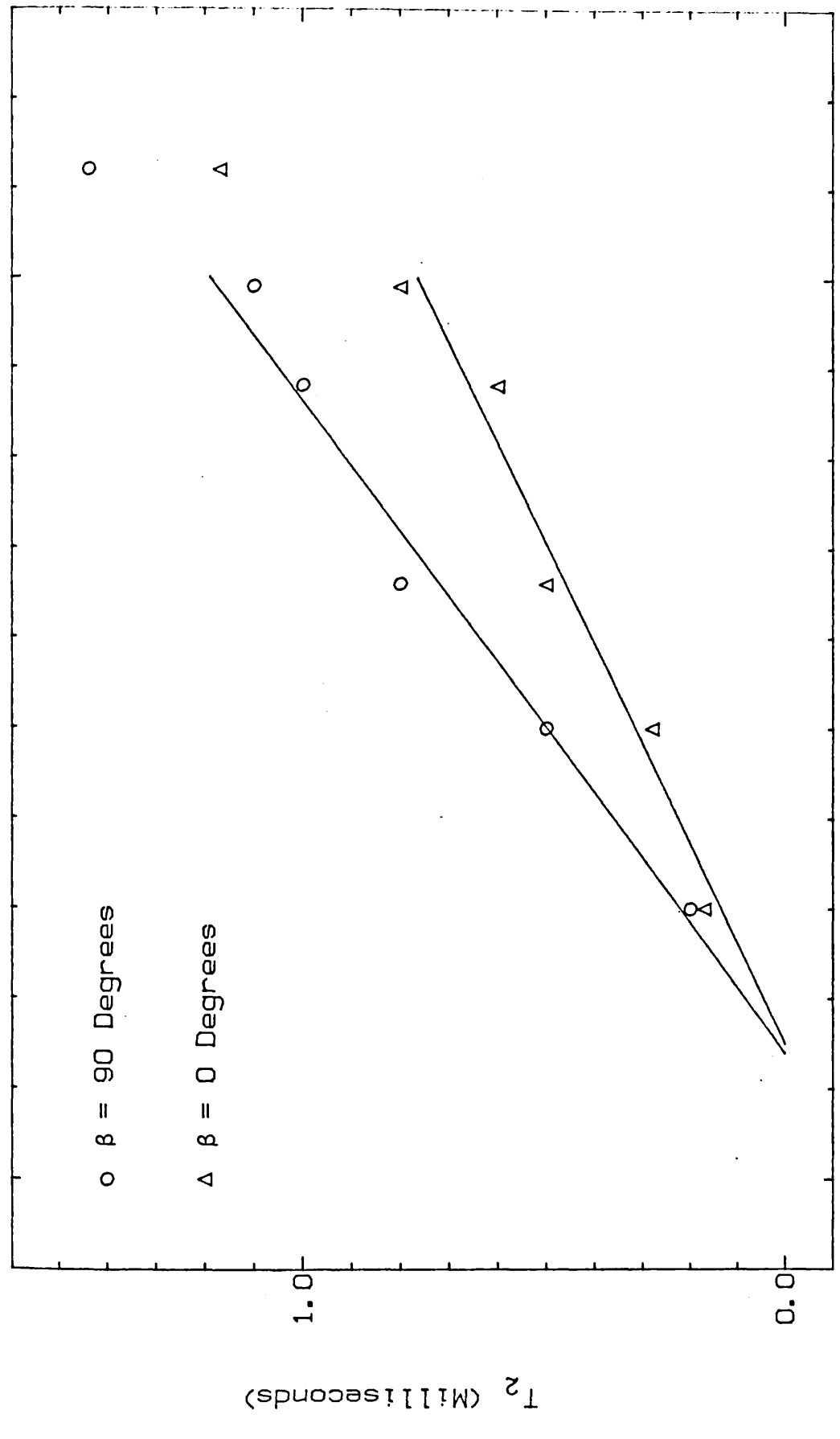

Figure 5.1, T_2 As A Function Of Coverage At Temperature 1.18 K, For Helium-3 Adsorbed On Mylar Film.

was in fact a single exponential validating the above expression.

The relaxation in a solid is rapid whilst in a fluid motional narrowing occurs, so $T_2'' >> T_2'$, therefore

$$T_2 \simeq \frac{X}{x} T_2' \qquad (5.2.2)$$

which is linear in X. An approximate calculation of the solid relaxation time using equation (2.8.4) gives $T_2' \simeq 100\mu s$. And at X = 1, $T_2 \simeq 1ms$ therefore $x \simeq 0.1$ monolayer.

The coverage dependence of T_2 at 4.2K is shown in figure 5.2, again there is a rapid increase of T_2 with coverage but this time it levels off at higher coverages to a value, $T_2 \simeq 14msec$. The spin lattice relaxation time appears to show no significant dependence on coverage at any temperature.

5.3 Temperature Dependence

The temperature dependence of T_1 and T_2 at X = 0.66 is shown in figure 5.3. Somewhat similar results were obtained at all the other coverages. T_2 increases fairly rapidly with temperature. Assuming that the adsorbed film is inhomogeneous as suggested in §5.2, this temperature dependence is due to both the thermal escape of particles from the patches of immobile solid combined with thermally activated vacancy tunnelling in these regions. A simple Arrhenius law with a single binding energy is insufficient to explain the observed increase of T_2 with temperature - there is almost certain to be a range of binding energies within the solid patches. Figure 5.4 shows the temperature dependence of T_2 at X = 0.88, the same general behaviour as the X = 0.66 results is observed for temperatures below 4.2K. However, at this coverage a few higher temperature points have

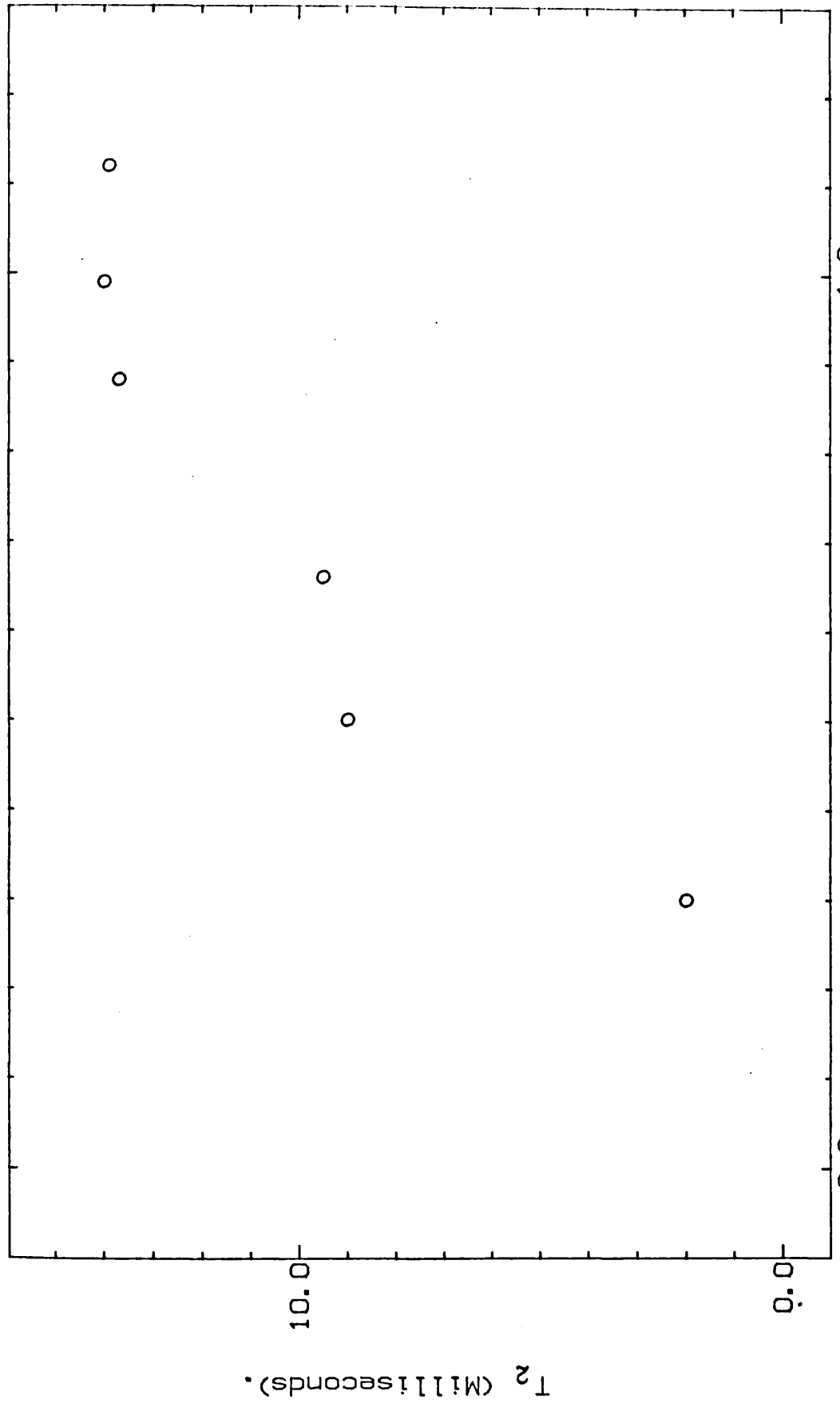

Figure 5.2. T_2 As A Function Of Coverage At Temperature 4.22 K, For Helium-3 Adsorbed On Mylar Film.

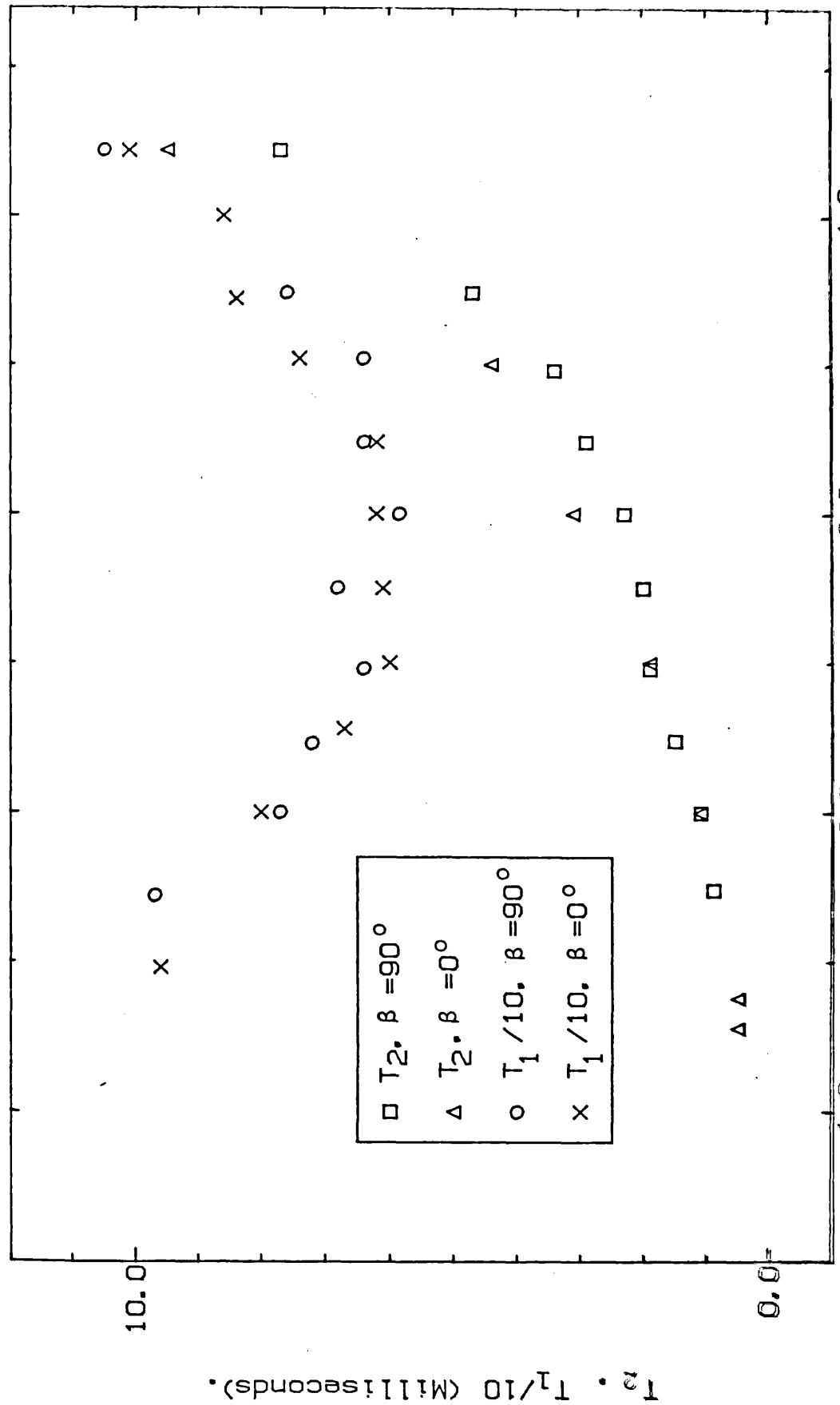

Figure 5.3, T_1 And T_2 As A Function Of Temperature For Helium-3 On Mylar Film, Coverage=0.66 Monolayer.

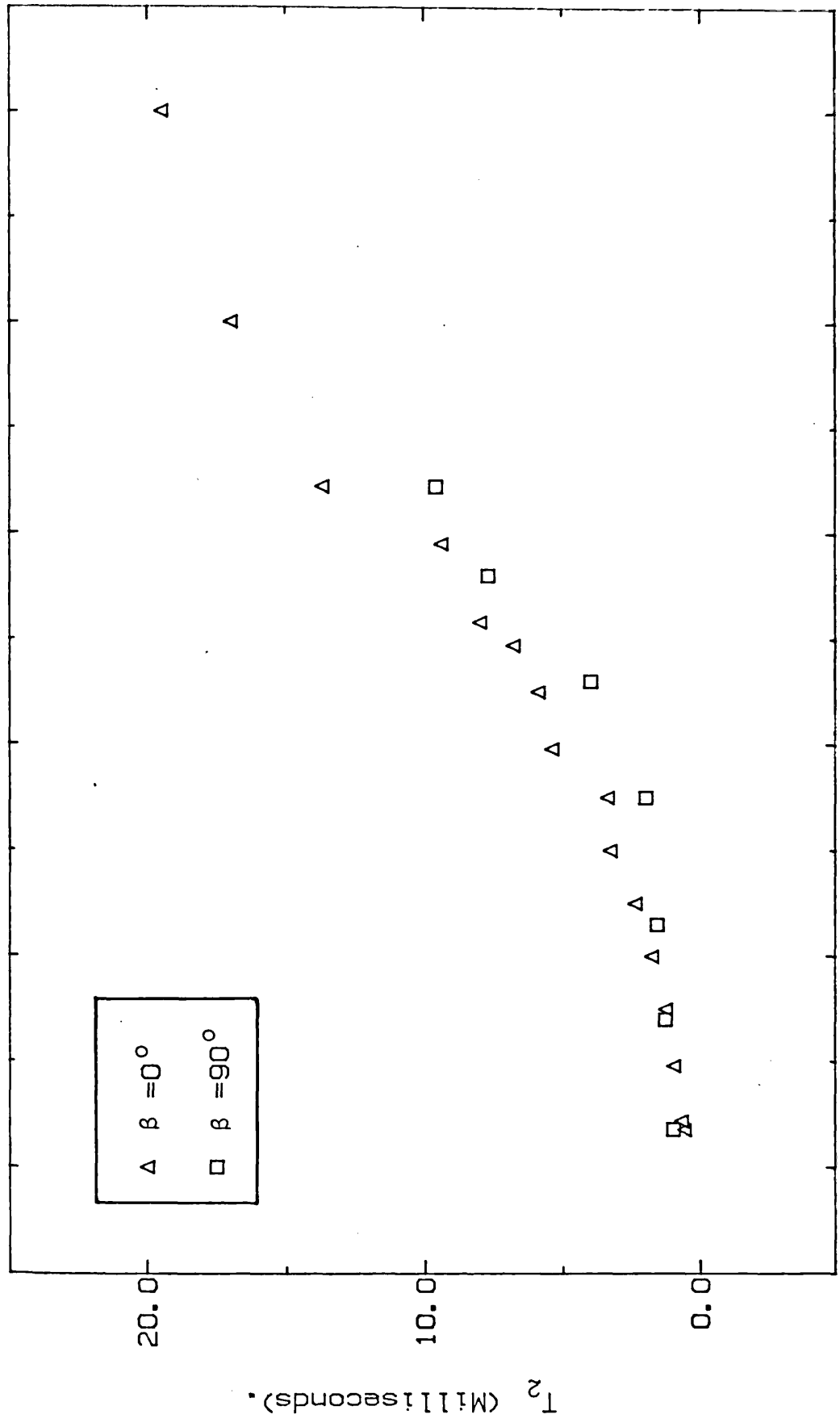

Figure 5.4, T_2 As A Function Of Temperature For Helium-3 On Mylar Film, Coverage=0.88 Monolayer.

been obtained showing a definite slow down in the rate of increase of T_2 with temperature. This suggests that at these temperatures the rapidly relaxing regions have contracted, due to thermal escape, to such an extent that it is no longer reasonable to neglect the contribution T_2'' from the rest of the adsorbate.

The T_1 data in figure 5.3 display a well defined minimum at $T \simeq 3K$, at which it has a value of 60msec. If T_1 is determined by dipole-dipole relaxation a minimum is expected when $\tau_c \simeq {}^{1}/_{\omega_o}$ [41] where τ_c is the dipolar correlation time. Since there is no dependence of T_1 on coverage it is clear that the solid patches which dominate T_2 do not have the same effect on T_1 results. Therefore, it is either the remaining part of the adsorbate or all of it that contributes to the T_1 process. The value of T_1 at the minimum is given by,

$$\frac{1}{T_1} \simeq \frac{M_2}{\omega_o} \tag{5.3.1}$$

where M_2 is the second moment of the CW lineshape and is given by,

$$M_2 = \frac{9}{512\pi^2}\,\mu_o^2\,\hbar^2\gamma^4\,g_o \tag{5.3.2}$$

This gives $T_1 \simeq 100$ ms at the minimum which is certainly of the correct order of magnitude. Putting the value of τ_c into equation (2.7.13) gives $T_2'' \simeq 10$ms which is of the correct order of magnitude to explain the levelling off of T_2 as a function of coverage at 4.2K in figure 5.2, and as a function of temperature in figure 5.4.

The fact that a minimum in T_1 as a function of temperature is observed also means that there is some temperature dependent motion. The value of τ_c obtained at the T_1 minimum $\sim 10^{-7}$ sec is far too long for a 2-D gas/fluid with unrestricted thermal motion at that temperature ($\tau_c \sim 10^{-11}$ sec is expected). However, it is

typical of the values obtained in a solid with rapid vacancy tunnelling [20].

A similar T_1 minimum at X = 0.5 is shown in figure 5.5, but no definite minima were seen at higher coverages. For X > 0.66 T_1 values at 1.2K were somewhat shorter than at 4.2K, figure 5.6, suggesting that any minimum is at lower temperatures or higher frequencies.

5.4 Anisotropy of the Relaxation Times

The anisotropy in T_1 and T_2 at T = 1.2K and at coverages 0.88 and 0.99 monolayers is shown in figures 5.7 & 5.8 respectively. Bearing in mind the experimental error ($\sim$ 10%) in T_1 measurements there is little or no anisotropy in T_1 at either coverage. This is to be expected so close to the T_1 minimum, see figure 2.5.

The orientation dependence of T_2 is, however, more interesting the solid curves through the data points are from expressions of the form,

$$\frac{1}{T_2} = A \ \langle|\frac{1}{3} - \cos^2\beta|\rangle + B\langle\sin^4\beta\rangle \qquad (5.4.1)$$

where the averages < > are taken over a spread of substrate orientations. The theoretical justification for using this expression is as follows :

It is assumed that the rapidly relaxing patches of solid are dominating the behaviour of T_2 at 1.2K. It is also assumed that there is a small amount of motion present (quantum exchange and/or vacancy tunnelling) within these patches. Using the Kubo-type expression for F(t), §2.3,

$$F(t) = \exp(-3\int_o^t (t-\tau)G_o(\tau)d\tau) \qquad (5.4.2)$$

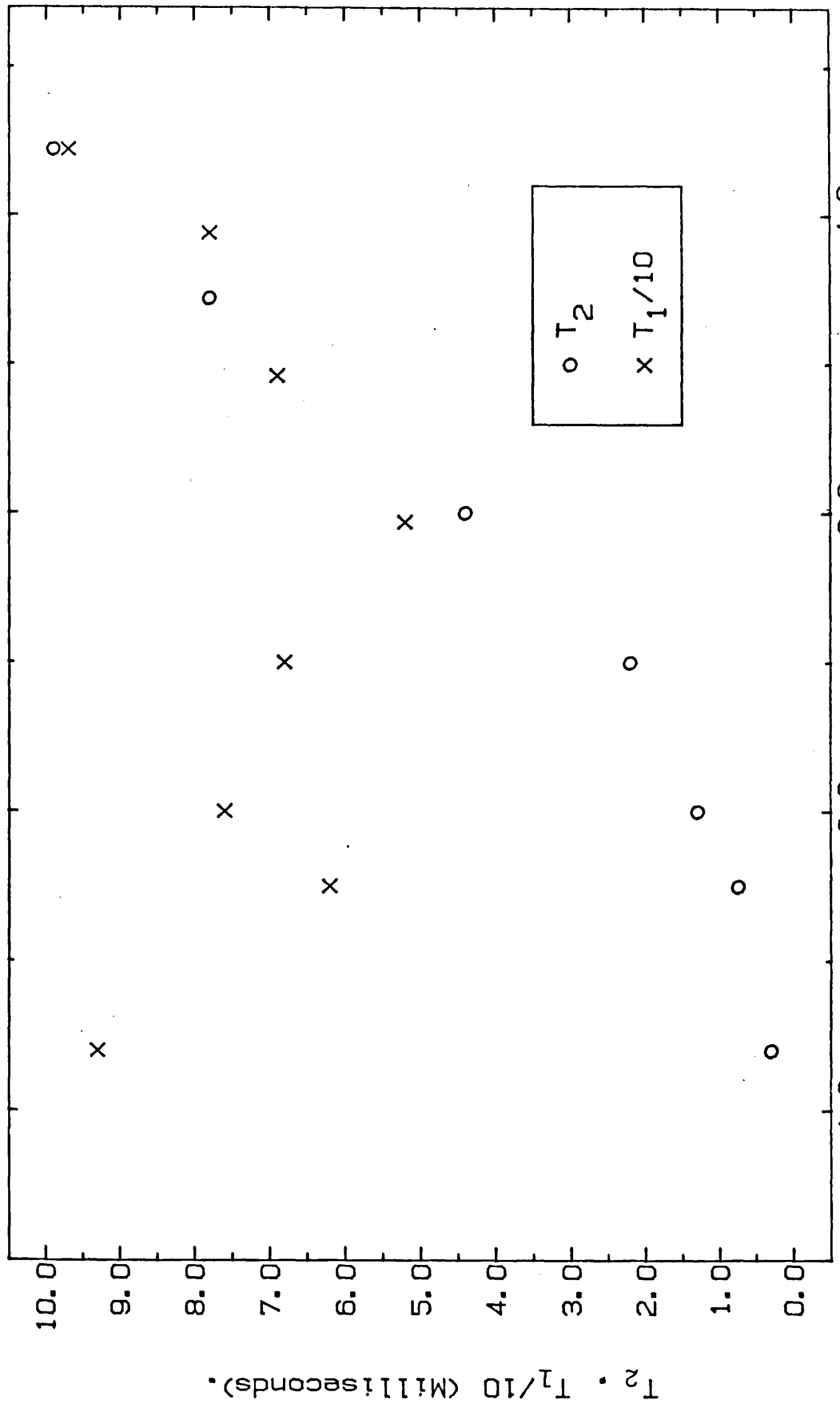

Figure 5.5, T_1 And T_2 As A Function Of Temperature For Helium-3 On Mylar Film, Coverage=0.5 Monolayer.

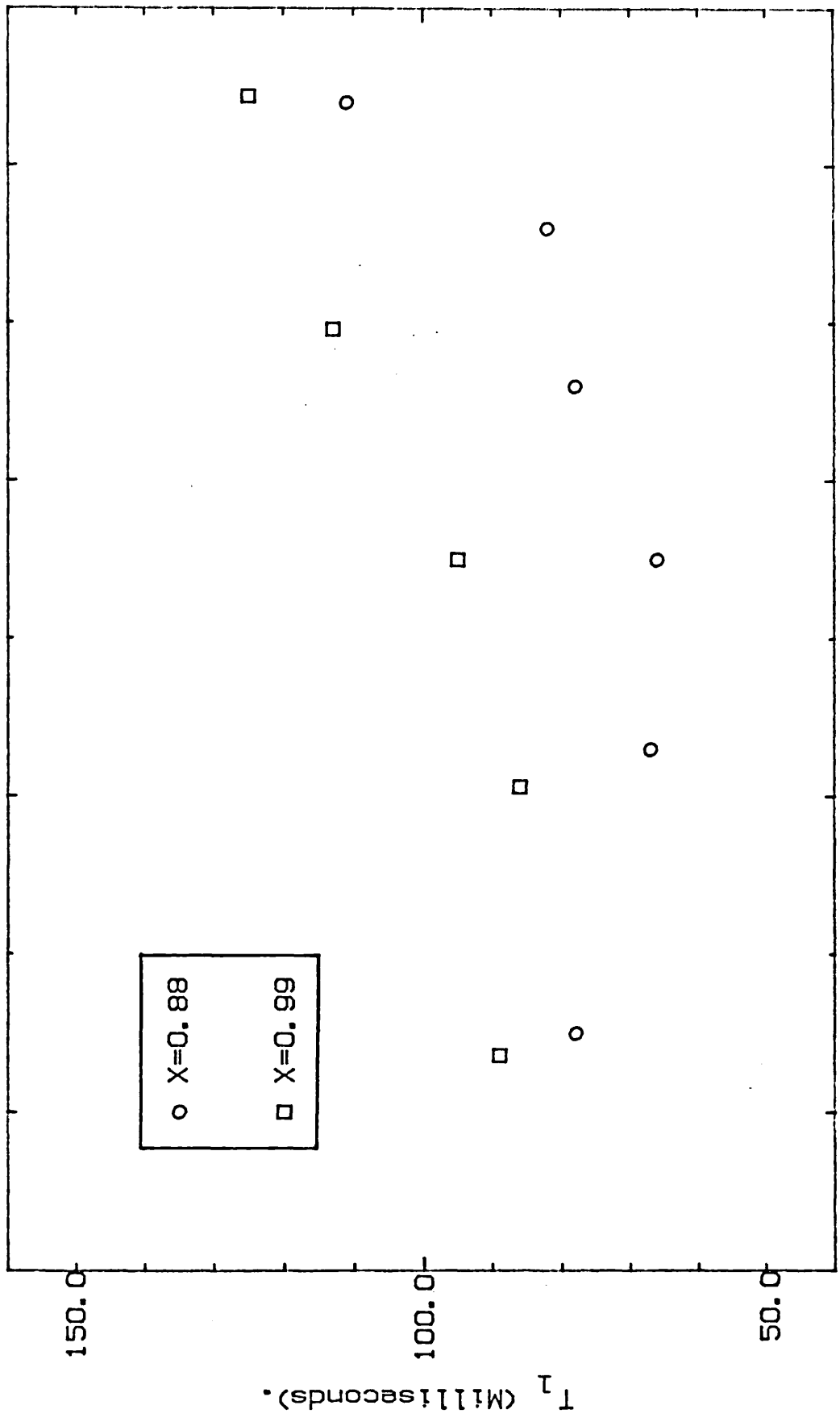

Figure 5.6. T_1 As A Function Of Temperature For Helium-3 Adsorbed On Mylar Film.

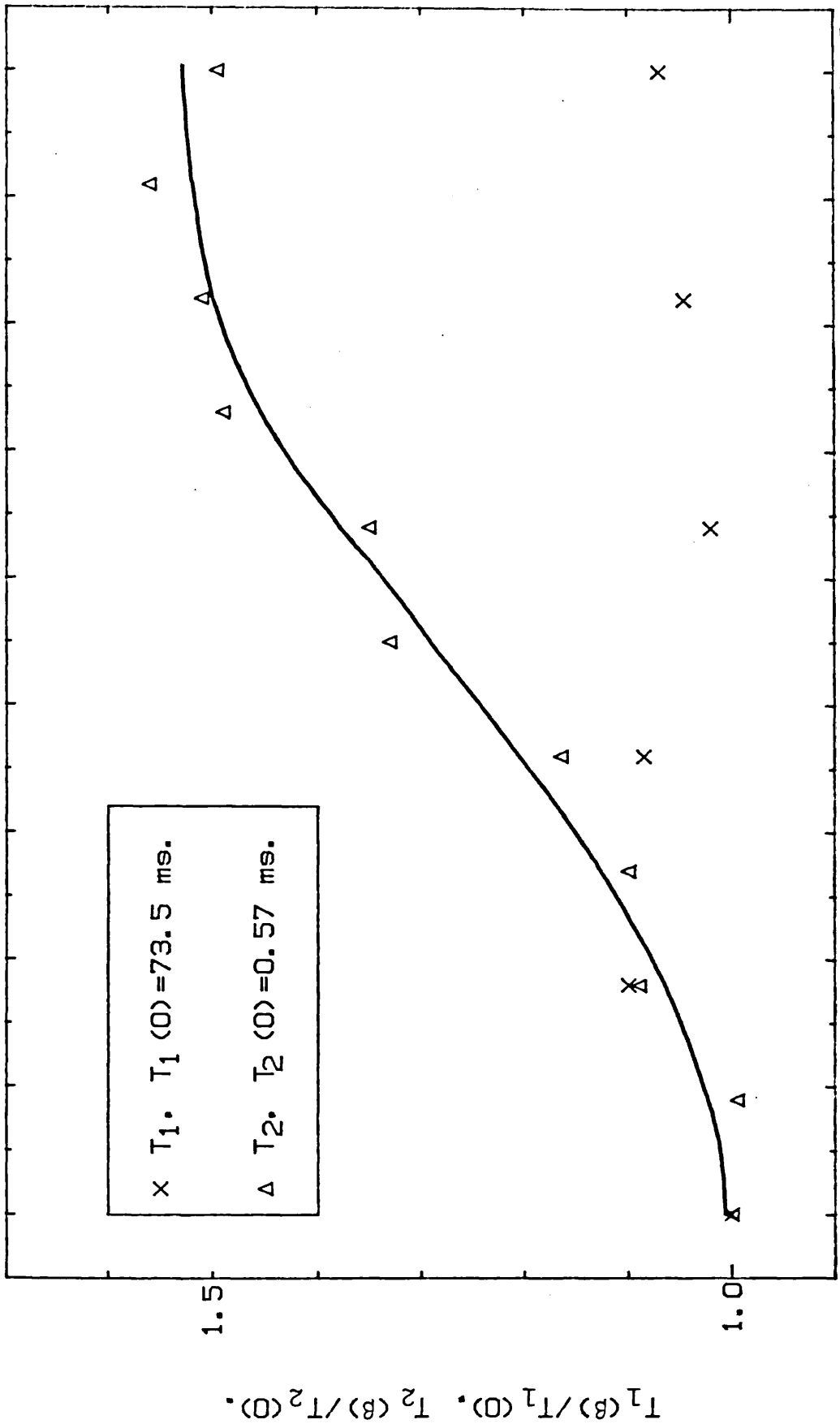

Figure 5.7. Anisotropy In T_1 And T_2 For Helium-3 On Mylar Film. Coverage=0.88 Monolayer, Temperature=1.18 Kelvin.

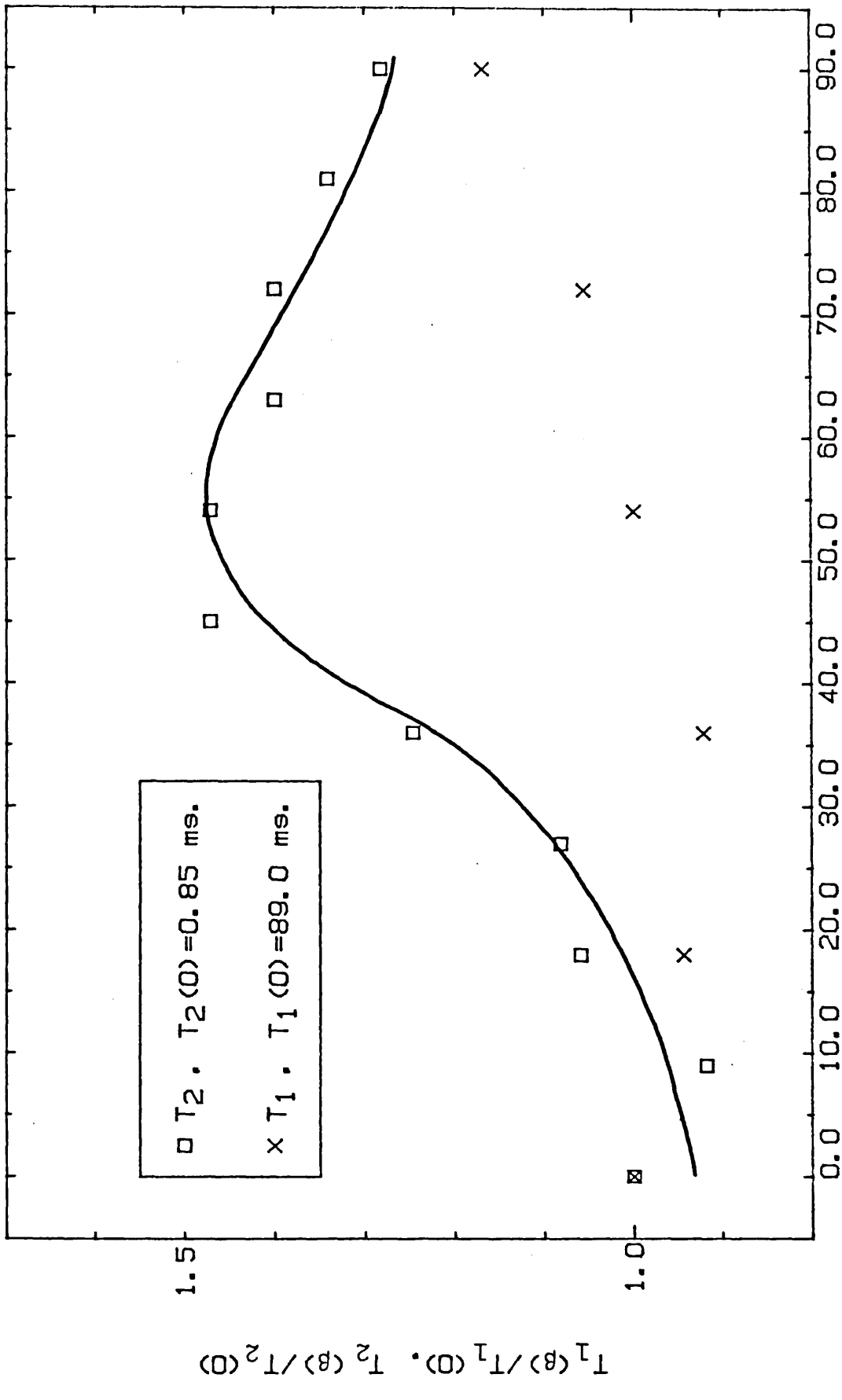

Figure 5.8. Anisotropy In T_1 And T_2 For Helium-3 On Mylar Film. Coverage=0.99 Monolayer, Temperature=1.18 Kelvin.

where only the dominant contribution to the dipolar autocorrelation function from the adiabatic $G_o(\tau)$ part has been retained,

$$G_o(\tau) = \frac{27}{1024\pi^2}\mu_o^2\hbar^2\gamma^4[(\frac{1}{3} - \cos^2\beta)^2 g_o(\tau) + \frac{\sin^4\beta}{2} g_2(\tau)] \quad (5.4.3)$$

The small amount of motion present is sufficient to motionally narrow the $g_2(\tau)$ part, however, the $g_o(\tau)$ part which is relatively insensitive to motion can be approximated by its zero time value. Evaluating the integral in equation (5.4.2) gives

$$F(t) = \exp - \frac{81}{2048\pi^2}\mu_o^2\hbar^2\gamma^4 g(0)[(\frac{1}{3} - \cos^2\beta)^2 t^2 + \tau_c t \sin^4\beta] \quad (5.4.4)$$

This decay is not a true exponential, but with the help of equation (2.8.5) a decay constant T_2' is assigned to a solid patch,

$$\frac{1}{T_2'} = \left[21n2 \frac{81}{2048\pi^2}\mu_o^2\hbar^2\gamma^4 g(0)(\frac{1}{3} - \cos^2\beta)^2\right]^{1/2} + \left[\frac{81}{2048\pi^2}\mu_o^2\hbar^2\gamma^4 g(0)\sin^4\beta\tau_c\right] \quad (5.4.5)$$

Now allowing for a spread in orientations β and remembering that the observed relaxation rate T_2 is related to T_2' by the "augmentation factor" $\frac{X}{x}$, leads to an expression of the type (5.4.1).

The spread in orientations refers solely to the solid patches. At regions of preferential adsorption on the surface which may be geometrical defects in the surface or points of contact between adjacent layers, clumps of helium-3 atoms will form. These clumps are the medium for relaxation and they are somewhere between ideal

2-D and 3-D systems. The device of a spread of β is used to describe this situation, the greater the spread of β the less the anisotropy and the nearer bulk behaviour is approached. For the purpose of the calculations a Gaussian spread of orientations is assumed, $\langle\beta^2\rangle^{1/2}$ being the r.m.s. spread of orientations. The rapid exchange of particles between the solid patches and the fluid permits the averaging of $T_2'(\beta)$.

Using eq. (5.4.5) the ratio of the factors A and B in eq. (5.4.1) is given by

$$\frac{B}{A} = \frac{\tau_c}{(21n2)^{1/2}} \left[\frac{81}{2048\pi} \mu_o^2 \hbar^2 \gamma^4 g(0)\right]^{1/2} \qquad (5.4.6)$$

If the motion is described by the Heisenburg exchange Hamiltonian eq. (2.8.10) then the exchange frequency J is related to τ_c by $J = 0.27/\tau_c$, [48]. Therefore J is given by the following expression

$$J = \frac{A}{B} \frac{0.27}{(21n2)^{1/2}} \left[\frac{81}{2048\pi^2} \mu_o^2 \hbar^2 \gamma^4 g(0)\right]^{1/2} \qquad (5.4.7)$$

Table 5.2 shows the values of J and $\langle\beta^2\rangle^{1/2}$ obtained by fitting eq. (5.4.1) to the data.

Table 5.2

X	A/B	J in S^{-1}	$\langle\beta^2\rangle^{1/2}$
0.88	7.3	1.7×10^5	30^o
0.99	5.7	1.3×10^5	20^o

The values of J obtained are typical of those found in 2-D and 3-D solid Helium-3 [32], also the reduction of J with increasing lateral pressure (increasing X) is as expected. These results justify the initial assumptions as to the nature of the solid patches.

Figure 5.9 shows the anisotropy at X = 0.88 and T = 4.2K, this result is somewhat confusing, there is no theory of relaxation in 2-D systems which predicts that $T_2(90^o)$ is significantly shorter than $T_2(0^o)$. It seems that at 4.2K the solid patches no longer dominate the behaviour of T_2 as they did at 1.2K.

5.5 Relative Susceptibility Results

The h(0) values obtained when the expression $F(t) = h(0)\exp - t/T_2$ was fitted to the magnet corrected F.I.D. data are plotted as a function of inverse temperature in figure 5.10. Within the limits of experimental error ($\sim$ 10%) the h(0) values lie on a straight line going through the origin. The zero time height of the F.I.D. is directly proportional to the magnetic susceptibility χ, so it appears that the system obeys Curie's Law. This is not so surprising since quantum degeneracy is unlikely at these temperatures and spin densities. However, the result is important because it indicates that the whole decay is described by a single exponential, including the part which is unobserved due to the receiver dead time.

5.6 Frequency Dependence of T_1 and T_2

The frequency dependence of the relaxation times was measured at X = 6 monolayers and T = 4.2K. T_2 was totally independent of frequency and had a value of 13ms, while T_1 was observed to increase approximately linearly with frequency. This linear relationship at frequencies below the T_1 minimum is characteristic of adsorbed systems and has recently been explained [73] as being related to the logarithmic divergence of the $j_o(\omega)$ spectral density function at

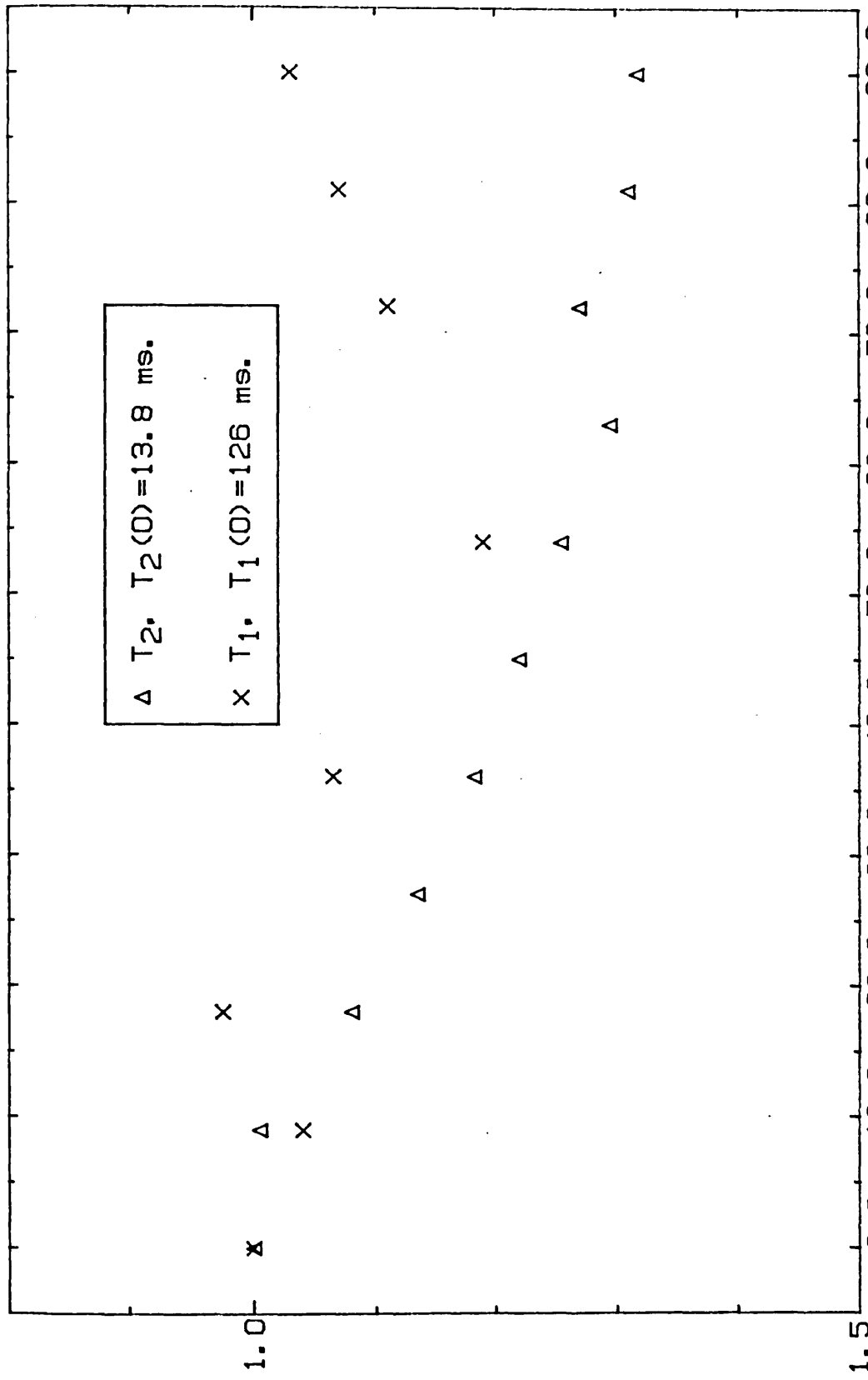

Figure 5.9, Anisotropy In T_1 And T_2 For Helium-3 On Mylar Film.
Coverage=0.88 Monolayer, Temperature=4.22 Kelvin.

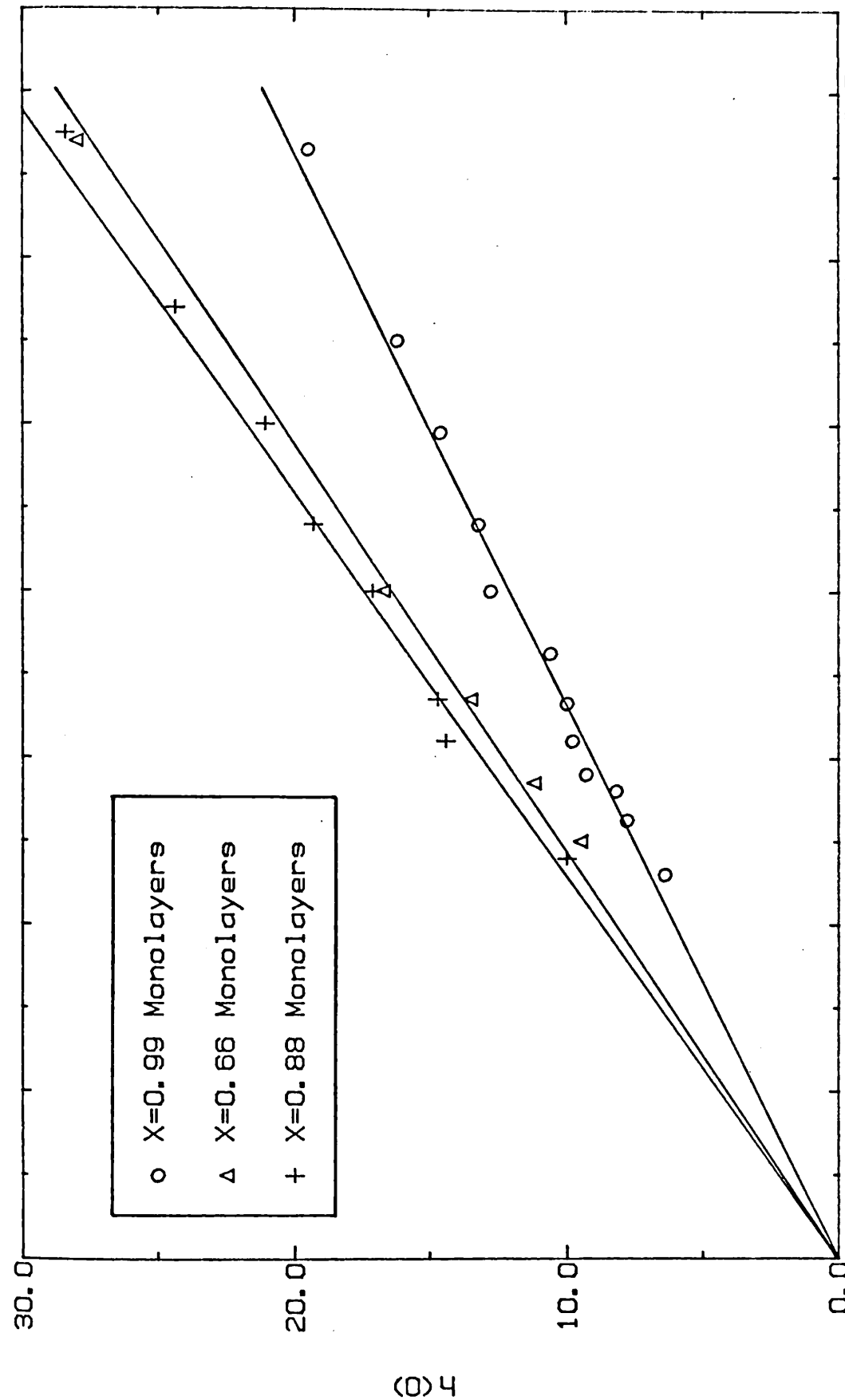

Figure 5.10. Plot Of h(0) As A Function Of 1/T For Helium-3 Adsorbed On Mylar Film.

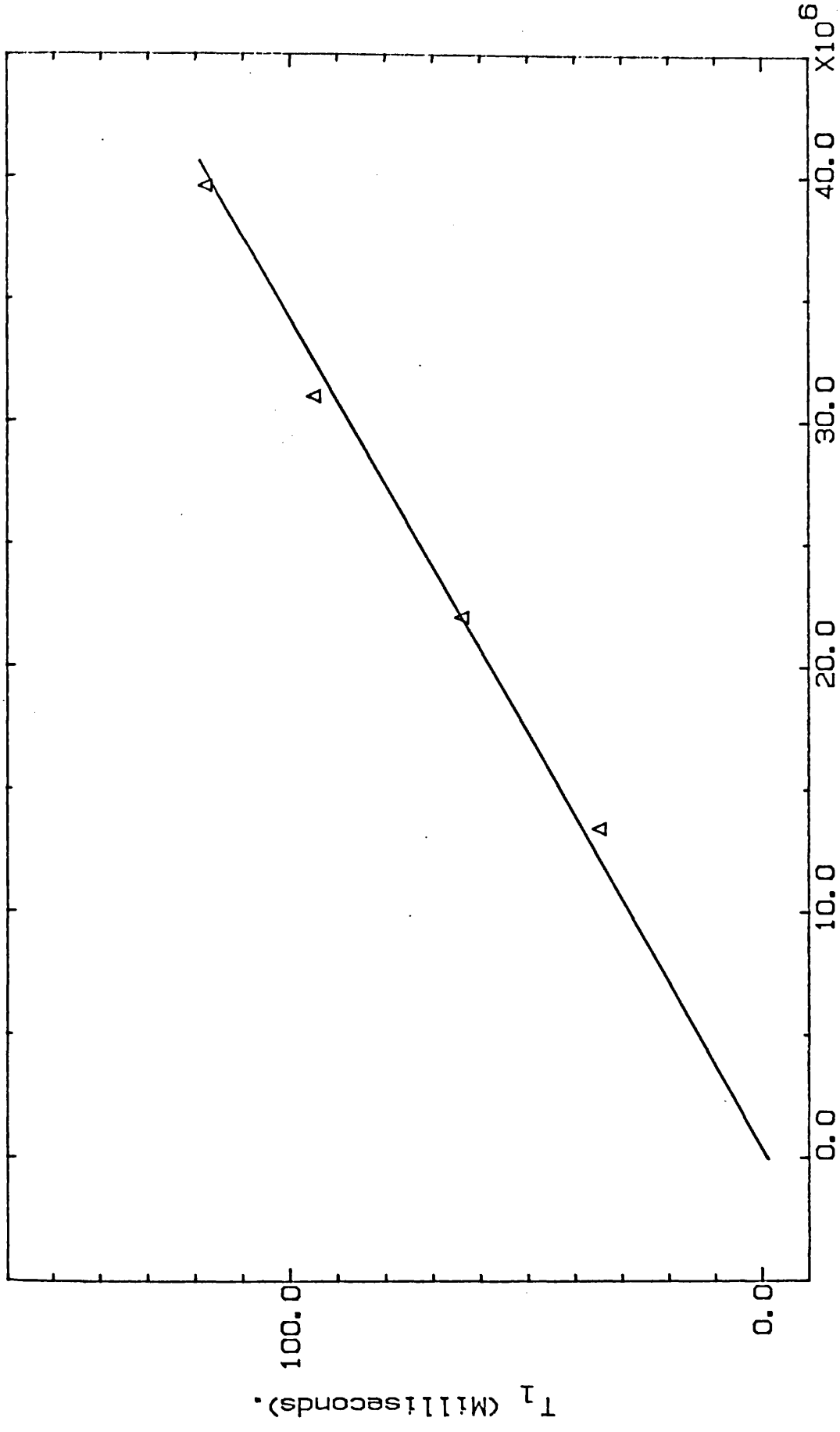

Figure 5.11, T_1 As A Function Of Larmor Frequency For Helium-3 Adsorbed On Mylar Film, T=4.22K, β=0 Degrees.

low frequencies. It is reasonable to make the assumption, based on T_1 - vs - T measurements at other coverages, that 4.2K is on the low frequency side of the T_1 minimum at X = 6. The best fit straight line through the data points has a slope (3.1 ±.1) x $10^{-9}s^2$ and intercepts near to the origin.

5.7 Conclusions

The results of NMR measurements on Helium-3 adsorbed on Mylar film indicate that the substrate is heterogeneous. Approximately 10% of the surface presents highly preferential adsorption sites, at which form patches of relatively immobile solid exhibiting quantum exchange or vacancy tunnelling at about 10^5Hz. These patches are the dominant medium for spin-spin relaxation and it is believed that they form in clumps of more than one atom deep. The remaining adsorbate is relatively mobile, though it appears that the motion is much less than is normally expected in a 2-D gas/fluid at the temperatures and densities investigated. There appears to be no evidence for the freezing of the adsorbate to a homogeneous whole.

It is likely that points of contact between adjacent layers of Mylar film account for the rather large area of inhomogeneity. However, it is only by packing as many sheets of Mylar into the sample chamber as possible that sufficient signal could be obtained to permit NMR measurements.

In so far as they can be compared, these conclusions are in qualitative agreement with those drawn from adsorption isotherm studies of Helium-4 adsorbed on Mylar film [18].

CHAPTER 6
THE NMR PROPERTIES OF VERY LOW DENSITY HELIUM-3 FILMS ON GRAFOIL, RESULTS AND DISCUSSION

6.1 Introduction

Some NMR results obtained in the very low coverage regime, $0.005 \lesssim X < 0.1$ monolayers, are presented in this chapter. The region around X = 0.01 monolayers is especially interesting, the results of thermodynamic experiments have been interpreted in two ways. The heat capacity results indicate the presence of a 2-D Debye type solid. Dash and co-workers consider it to be a low density solid formed at graphite edge planes [8][74]. While on the other hand, Elgin and Goodstein interpret their results in terms of patches of relatively high density solid formed at regions of high substrate inhomogeneity [6]. The strong d^6 dependence of the second moment and hence the nuclear magnetic relaxation time T_2 on internuclear separation d makes NMR an ideal tool for resolving this problem. However, at such low coverages there are difficulties with low signal levels and so it was not possible to make any measurements below X = 0.005.

6.2 Dependence of Relaxation Times on Coverage

The dependence of T_2 on coverage at 5.1MHz and 1.2K is shown in figure 6.1 for coverages up to 0.1 monolayer. There are three distinct features. For $X < 0.015$, T_2 levels off to a constant value of about 370μs. Between X = 0.015 and 0.07 there is a nearly linear increase of T_2 with coverage. Above X = 0.7 the rate of this increase slows considerably. These results are interpreted in terms of a "patchy solid" model as in the case of ^{3}He on Mylar film, see Chapter 5, where in this case approximately 1.5% of the surface presents highly preferential adsorption sites.

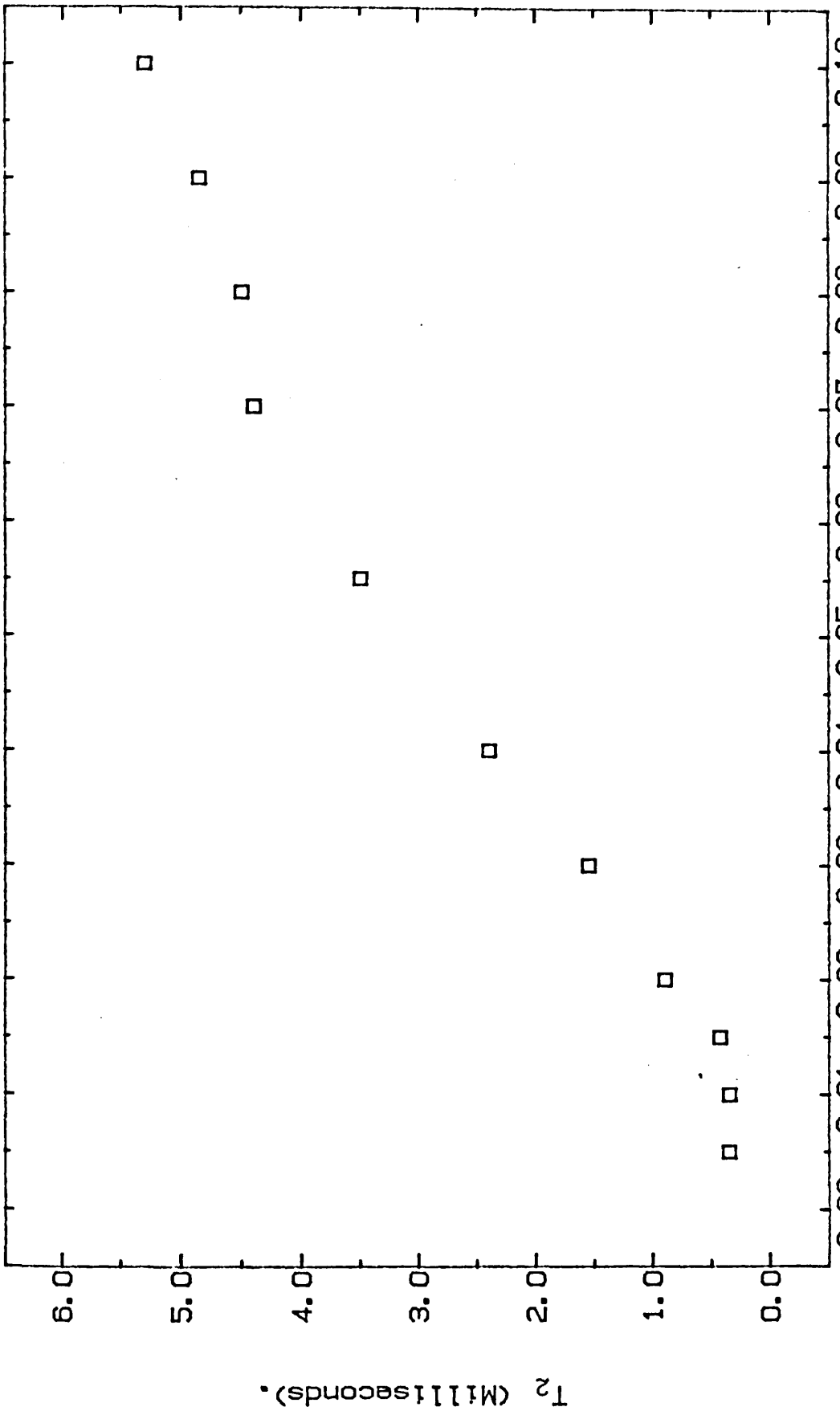

Figure 6.1. T_2 As A Function Of Coverage For Helium-3 On Grafoil, $\omega_o/2\pi$=5.1 MHz, β=90°, & Temperature=1.2K.

For coverages X less than 0.015 practically all of the adsorbed helium atoms will be attracted to the preferential sites. The solids formed are expected to have fairly rapid spin-spin relaxation rates. The measured value, 370μs, is the same as observed in the incommensurate solid phase of ^{3}He on Grafoil, when X ≃ 0.95 [25] [29]. It is clear, therefore, that these solids are of relatively high density. By way of comparison, the relaxation time for a low density solid corresponding to X = 0.005 can be calculated using the expressions (2.8.4) and (2.8.5) and using for the interatomic spacing, d ;

$$d = 3.27/\sqrt{X} \ \text{Å} \qquad (6.1.1)$$

Giving $T_2 \simeq 100$ ms which is clearly far too long. Even allowing for the effect of Grafoil local fields would, at the most, only reduce this to about 2 ms which is still too long to explain the observed result.

When all of the preferential adsorption sites are "filled" any remaining atoms behave as a two-dimensional gas. This is the case for X larger than 0.015. The resulting two phase system has been discussed in Chapter 5, leading to the result,

$$T_2 = T_2^s \frac{X}{x} \qquad (6.1.2)$$

where T_2^s is the relaxation time in the solid and x is the fraction of a monolayer that is solid. This explains the increase of T_2 with coverage above X = 0.015, however, a line drawn through the data points does not intercept through the origin as predicted by eq. (6.1.2). A qualitative explanation for this may be given as follows: The solid patches are continually exchanging atoms with the 2-D gas "reservoir". It is quite reasonable to expect that

the rate of this exchange would increase with an increase in the number of atoms in the gas phase (higher probability of collison). This disturbance of the solid is highly likely to result in increasing vacancy tunnelling type motion within it, and hence, the increase of T_2 with coverage will be faster than predicted by the "augmentation factor" (X/x) alone.

As the coverage is further increased, X > 0.07, the fluid phase becomes dominant. The contribution from this phase acts to slow down the rate of increase of T_2 with coverage in this region. The results suggest that the relaxation time in the fluid phase is of the order 10 ms rather than 100's of seconds as predicted theoretically for dipolar relaxation, this is probably due to relaxation in the Grafoil local fields.

Unfortunately it proved too difficult to obtain accurate measurements of the spin lattice relaxation time T_1 over this range of coverage. The value obtained at X = 0.055, which is accurate, is .51 seconds. T_1 will be considered in more detail in §6.4 and Chapter 7.

6.3 The Anisotropy in T_2

Figure 6.2 shows the anisotropy in T_2 at X = 0.01, X = 0.055 and X = 0.1. The anisotropy is largest when all of the adsorbate is in the solid phase X = 0.01. At X = 0.055 the anisotropy is greatly reduced. This behaviour is expected if the relaxation is due to internuclear dipolar interactions - the anisotropy decreases as the motion increases, see §2.7 and §2.8. The solid line through the X = 0.055 data is from eq. (5.4.1) with the parameters as shown below ;

$$\langle \beta^2 \rangle^{1/2} = 30^{\circ}$$

$$\frac{A}{B} = 13.3$$

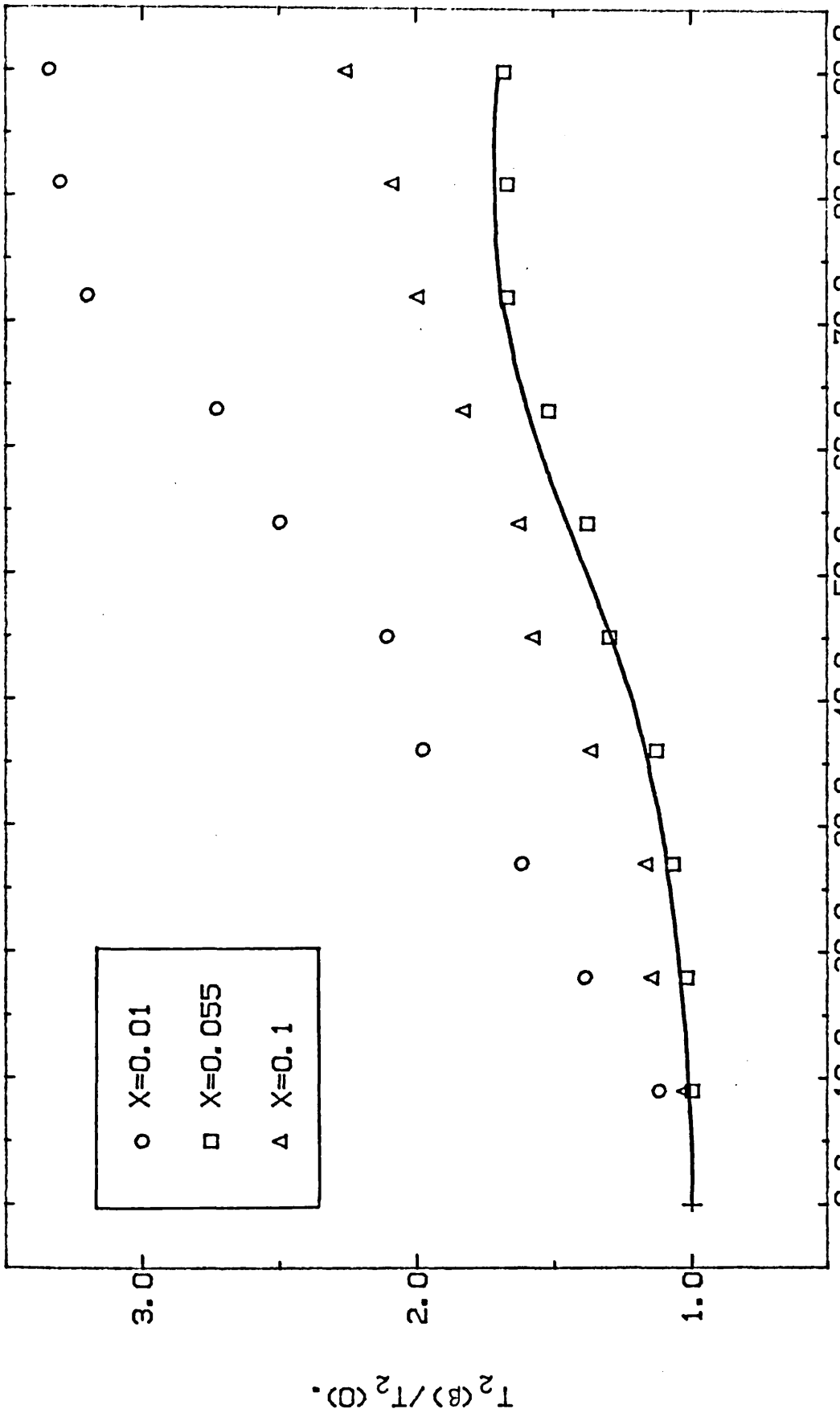

Figure 6.2, The Anisotropy In T_2 For Helium-3 On Grafoil, $\omega_o/2\pi$=5.1 MHz, & Temperature=1.2K.

The value of the r.m.s. mis-orientation of the solid patches $\langle\beta^2\rangle^{1/2}$ is certainly not unreasonable for the Grafoil surface, and it is also likely that the solid patches are more than one atom deep like on the Mylar substrate. The value of the ratio A/B leads to a value of the correlation time for motion within the solid patches of 3.3×10^{-6}s. At X = 0.1 the increased anisotropy marks the change in the dominant relaxation process as the fluid phase contribution becomes more important.

Figure 6.3, shows the anisotropy in T_2 at X = 0.055 and at various temperatures. The situation is rather hard to interpret quantitatively since as the temperature increases the solid patches will start to loose atoms to the fluid phase. However, it is certain that increasing temperature leads to increasing adatom motion and the results indicate that at $\beta = 0^\circ$ T_2 is not as sensitive to motion as it is at $\beta = 90^\circ$. This is in agreement with the theory which demonstrates that at $\beta = 0^\circ$ only variations in interparticle separation affect relaxation which is not as efficient a process as the variation of interparticle orientation which has most effect at $\beta = 90^\circ$.

6.4 Temperature and Frequency Dependence of T_1 and T_2

Measurements of the temperature dependence of the relaxation times were not possbile for X < 0.05 due to signal size difficulties. The results obtained at X = 0.055 are shown in figure 6.4. They are plotted on a $\sqrt{T}$ axis, if the adsorbate were a 2-D classical gas the T_2 data would be expected to lie on a straight line passing through the origin. The higher temperature, T > 2K, data appears to lie on such a line, however, the lower temperature data deviates from it. This behaviour may be associated with the break up of the solid patches - at low temperatures the solid patches mediate T_2 but as the temperature is raised they 1 ose atoms through

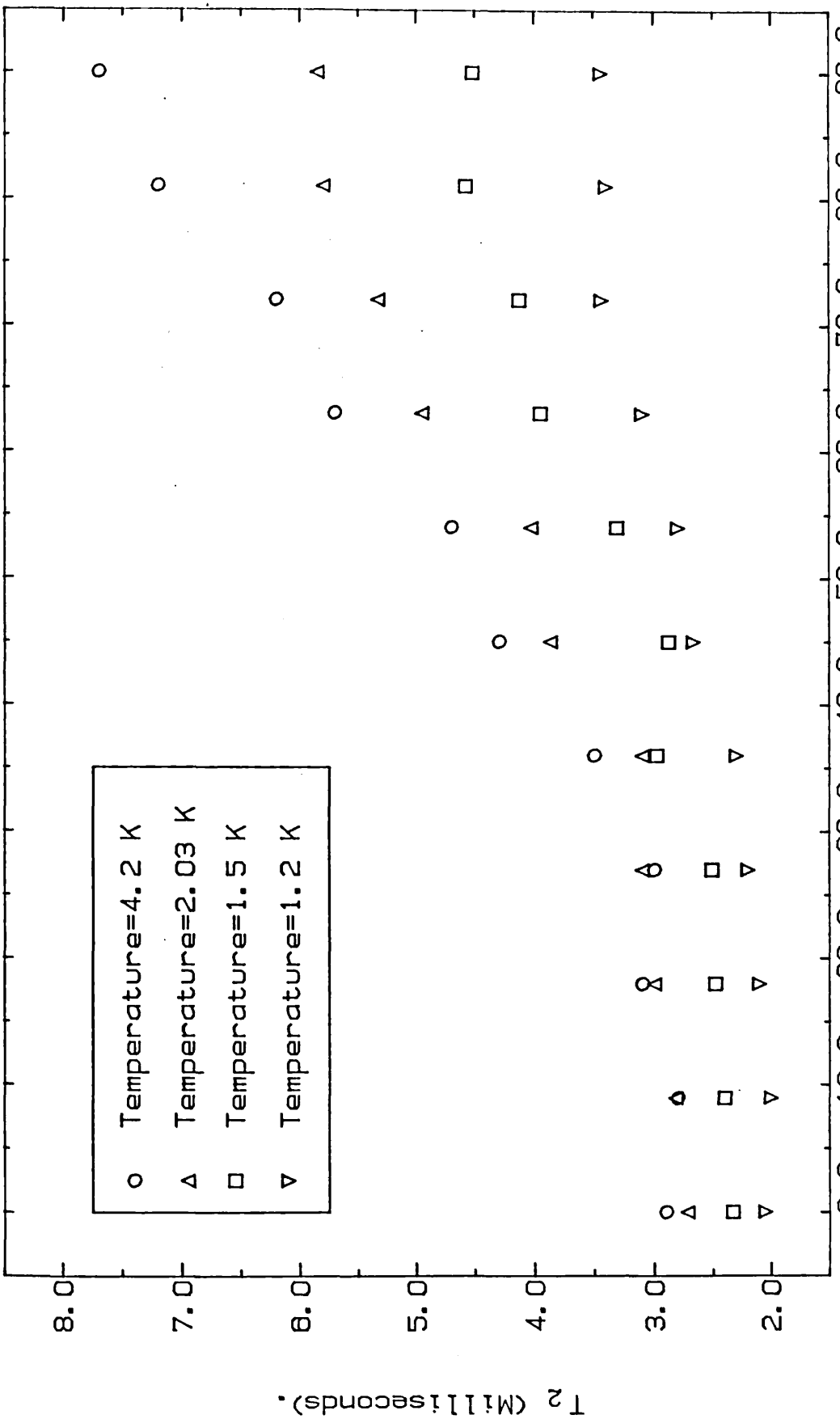

Figure 6.3. Anisotropy In T_2 For Helium-3 Adsorbed On Grafoil, Coverage=0.055 Monolayers, $\omega_o/2\pi$=5 MHz.

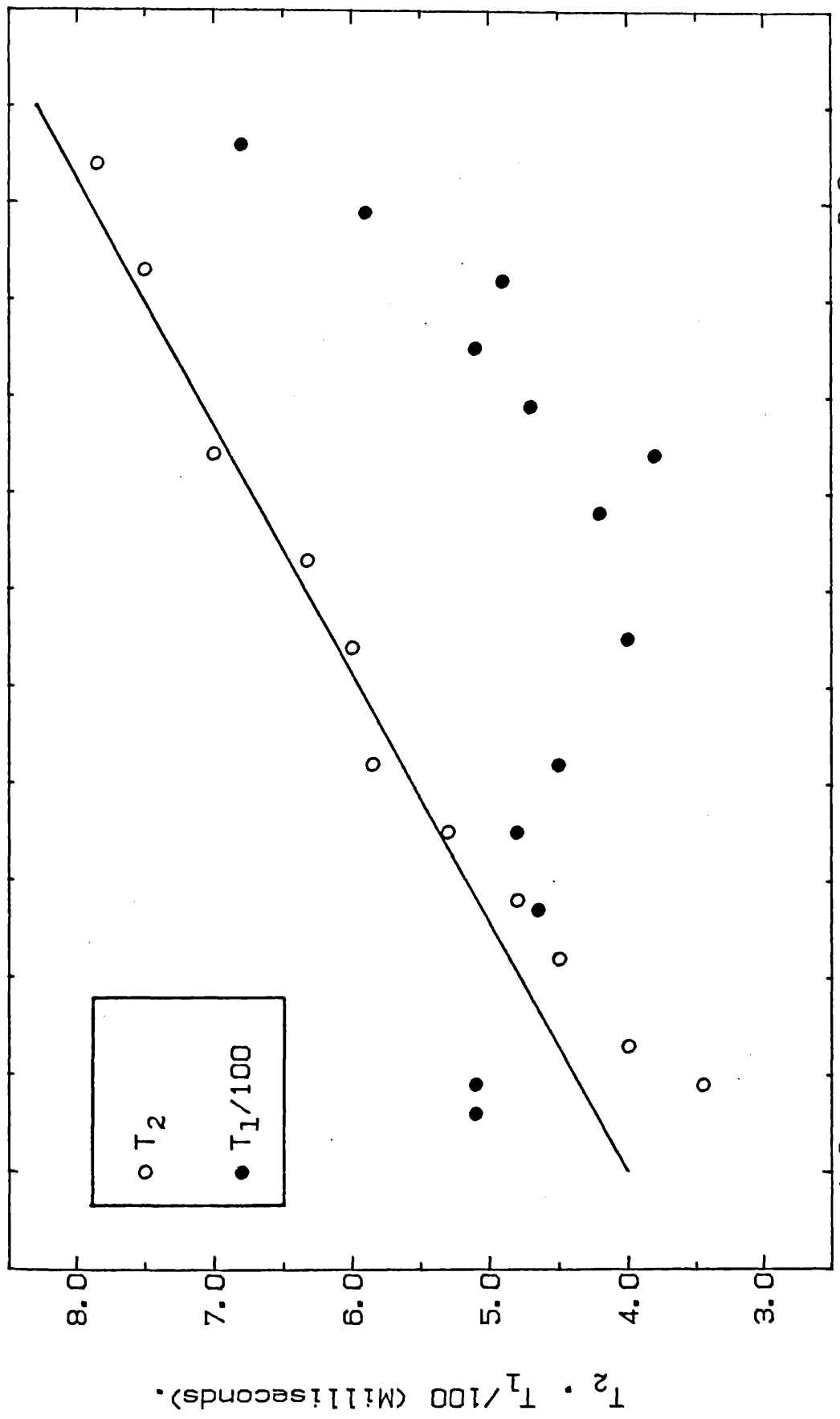

Figure 6.4, T_1 And T_2 As A Function Of The Square Root Of Temperature, $\omega_o/2\pi$=5.1 MHz, X=0.055, & β=90 Degrees.

thermal escape and eventually become small enough that the fluid phase is dominant. The T_1 data displays a definite minimum at about 2.6 Kelvin. Similar minima are observed near to the melting of the incommensurate solid phase [76], and they are due to the large changes in motion within the solid as it melts. By analogy the minimum in figure 6.4 may be associated with the 'melting' of the solid patches as the temperature is raised.

The lowest coverage at which it was possible to measure T_2 at more than one frequency was X = 0.01. At this coverage and at a frequency of 7.5MHz $T_2 \simeq 320\mu s$. Some frequency dependence in T_2 at low coverages is to be expected since the various regions of the substrate at which the solid patches can form may be expected to have a range of different local fields associated with them. However, bearing in mind that at 5MHz $T_2 \simeq 370\mu s$ it is clear that the dipolar component is dominant within the solid patches. At X = 0.055 somewhat more in the way of frequency dependence was seen, figure 6.5. The data indicates a linear dependence of the relaxation rate, T_2^{-1}, on frequency rather than the expected frequency squared relationship eq. (2.9.2). Detailed study of the frequency dependence is left until the next chapter.

6.5 Summary and Conclusions

The results of NMR measurements of very low density Helium-3 adsorbed of Grafoil indicate that for $X \lesssim 0.015$ the adsorbate forms in patches of relatively high density solid. This is in agreement with the thermodynamic analysis of Elgin and Goodstein. The value of x about 0.015 is in good agreement with thermodynamic results [75], which give $x \simeq 0.02$.

At coverages above 0.015 a two phase system exists, the solid plus a 2-D fluid. At sufficiently high coverages X > 0.07, the fluid phase appears to become dominant as far as NMR measurements are

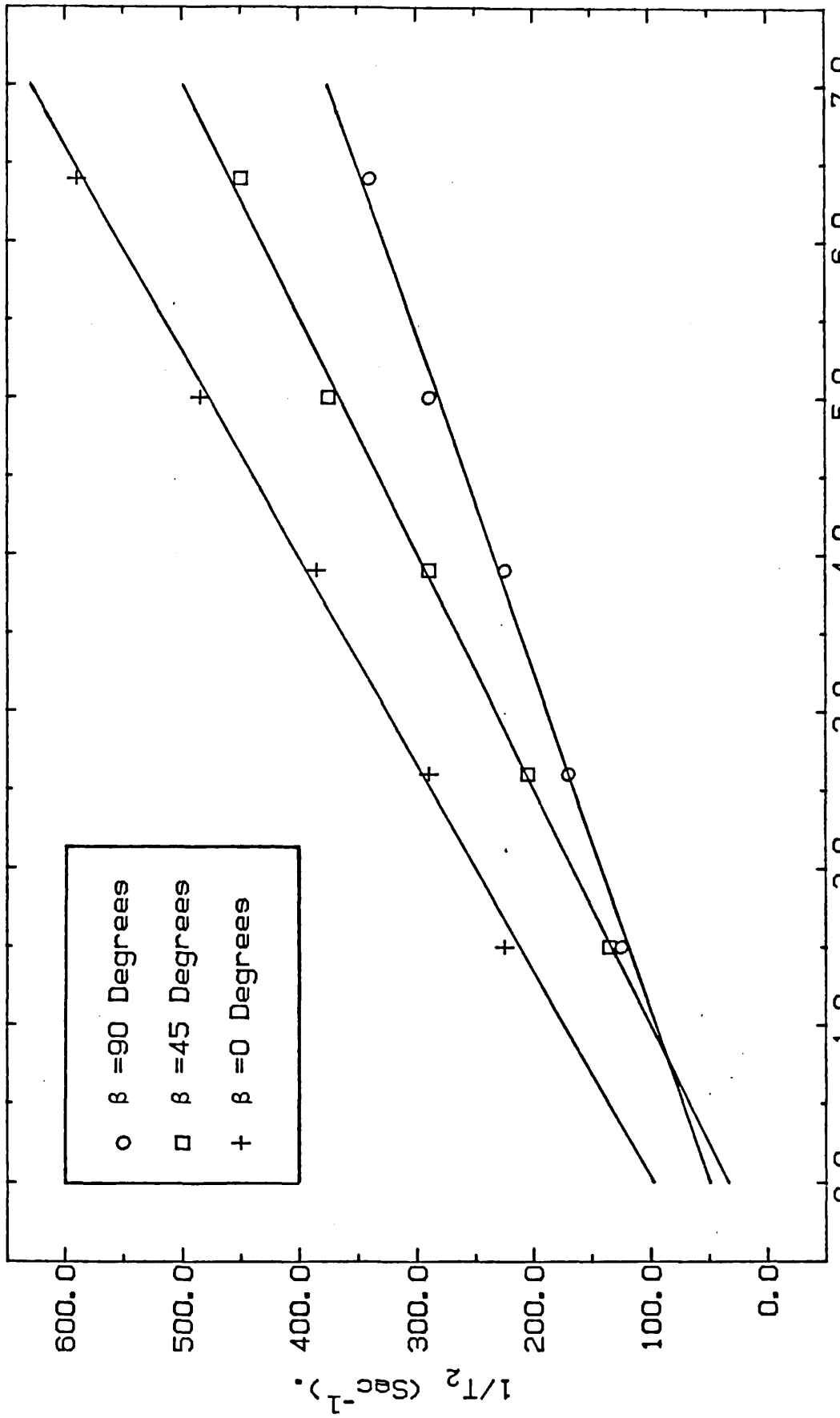

Figure 6.5, T_2 As A Function Of Larmor Frequency For Helium-3 On Grafoil, X=0.055 Monolayer, & Temperature=1.2K.

concerned.

While it is found that the Grafoil local fields have a negligable effect on the relaxation in the solid phase, their effect on the relaxation in the fluid phase is important.

The above conclusions are based on results taken at a temperature of 1.2K. At higher temperatures there is a loss of atoms from the solid patches, as well as an increase in motion of the fluid and of defects (probably vacancies) within the solid.

CHAPTER 7

THE NMR PROPERTIES OF HELIUM-3 ADSORBED ON GRAFOIL
RESULTS FOR 0.1 < X < 0.6

7.1 Introduction

In this chapter are presented, in bare data form, the results of an extensive study of the NMR properties of Helium-3 adsorbed on Grafoil in the range of coverages from 0.1 monolayers to about 0.6 monolayers, a range over which the film is expected to behave as a 2-D gas/fluid.

Particular attention is paid to the effect of the Grafoil local fields which, as far as T_2 measurements are concerned, appear to dominate the NMR properties in this range of coverages. The ease of frequency changing with the new broadband NMR spectrometer system, see Ch.3, facilitated this study.

The main part of the analysis and discussion of the data presented in this chapter are deferred until the next chapter.

7.2 General Points

Over the range of coverages, temperatures, frequencies and substrate orientations studied the spin-lattice relaxation appeared to be a single exponential decay, with decay constant $1/T_1$.

The spin-spin relaxation was, in general, non-exponential, see figures 7.1 and 7.2. While for long times the echo relaxation is very nearly exponential, at shorter times the echo height appears to be levelling off. This behaviour is more noticeable in the higher temperature/lower frequency data. At first this behaviour was believed to be an artefact and somehow related to the performance of the spectrometer system. However, the results of tests on the spectrometer system showed this not be the case.

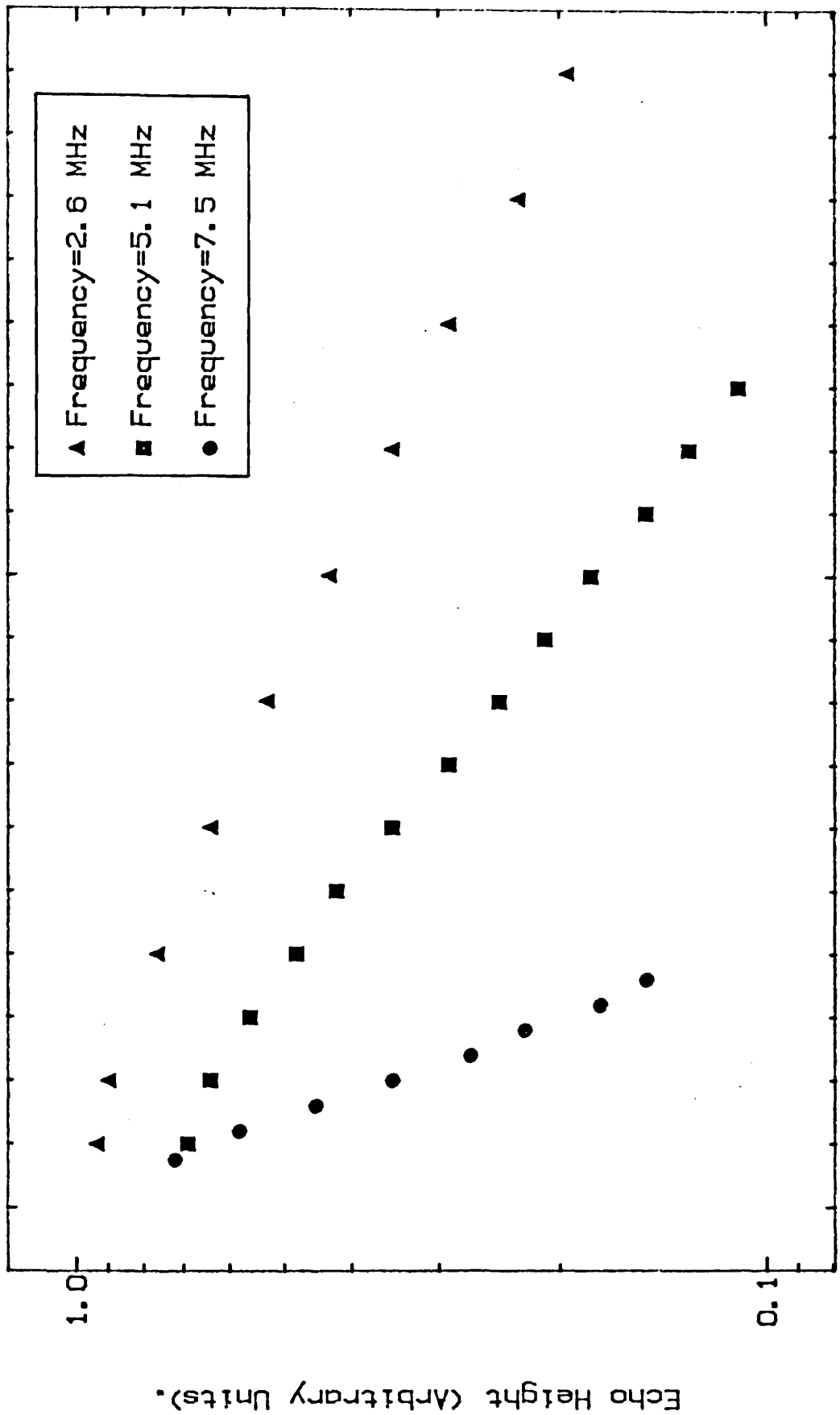

Figure 7.1. Spin Echo Decay For Helium-3 Adsorbed On Grafoil. X=0.3
β =90 Degrees & Temperature=1.2 K.

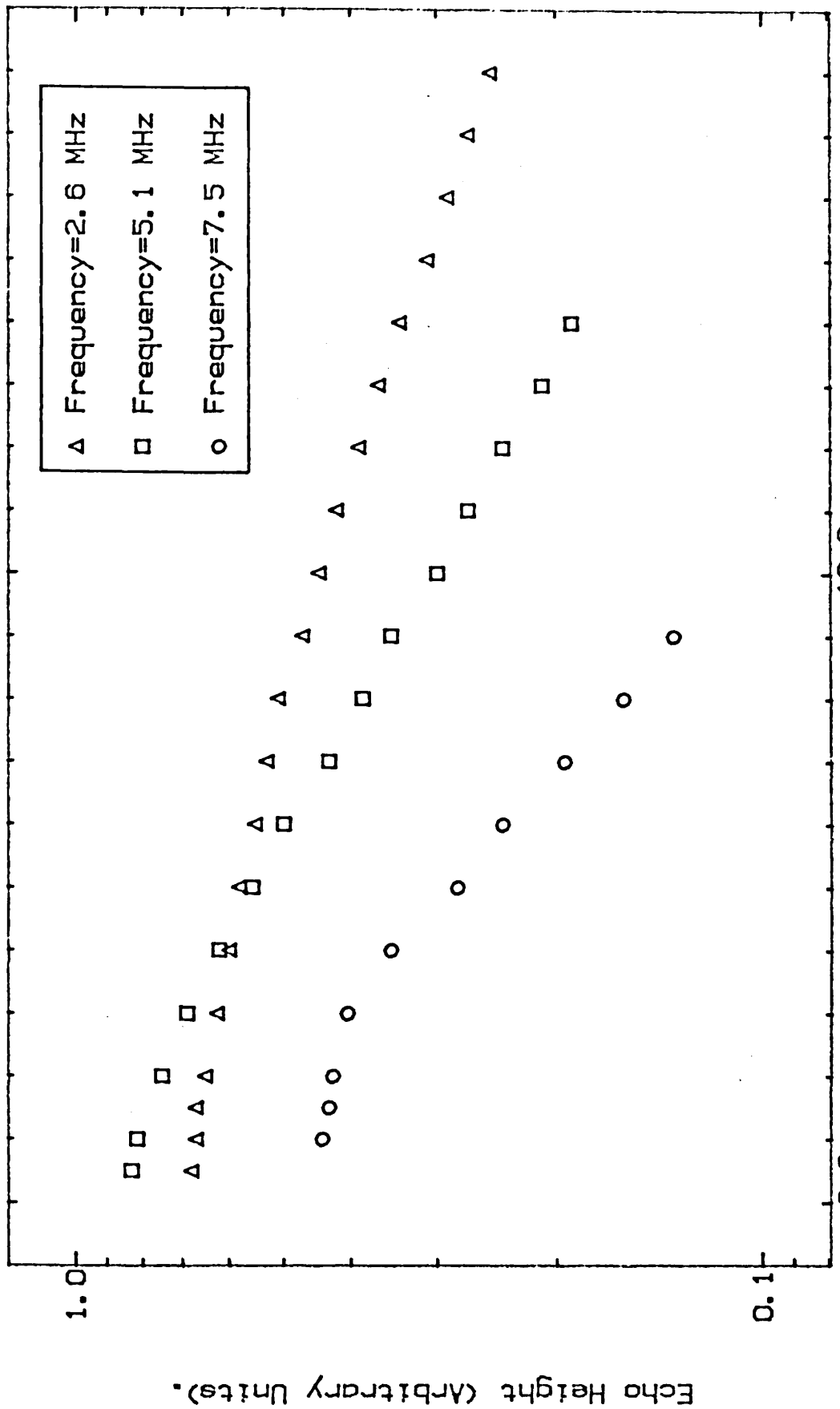

Figure 7.2. Spin Echo Decay For Helium-3 Adsorbed On Grafoil. X=0.3
β=90 Degrees & Temperature=4.2 K.

The T_2 values quoted in the following sections are the decay constants of the near exponential decays at long times. For clarity no error bars are shown on the graphs, errors in T_2 are better than 5% at these coverages and T_1 values are accurate to within 10%. In any case, it is the general trends followed by the data points that are important and the errors are sufficiently small to render these trends unambiguous.

7.3 The Relaxation Times as a Function of Coverage

Figure 7.3 shows T_2 as a function of coverage up to $X = 0.6$ and at various temperatures. These data were taken at an NMR frequency of 5MHz and a substrate orientation of 90^{o}.

In the region $X < 0.1$ there is a rapid increase of T_2 with coverage; this feature has been discussed in Ch.6. There is a maximum in the values of T_2 at a coverage between 0.1 and 0.3 monolayers, the exact position depending on temperature. At higher temperatures the maximum occurs at lower coverages. Following the maximum there is a gradual decrease in T_2 with increasing coverage.

Figure 7.4 shows T_1 as a function of coverage. The main point to note is the monotonic increase of T_1 over the whole range of coverages investigated. The rate of increase appears to slow down as the coverage is increased.

7.4 Temperature Dependence of the Relaxation Times

The dependence of T_2 on temperature at three coverages, 0.1, 0.3 and 0.5, plotted on a square root of temperature scale is shown in figure 7.5. The NMR frequency was 5.1MHz and the substrate orientation 90^{o}. At lower temperatures $T < 2.2K$ the data fits on a

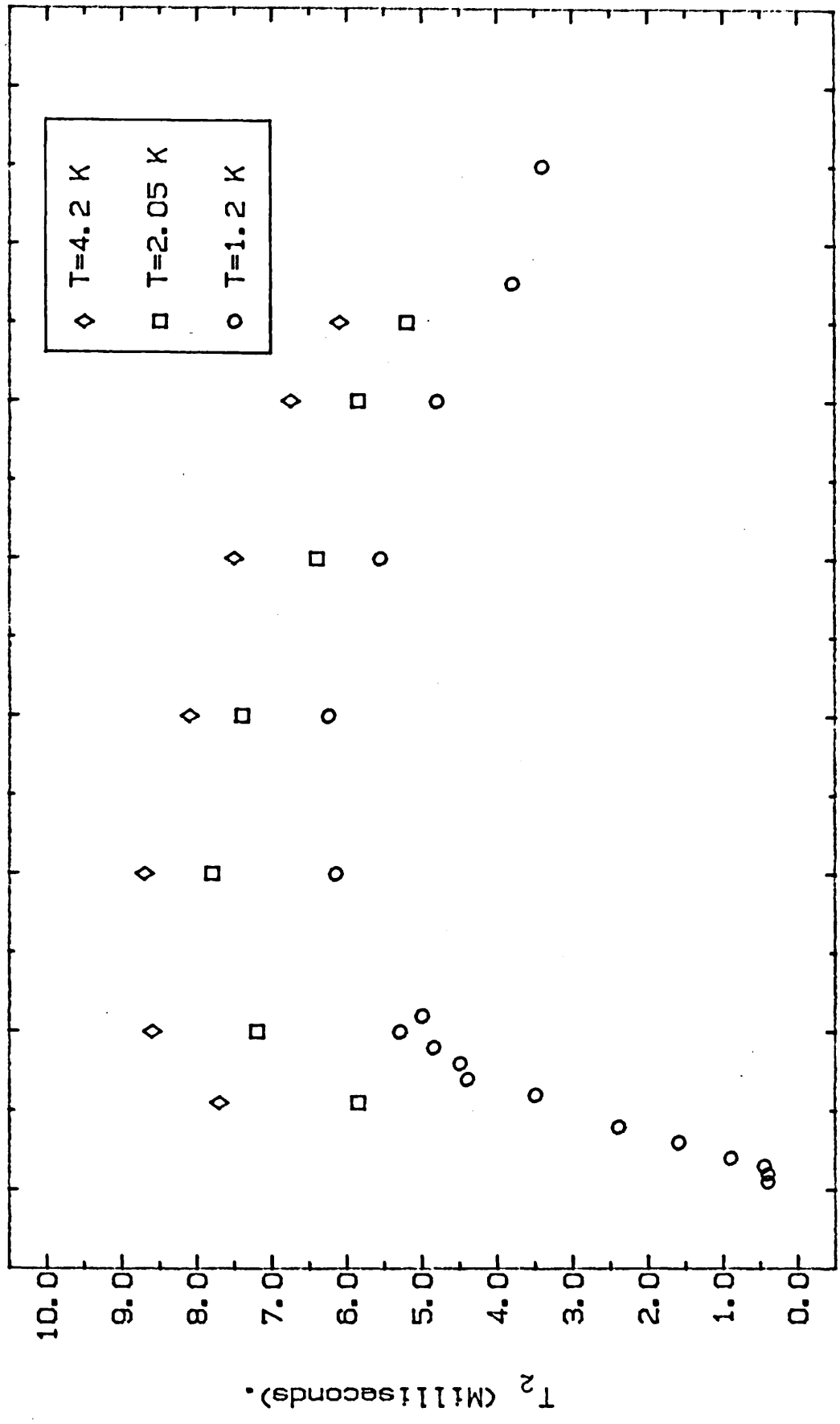

Figure 7.3. T_2 As A Function Of Coverage For Helium-3 Adsorbed On Grafoil. β =90 Degrees & Frequency=5.1 MHz.

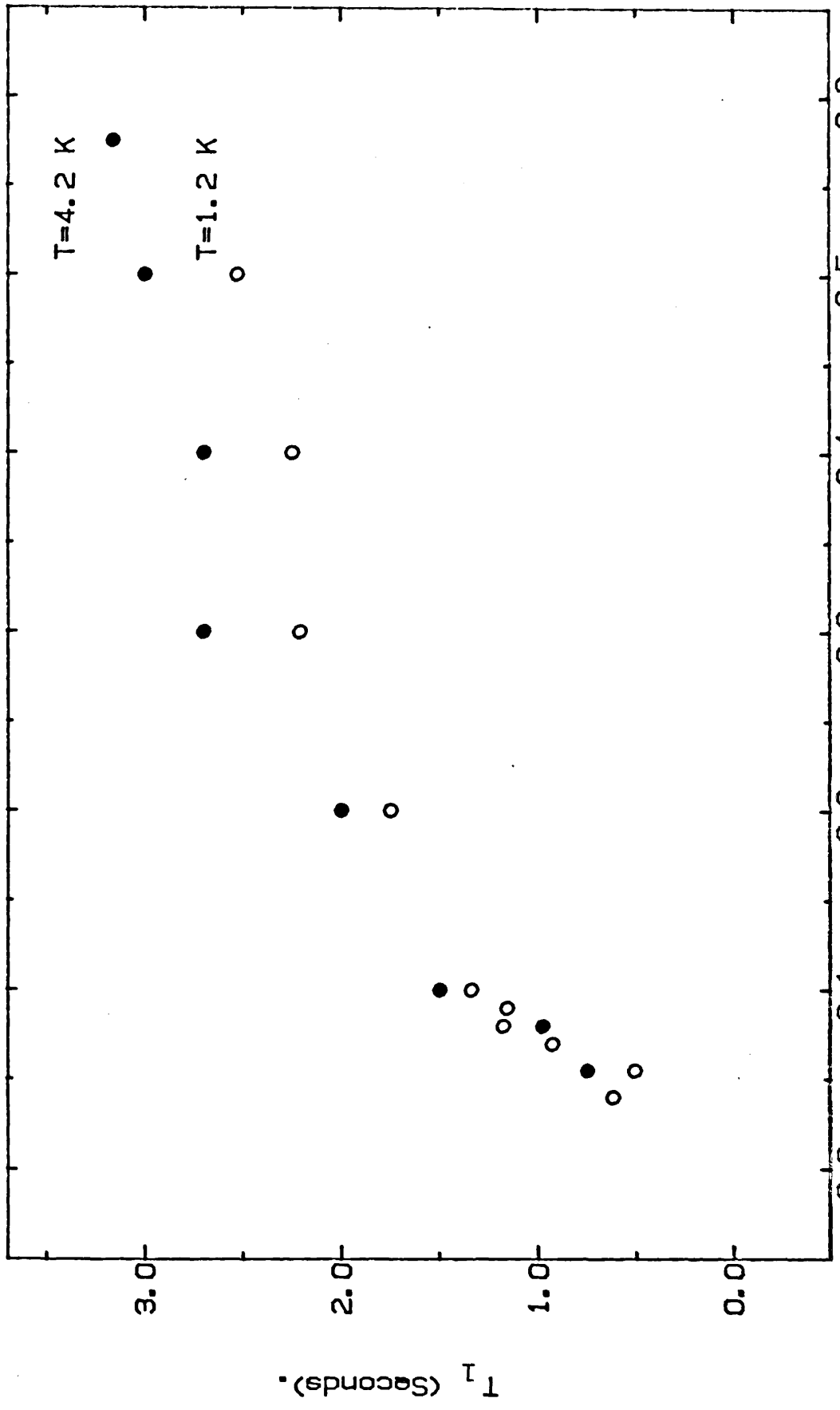

Figure 7.4, T_1 As A Function Of Coverage For Helium-3 Adsorbed On Grafoil. β =90 Degrees & Frequency=5.1 MHz.

straight line passing through the origin, while at higher temperatures T_2 levels off to a near constant value. This high temperature value was found to change little even when the temperature was increased to 10K. The non-exponential character of the spin-spin relaxation, §7.2, became more marked at these high temperatures. Table 7.1 summarizes the slopes of the low temperature $T_2 \propto \sqrt{T}$ data and the high temperature values of T_2 at all coverages investigated.

Figure 7.6 shows T_2 as a function of the square root of temperature again, this time at X = 0.4, $\beta = 90^{o}$ and at three frequencies 2.6, 5.1 and 7.5MHz. The same general trend is followed at all frequencies. Table 7.2 summarizes the main features.

Finally, in figure 7.7 is shown the dependence of T_2 on temperature at X = 0.3, an NMR frequency of 5.1MHz and at various substrate orientations. Again the same trends are observed at all orientations. Table 7.3 summarizes the slopes of the $T_2 \propto \sqrt{T}$ data and the high temperature values of T_2.

The temperature dependence in T_1 is rather weak, T_1 being only some 20% longer at 4.2K than at 1.2K regardless of coverage, frequency or substrate orientation. This difference is only twice the experimental error (10%) incurred in measurements of T_1.

7.5 Anistropy of the Relaxation Times

The anistropy in T_2 with respect to the angle β made between the normal to the substrate plane and the magnetic field direction is shown in figure 7.8. The data was taken at a temperature of 1.2K, an NMR frequency of 5.1MHz and at four coverages. The anistropy is nearly the same in each case with $T_2(90)/T_2(0) \simeq 2.3$, and it is quite different from any of the theoretical plots in Ch.2.

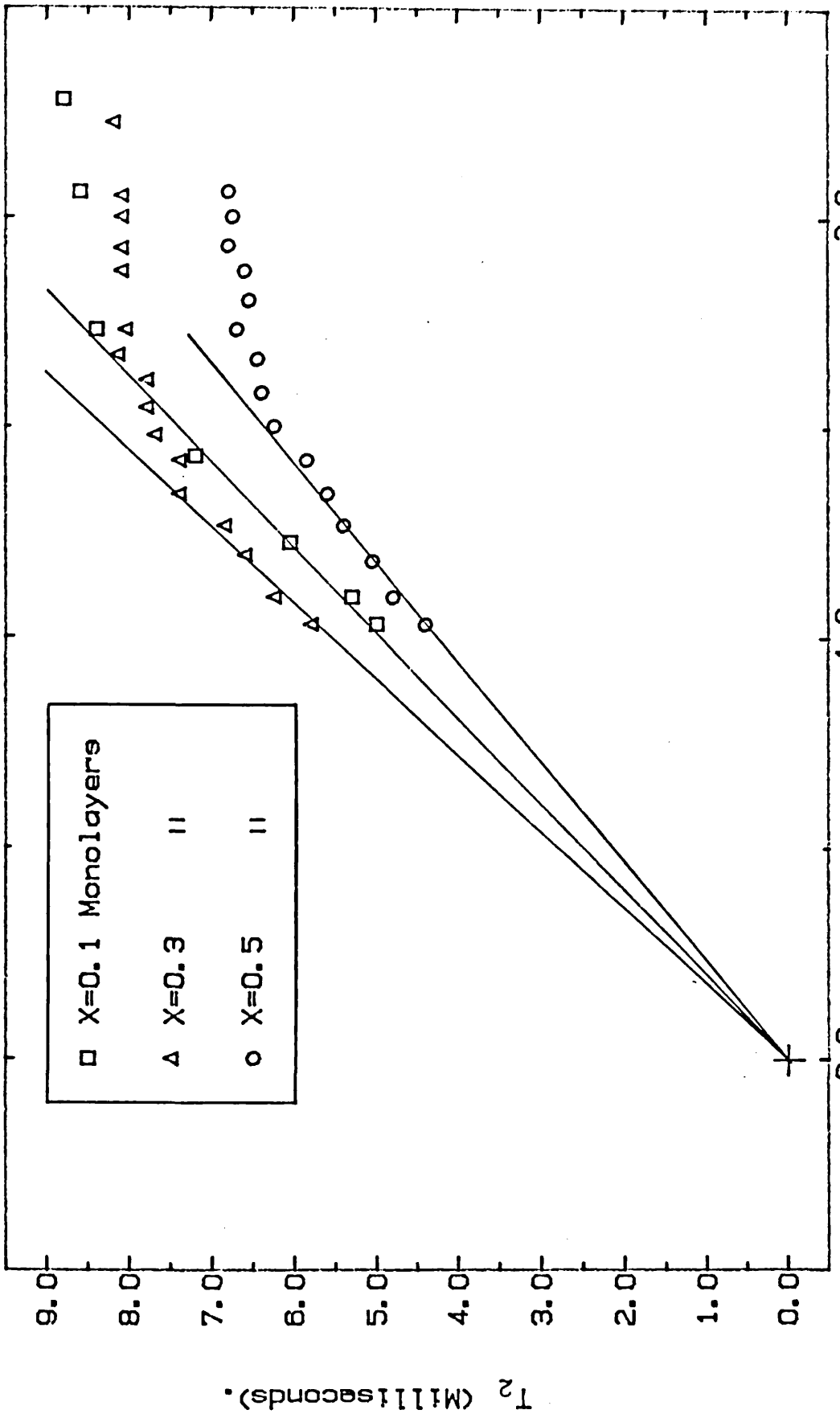

Figure 7.5. T_2 -vs-Square Root Of Temperature For Helium-3 Adsorbed On Grafoil. β =90 Degrees & Frequency=5.1 MHz.

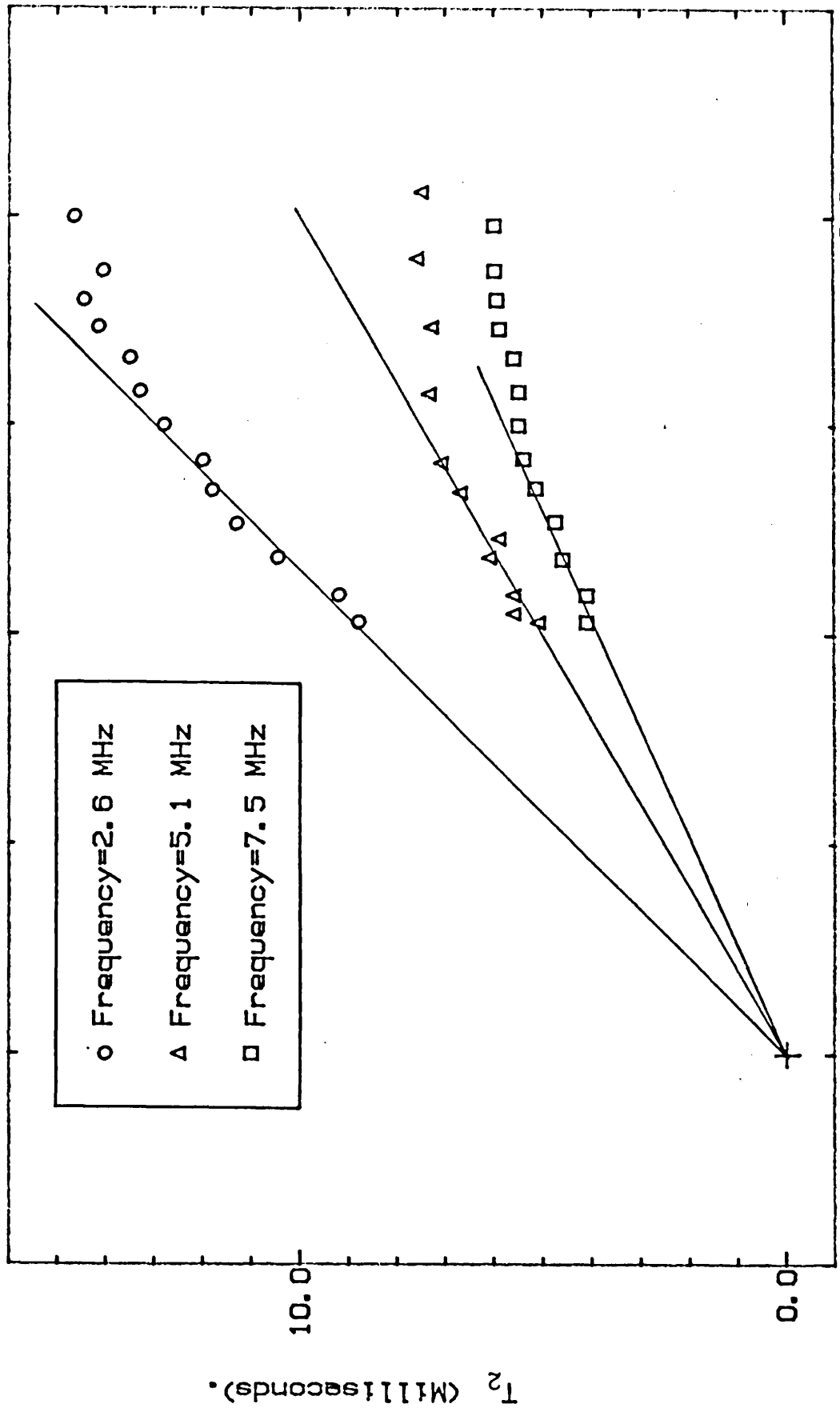

Figure 7.6. T_2 -vs-Square Root Of Temperature For Helium-3 Adsorbed On Grafoil. X=0.4 Monolayers & β =90 Degrees.

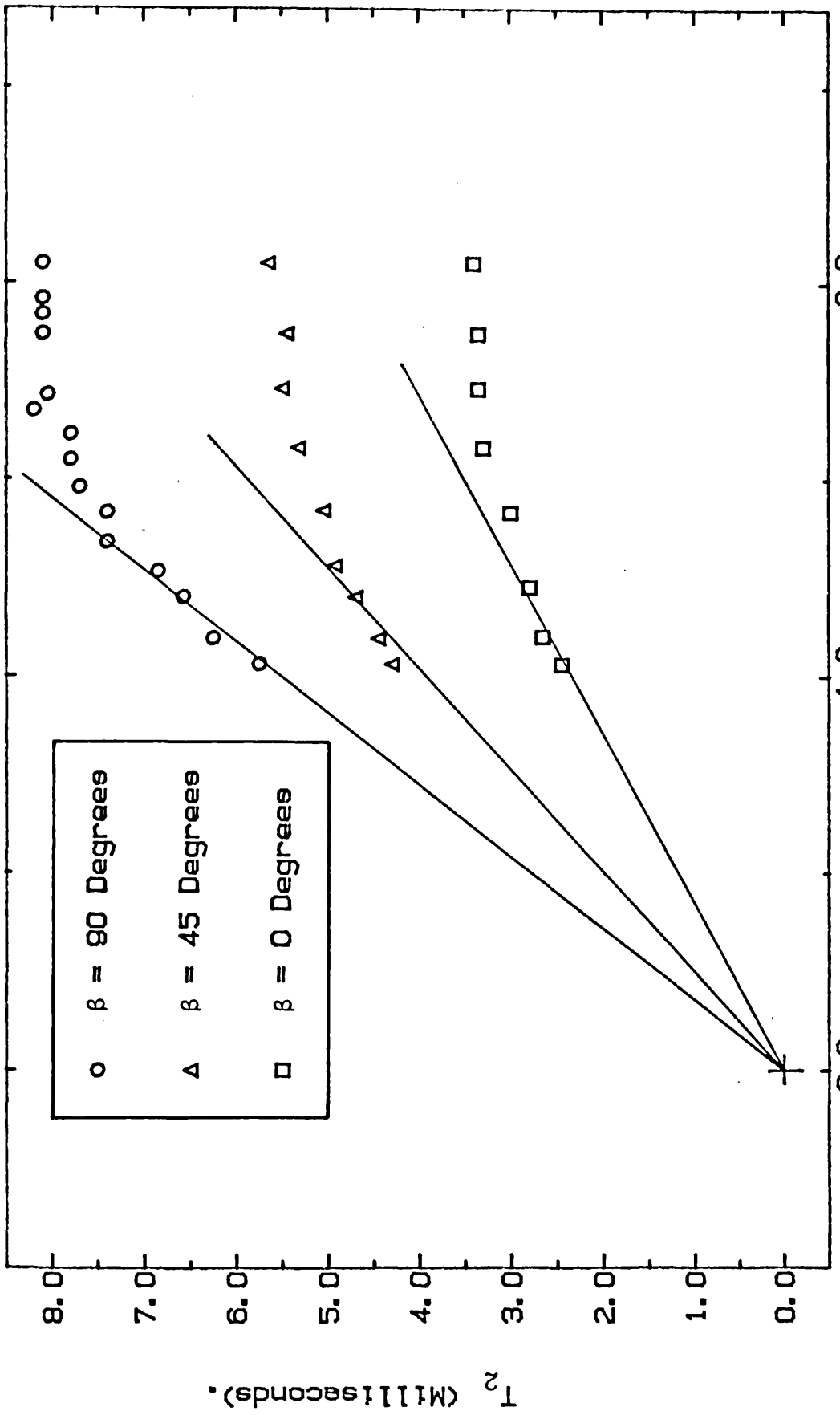

Figure 7.7. T_2 -vs-Square Root Of Temperature For Helium-3 Adsorbed On Grafoil. X=0.3 Monolayers & Frequency=5.1 MHz.

Table 7.1 Slope of $T_2 \propto \sqrt{T}$ data and high temperature value of T_2 $\beta = 90^o$, $\omega_o/2\pi = 5.1$MHz

Coverage X	Slope of $T_2 \propto \sqrt{T}$ part (ms $K^{-\frac{1}{2}}$)	High temperature value (ms)	
0.055	3.95 ± .05	7.7 ± .1	3.90
0.1	4.88 ± .05	8.6 ± .1	3.1
0.2	5.75 ± .1	8.7 ± .1	2.29
0.3	5.5 ± .05	8.1 ± .1	2.17
0.4	5.0 ± .1	7.5 ± .1	2.25
0.5	4.25 ± .05	6.75± .1	2.52
0.55	3.5 ± .15	6.1 ± .1	3.07

Table 7.2 $\beta = 90^o$ and X = 0.4

$\omega_o/2$	Slope of $T_2 \propto \sqrt{T}$ part (ms $K^{-\frac{1}{2}}$)	High temperature value (ms)	
2.6	8.7 ± .05	14.4 ± .2	2.74
5.1	5.0 ± .1	7.5 ± .1	2.25
7.5	3.8 ± .05	6 ± .1	2.49

Table 7.3 $\omega_o/2\pi = 5.1$MHz and X = 0.3

β	Slope of $T_2 \propto \sqrt{T}$ part (ms $K^{-\frac{1}{2}}$)	High temperature value (ms)	
90	5.5 ± .05	8.1 ± .1	2.17
45	4.0 ± .1	5.5 ± .1	1.89
0	2.4 ± .1	3.3 ± .1	1.89

The solid line through the X = 0.3 data is given by

$$T_2^{-1} = (A + B\cos 2\beta) \tag{7.5.1}$$

where

$$A = \tfrac{1}{2}\left(\frac{1}{T_2(0)} + \frac{1}{T_2(90)}\right) \tag{7.5.2}$$

and

$$B = \tfrac{1}{2}\left(\frac{1}{T_2(0)} - \frac{1}{T_2(90)}\right) \tag{7.5.3}$$

It is clearly a very good fit to the data, the deviations of the points from the curve may be attributed to a small ($\sim 3^{\circ}$) error in alignment of the orientation sensor with respect to the Grafoil planes.

Figure 7.9 shows the effect on the anisotropy of changing the NMR frequency. At X = 0.3 and a temperature of 1.2K. Increasing the frequency results in slightly increased anisotropy as measured by $T_2(90)/T_2(0)$. The solid lines are from eq. (7.5.1) fitted to the 2.6, 5.1 and 7.5MHz data.

Figure 7.10 shows the anisotropy at X = 0.3, NMR frequency 5.1MHz and at two temperatures. The point to note here is that the anisotropy increases only slightly with increasing temperature. A decrease is expected if the relaxation were dipolar in origin. There is also no evidence to suggest that, at this coverage, T_2 is any more sensitive to motion at $\beta = 90^{\circ}$ than it is at 0°.

There was little or no anisotropy in the spin-lattice relaxation time T_1 values.

7.6 The Frequency Shift

While making the anisotropy measurements it was found necessary to re-tune the spectrometer frequency each time the orientation of the sample chamber was changed. This was to correct for a slight shift in the Larmor frequency due to the anisotropy in the bulk susceptibility of the Grafoil. The shift was ascertained

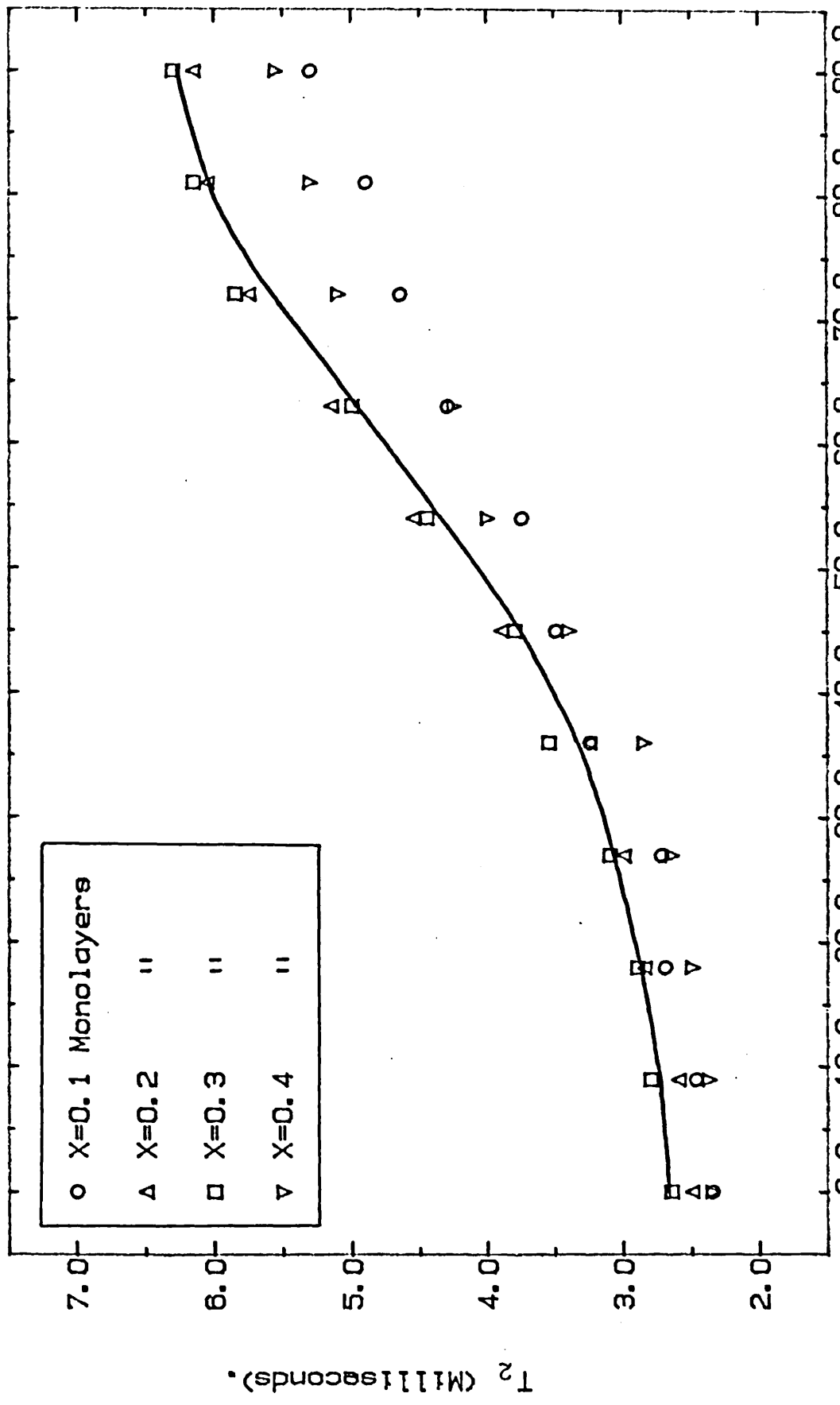

Figure 7.8. Anisotropy In T_2 For Helium-3 Adsorbed On Grafoil, Frequency=5.1 MHz & Temperature=1.2 Kelvin.

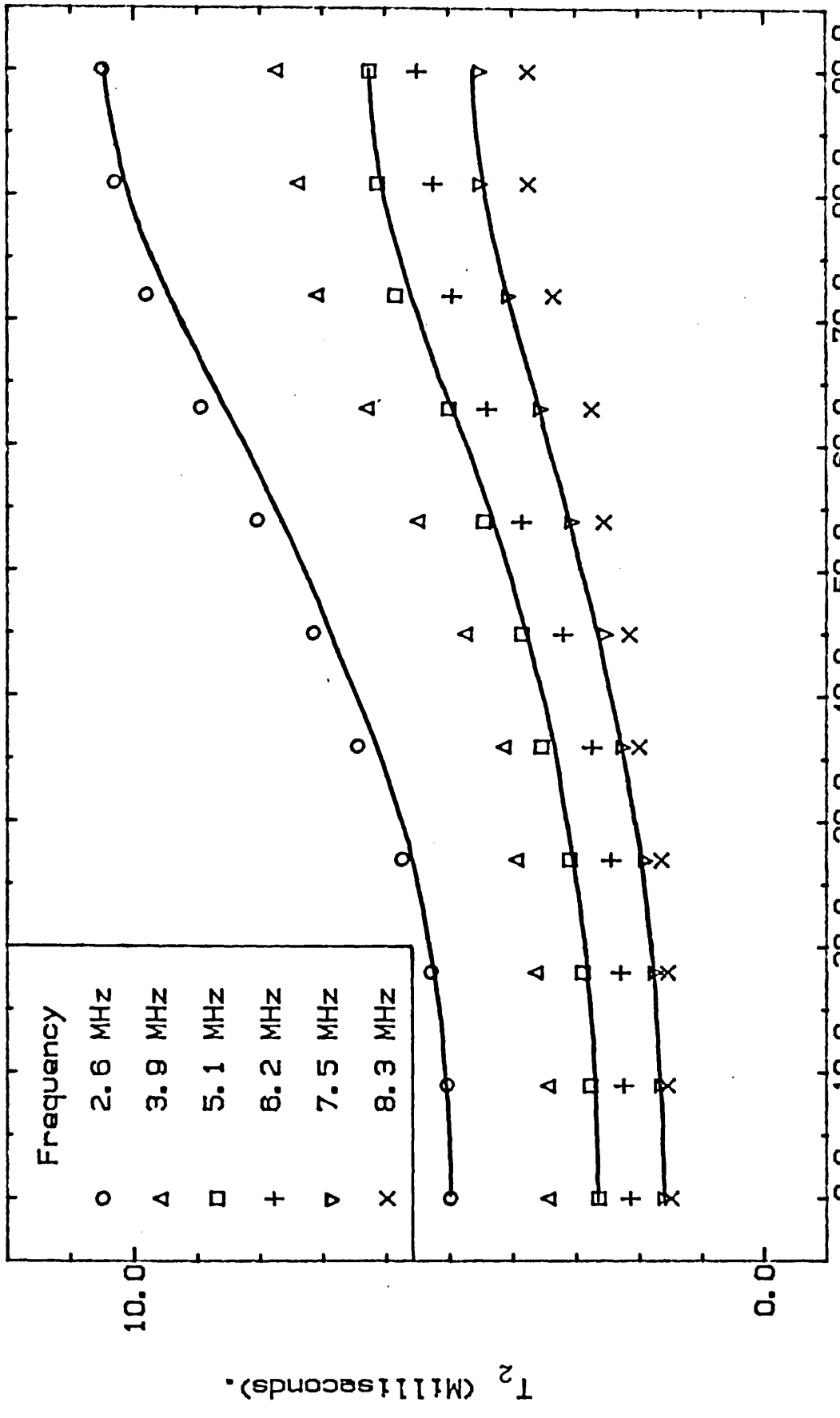

Figure 7.9. Anisotropy In T_2 For Helium-3 Adsorbed On Grafoil, X=0.3 Monolayers & Temperature=1.2 Kelvin.

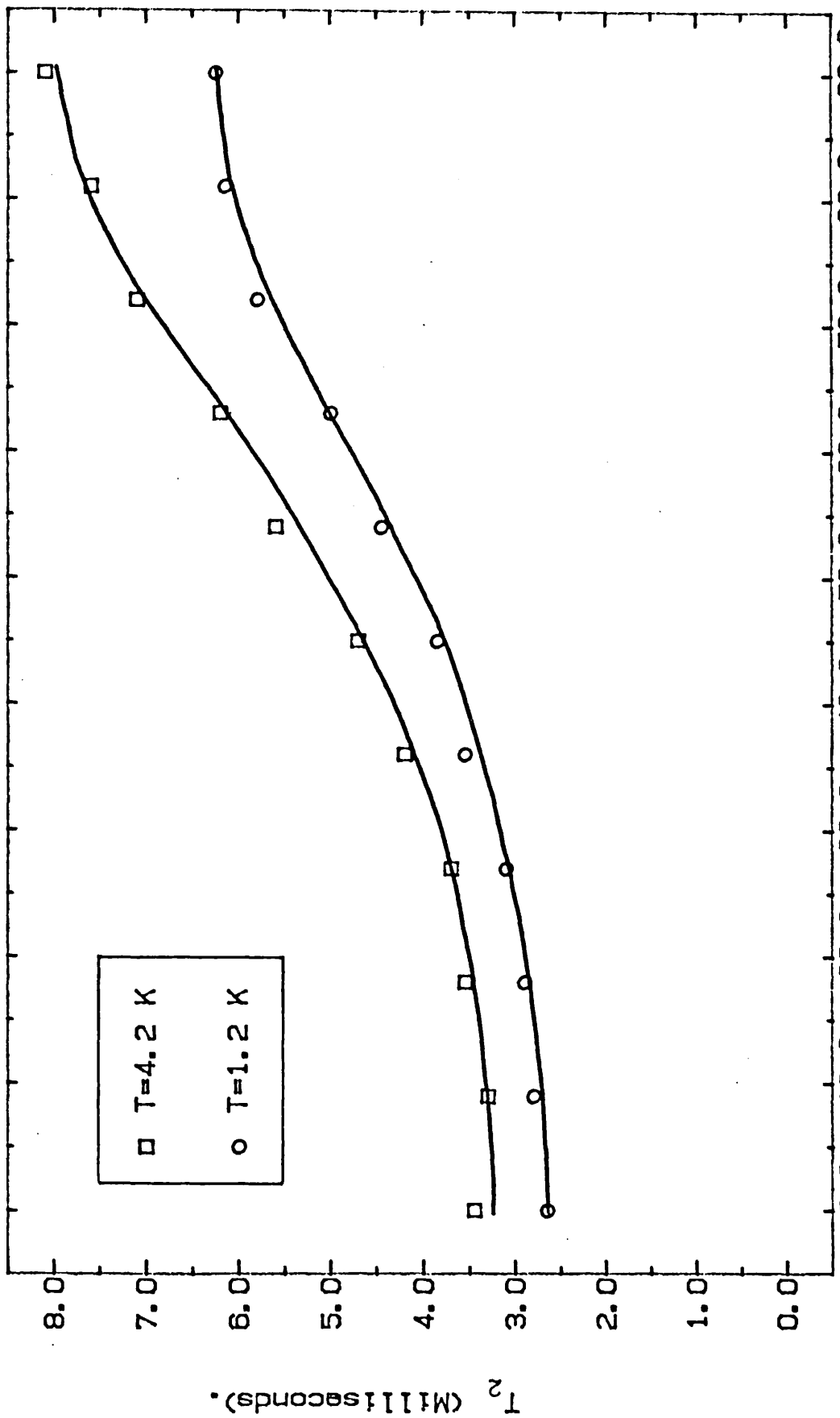

Figure 7.10. Anisotropy In T_2 For Helium-3 Adsorbed On Grafoil, Frequency=5.1 MHz & X=0.3 Monolayer.

by measuring the change in the beat frequency of an off tune FID. The results obtained at a coverage of 0.1 and a nominal frequency of 5MHz are shown in figure 7.11.

The total frequency shift, $\Delta\omega/2\pi$, experienced when changing β from 0^o to 90^o is 470Hz, the frequency being highest at $\beta = 0^o$. The solid line through the data points is from

$$\Delta\omega/2\pi = 240(1 - \cos 2\beta) \qquad (7.6.1)$$

and is quite a respectable fit to the data.

7.7 Frequency Dependence of the Relaxation Times

The strength of the Grafoil local fields is proportional to the field B_o, therefore in order to reach an understanding of the effects of the local fields it is essential to look at the frequency dependence of the relaxation times. It is expected that T_2^{-1} will be proportional to ω^2, see §2.10. However, in the last chapter we found that at X = 0.055, T_2^{-1} was linearly dependent on frequency. In the present range of coverages the relaxation times have been measured at frequencies between 1.3 and 8.3MHz.

Figures 7.12 and 7.13 show T_2^{-1} as a function of frequency taken at a temperature of 1.2K, an orientation of 90^o and at various coverages. The results show a definite linear relationship. The slopes and intercepts of the straight lines fitted by a least squares program are summarized in table 7.4, the correlation coefficients were between 0.995 and 0.999 in all cases. The importance of the intercept is that it gives the frequency independent (dipolar?) contribution to the relaxation time. Figure 7.14 shows T_2^{-1} as a function of frequency at a temperature of 4.2K, otherwise the conditions are the same as above. Again, it is found that T_2^{-1} is proportional to ω, the slopes

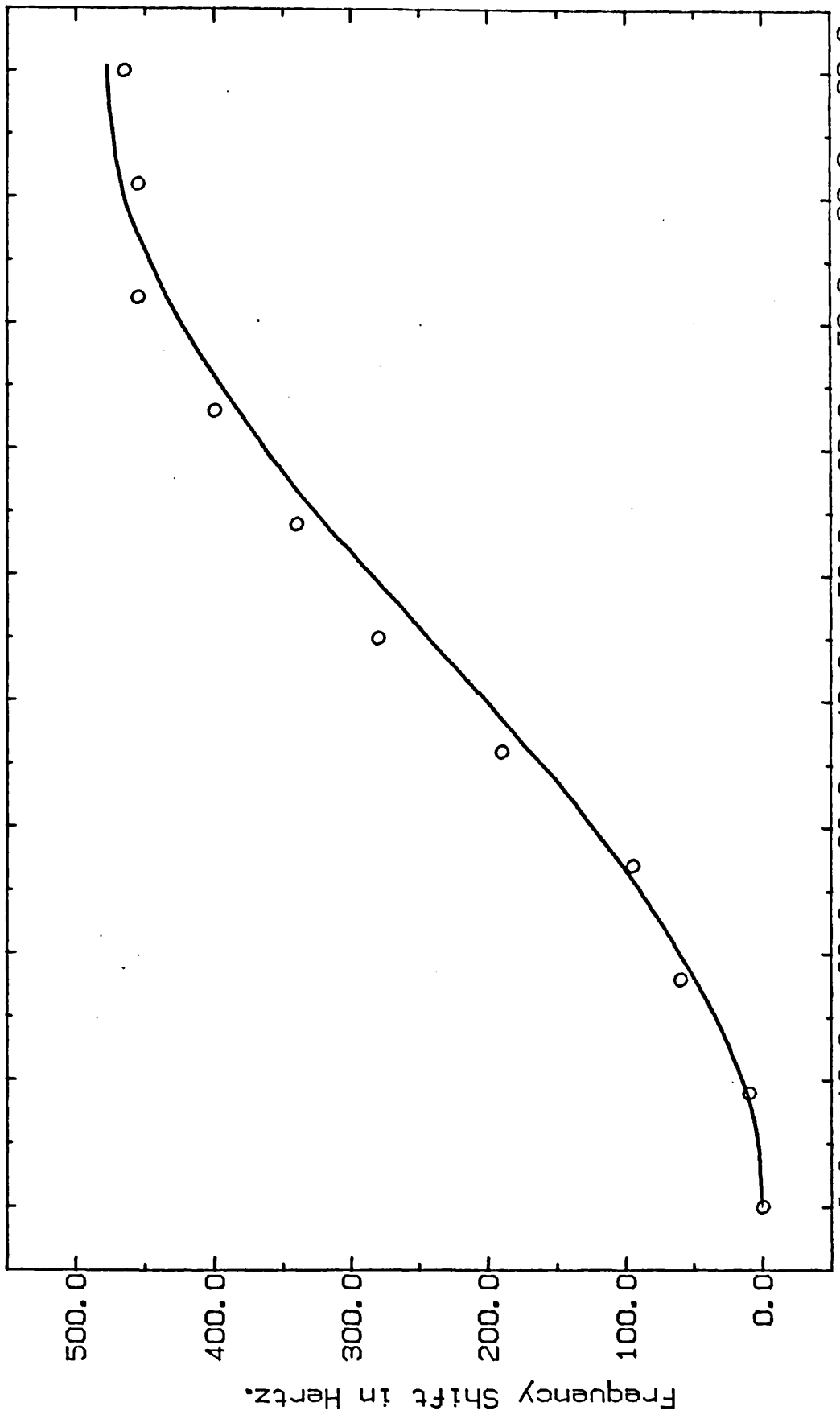

Figure 7.11. Shift In Larmor Frequency Of He-3 On Grafoil As A Function Of Substrate Orientation, $\omega_o/2\pi$=5 MHz At β=0 Degrees.

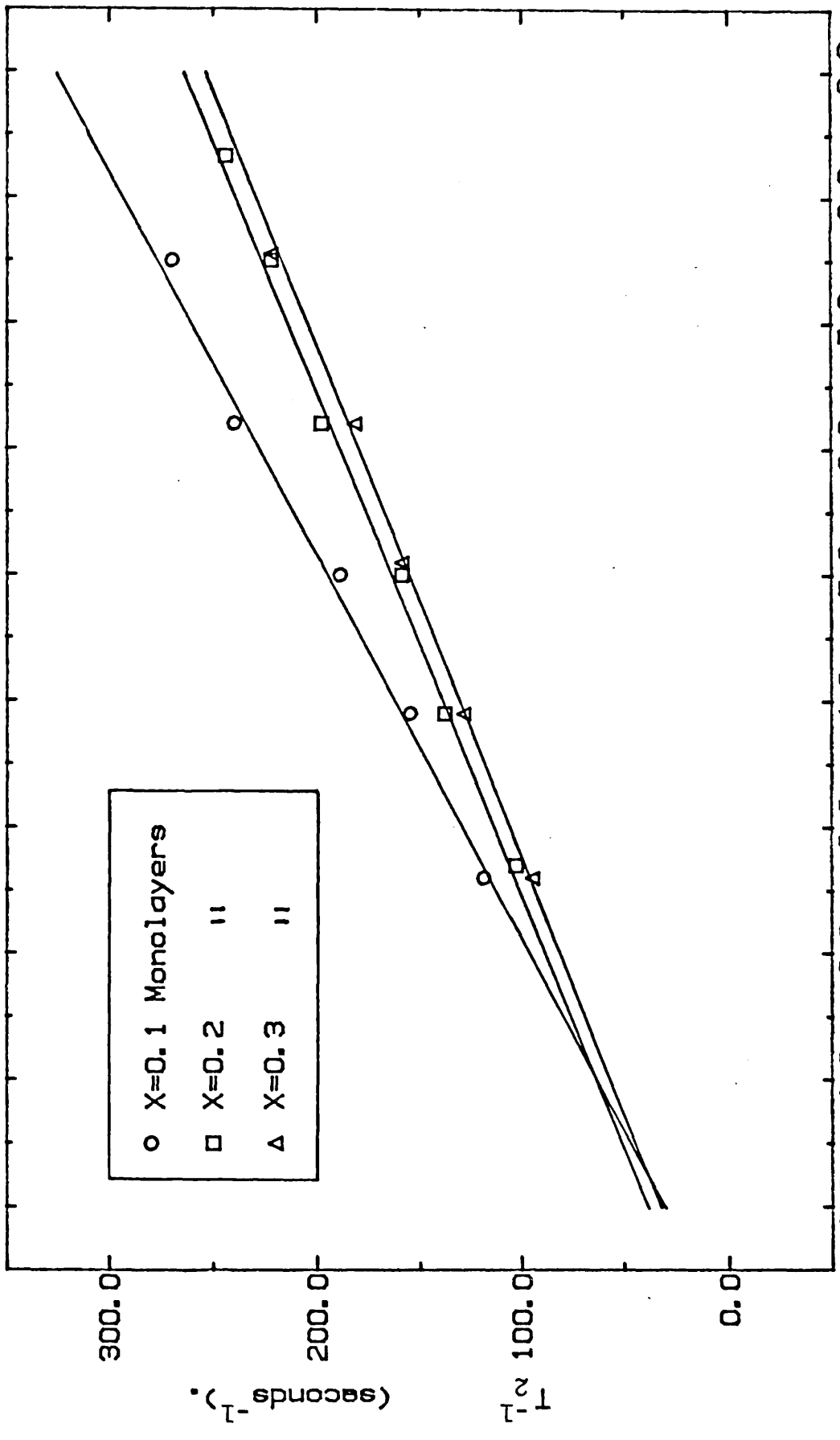

Figure 7.12, T_2^{-1} As A Function Of Larmor Frequency For Helium-3 On Grafoil. β=90 Degrees & temperature=1.2K.

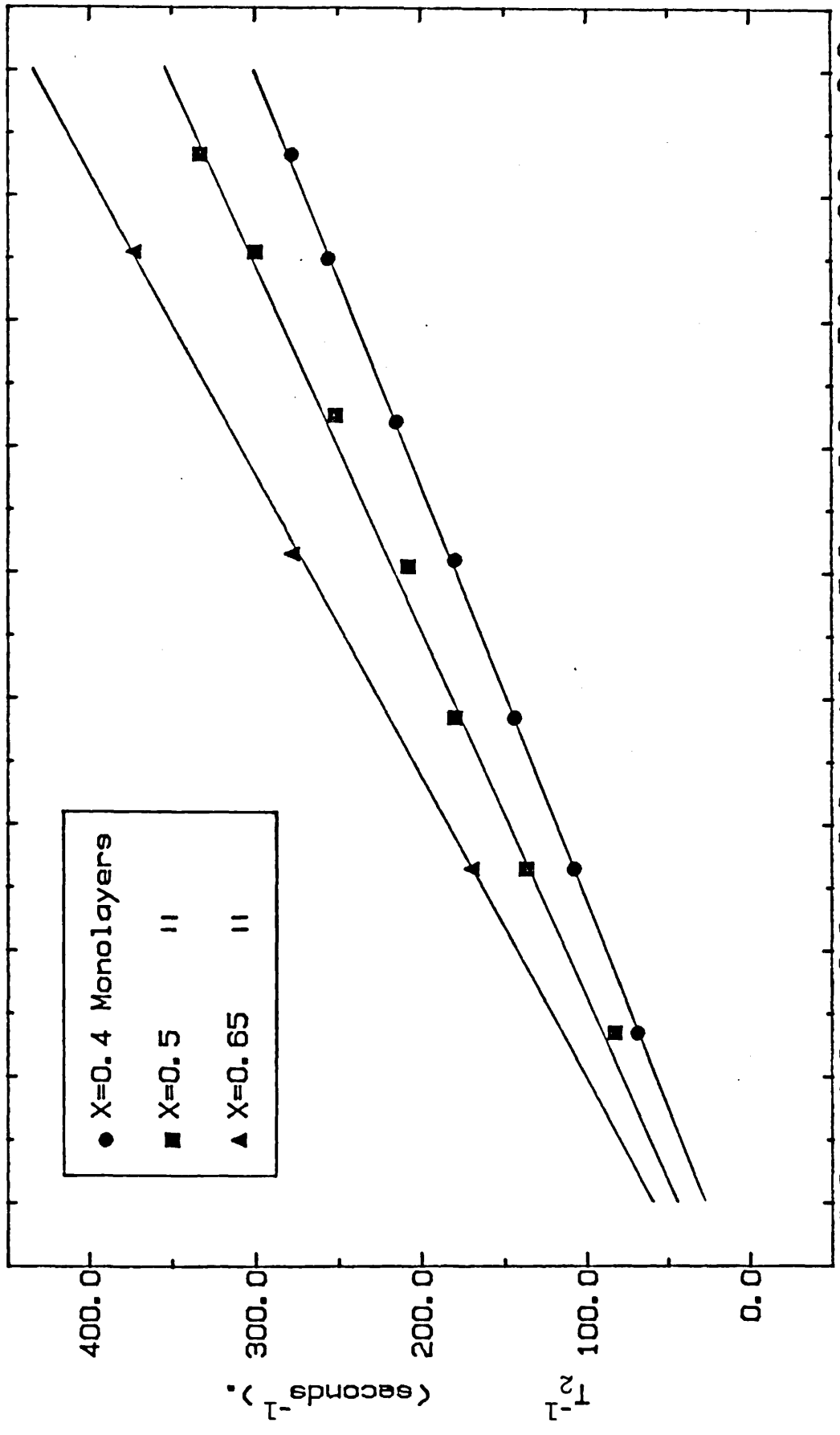

Figure 7.13. T_2^{-1} As A Function Of Larmor Frequency For Helium-3 On Grafoil. β=90 Degrees & Temperature=1.2K.

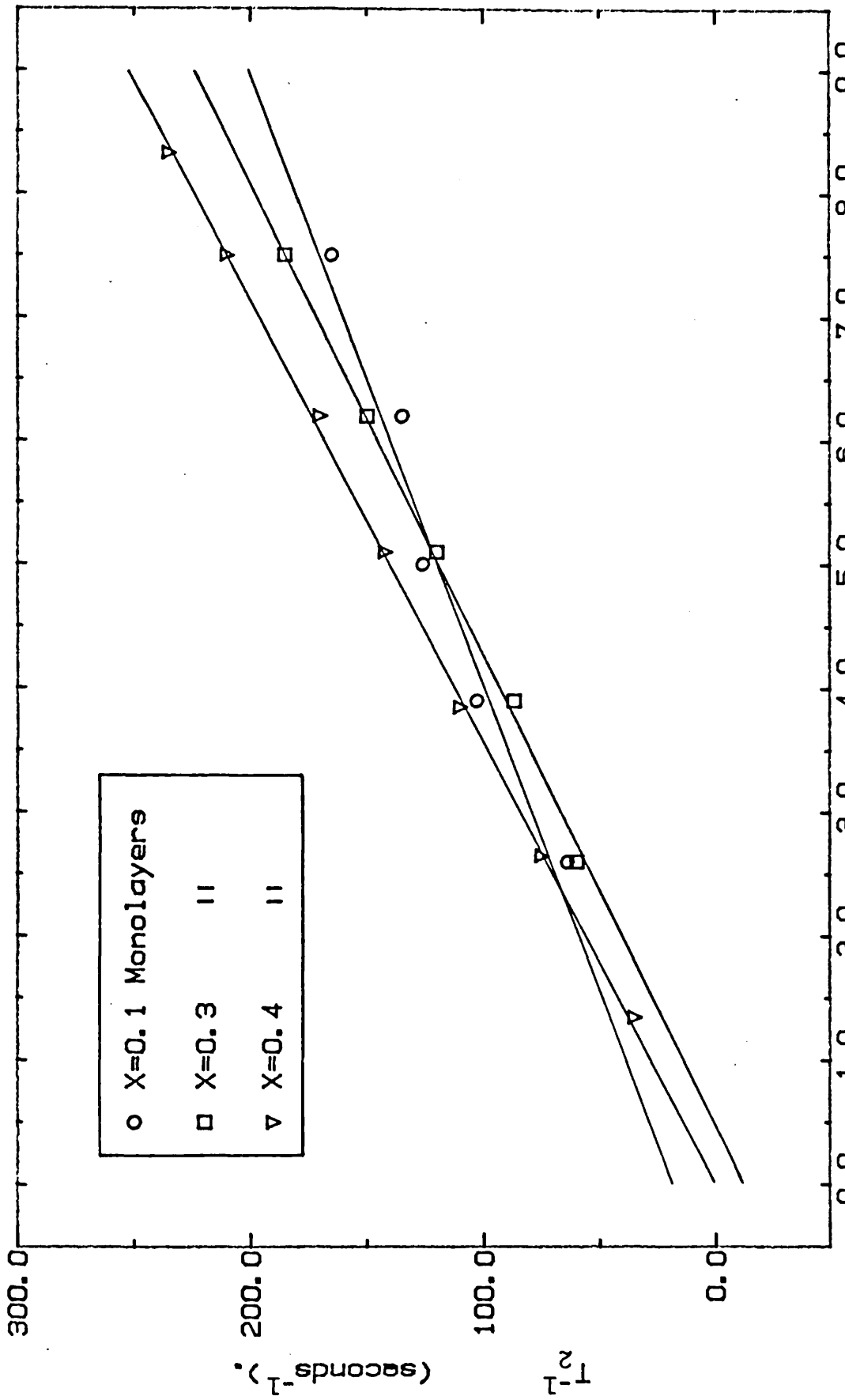

Figure 7.14. T_2^{-1} As A Function Of Larmor Frequency For Helium-3 On Grafoil. β=90 Degrees & Temperature=4.2K.

Table 7.4 Slopes and intercepts of frequency dependence
$\beta = 90^{o}$, T = 1.2K

X	Slope $X10^{-6}$	Intcpt ms^{-1}
0.055	45.1 ± 1.8	55.4 ± 7.5
0.1	30.7 ± .81	36.8 ± 4.3
0.2	24.8 ± .85	38.6 ± 5.0
0.3	25.3 ± .85	29.6 ± 4.5
0.4	30.1 ± .2	28.6 ± 1.1
0.5	34.9 ± .83	37.4 ± 4.6
0.65	41.4 ± 1.2	61.7 ± 6.4

Table 7.5 $\beta = 90^{o}$, T = 4.2K

X	Slope $X10^{-6}$	Intcpt s^{-1}
.1	19.45 ± 1.6	1.89 ± 8.6
.3	26.1 ± .74	-1.12 ± 4
.4	28.2 ± 0.4	-1.4 ± 2

and intercepts are summarized in table 7.5. At X = 0.1 the slopes of the 1.2K and 4.2K data differ quite considerably; however, at X = 0.3 and 0.4 there is no significant change of slope. The intercepts of the 4.2K data are all, with the limits of experimental accuracy, at or very close to the origin.

As well as being dependent on the strength of B_o, the size of the local fields is also strongly dependent on the direction of B_o with respect to the substrate plane. Figures 7.15, 7.16 and 7.17 show the frequency dependence of T_2 at X = 0.1, 0.3 and 0.4 respectively, the data being taken at an orientation of $\beta = 0^o$ and a temperature of 1.2K. At this orientation it appears that while the low frequency data appears to follow the now familiar $T_2^{-1} \propto \omega$ form, the higher frequency data is tending towards an ω^2 dependence. This is suggestive of a quadratic frequency dependence,

$$T_2^{-1} = A + B\omega + C\omega^2 \qquad (7.7.1)$$

At low frequencies, $\omega << B/C$, $T_2^{-1} = A + B\omega$ so the frequency independent part, A, may be obtained by fitting a straight line to the low frequency data. Tables 7.6, 7.7 and 7.8 summarize the slopes and intercepts of the low frequency ($T_2^{-1} \propto \omega$) data points taken at various orientations, and at X = 0.1, 0.2 and 0.4 respectively. Note how the slope is 2 to 3 times larger at $\beta = 0^o$ than at $\beta = 90^o$. The intercept is also strongly dependent on the orientation, it being significantly smaller at 0^o than at 90^o at all coverages. As the angle β is increased so is the frequency at which the data is first seen to depart from the linear dependence. For β greater than about 45^o the linear dependence is obeyed at all frequencies investigated.

The frequency dependence in T_1 was much weaker than in T_2, it being some 50% larger at 7.5MHz than at 2.6MHz. T_1 is approximately

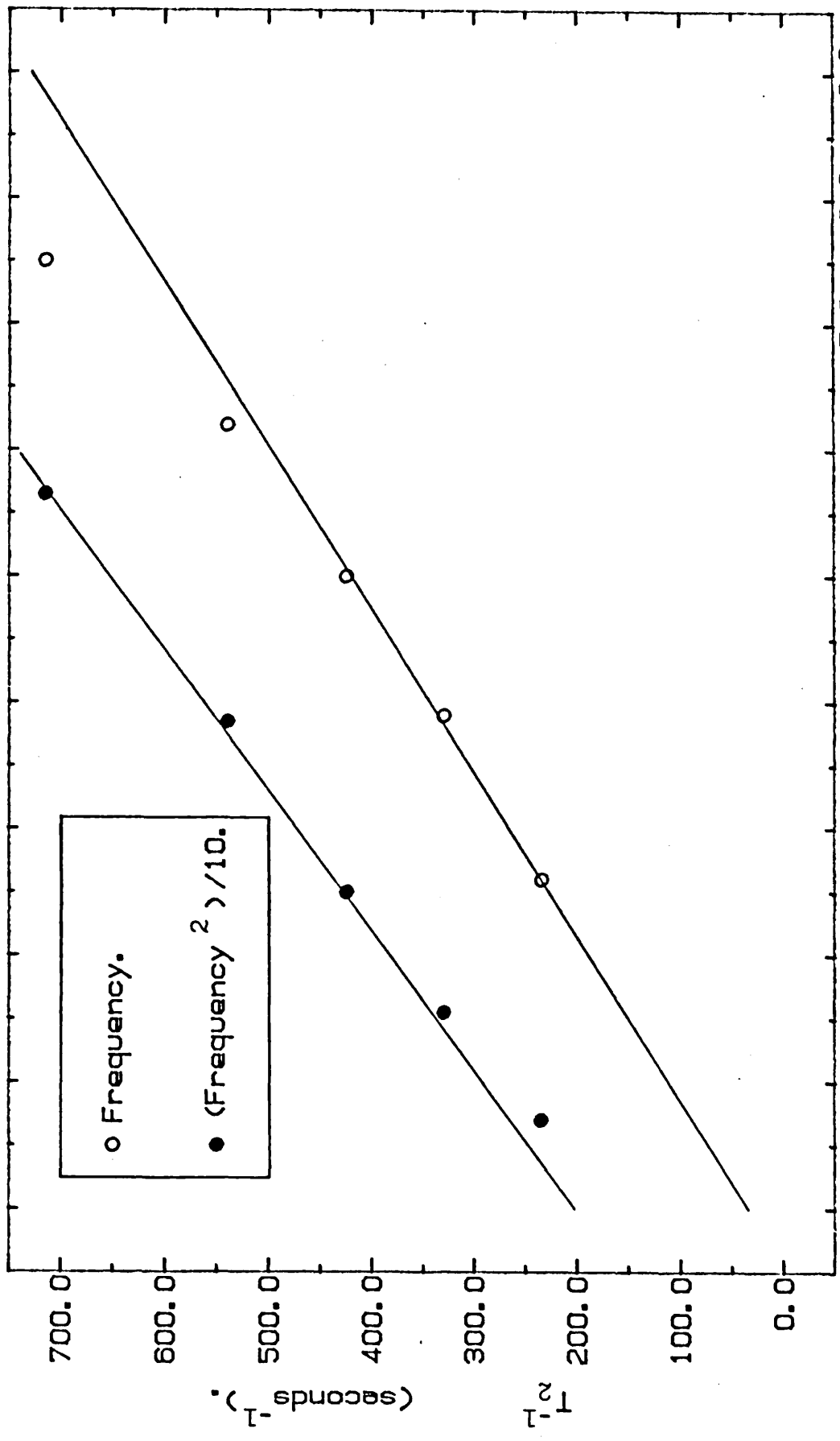

Figure 7.15. T_2^{-1} As A Function Of Larmor Frequency For Helium-3 On Grafoil. X=0.1, β= 0 Degrees & Temperature=1.2K.

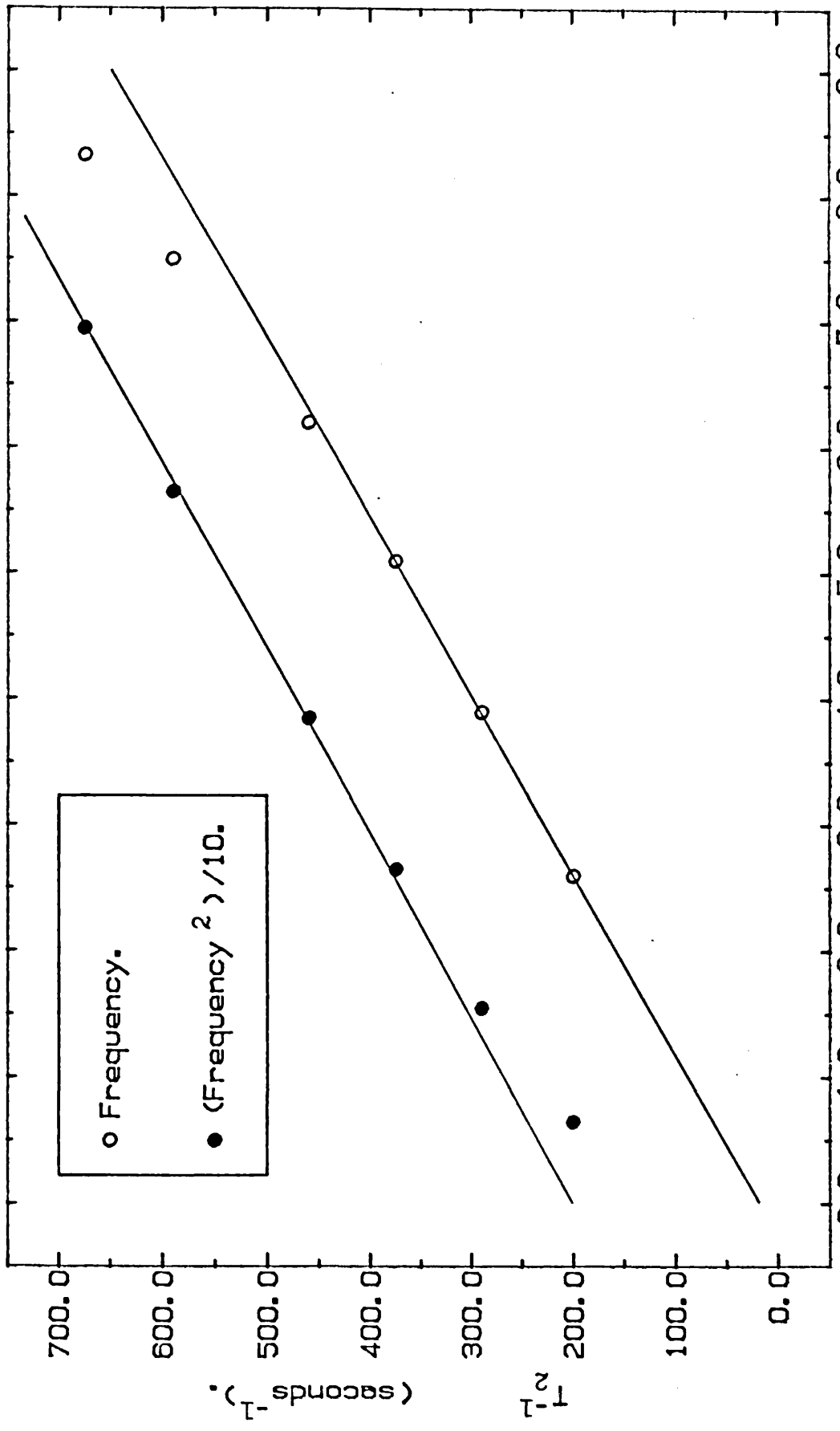

Figure 7.16. T_2^{-1} As A Function Of Larmor Frequency For Helium-3 On Grafoil. X=0.3, β= 0 Degrees & Temperature=1.2K.

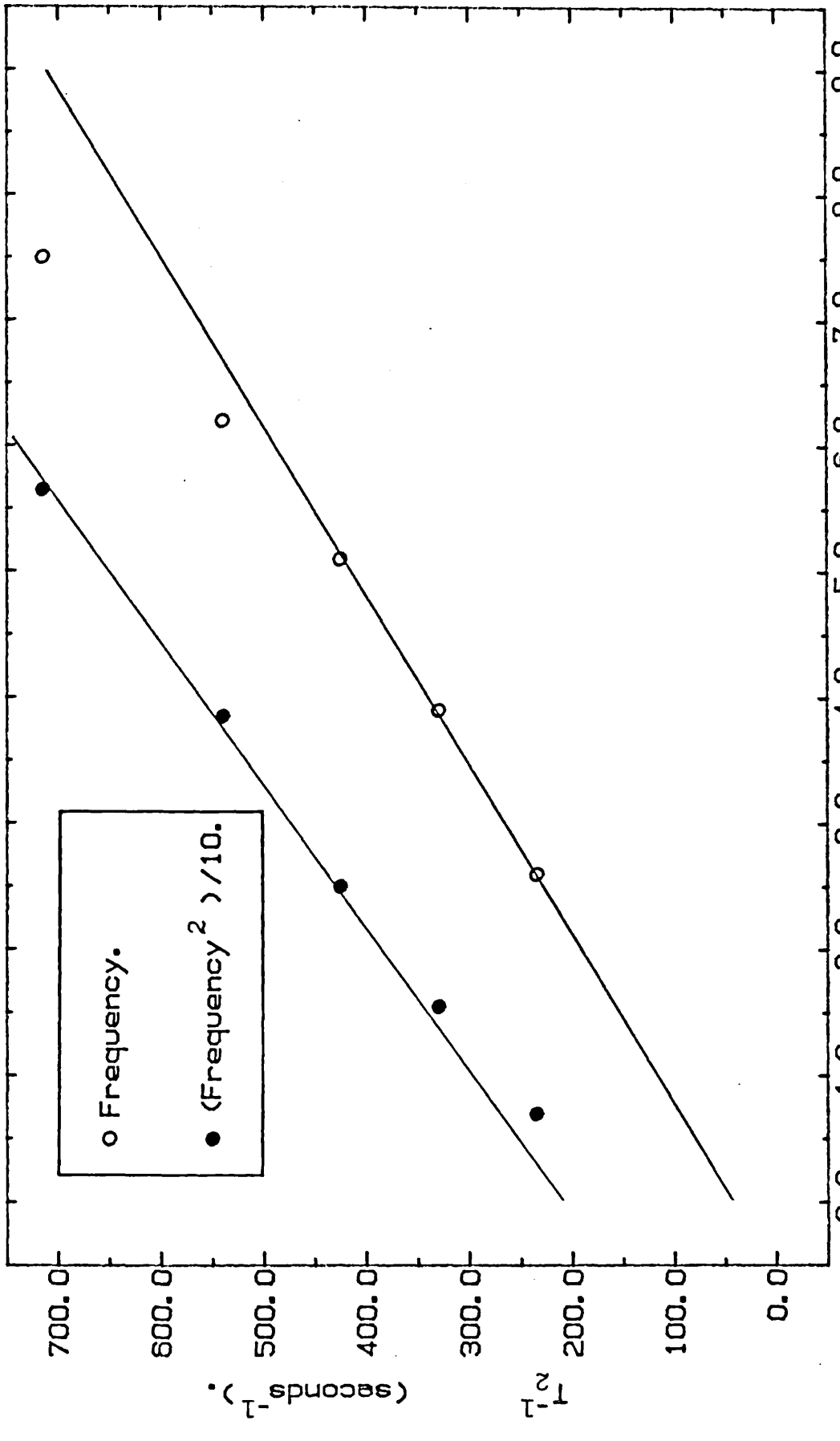

Figure 7.17. T_2^{-1} As A Function Of Larmor Frequency For Helium-3 On Grafoil. X=0.4, β = 0 Degrees & Temperature=1.2K.

Table 7.6 Slopes and intercepts of frequency dependence at X = 0.1

β	Slope	Intercept
0	86.8 ± 7.54	-6.16 ± 35
9	82.8 ± 1.97	-3.98 ± 9.1
18	77.4 ± 7.23	-7.08 ± 33.4
27	70.1 ± 6.01	8.49 ± 27.8
36	58.0 ± 1.48	22.3 ± 6.8
45	53.05± 2.7	22.4 ± 12.3
54	48.0 ± 3.1	15.6 ± 14.2
63	39.5 ± 1.8	35.8 ± 9.6
72	30.3 ± 2.5	50.2 ± 13.3
81	31.5 ± 2.4	42.4 ± 12.7
90	30.7 ± 0.81	36.8 ± 4.3

Table 7.7 Slopes and intercepts of frequency dependence at X = 0.3

β	Slope (ω)	Intercept
0	71.8 ± 0.7	11.9 ± 3.1
9	66.2 ± 2.1	28.0 ± 9.6
18	69.5 ± 3.9	3.40±18.1
27	63.6 ± 2.7	6.3 ±12.6
36	55.5 ± 5.2	12.8 ±24.4
45	47.6 ± 1.7	19.3 ± 7.9
54	37.5 ± 2.0	30.4 ± 9.3
63	32.2 ± 2.0	30.7 ± 9.3
72	27.5 ± 0.63	31.8 ± 2.9
81	25.5 ± 0.55	33.0 ± 2.9
90	25.3 ± 0.85	29.6 ± 4.5

Table 7.8 X = 0.4

β	Slope (ω)	Intercept
0	76.5 ± 1.6	15.3 ± 6.1
45	52.8 ± 1.5	19.1 ± 8.5
90	30.1 ± 0.2	28.6 ± 1.1

linearly dependent on frequency, figure 7.18, but the intercept is not at the origin as found with the Mylar substrate, see Ch. 6. The results shown in figure 7.18 were taken at $X = 0.3$, $\beta = 90^{o}$ and a temperature of 1.2K, and are typical of those taken at all other coverages/orientations/temperatures.

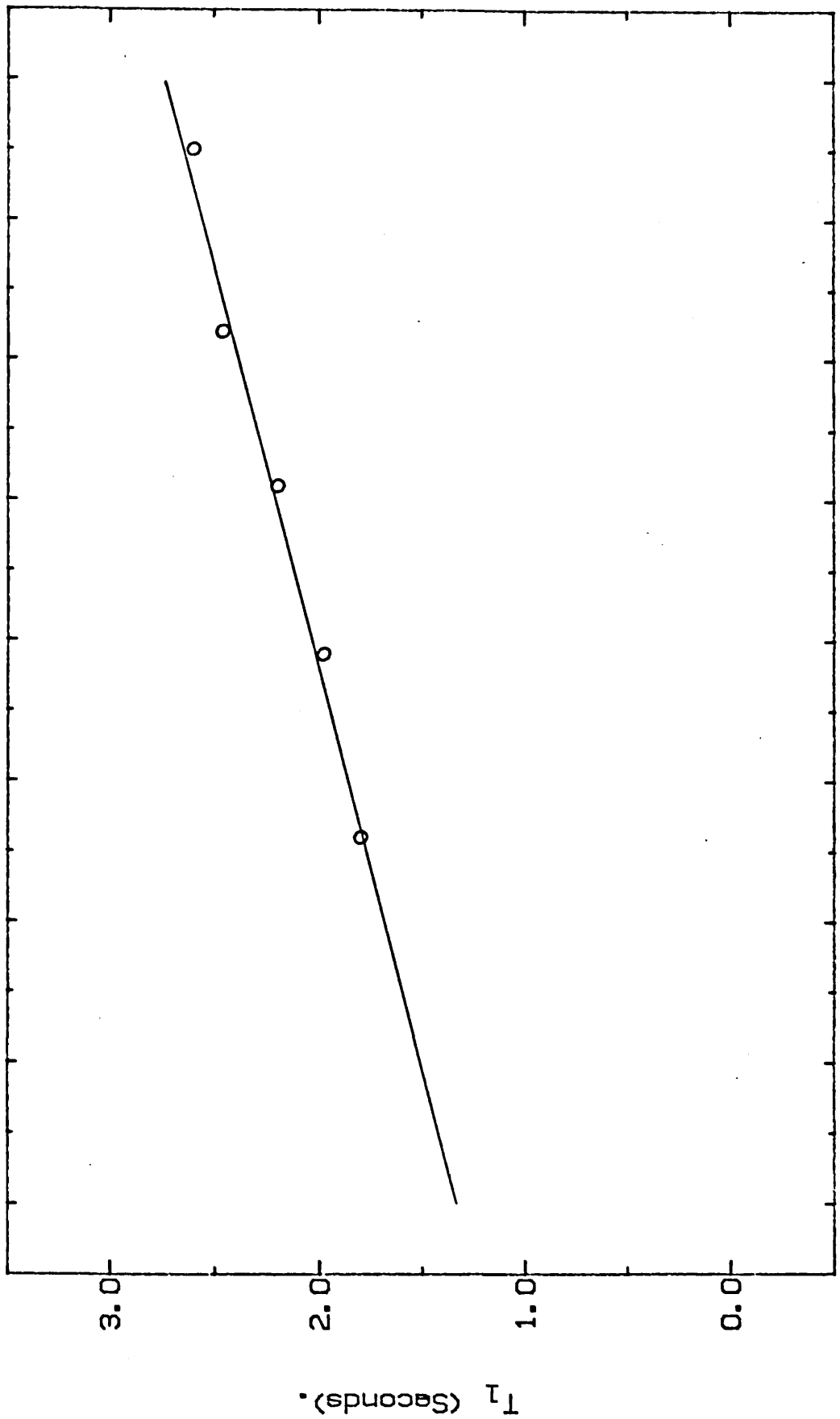

Figure 7.18, T_1 As A Function Of Larmor Frequency For Helium-3 On Grafoil. X=0.3, β=90 Degrees & Temperature=1.2K.

CHAPTER 8
THE NMR PROPERTIES OF HELIUM-3 ADSORBED ON GRAFOIL, 0.1 < X < 0.6 ANALYSIS AND DISCUSSION OF RESULTS

8.1 Spin Lattice Relaxation

The values of T_1 measured, of the order seconds, are much too short to be attributed to dipolar processes within a 2-D diffusive fluid - for X = 0.3 and T = 1.2K the time τ_d in eq. (2.7.5) is given by,

$$\tau_d = \frac{a^2}{2D} = 4Xa\sqrt{\frac{m}{2kT}} = 4.8 \times 10^{-12} \text{ sec}$$

for an orientation, $\beta = 90^o$ we obtain an estimate of $T_1 \simeq 1000$ seconds!. One possible interpretation is that the solid patches, which were discussed in connection with the very low coverage T_2 results in Chapter 6, mediate T_1 in the same way as they do T_2. This is consistent with the observed increase of T_1 with coverage, figure 7.14. The very slight increase of T_1 with temperature suggests that we may be looking at the high frequency/fast motion side of a T_1 minimum and not far from it. Therefore the characteristic frequency of the motion in the solid patches is $J \gtrsim \omega_o = \pi \times 10^7 \text{ s}^{-1}$. This figure is too fast and is inconsistent with the short T_2 values in Chapter 6. It is therefore necessary to find an alternative process to explain the T_1 values. A likely candidate is relaxation through interaction with paramagnetic impurities embedded in the Grafoil.

The relaxation time due to interaction with paramagnetic impurities is given by [29], [35],

$$\frac{1}{T_1} \simeq \frac{1}{T_1^d} \frac{\gamma_s^2}{\gamma_n^2} \frac{x_s}{X} \frac{S\ (S+1)}{I\ (I+1)} \left(\frac{a}{d}\right)^4 \qquad (8.1.1)$$

where T_1^d is the dipolar relaxation time, γ_n and γ_s are the magnetogyric ratios of the helium nuclei and the paramagnetic impurity respectively, X is the coverage, x_s represents the number of impurity atoms sufficiently close to the surface to have an effect and d is the distance separating the adatoms from the impurities. The effectiveness of this relaxation process is a result of γ_s being some 1000 times large than γ_n. Subject to all of the adsorbed oxygen being removed by the substrate heat treatment a typical estimate of the concentration of paramagnetic impurities is about 100 ppm distributed throughout the bulk of the Grafoil [14], this leads to a value of $x_s \simeq 0.02$ monolayers. Subject to the same conditions as before (X = 0.3, T = 1.2K and $\beta = 90^o$) we obtain,

$$T_1 \simeq 1 \text{ second}$$

provided that $d \sim 10\text{Å}$. This value is much closer to the measured T_1's and the required value of d is not unreasonable. This model for T_1 predicts correctly an increase in T_1 with coverage, with the rate of increase slowing down at higher coverages due to the increasing τ_d. Another feature of the results, the lack of significant anisotropy is also predicted correctly - the vectors joining the adatom nuclei and the impurities are not in the plane of the substrate as are the ^{3}He internuclear vectors.

Based on this model for spin-lattice relaxation we might expect little in the way of frequency dependence on the low frequency/fast motion side of the T_1 minimum. Looking at the results, figure 7.18 reveals that this is indeed the case. If internuclear dipolar relaxation processes were responsible for determining T_1, then in a 2-D system T_1 is expected to be proportional to frequency with the intercept at or near the origin [73].

8.2 Spin-Spin Relaxation, General Points

The measured T_2 values are all of the order milliseconds, significantly shorter than the tens of seconds predicted theoretically for dipolar relaxation in a 2-D diffusive fluid, eq. (2.7.13). This is no surpise, it has long been supposed that the dominant relaxation process in the fluid phase is relaxation through diffusion in the Grafoil local fields, see §1.3. However, difficulty in interpretation arises because the current theory of relaxation in Grafoil local fields, see §2.9, predicts that the relaxation rate T_2^{-1} is proportional to the square of the field or Larmor frequency, while most of the experimental results indicate a linear dependence. Furthermore, the theory also predicts a $\cos 4\beta$ angular dependence but the data follow a $\cos 2\beta$ form. So both the frequency dependence and anisotropy results seem to contradict the naive assumption - that is the relaxation rate is proportional to the mean square local field variation.

An estimate of the expected value of T_2 may be obtained using eq. (2.9.2), eq. (2.9.5) being used to calculate the mean square local field variation $\langle \Delta\omega^2 \rangle / \gamma^2$. To do this it is first necessary to find the rms mis-orientation δ of the Graphite platelets in our sample of Grafoil. This may be deduced from the frequency shift data, §7.6. If the platelets were all perfectly aligned in the plane then the component of the field parallel to the external field B_o, within the cylindrical sample is given by,

$$B' \simeq \left(1 + \frac{\chi_c \cos^2\beta}{2}\right) B_o \qquad (8.2.1)$$

where χ_c is the c-axis susceptibility of the graphite, (corrected for the lower density of Grafoil compared with natural Graphite) and β is the angle between the c-axis (which is normal to the substrate plane) and B_o,

$$\therefore \quad \Delta B \simeq \frac{\chi_c B_o}{2} \cos^2\beta \qquad (8.2.2)$$

Now the overall effect of the spread in orientations of the graphite platelets in the Grafoil is to bring about a reduction in ΔB. Assuming a Gaussian spread of orientations within the plane with RMS value δ , and averaging.

$$\overline{\Delta B} = \frac{\chi_c B_o}{2} (1 + e^{-2\delta^2} \cos 2\beta) \qquad (8.2.3)$$

This gives the $\cos 2\beta$ angular dependence as seen in figure 7.11. The total frequency shift in going from $\beta = 0$ to 90^o is then given by,

$$\frac{\Delta\omega}{\omega} = \frac{-470}{5 \times 10^6} = \frac{\chi_c}{2} \exp - 2\delta^2 \qquad (8.2.4)$$

At temperatures less than the Fermi temperature of Graphite, 520K [31] , χ_c = - 0.00025 MKS units per unit volume, therefore

$$\delta = 23^o$$

Putting this into eq. (2.9.5) and using eq. (2.9.2), gives for $\beta = 90^o$, X = 0.3 and T = 1.2K,

$$T_2^{-1} \simeq 1.5 \times 10^{-17} \omega_o^2 \qquad (8.2.5)$$

Hence, at an NMR frequency of 5MHz, $T_2 \simeq 70$ seconds, the same order of magnitude as the internuclear dipolar relaxation time and much longer than the experimental results. Evidently there is another, dominant, relaxation process some possible sources of which are as follows :

(i) The solid patches which had a considerable effect on the relaxation at very low coverages may still be mediating T_2 at these higher coverages. At X = 0.015 all of the adsorbate is in the solid patches and $T_2 \simeq 370\mu s$, therefore using the augmentation factor $^{X}/_{x}$ gives at X = 0.3 $T_2 \simeq 7.4ms$ which is the same order of magnitude as the experimental results. It might at first be thought that this also explains the linear frequency dependence, since for a solid $T_2^{-1} \propto \langle \Delta\omega_z^2 \rangle^{1/2}$. However, it must be remembered that we are measuring the echo relaxation, and for times short compared to the time taken by a spin to diffuse the correlation length of the local fields the echo decay goes as e^{-At^3} where the coefficient A is proportional to $\langle \Delta\omega_z^2 \rangle$.

(ii) While considering the demagnetizing field of the graphite platelets in §2.9 we did not consider the effects of the platelet edges, in the vicinity of which we might expect the local fields to be stronger than they are elsewhere. Then the major contribution to the relaxation of a spin is the field it experiences as it traverses plate boundaries, similar effects are likely at the edges of the areas of uninterrupted basal planes. The relaxation will be dependent on how long it takes for a spin to diffuse to one of these regions, the length of time it takes to cross it (if the region is small this will be ballistically) and the strength of the field there.

(iii) As well as the oriented platelets Grafoil contains particles of graphite "dust" and some large randomly oriented crystallites [78]. The local fields in the proximity of these can be expected to be at least an order of magnitude stronger than those associated with the oriented platelets due to the larger shape factors. A reasonable estimate of the average distance between these defects is that it is approximately equal to the typical size of a platelet $\sim 10^{-6}$m. Assuming a shape factor S ≃ 2/3 and bearing in mind that these graphite crystals are randomly oriented, i.e., the r.m.s. spread of orientation is large. Then, using eq. (2.9.2) gives $T_2 \simeq 7 \times 10^{-14}\ \omega_o^2$ sec. Therefore at an NMR frequency of 5MHz T_2 = 14 milliseconds. This figure is comparable to the results, however, an ω_o^2 dependence is still to be expected and no angular dependence is predicted.

8.3 The Frequency Dependence

8.3a Intercepts of T_2^{-1} vs ω_o,

The frequency independent or dipolar contribution to the relaxation is given by the zero frequency intercept on the T_2^{-1} vs ω_o graphs. These intercepts are plotted as a function of coverage in figure 8.1. The original data being recorded at $\beta = 90^o$ and T = 1.2K. Note the large errors associated with the determination of the intercepts. There is a well defined maximum in the value of the $(\text{intercept})^{-1}$ at X ≃ 0.35. The value of T_2^d corresponding to the maximum is approximately 35ms, still far too short for a 2-D diffusive fluid. At this coverage and temperature eq. (2.7.13) gives $T_2 \simeq 50$ seconds. What we are probably seeing is the effect of the solid patches as discussed in Chapter 6, this explains the increase of T_2^d with coverage for X < 0.35. The turnover at higher coverages

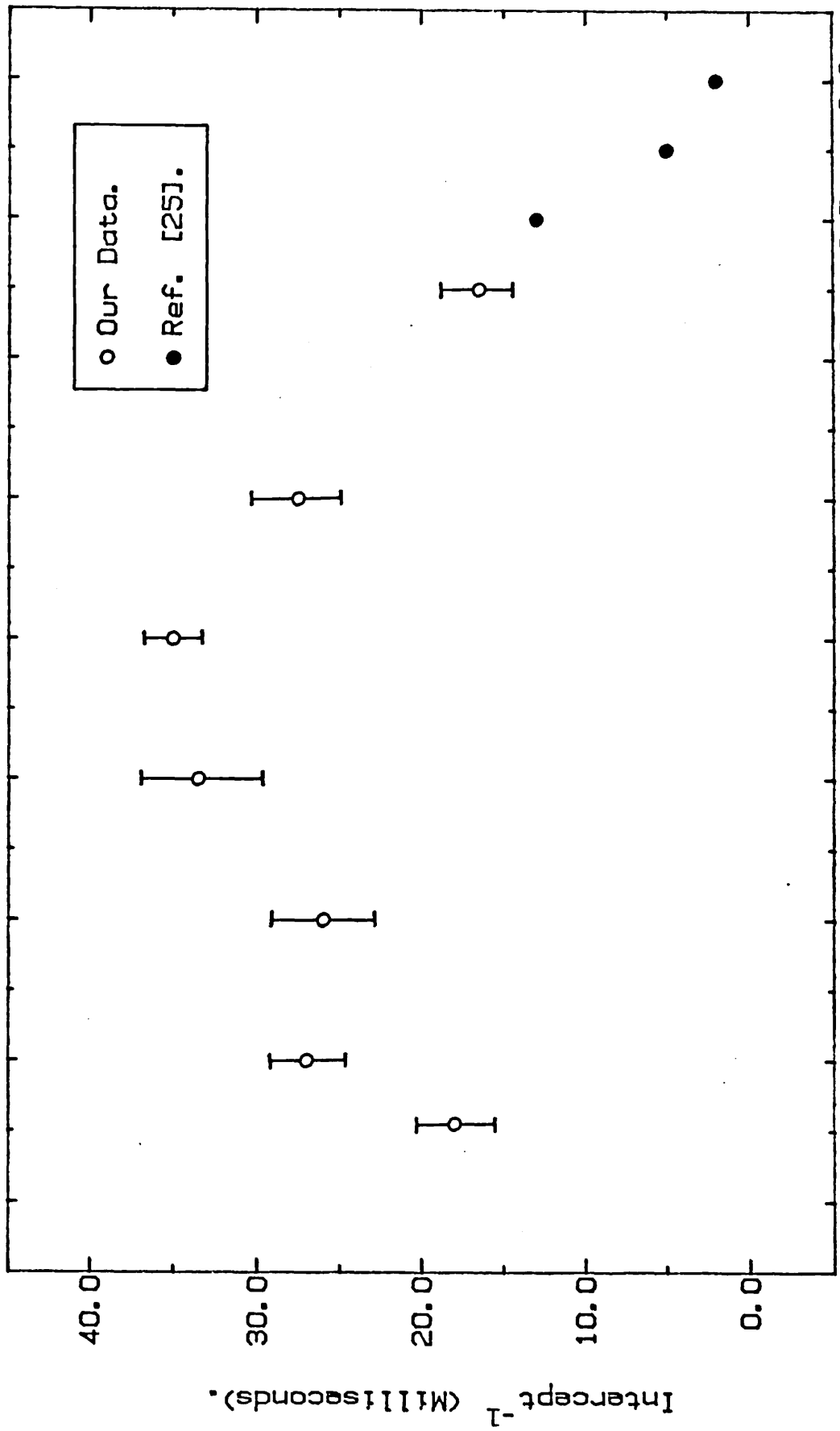

Figure 8.1. Intercepts Of T_2^{-1}-vs-Larmor Frequency Results, As A Function Of Coverage. β=90 Degrees & Temperature=1.2K.

might be due to growth of the solid patches due to increased lateral pressure and reduced motion. The three points at coverages extending into the solid phase are from [25], they appear to follow the trend well. This smooth transition into the solid phase suggests that solidification may take place by growth of the solid patches.

As the temperature is increased the intercept moves towards the origin i.e. T_2^d increases. This is simply due to the break up of the solid patches at the higher temperatures.

The anisotropy in the intercept is rather difficult to interpret at small angles the intercept appears to become negative at some coverages, see table 7.6. A negative relaxation rate is unphysical, this result is probably a consequence of fitting a straight line to the quadratic form. Directly fitting the expression $T_2^{-1} = A + B + C\omega^2$ to the X = 0.3, $\beta = 0^o$ data gives a zero frequency value $T_2^d \simeq 13.5$ms. This degree of anisotropy is consistent with theory for a 2-D solid with internal motion, as it should be if the solid patches mediate the frequency independent contribution to the relaxation.

8.3b Slopes of T_2^{-1} vs ω_0

At small angles β the slope is not well defined because the data neither follows a strict linear or square frequency dependence. At all other orientations a good linear dependence is observed regardless of temperature or coverage. The slopes of the $\beta = 90^o$, T = 1.2K data are plotted as a function of coverage in figure 8.2. At coverages X > 0.8 where all of the adsorbate is a relatively immobile high density solid the slope becomes very small. We associate the dramatic decrease for X > 0.65 with the solidification of the film.

In the region 0.05 < x < 0.65 it is expected that provided

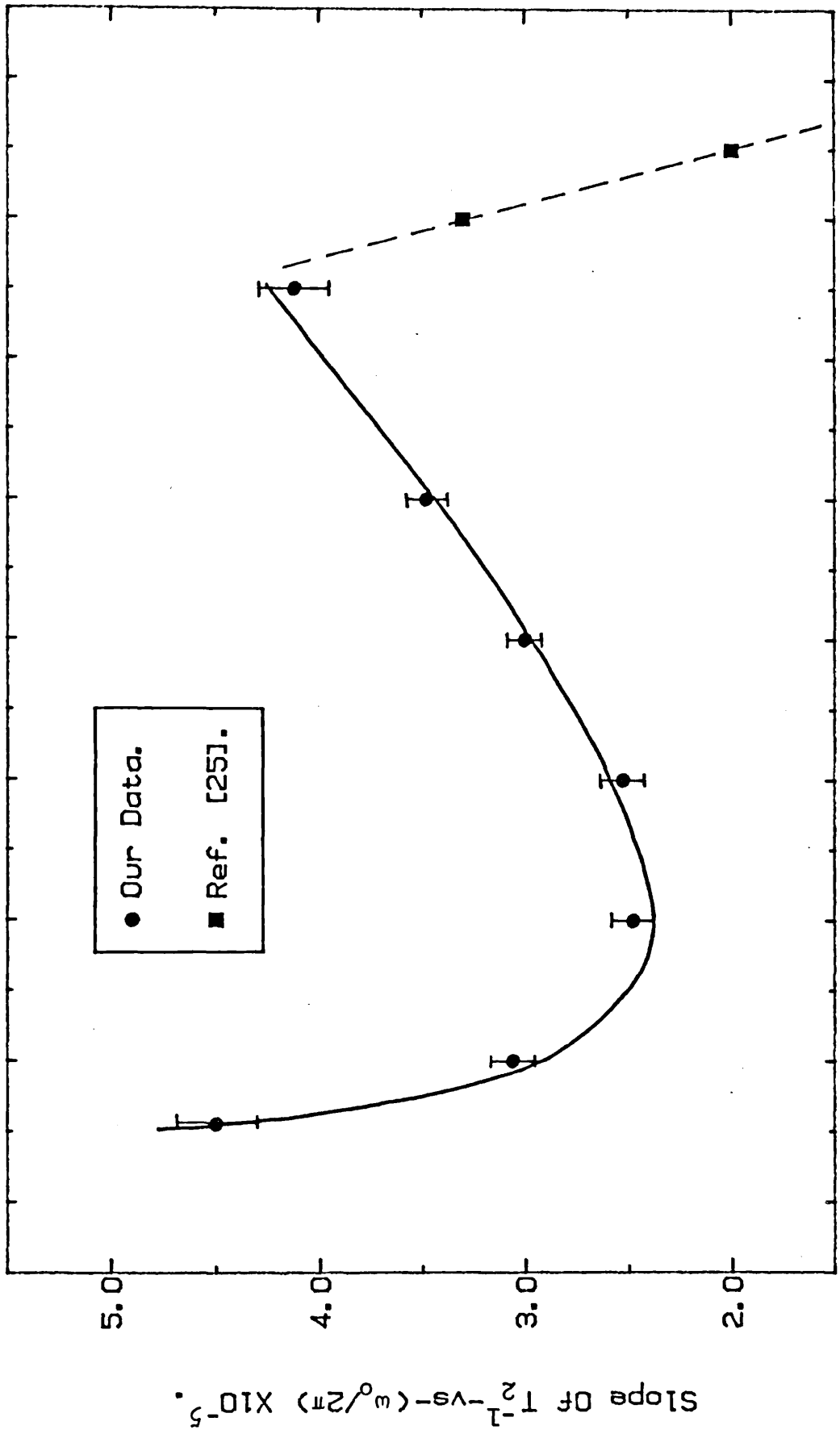

Figure 8.2, Slope Of T_2^{-1}-vs- Larmor Frequency, As A Function Of Coverage. β=90 Degrees & Temperature=1.2K.

we were in the motional narrowing regime ($\langle\Delta\omega^2\rangle^{1/2} a^2/D) < 1$, as the coverage is reduced and the motion within the fluid phase increases there would be better averaging of the local fields and hence a monotonic decrease in the values of the slope. What is in fact seen is a reduction in going from X = 0.65 to X = 0.25, the dependence being approximately linear, but then for X < 0.25 a rapid increase. The solid line through the data is given by,

$$(\text{Slope}) = \frac{A}{X} + BX \qquad (8.3.1)$$

where $A = 0.24 \times 10^{-5}$ and $B = 5.94 \times 10^{-5}$. A possible explanation for this is as follows: We already know that the solid patches show some frequency dependence, see §6.4, now assuming that this is linear with slope S (this is not an unreasonable assumption bearing in mind the generality of the linear frequency dependence) then at a coverage X this slope is decreased by a factor $^{x}/_{X}$ where x is the solid fraction. Hence we have a contribution to the overall slope at a coverage X of xS/X. The fluid part of the adsorbate also contributes to the frequency dependence, the slope being proportional to the correlation time τ_c which for a 2-D fluid is given by,

$$\tau_c = \frac{a^2}{2D} = 4Xa\sqrt{\frac{m}{2kT}} \qquad (8.3.2)$$

So by combining these two contributions we obtain for the slope of the frequency dependence at coverage X,

$$(\text{Slope}) = \frac{xS}{X} + BX \qquad (8.3.3)$$

B is a constant. This expression is the same as eq. (8.3.1) if we put A = xS. Now x = 0.015 and $A = .24 \times 10^{-5}$ hence the slope S of the frequency dependence in the solid phase is 1.6×10^{-4}. For

$X < 0.015$ and 5MHz this represents a contribution to T_2 of about 1.2ms it is in good agreement with the result obtained at $X = 0.01$.

It is clear from the results in tables 7.6 - 7.8 that the frequency dependence gets stronger as β is reduced. We expect that the local fields are going to be stronger as the angle between the graphite c-axis and the field is reduced. However, the slope should be proportional to the variations in local field experienced by a spin as it moves on the surface which are not very orientation dependent.

8.4 The Temperature Dependence

At an NMR frequency of 1MHz, T_2 was found to be proportional to the square root of temperature over the range $T = 0.5K$ to $T = 5K$, [25]. This is to be expected for a 2-D diffusive fluid motionally narrowing whatever local fields, $T_2 \propto \tau_c^{-1} \propto \sqrt{T}$. Results taken at 10MHz, [29] were found to show little temperature dependence between 1.2 and 4.2K except for a small peak near 3K. Perhaps not surprisingly, therefore, our results taken at intermediate frequencies display intermediate behaviour. At low temperatures T_2 is approximately proportional to $\sqrt{T}$ while at higher temperatures it levels off.

If only a single relaxation process were involved this behaviour would only be possible if there is a temperature above which motion in the film no longer increases - highly unlikely. There must therefore be at least two processes. The motional narrowing process dominant at low temperatures giving $T_2 \propto \sqrt{T}$ is shorted out at higher temperatures by a temperature independent process. This interpretation is consistent with the non-exponential relaxation seen at the higher temperatures. We define a turnover temperature as the point on the temperature scale where the lines extrapolating the low temperature data to higher temperatures and the high temperature data to lower

temperatures intersect. Table 8.1 shows how this temperature varies with coverage; note the minimum around X = 0.3, the increase at lower coverages being much faster than at higher coverages - a similar trend to that seen in the slopes of the frequency dependence. In table 8.2 we see the variation with frequency of the turnover temperature, the increase with decreasing frequency below 5.1MHz is consistent with no levelling off being observed at 1MHz. Table 8.3 shows how this temperature depends on substrate orientation, the change is only small but the temperature seems to decrease as β is reduced.

8.5 The Anisotropy

The relaxation rate was found to show a $\cos 2\beta$ angular dependence with $T_2(90)/T_2(0) \simeq 2.3$ regardless of coverage. The anisotropy changed little with variations in temperature or frequency. This is to be expected because for relaxation in substrate local fields the anisotropy should depend only on the structure of the substrate surface. It is notable that the expression $T_2^{-1} = (A + B\cos 2\beta)$ fits the data so well. This angular dependence suggests that the relaxation rate might be proportional to the mean local field variation which, based on the present model for the Grafoil surface, we would expect to have a $\cos 2\beta$ angular dependence. This would also explain the linear frequency dependence. Unfortunately though, it is not hard to see that the mean local field variation is going to be zero.

8.6 Conclusions

The T_1 results can be described quite well in terms of the relaxation being due to dipolar interactions with a small number of paramagnetic impurities embedded in the Grafoil.

The spin-spin relaxation may be split into two components,

Table 8.1

Turnover temperature at various coverages, $\frac{\omega_o}{2\pi}$ = 5.1MHz, $\beta = 90^o$

Coverage, X	Temperature (K)
0.055	3.8 ±.2
0.1	3.1 ±.15
0.2	2.3 ±.1
0.3	2.17 ±.1
0.4	2.25 ±.15
0.5	2.5 ±.15
0.55	3.0 ±.4

Table 8.2

$\frac{\omega_o}{2\pi}$ = 5.1MHz and X = 0.4

$\omega_o/2$ (MHz)	Temperature (K)
2.6	2.75 ±.1
5.1	2.25 ±.15
7.5	2.5 ±.15

Table 8.3

$\frac{\omega_o}{2\pi}$ = 5.1MHz and X = 0.3

Degrees	Temperature (K)
90	2.17 ±.1
45	1.9 ±.15
0	1.8 ±.25

one of which is frequency dependent and the other frequency independent. The latter contribution is due to the dipolar component of the relaxation of the solid patches described in Chapter 6. The dominant, frequency dependent, contribution has proved impossible to interpret in terms of the current ideas. One thing we can say is that the frequency dependence is due to some sort of substrate local magnetic fields. Although an ω_o^2 frequency dependence is then expected, the linear dependence has been shown to persist over a wide range of conditions.

One of the more intriguing features of the results is that while some of them, the $\sqrt{T}$ dependence at low temperatures and the coverage dependence, suggest the motional narrowing of local fields is taking place. Other results, the frequency and orientation dependence suggest to the contrary.

Clearly the conclusion that relaxation is due to bounded diffusion in a field gradient set up by the anisotropic diamagnetism of the graphite, which was based on insufficient experimental data and incorrect calculation of the likely strengths of Grafoil local fields, needs substantial modification. We do not at present have any alternative explanation for the results, and it would appear that before we can find one a more realistic model to explain the magnetic properties of Grafoil will have to be developed.

CHAPTER 9

SUMMARY AND PROJECTIONS

9.1 Summary of this work

A versatile and high performance NMR spectrometer system has been developed and used to study the properties of Helium-3 adsorbed on Mylar film and Grafoil.

Mylar film was found to be a planar and non-magnetic substrate. Unfortunately there proved to be a large surface heterogeneity, providing areas of preferential adsorption amounting to about 10% of the total area. This we deduced from the fact that the adsorbate was found to consist of two distinct phases, one in which the adatoms are mobile on the surface, the other in which they form in clumps of relatively immobile solid. The adsorbed film displayed NMR behaviour characteristic of dipolar relaxation in 2-D systems, i.e. $T_1 \neq T_2$ and $T_1 \propto \omega_o$ on the fast motion/low frequency side of the T_1 minimum, also the anisotropy in T_2 with respect to the orientation of the substrate in the field.

The properties of Helium adsorbed on Grafoil (exfoliated graphite) were studied throughout the range $0.005 \lesssim X \lesssim 0.65$. The very low coverage results, $X < 0.1$, were found to be dominated by the effect of high density solids formed at areas of preferential adsorption on the substrate - just like in the case of Mylar film except that a much smaller proportion of the Grafoil surface displays such heterogeneity (about 1.5%). At the higher coverages this effect was shorted out by the relaxation of the bulk of the adsorbate in the substrate local fields. The expected frequency and angular dependence were not seen. In fact the observed linear frequency dependence was shown to persist over a wide range of conditions. The precise mechanism for relaxation we still do not understand. However, for the first time sufficient accurate and detailed data has been obtained

to at least empirically characterize some aspects of this relaxation process, and to motivate and encourage a new theoretical study of it.

9.2 Comparison With the Work of Others

It is important to compare, where possible, our results and conclusions with those obtained independently by other groups. This has already been done in places, e.g. when considering the temperature dependence of T_2 in §8.4.

There has been no NMR study of the properties of Helium adsorbed on Mylar film prior to this work. A limited thermodynamic study was carried out [18] the results of this have been commented on in Chapters 1 and 5.

A number of independent NMR studies of submonolayer Helium on Grafoil have been conducted, see Chapter 1. Two of the most extensive were carried out by the Sussex University group [25], [76], and the Japanese group Satoh and Sugarawa [29], to which regular references have been made throughout the work.

In the very low coverage regime, the Sussex group found that T_2 increased with coverage up to $X \sim 0.2$ as we have, but the lowest coverage investigated in their case was $X = 0.03$ - too high for the levelling off of T_2 to be observed.

The Japanese group did not present much data for coverages less than approximately 0.5. That which they did tends to agree qualitatively with our results. However, even when the frequency difference is taken into account, quantitative agreement between our respective sets of results is poor. The anisotropy results are a good example. At $X = 0.38$ a frequency of 10 MHz and a temperature of 4.2K their results, displayed an approximate $\cos 2\beta$ angular dependence with a total anisotropy as measured by $T_2(90)/T_2(0)$ being equal to about 1.7. Our results for $X = 0.4$, a frequency of 5MHz

and a temperature of 1.2K also display a $\cos 2\beta$ angular dependence but $T_2(90)/T_2(0) \simeq 2.3$. Now, we observed that when the temperature and frequency were increased then, if any change was noticeable, the anisotropy increased slightly. So taking this into account we see that our results display a significantly greater anisotropy than those of the Japanese group. Such differences can be put down to the use of different samples of Grafoil by our two groups. In this range of coverages the substrate properties have a profound effect on the NMR properties of the adsorbed film.

It just so happens that our Grafoil sample was previously used by the Sussex group so we expect our results to agree quantitatively with theirs. They picked out the coverage X = 0.3 for particular attention. Where they found at T = 1K and $\beta = 90^{\circ}$ a linear frequency dependence between 0.3 and 2 MHz, with a slope of 28×10^{-6} and an intercept of 0.038 ms^{-1}. These figures are in excellent agreement with our values, slope = 25×10^{-6} and intercept = 0.034 ms^{-1}. Their T_2 - vs - $\sqrt{T}$ results at X = 0.3, a frequency of 1 MHz, and $\beta = 90^{\circ}$ have a slope of 17 ms $k^{-1/2}$ while we would expect, based on our results extrapolated to lower frequencies, a slope of 23 ms $k^{-1/2}$. These figures do not agree that well, however, at the higher frequencies we have the added complication of the apparently temperature independent component of T_2.

As far as T_1 is concerned we all managed to obtain values between 1 and 10 seconds but there are some differences between us regarding the temperature dependence. The Sussex group claim to have observed a $T_1 \propto \sqrt{T}$ relationship at low coverages. Our results display a somewhat weaker temperature dependence, as do those of the Japanese group. We do, however, all agree on there being no significant anisotropy or frequency dependence in T_1. There is some difference between our various groups as to the precise mechanism for spin-lattice relaxation. The Sussex group talk in terms of there being

some sort of "deep centres" at which relaxation takes place. The Japanese group opt for paramagnetic impurities as the explanation, as we do, except that they believe that the relaxation takes place in the solid patches.

It is difficult to make similar comparisons with some of the other published material [26], [27], [77] for the following reasons : The other data was taken at high frequencies where severe RF heating of the sample affected the results. The substrate preparation techniques vary widely between the different groups as do the sample annealing procedures. And finally, very little data has been taken at low coverages ($X < 0.5$). Grimmer and Lusczynski [77] found $T_2 \simeq 1$ms at $X \simeq 0.3$, $T = 1.2$K and a frequency of 20 MHz they also reported that T_2 approximately doubled when the frequency was halved to 10 MHz, indicating that the linear frequency dependence extends to much higher frequencies. Extrapolating our $X = 0.3$ results to 20 MHz predicts $T_2 \simeq 2$ms this difference may be attributed to the different Grafoil samples used.

9.3 Projections for Future Work

What follows now is a short list of suggestions for future study.

(a) A new theoretical approach to the problem of relaxation in Grafoil local fields is desperately needed. This will require the development of a new model for the magnetic properties of the Grafoil surface which in turn may call for further information on the structure of Grafoil. Various avenues worth exploring are, the effects of plate and basal plane edges, dust and randomly oriented crystallites, and the solid patches.

As a result of this work there is now sufficient accurate experimental data to assist such a study. However, as work proceeds even more experimental data may be called for.

(b) The work on Mylar film could be improved in two ways, firstly, it may be worth trying to pre-plate the surface with ^{4}He or a heavier noble gas to fill in the preferential adsorption sites. Secondly, the Mylar sheets might be spaced apart to avoid problems associated with contact between adjacent layers. This second improvement will demand the use of a low temperature pre-amplifier to make up for the lost signal, there being no room for improvement in the present electronics.

(c) Further work with other alternative substrates should be carried out to find a non-magnetic planar substrate without the severe surface heterogeneity of Mylar film. A possible candidate is wafers of a semiconductor material e.g., Si.

(d) To find out exactly how paramagnetic impurities affect spin-lattice relaxation in 2-D systems controlled doping of the substrate with known impurities could be carried out prior to T_1 measurement.

(e) It has been demonstrated in this work that measurement of the frequency and orientation dependence of the relaxation times gives valuable extra insight into the relaxation processes and hence the properties of the system. It is well worth applying these techniques in detail to the registered phase of ^{3}He on Grafoil, the incommensurate solid phase and the melting transition. With reference to this last property, the rapid change of slope of the T_2^{-1} - vs - frequency results for $X \gtrsim 0.7$ shown in figure 8.2 is well worth investigating further.

(f) Many of the published results relating to the incommensurate solid phase of ^{3}He on Grafoil where dipolar relaxation processes are predominant should be re-analysed in terms of the recent theories of NMR in two-dimensional systems.

APPENDIX 1
TEMPERATURE MEASUREMENT AND REGULATION SOFTWARE

A.1.1. Introduction

In order to illustrate the operation of the microcomputer and interface unit described in Chapter 3, what follows is a listing of the temperature measurement and regulation software. The software is split into two parts, the machine code package and the master program written in Basic. The listings include comment lines to describe their operation. In the assembly language listing comments are preceded by a semi-colon, ;. In the "Basic" program comments are preceded by the statement, REM. In the working software the comment lines are removed to speed up operation.

The I/O port addresses are tabulated below ;

	Data in†	Data out	Status in	Control out
Data	00	01	04	05
Port Control††	02	03	06	07

† In or out relative to CPU.

†† This is the address to which the PIO port control data is sent. It is this byte which configures the PIO ports to the required mode of operation.

```
; A1.2  Machine Code Package
;
;*************************************************************
;* This package of machine code routines, written in Z80     *
;* assembly language, interfaces the SHE conductance         *
;* bridge to the MPU.                                        *
;* The first section configures the I/O ports in the         *
;* microcomputer and initializes the interrupts.             *
;*************************************************************
;
; Assignments_replace a hexadecimal number with a mnemonic.
;
      BDOS    EQU   05H
      PRBUF   EQU   09H
      CR      EQU   0DH
      LF      EQU   0AH
;
PORT:                          ;Configure I/O Ports.
      ORG     7C00H            ;Starting address of routine.
      IM2                      ;Set CPU interrupt mode-2
      EI                       ;Enable interrupts.
      LD      HL,7C32H         ;Interrupt service routine
                               ;starting address.
      LD      (9000H),HL       ;Put into starting address table.
      LD      A,90H            ;High order byte of interrupt
                               ;vector.
      LD      I,A
      LD      A,01001111B      ;PIO control byte_input mode.
      OUT     (02H),A
      OUT     (06H),A
      LD      A,00001111B      ;PIO control byte_output mode.
      OUT     (03H),A
      OUT     (07H),A
      LD      A,00H            ;Low order byte of interrupt
                               ;vector, when added to high
                               ;order byte forms address of
                               ;interrupt service routine
                               ;starting address table.
      OUT     (06H),A
      LD      A,0FFH           ;Control unit main reset instruc-
                               ;tion.
```

```
      OUT     (05H),A
      LD      A,10000111B   ;Enable interrupts.
      OUT     (06H),A
;
; Put message "All port control words now sent" on monitor.
;
      LD      C,PRBUF
      LD      DE,MSG        ;Starting address of the message.
      CALL    BDOS          ;Call operating system to output
                            ;message.
      RET                   ;End of initialization procedure
                            ;return to BASIC interpreter.
;
;*************************************************************
;* The following routines are used to read in data from     *
;* the conductance bridge and to write the calculated       *
;* temperature to the display.                               *
;*************************************************************
;
ISR:                        ;Interrupt service routine.
      ORG     7C32H         ;Starting address.
      EX      AF,AF'
      EXX                   ;Exchange with auxilliary regis-
                            ;ters to save data for re-start
                            ;after interrupt.
      IN      A,(04H)       ;Read data at status port.
      CP      0FH
      JP      Z,OFLOW       ;If data is 0FH then overflow
                            ;has been detected, so jump to
                            ;overflow handling subroutine.
      LD      A,10000011B
      OUT     (06H),A       ;If not overflow ignore and
                            ;enable interrupts again.
      EX      AF,AF'
      EXX                   ;Return registers' pre-interrupt
                            ;contents.
      EI
      RETI                  ;Return from interrupt.
;
OFLOW:                      ;Conductance bridge overflow
                            ;handling subroutine.
```

```
; Put message "*BRIDGE OVERFLOW*" on monitor screen and
; sound warning siren in control unit. The operator must
; respond by changing the range on the bridge.
;
      LD      DE,MSG1          ;Starting address of message.
      LD      C,PRBUF
      CALL    BDOS
      LD      A,00001000B      ;Turn on alarm instruction.
      OUT     (05H),A
      CALL    PAUSE
      CALL    PAUSE            ;Wait a second.
      LD      A,00001001B      ;Turn off alarm.
      OUT     (05H),A
      LD      A,10000011B      ;Enable interrupts again.
      OUT     (06H),A
      EX      AF,AF'
      EXX
      EI
      RETI
;
PAUSE:                         ;Generates approx. 1/2 second
                               ;delay, using nested loops.
      LD      A,255D
LOOP1:
      PUSH    AF
      LD      A,255D
LOOP2:
      NOP
      NOP                      ;Do nothing (No Operation).
      DEC     A
      JR      NZ,LOOP2
      POP     AF
      DEC     A
      JR      NZ,LOOP1
      RET                      ;End of delay.
;
PUTDSP:                        ;Subroutine writes temperature
                               ;to digital display on resistor
                               ;selector unit.
      ORG     7C72H            ;Starting address.
```

```
        LD      HL,8000H        ;Starting address of block of
                                ;memory where temperature data
                                ;has been poke'd by the BASIC
                                ;program.
        LD      A,71H           ;Interface board reset instruc-
                                ;tion, low order four bits are
                                ;the board address.
        OUT     (05H),A
        LD      A,41H           ;Peripheral take data instruction.
        OUT     (05H),A
        LD      A,20H
        OUT     (01H),A         ;A dummy write resets peripheral
                                ;internal counter.
        LD      B,05H
LOOP3:
        LD      A,41H
        OUT     (05H),A
        LD      A,20H
        ADD     A,(HL)          ;Put digit into correct form for
                                ;display.
        OUT     (01H),A         ;Write to display.
        INC     HL              ;Get next digit on next pass.
        DJNZ    LOOP3           ;Loop to output all digits & dp.
        LD      A,71H
        OUT     (05H),A
        RET                     ;Return to BASIC interpreter.
;
RDDTA:                          ;Subroutine reads data from
                                ;conductance bridge and places
                                ;it in a region of memory where
                                ;the BASIC program can access it.
        LD      HL,8010H        ;Starting address of block of
                                ;memory used for storing temp-
                                ;erature data.
        LD      A,71H
        OUT     (05H),A
        LD      B,09H           ;Loop counter.
        LD      C,11H
LOOP4:
        LD      A,41H
```

```
        OUT     (05H),A
        LD      A,C
        OUT     (01H),A         ;Data tells interface which
                                ;"digit" we wish to read.
        LD      A,31H           ;Peripheral write data to
                                ;CPU instruction.
        OUT     (05H),A
        NOP                     ;Short pause for interface
                                ;to respond.
        IN      A,(00H)         ;Read in data.
        LD      (HL),A          ;Store in memory.
        INC     C
        INC     HL
        DJNZ    LOOP4           ;Loop to read in all data.
        LD      A,71H
        OUT     (05H),A
        RET                     ;Return to BASIC interpreter.
;
; ASCII messages now follow.
;
MSG:
        DEFM    'All port control'
        DEFM    ' words now sent'
        DEFB    CR,LF,'$'       ;Carriage return,Linefeed.
;
MSG1:
        DEFM    '*BRIDGE OVERFLOW*'
        DEFB    CR,LF,$
;
;
; This file is stored on disk as PORTSET.ZSM .  It may be
; assembled by typing ZASM PORTSET.HEX.  The resulting
; Intel format hex file may be loaded into memory using
; the CP/M Dynamic Debuging Tool, type DDT PORTSET.HEX.
; It may then be Called by the BASIC program.
;
        END                     ;End of machine code package.
```

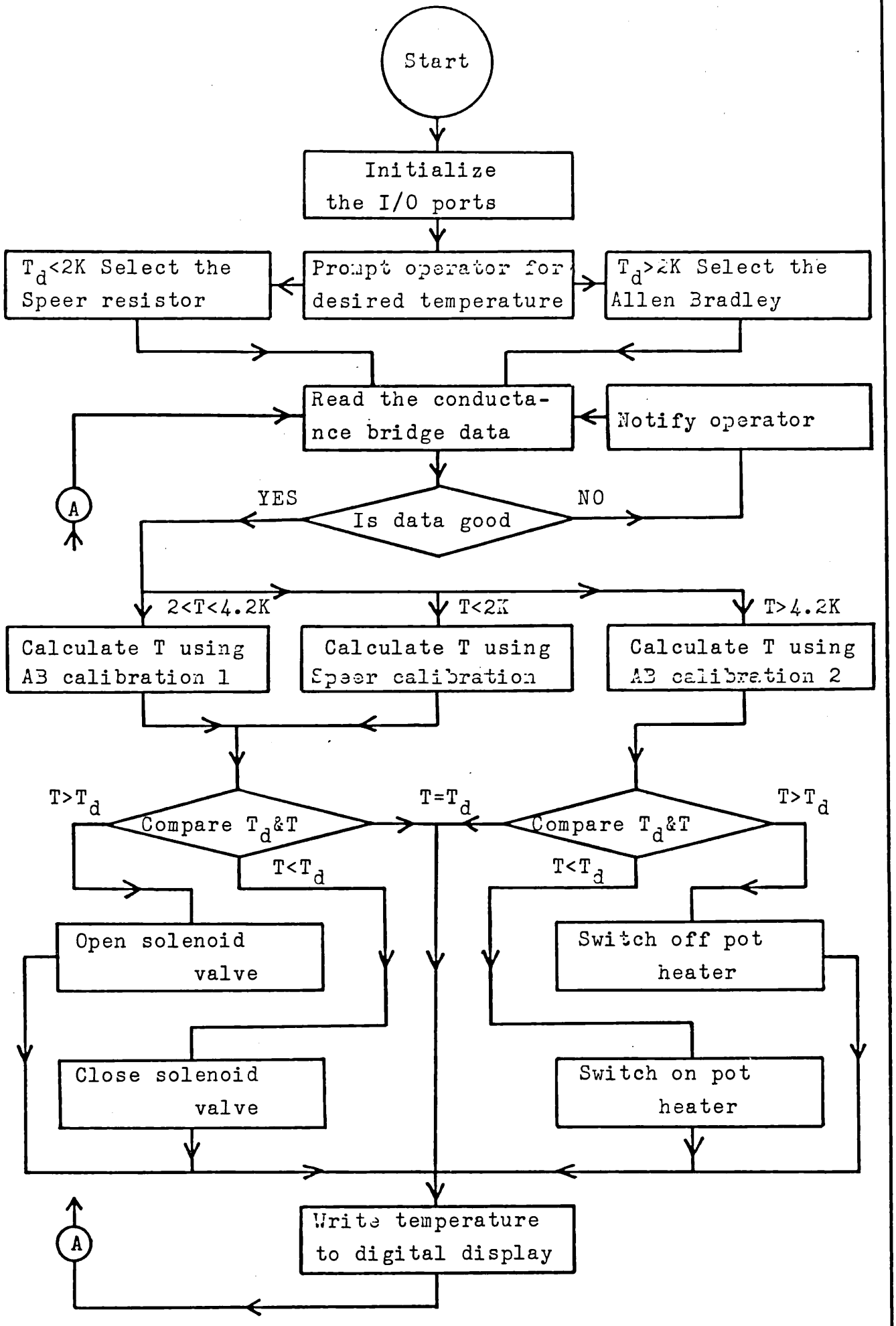

Figure A1.1, POTREG program flow diagram.

```
01 REM   A1.3 BASIC Program ("POTREG")
02 REM
03 REM  Program calculates the Helium-4 pot temperature
04 REM  using the conductance bridge data and the resistor
05 REM  calibrations.  It also takes the necessary
06 REM  action to maintain the temperature at a requested
07 REM  value.
08 REM
09 REM
10 LET K=1:REM Bad data counter.
20 CALL &7C00:REM Call machine code routine which initia-
lizes I/O ports.
30 INPUT "REQUIRED TEMPERATURE (KELVIN) ?";TR
40 INPUT "TOLERANCE (millikelvin)";TL:REM Obtain desired
pot temperature and tolerance value.
50 TL=TL/1000
60 IF TR<2 THEN GOTO 240
70 IF TR>4.2 THEN GOTO 160
80 LET FLAG=0:REM 2<T<4.2K
90 OUT 5,&41:REM Peripheral take data instruction.
100 OUT 1,&30+5:REM Select resistor data, pot AB.
110 GOSUB 320
120 GOSUB 470
130 GOSUB 1220
140 GOSUB 730
150 STOP
160             LET FLAG=2:REM T>4.2K
170             OUT 5,&41
180             OUT 1,&30+5:REM Select resistor data, pot AB.
190             GOSUB 320
200             GOSUB 470
210             GOSUB 1190
220             GOSUB 730
230             STOP
240                         LET FLAG=1:REM T<2K
250                         OUT 5,&41
260                         OUT 1,&30+4:REM Select pot SP.
270                         GOSUB 320
280                         GOSUB 470
290                         GOSUB 1250
300                         GOSUB 730
310                         STOP
```

```
320 REM Subroutine to read conductance bridge data,
330 REM it calls the machine code routine RDDTA at
340 REM location &7C94.
350 REM
360 CALL &7C94
370 REM Now check for bad data,
380 IF PEEK(&8010)>9 THEN GOTO 1280
390 IF PEEK(&8017)=1 THEN LET J=2
400 IF PEEK(&8017)=2 THEN LET J=6
410 IF PEEK(&8017)=4 THEN LET J=4
420 LET J=8
430 FOR N=0 TO J:REM Pause for a time comparable to the
conductance bridge time constant.
440 CALL &7C63:REM Machine code routine_PAUSE.
450 NEXT N
460 RETURN
470 REM Now assemble BCD data from bridge to give a
480 REM value for the resistance.
490 LET D1=PEEK(&8010)
500 LET D2=10*PEEK(&8011)
510 LET D3=100*PEEK(&8012)
520 LET D4=1000*PEEK(&8013)
530 LET D5=10000*PEEK(&8014)
540 D=D1+D2+D3+D4+D5
550 REM Now work out the position of the decimal point
560 REM using the conductance bridge range switch setting,
570 REM stored in location &8015. (8015 HEX).
580 IF PEEK(&8015)=1 THEN GOTO 630
590 IF PEEK(&8015)=2 THEN GOTO 650
600 IF PEEK(&8015)=0 THEN GOTO 670 :REM Bridge fault.
610 IF PEEK(&8015)=8 THEN GOTO 690
620 GOTO 1280 :REM Bad data
630       R=10E7/D
640       GOTO 720
650                 R=10E6/D
660                 GOTO 720
670                           R=10E5/D
680                           GOTO 720
690                                     R=10E4/D
700                                     GOTO 720
710 REM R is value of resistance in Ohms.
```

```
720 RETURN
721 REM
722 REM Subroutine compares the measured temperature with
723 REM the requested value. If they are not the same
724 REM within the required tolerance limits then,
725 REM depending on whether the desired temperature is
726 REM above or below 4.2K, the pot heater is switched
727 REM on/off or the pot pumping line solenoid valve
728 REM is opened/closed.
729 REM
730 IF FLAG=2 THEN GOTO 810:REM Heater required T>4.2K.
740 IF T<(TR-TL) THEN GOTO 770:REM Temperature low.
750 IF T>(TR+TL) THEN GOTO 790:REM Temperature high.
760 GOTO 870
770 OUT 5,&81:REM Switch off solenoid valve instruction.
780 GOTO 870
790 OUT 5,&80:REM Switch on solenoid valve instruction.
800 GOTO 870
810 IF T>(TR+TL) THEN GOTO 840
820 IF T<(TR-TL) THEN GOTO 860
830 GOTO 870
840 OUT 5,&83:REM Switch off pot heater instruction.
850 GOTO 870
860 OUT 5,&82:REM Switch on pot heater instruction.
870 LET I=0
871 REM
872 REM Put temperature into format for writing to
873 REM digital display. First find the place of the
874 REM decimal point.
875 REM
880 IF INT(T)=0 THEN GOTO 920
890 T=T/10
900 I=I+1
910 GOTO 880
920 IF I>0 THEN GOTO 950
930 T=T/10
940 LET I=1
950 IF 10*(10000*T-INT(10000*T))>5 THEN T=T+0.0001:REM
Round up.
960 REM
970 REM Now POKE digits into memory scratchpad for
```

```
980 REM access by the machine code routine starting at
990 REM location &8000.
1000 REM
1010 T4=INT(10*T):REM Most significant digit.
1020 POKE (&8003),T4
1030 T=10*T-T4
1040          T3=INT(10*T)
1050          POKE (&8002),T3
1060          T=10*T-T3
1070                   T2=INT(10*T)
1080                   POKE (&8001),T2
1090                   T=10*T-T2
1100                            T1=INT(10*T)
1110                            POKE (&8000),T1
1120 REM Not forgetting the decimal point.
1130 REM
1140 POKE (&8004),(5-I)
1150 CALL &7C72:REM Machine code routine PUTDSP.
1160 IF FLAG=2 THEN GOTO 190:REM Go back to start.
1170 IF FLAG=1 THEN GOTO 270
1180 IF FLAG=0 THEN GOTO 110
1190 LR=0.4343*LOG(R):REM Temperature calibration sub-
routine, pot AB T>4.2K.
1200 T=1/((0.485/LR)-0.934+0.377*LR)
1210 RETURN
1220 LR=0.4343*LOG(R):REM Pot AB T<4.2K.
1230 T=1/((1.189/LR)-1.5686+0.5156*LR)
1240 RETURN
1250 LR=0.4343*LOG(R):REM Pot SP T<2K.
1260 T=0.02+10^((109.04/LR)-62.005+8.793*LR)
1270 RETURN
1280 LET K=K-1:REM Bad Data.
1290 IF K=0 THEN GOTO 1310
1300 GOTO 320:REM Read in fresh data.
1310 OUT 5,&04:REM Sound bleeper in control unit, there
are always some bad datas so occasional bleeping is an
indication that the system is working.
1320 LET K=10:REM Reset bad data counter.
1330 GOTO 1300
1340 END
```

APPENDIX 2
THE PULSE GENERATOR

A2.1 Introduction

In §3.10 the reasons for developing an advanced microprocessor based pulse generator were outlined. The circuit hardware of the resulting prototype is relatively simple, the real versatility and sophistication being in the software.

As stated in §3.10 the key feature of this design is that only two programmable mark/space generators are used, the idea being that while one is counting the other is being programmed for the next pulse/delay. To implement this approach the interrupt facility on the microprocessor is used. As its name suggests this is a facility whereby on receipt of a particular signal the CPU immediately suspends current operations and attends to the interrupting device.

The interrupt facility on the Zilog Z80 chip family is particularly powerful, it being of the vectored kind. This means that the interrupting device supplies a byte which forms the lower eight bits of an address to a location in memory where the starting address of the interrupt servicing routine is stored. This is one of the primary reasons for deciding to use this particular chip family in the instrument.

The complete pulse generator is constructed on five separate boards, each having its own specific function. These are interconnected via a 43 line backplane, see figure 3.17. What now follows is a brief description of the hardware, taking each board in turn.

A2.2 The CPU Board

The "nerve centre" of the system. This board is based around the Z80A CPU running at 4MHz. It contains the memory, 4K-bytes of ROM (read only memory) for program storage and 2K-bytes of RAM (random access memory) for data and stack storage. The ROM address

range starts at 0000H, that is where program execution starts after a CPU reset or power-up. The RAM address range starts at 1000H, immediately above the ROM. The contents of RAM are preserved during power down periods by the provision of a NiCd backup battery. The board, totally conventional in design, also contains the necessary address decoding for the memory, and the data bus buffering chips.

A2.3 The Keypad and Display Interface Board

Front panel control is via a 32 key pad and an 8 digit seven segment LED display. These are interfaced via the keypad and display board which is designed around the Intel 8279C. This chip connects directly to the CPU bus and it releases the CPU from the tasks of polling the keypad and strobing the display. It generates an interrupt when a key is struck and enters the keycode into an internal stack to be read by the CPU. Another stack which is written to by the CPU holds the display data.

A2.4 The Pulse Generating Board

This board is designed around five Z80A CTC's (Counter Timer Circuits) configured as two programmable mark space timers and a repeat timer. Each CTC contains four independent programmable 8-bit down counters but due to packaging limitations only three have their zero count outputs accessible and so are usable in this design. These chips interface directly to the Z80 CPU bus and can be programmed to generate interrupts when they reach zero count.

The 4MHz system clock is divided by four to give a board clock rate of 1MHz, this gives a minimum timing period of 1μs.

The basic mark or space timing module using a CTC is shown in figure A2.1. The operation is as follows : assuming the SR flip-flop is in the reset state and the inhibit line is inactive; the start trigger pulse sets the flip-flop thus allowing the clock pulses

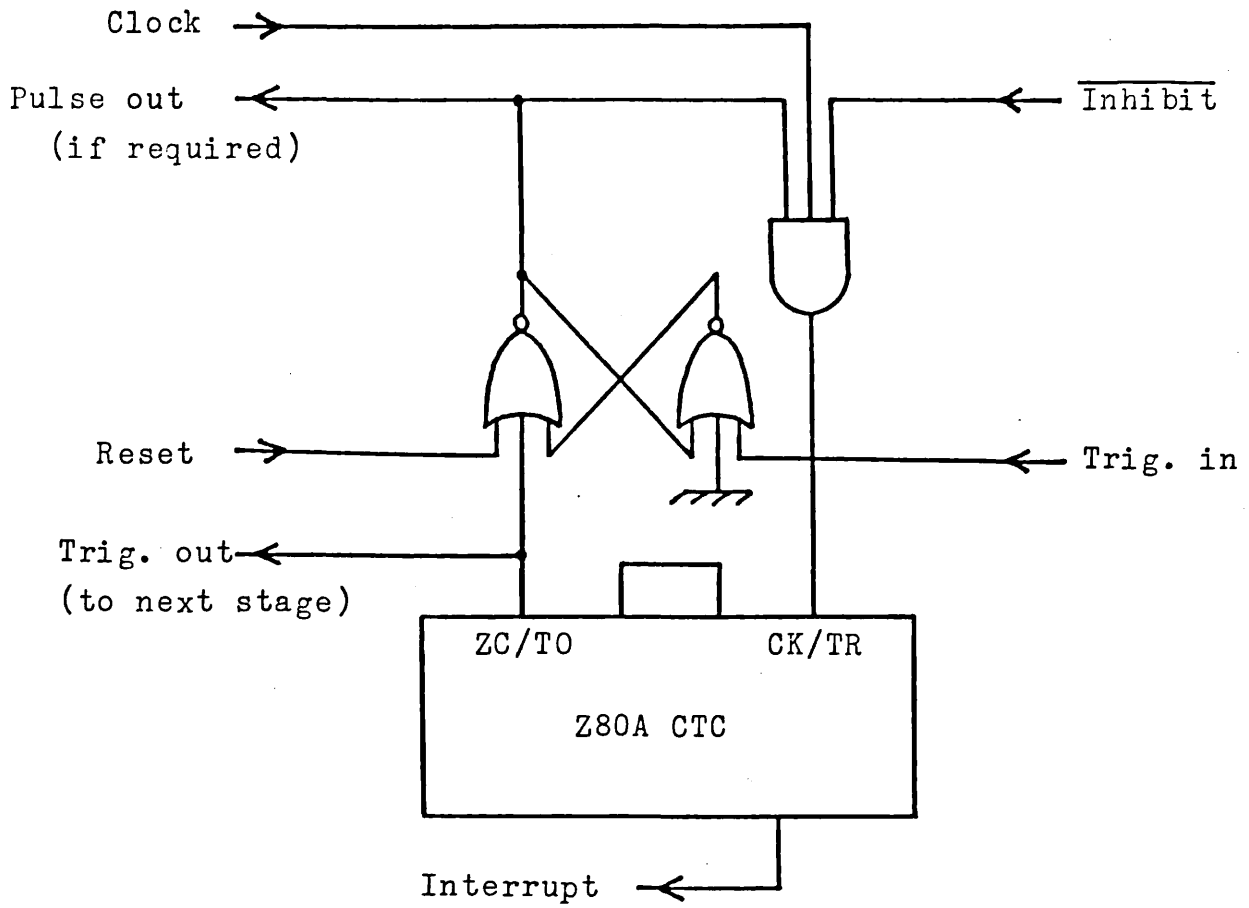

Timing diagram;

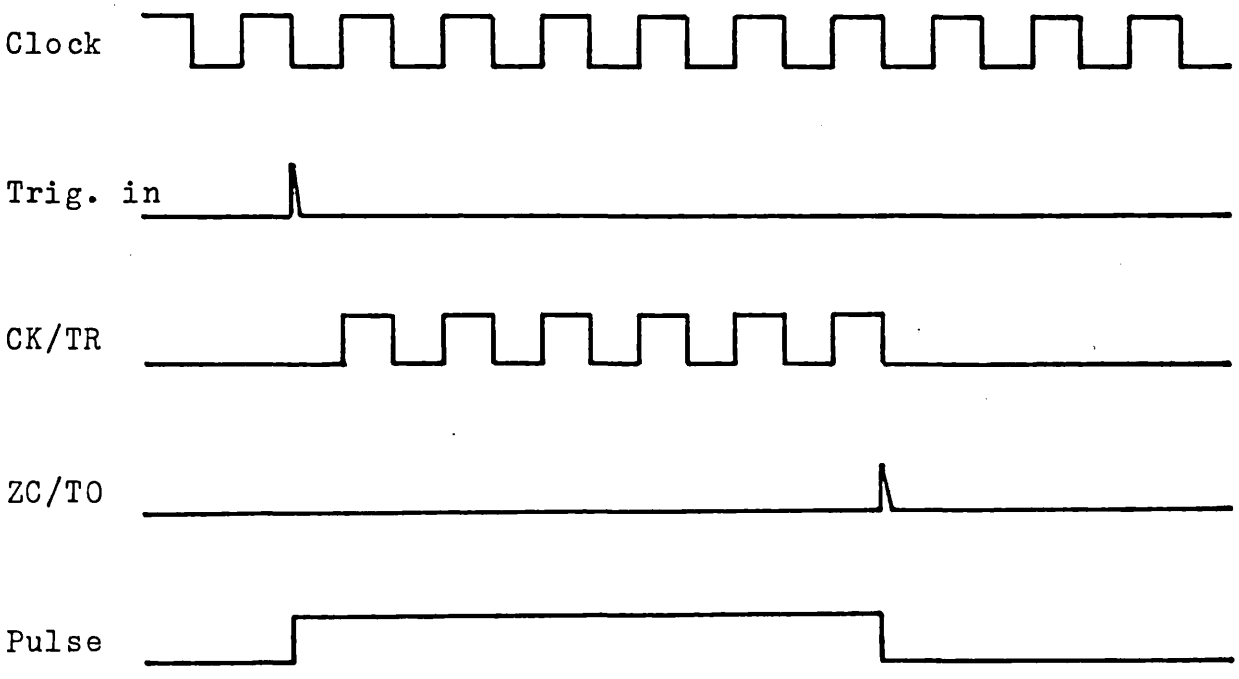

Figure A2.1, Pulse/Delay Timing Module, Using Z80A CTC.

to reach the CK/TR input of the CTC, two cascaded programmable counters are used the first being used as a programmable divider. After the programmed count has been completed a pulse is output from the ZC/TO pin on the CTC. This resets the flip-flop shutting off the clock and also triggers the next stage. Simultaneously with the zero count output the interrupt line on the CTC is pulled low indicating to the CPU that the count is completed and the CTC is ready for new data.

A mark/space timer consists of a pair of these modules cascaded, the sequence repeat timer uses just one but the clock is much slower allowing for repeat times of up to 100 secondsif T_1 is long.

A2.5 The Output Demultiplexing Board

The output from the pulse generating board consists of a train of pulses on a single line, for our purposes it is desirable to divert each pulse to a separate output and have the facility to combine two or more pulses on a common output. The output demultiplexing board provides these facilities. It consists of a counter, counting the pulses in the sequence, coupled to a demultiplexer. Each pulse is therefore routed to a separate output which is dependent on its position in the sequence. The counter is reset at the end of each sequence. Pulses are re-combined on a common output as desired by simply using a bank of switches.

A2.6 Pre-trigger and Remote Control Interface Board

This board performs two functions, it generates under software control the pre-trigger pulse and it contains the necessary circuitry to interface the pulse generator to a microcomputer. The interfacing circuitry is quite straight forward, it is based around a Z80A PIO (Parallel Input/Output) chip. This device interfaces directly to the Z80 system bus and provides two 8 bit bi-directional

ports plus handshake lines for interfacing.

The pre-trigger is a particularly useful facility, while being prohibitively complex to include in a conventional hard wired pulse programmer, it is relatively easy to incorporate in this microprocessor based design. To illustrate the need for this facility consider a $90^{o} - \tau - 180^{o} - \tau$ - echo experiment. Normally the oscilloscope or transient recorder is triggered by the 180^{o} pulse and the timebase adjusted so that the echo is within the field of view. As the time τ between the 90^{o} and 180^{o} pulses is increased the echo is observed to move across the screen to the right. It will eventually reach the edge of the screen necessitating a reduction in the timebase speed. It is possible, especially in cases where T_2 is long but T_2^* is very short, that the echo will be very narrow and resolution will suffer (too few horizontal channels of the digitizer to accurately define the echo). To overcome this problem the delayed timebase facility may be used, the timebase is then adjusted to give adequate resolution of the echo and the delay to place it in the field of view. Of course every time τ is changed it is necessary to adjust the timebase delay to re-position the echo. This can be very inconvenient especially if it is planned to automate measurements.

The pre-trigger overcomes these problems in the following way : given the oscilloscope or transient recorder timebase setting the CPU calculates the precise timing of the trigger pulse to place the echo dead centre on the screen. It then programs the counters in the two CTC's on the pre-trigger board which are arranged with some TTL dividers to produce the trigger pulse any time between 1μs and 10s, in steps of 1μs, after a given pulse in the sequence. Every time τ is changed the CPU automatically re-calculates the timing of the trigger pulse to keep the echo in the centre of the display screen.

A2.7 The Software

The bulk of the system software is concerned with the front panel control of the instrument. Starting at address 0000H, where execution starts after a reset, is a short routine which initializes the system. Execution is then suspended pending a non-maskable interrupt from the keypad interface. When this is received execution re-starts at 0066H where there is a routine which fetches the keycode and depending on what it is branches to the relevant subroutine.

The special feature, as far as this design is concerned, is the interrupt servicing procedure. When a CTC interrupts it is essential to re-program it in the shortest time possible as it is this time which limits the ultimate performance of the instrument. Every effort is made to speed up these routines even at the expense of ROM useage, for instance it is quicker to repeat a series of instructions n times than it is to make n calls to a subroutine comprising that same set of operations. The following brief extract of code is an interrupt service routine which loads one of the counters,

```
Clock    ISR :
Cycles   ; Interrupt service routine
                    ORG 0B00H     ; Starting address
                    CTC1 EQU 10H  ; Divider address
                    CTC2 EQU 11H  ; Counter address
                    CWD EQU 57H   ; Control byte
         ;
  4                 LD   A, CWD
 11                 OUT  CTC1, A
 11                 OUT  CTC2, A
  4                 LD   A,[1220H]; Desired count
         ; Stored in RAM location 1220H
 11                 OUT  CTC2,A
  4                 LD   A,[1221H]; Dividing factor
```

```
       11          OUT  CTC1,A
        4          EI              ; Enable interrupts
       14          RETI            ; Return from interrupt
Total  74
```

The routine takes 74T states, that is 18½μsec for a 4MHz Z80A. Clearly to allow for this time the minimum total mark/space timing period of the other generator must be about 20μsec . It is obvious therefore that the limit on performance at present is the speed of the CPU, not the speed of the counters.

A2.8 Future Developments

Continual advances in microelectronics are resulting in the availability of faster microprocessor chips. For instance the 8MHz version of the Z80, Z80H. Using one of these in the pulse generator would reduce by half the time taken to re-load the CTC's. Further improvements in CPU speed are likely in future. The use of a 16 bit CPU could double the data transfer rate provided that it executes instructions at the same speed as the 8 bit machine. However, the use of a 16 bit CPU would complicate hardware design and construction.

It is possible to construct using TTL integrated circuits programmable counters which are compatible with the CPU system in the pulse generator. These should have an improved performance over the CTC's used in the prototype in terms of accuracy and pulse length jitter. Such counters would be quite complicated in design compared to the CTC based mark/space generators, but only two such counters will be required in this pulse generator.

The imagination of the programmer and of course memory requirements are the only limits to the improvements that can be made to the facilities provided on the present design simply by expanding the software.

REFERENCES

[1] J. G. Dash, "Two Dimensional Matter". Scientific American, Vol. 228, No. 5, p.30 (May 1973).

[2] J. G. Dash, "Films on solid surfaces", (Academic Press, New York, 1975).

[3] M. H. Polley, W.D. Schaeffer and W.R. Smith, J. Phys. Chem., 57, 469 (1953).

[4] A. Thomy and X. Duval, J. Chim. Phys. Physiochem. Biol., 66, 1966 (1969) and 67, 286, 1011 (1970).

[5] S. Brunauer, P.H. Emmett and E. Teller, J. Amer. Chem. Soc., 60, 309 (1938).

[6] R. L. Elgin and D.L. Goodstein, Phys. Rev., A9, 2657 (1974).

[7] M. Bretz and J.G. Dash, Phys. Rev. Lett., 26, 963 (1971).

[8] M. Bretz, J.G. Dash, D.C. Hickernell, E.O. McLean and O.E. Vilches, Phys. Rev., A8, 1589 (1973).

[9] E. Lerner and J.G. Daunt, J.L.T.P., 10, 299 (1973).

[10] M. Bretz and J.G. Dash, Phys. Rev. Lett., 27, 647 (1971).

[11] D. C. Hickernell, E.O. McLean and O.E. Vilches, Phys. Rev. Lett. 28, 789 (1972).

[12] M. Nielsen, J.P. McTague and W. Ellenson, Journal de Physique, 38, C4 Supp. 10, 10 (1977).

[13] S. V. Hering, S.W. Van Sciver and O.E. Vilches, J.L.T.P., 25, 793 (1976).

[14] G. J. Goellner, J.G. Daunt and E. Lerner, J.L.T.P., 21, 347 (1975).

[15] A. D. Novaco, J.L.T.P., 21, 359 (1975).

[16] S. W. Van Sciver and O. E. Vilches, Phys. Rev. B18, 285 (1978).

[17] M. Bretz in "Monolayer and Submonolayer Helium Films" (Plenum Press, New York, 1973).

[18] M. Bienfait, J.G. Dash and J. Stoltenburg, Phys. Rev. B21, 2765 (1980).

[19] M. Santini, M.Cirera and G. Careri, Phys. Lett., 5, 102 (1963).

[20] M. G. Richards from "Phase Transitions in Surface Films" edited by J. G. Dash and J. Ruvalds (Plenum, New York, 1980).

[21] G. Careri, M. Santini and G. Signorelli, from "Low Temperature Physics", LT9, Vol. A, 364 (Plenum, New York, 1965).

[22] H. T. Weaver, J. Phys. Chem. Solids, 34, 421 (1972).

[23] D. J. Creswell, D.F. Brewer and A. L. Thomson, Phys. Rev. Lett., 29, 1144 (1972).

[24] R. J. Rollefson, Phys. Rev. Lett., 29, 410 (1972).

[25] J. Owers-Bradley, Ph.D. Thesis, University of Sussex (1978).

[26] D. C. Hickernell, D. L. Husa and J.G. Daunt, Phys. Lett. 49A, 435 (1974).

[27] S. G. Hedge, E. Lerner and J.G. Daunt, Phys. Lett. 49A, 437 (1974).

[28] S. G. Hedge and J.G. Daunt, J.L.T.P., 32, 765 (1978).

[29] K. Satoh and T. Sugarawa, J.L.T.P., 38, 37 (1980).

[30] D. C. Hickernell, D. L. Husa, J.G. Daunt and J.E. Piott, J.L.T.P., 15, 29 (1974).

[31] N. Ganguli and K.S. Krishnan, Proc. Roy. Soc. (London) A177, 168 (1941).

[32] B. P. Cowan, M.G. Richards, A.L. Thomson and W.J. Mullin, Phys. Rev. Lett., 38, 165 (1977).

[33] J. M. Kosterlitz and D.J. Thouless, J. Phys. C6, 1181 (1973).

[34] M. F.Secca, Ph.D. Thesis, University of Sussex (1983).

[35] A. Abragam,"The Principles of Nuclear Magnetism", (Oxford, 1961).

[36] C. P. Slichter, "Principles of Magnetic Resonance", (Springer-Verlag, Berlin, 1978).

[37] R. Kubo and K. Tomita, J. Phys. Soc. Japan, 9, 888 (1954).

[38] B. P. Cowan, J. Phys. C10, 3383 (1977).

[39] A. Landesman, Ann. Phys. Paris, 8, 53 (1973).

[40] R. Kubo, J. Phys. Soc. Japan, 17, 1100 (1962).

[41] N. Bloembergen, E.M. Purcell and R.V. Pound, Phys. Rev., 73, 679 (1948).

[42] E. L. Hahn, Phys. Rev., 80, 580 (1950).

[43] H. Y. Carr and E.M. Purcell, Phys. Rev., 94, 630 (1954).

[44] D. M. Brink and G.R. Satchler, "Angular Momentum", (London: OUP, 1968).

[45] H. C. Torrey, Phys. Rev., 92, 962 (1953).

[46] A. Avogadro and M. Villa, J. Chem. Phys., 16, 2359 (1977).

[47] A. A. Kokin and A.A. Izmeslev, Russian J. Phys. Chem., 39 309 (1965).

[48] B. P. Cowan, J. Phys., C13, 4575 (1980).

[49] J. H. Van Vleck, Phys. Rev., 74, 1168 (1948).

[50] W. J. Mullin, D.J. Creswell and B.P. Cowan, J.L.T.P., 25, 247 (1976).

[51] M. G. Richards, Adv. Mag. Res., 5, 305 (1971).

[52] R. Chapman and M. Bloom, Can. J. Phys., 54, 861 (1976).

[53] J. M. Delrieu, M. Roger and J.H. Hetherington, J.L.T.P., 40, 71 (1979).

[54] A. G. Redfield, Phys. Rev., 116, 315 (1959).

[55] B. Robertson, Phys. Rev., 151, 273 (1966).

[56] R. C. Wayne and R.M. Cotts, Phys. Rev., 151, 264 (1966).

[57] A. C. Rose-Innes, "Low Temperature Laboratory Techniques", (The English Universities Press, 1973).

[58] F. E. Hoare, L.C. Jackson and N. Kurti, "Experimental Cryophysics", (Butterworths, London, 1961).

[59] M. Waite and J. Angermeyer, "CP/M Bible", H.W. Sams (1983).

[60] D. I. Hoult and R.E. Richards, Proc. R. Soc. Lond., A344, 311 (1975).

[61] D. I. Hoult and R.E. Richards, J. Mag. Res., 24, 71 (1976).

[62] I. J. Lowe and C.E. Tarr, J. Phys. E.Sci. Instrum., 1, 320 (1968).

[63] I. J. Lowe and M. Englesberg, Rev. Sci. Instrum., 45(5), 631 (1974).

[64] D. I. Hoult, Rev. Sci. Instrum., 50(2), 193 (1979).

[65] F.N.H. Robinson, "Noise and Fluctuations in Electronic Devices and Circuits", (Clarendon Press, Oxford, 1974).

[66] "Mospower Design Catalog", (Siliconix Incorporated, Jan. 1983).

[67] "The Radio Amateurs Handbook", 60th Edition (American Radio Relay League, Newington CT, USA, 1983).

[68] J. D. Ellet, M.G. Gibby, V. Haeberlen, L.M. Huber, M. Mehring, A. Pines and J.S. Waugh, Adv. Mag. Res., 5, edited by J.S. Waugh (Academic Press, New York, 1971) pp.117-176.

[69] J. C. Culey, "Interfacing to Microprocessors", (Macmillan, 1983).

[70] Kaye and Laby, "Tables of Physical and Chemical Constants", 14th Edition (Longman, London, 1975) p. 20 and p. 51.

[71] B. P. Cowan and A.J. Kent, J.L.T.P., 57, 587 (1984).

[72] J. R. Zimmerman and W. E. Brittin, J. Phys. Chem., 61, 1328 (1957).

[73] B. P. Cowan, J.L.T.P., 50, 135 (1983).

[74] J. G. Dash in "Low Temperature Physics - LT13", Vol. 1, (Plenum, New York, 1972).

[75] R. L. Elgin, J.M. Greif and D.L. Goodstein, Phys. Rev. Lett., 41, 1723 (1978).

[76] B. P. Cowan, Ph.D. Thesis, University of Sussex (1976).

[77] D. P. Grimmer and K. Lusczynski, J.L.T.P., 30, 153 (1978).

[78] J. K. Kjems, L. Passell, H. Taub, J.G. Dash and A.D. Novaco, Phys. Rev., B13, 1446 (1976).